2808905045

REFERENCE ONLY

UNIVERSITY OF LONDON THESIS

Degree PhD Year 2006 Name of Author KENDREW Sarah

COPYRIGHT
This is a thesis accepted for a Higher Degree of the University of London. It is an unpublished typescript and the copyright is held by the author. All persons consulting the thesis must read and abide by the Copyright Declaration below.

COPYRIGHT DECLARATION
I recognise that the copyright of the above-described thesis rests with the author and that no quotation from it or information derived from it may be published without the prior written consent of the author.

LOANS
Theses may not be lent to individuals, but the Senate House Library may lend a copy to approved libraries within the United Kingdom, for consultation solely on the premises of those libraries. Application should be made to: Inter-Library Loans, Senate House Library, Senate House, Malet Street, London WC1E 7HU.

REPRODUCTION
University of London theses may not be reproduced without explicit written permission from the Senate House Library. Enquiries should be addressed to the Theses Section of the Library. Regulations concerning reproduction vary according to the date of acceptance of the thesis and are listed below as guidelines.

A. Before 1962. Permission granted only upon the prior written consent of the author. (The Senate House Library will provide addresses where possible).

B. 1962 - 1974. In many cases the author has agreed to permit copying upon completion of a Copyright Declaration.

C. 1975 - 1988. Most theses may be copied upon completion of a Copyright Declaration.

D. 1989 onwards. Most theses may be copied.

This thesis comes within category D.

☐ This copy has been deposited in the Library of UCL

☐ This copy has been deposited in the Senate House Library, Senate House, Malet Street, London WC1E 7HU.

C:\Documents and Settings\lproctor\Local Settings\Temporary Internet Files\OLK8\Copyright - thesis (2).doc

Lightweight deformable mirrors for ground- and space-based imaging systems

Sarah Kendrew

Thesis submitted for the Degree of Doctor of Philosophy
of the University of London

Department of Physics & Astronomy
UNIVERSITY COLLEGE LONDON

ProQuest LLC
789 East Eisenhower Parkway
P.O. Box 1346
Ann Arbor, MI 48106-1346

I hereby declare that the work presented in this thesis, unless otherwise specified, is my own.

[redacted]

To my wonderful family

In memory of Dr. Richard Bingham and Ms. Els Leemans, with much respect and gratitude

ABSTRACT

The next generation of ground- and space-based astronomical observatories will generate an increased requirement for lightweight and robust deformable optics. In space ultra-lightweight actively controlled mirrors will enable a continuing increase of aperture sizes, whilst large adaptive mirrors will become increasingly standard features in the optical design of adaptive optics-optimised Extremely Large Telescopes on the ground. This thesis presents results from a project to design, manufacture and test a prototype active mirror in a nickel-carbon fibre reinforced polymer (CFRP), which has been suggested in the literature to be a promising candidate material for such applications. Extensive finite element analysis results from gravitational sag and thermal models, as well as finite element-based predictions of the central actuator influence function profile, are presented. The main problems were encountered as a result of the in-mold nickel coating process, which resulted in residual form errors, and poor design of the support structures, leading to deterioration of the mirror surface quality. No fundamental reason ruling this material out for the use of precision deformable optics was identified. The finite element analysis results show significant promise for increased use of the method in optical design, as well as in integrated optical simulations for Extremely Large Telescopes.

CONTENTS

LIST OF FIGURES

LIST OF TABLES

CHAPTER 1

Lightweight optics in astronomy

> "In the middle of every difficulty lies opportunity."
>
> – Albert Einstein

Since the earliest developments in telescope optics in the 17th century, optical elements have steadily increased in size. The second half of the 20th century in particular has seen very rapid technological developments that have enabled astronomy to progress in leaps and bounds. Several telescopes with primary mirrors measuring 8-10 m in size are in operation today using highly advanced optical configurations; 1990 saw the launch of the first optical space telescope, the Hubble Space Telescope, with a primary mirror diameter of 2.4 m, which revolutionised our view of the Universe and enabled major advances in all areas of astronomy. Work is currently under way for the next generation of both ground- and space-based observatories.

In space, the successor to Hubble is planned for launch in 2013. The James Webb Space Telescope (JWST), optimised for operation in the infrared, will feature a 6.5 m diameter metallic deployable primary mirror. On the ground, the next generation of optical/IR observatories will use optics with sizes of the order of 30 to 100 m - a dramatic increase in size from those currently in use. All these projects pose strong challenges to engineers and scientists alike, but promise huge advances in astronomy, cosmology and planetary science.

1.1 Approaches to producing lightweight optics

Optical lightweighting has enabled the continued scaling up in size of astronomical observatories in space and on the ground in the last decades. The issue to address when producing lightweight optics is *how to save weight whilst maintaining a satisfactory mirror form*. For ground-based applications, a mirror's gravitational sag is given by (Rozelot, 1995):

$$W \propto \frac{\rho d^4}{D} \tag{1.1}$$

for a circular disk of thickness h where W is the deflection, ρ the material density, d the distance between supports (equal to the diameter for an edge support), and D is the plate's bending stiffness, given by

$$D = \frac{Eh^3}{12(1-\nu^2)} \tag{1.2}$$

with E the Young's modulus and ν the Poisson's ratio, giving $W \propto d$ for a given aspect ratio d/h. According to this law, scaling up telescope sizes also leads to increasing mirror thicknesses in order to maintain rigidity performance, and masses will quickly reach excessive values. Thus scaling up a 4 m diameter mirror to 16 m with a given aspect ratio, will increase the sag 4 times and the mass 64 times.

Reducing the weight of telescope optics, both for space- and ground-based observatories, has many advantages. For space missions, where the cost is strongly driven by weight, low weight imaging optics can save significant cost. Conversely a mission can add extra payload for a given cost. For ground-based telescopes the main advantage lies in the reduced overall telescope mass. A higher telescope stiffness can affect the guiding accuracy; guiding errors in turn blur the image and deteriorate the resolution (Enard *et al.*, 1996).

A lower-mass primary also has lower thermal inertia, allowing the mirror to reach thermal equilibrium with the surrounding air in a shorter time[1]. Parks *et al.* (1990) cite as a first approximation that the thermal response time of a mirror is directly proportional to the thickness of its faceplate. For traditional solid mirrors, this quantity increases linearly with thickness and further adds to the problems of gravitational sagging.

In space optics, the required stiffness is dictated by the launch conditions, in which the craft can be subjected to forces of up to 5g and vibrations. The main source of aberrations in orbit is thermal gradients which cause the mirror to distort (Angel and Woolf, 1998). The transition from the 1 g environment on Earth to zero gravity in space can also give rise to alignment and decentering problems.

The first suggestion of lightweighting telescope mirrors came as early as 1924 from the American optician Ritchey:

> "... how inefficient, how primitive it was to work with thick solid mirrors, obsolete mirror-curves, equatorial telescope-mountings ... requiring enormous domes and buildings, and similar anomalies in a progressive age." (McCray, 2004)

He suggested a 'cellular mirror', a primary mirror composed of thin glass ribs in between glass facesheets. His attempts to produce such a structure remained unsuccessful at the time (Enard *et al.*, 1996). Some 15 years later the first lightweighted mirror was brought into use with the Hale Telescope on Mt. Palomar. Composed of an open-back moulded Pyrex structure, the mirror measured 5 m in diameter and weighed 13 tons, 66% of its equivalent solid weight.

---

[1] the thermal properties of a mirror are, of course, strongly determined by the choice of material

Since then several strategies have been developed to reduce the mass of telescope optics. These method can be subdivided into active and passive methods. The passive methods are based on either removal of material, similar to the configuration by Ritchey, or by using innovative lightweight materials. Active methods use a form of shape control for the mirror faceplate, usually employing actuation methods to correct for any aberrations that arise during operation. Many mirrors in operation at telescopes today use one, or a combination of several, of these methods.

A first method of passive lightweighting relies on material removal methods, either by sparing volumes of material during casting with the use of mandrels, or mechanically drilling away material from the mirror's back face after production. The 640 mm diameter mirror for the Infrared Space Observatory (ISO) satellite was manufactured in this way (Rozelot, 1995). Mueller *et al.* (1990) report a weight-saving of around 85% using a fusion method, in which a rib structure is created by welding prefabricated thin plates to a faceplate. They also report an alternative method in the same publication; a 'slumping' technique using material removal, where thin plane-parallel plates are cut from conventionally manufactured glass castings. A high-temperature process then results in the required thin meniscus shape.

The same technique can be used to manufacture sandwich plate mirrors, where a back plate is added to the lightweighted structure to form a closed-back mirror structure. Matson and Mollenhauer (2003) describe a process under development at MSNW Inc. in the US in which arrays of near-zero thermal expansion glass microspheres are bonded to glass facesheets to create ultra-lightweight stiff sandwich mirrors. The use of small spherical core fillers as opposed to a rib structure should decrease the sagging in between supports.

Several disadvantages exist with these material removal solutions (Rozelot, 1995). Firstly, the method is difficult and often costly to carry out, especially for large diameters. Material removal post-casting implies a large expenditure of effort, which is not cost-effective. Second, the stiff rib structure produces a 'footprint' on the faceplate, i.e. maps out discrete regions of increased stiffness compared with the sections between the ribs. This can cause difficulties during the polishing process and a print-through on the final surface with sagging in between the supports. Parks *et al.* (1990) use plate bending theory for the case of a plate with clamped edges to derive an expression for the required minimum faceplate thickness t in mm of rib-supported lightweight mirrors from the maximum allowable light loss from the central maximum of the image f and polishing load, i.e. the maximum pressure applied to the faceplate during polishing, q:

$$t = \left(\frac{5.735 \times 10^2 q a^4}{\lambda E \sqrt{f}}\right)^{1/3} \tag{1.3}$$

where a is the separation of the ribs, E the Young's modulus of the mirror material and λ the light wavelength. f is derived from an approximation to the Strehl ratio:

$$f = \exp[-(\frac{2\pi\sigma}{\lambda})^2] \tag{1.4}$$

for small figure errors. Thus, f of 0.01 represents a 1% light loss from the central peak of the image.

Closed-back structures can improve the overall mirror stiffness. This approach, further strengthened with thickened edges, was used in the 8.4 m mirrors of the Large Binocular Telescope (LBT) and in the 2.4 m primary of the Hubble Space Telescope (HST) (Burge *et al.*, 2000).

A second passive lightweighting method is to use novel materials that have a higher specific stiffness, i.e. a higher stiffness-to-weight ratio, than traditional glass or metallic materials. From the middle of the 19th century until some decades ago glass was the preferred material for manufacturing telescope mirrors. Many types of glasses have been developed with favourable properties for telescope mirrors, such as low thermal expansion and a high chemical homogeneity, but the increased sizes and precision requirements have driven the search for alternative substrates. A detailed discussion of mirror materials in use or under investigation is found in section 1.2.

Active lightweighting entails the continued monitoring and control of the mirror using methods of actuation. The mirror thickness is greatly reduced with respect to the thickness required by the rigidity law of equation 1.2. Instead, the stiffness is provided by mechanical and/or electrical techniques. The main consequence of this method is that tolerances on mirror figure are greatly relaxed, as small deformations can be corrected in operation. The introduction of active control methods has allowed the development of advanced mirror configurations. The Very Large Telescopes (VLT), for example, use large monolithic membrane mirrors, manufactured by fusing an array of hexagonal segments, cut from carefully selected CTE-matched boules of the raw vitreous ceramic. The resulting slab was machined and then slumped over a mould to achieve a close-to-final shape (Mueller *et al.*, 1990).

The spin-casting method is used by the Steward Observatory Mirror Labs and utilises borosilicate glass (pyrex), which is cast in a mold containing friable ceramic forms creating empty volumes in the final glass structure for lightweighting. The whole furnace containing the mold is then spun to generate the curved optical surface. After the mirror is cooled and annealed, the friable ceramic forms are washed away with a high-pressure water-jet. The curved faceplate, outer wall and internal webs are all ¡ 50 mm thick, although the depth of the structure is of order of 1/6 of the mirror diameter. This thinness allows rapid thermal equilibration and prevents residual thermal anomalies from having much effect, despite the much higher CTE (than Zerodur) of borosilicate glass.

The Keck telescopes use active optics with a segmented primary mirror. The 10 m primary is made up of 36 hexagonal segments whose alignment is continually adjusted throughout the telescopes' operation. Though these mirror segments pose tough manufacturing and polishing demands, they are easier to handle and replace in case of failure (Rozelot, 1995).

Research into lightweight space optics is especially topical with the advent of a new generation of space-based observatories. The Hubble 2.4 m primary mirror made from low-expansion glass displayed an aerial density of 180 kg/m^2; scaling this up to the proposed 6.5 m size for its successor JWST the mirror alone would be too heavy for launch. A multi-million dollar program was started in 1998 to identify new material and manufacturing technologies aimed at reducing this to a mere 15-20 kg/m^2 for the JWST primary and developing segmentation and deployment technologies. This resulted in a selection of four mirror designs for implementation and testing.

Stahl (2003) and Bely (2000) give a good overview of the optical manufacturing requirements for future space telescopes. Using combinations of methods used in ground-based optics, the approaches fall into three categories (Bely, 2000): semi-rigid designs, actuated meniscuses and hybrid designs. The semi-rigid approach uses a lightweight material with traditional lightweighting methods of material removal to form open- or closed-back cored structures. These designs are completely passive and therefore require very stiff and thermally stable materials.

The actuated meniscus approach is essentially an active optics solution, where low spatial frequency errors are corrected by actuation of the mirror faceplate. A big advantage is that the rigid backing structure need not have an optical surface quality or matching coefficient of thermal expansion (CTE) with the faceplate. The hybrid designs feature a thin reflective faceplate cemented to a stiff lightweight backing structure. This eliminates the need for actuators but does require the materials to have closely matched thermal expansion coefficients over a range of temperatures to secure a strong bond.

Several 10 m-class telescopes using segmented primary mirrors are currently under construction, such as the Southern African Large Telescope (SALT), and the Gran Telescopio Canarias (GTC). There is in principle no limitation on the maximum size of a segmented mirror; in practice, however, timescales and cost will impose an upper limit.

In summary, the next generation of observatories on the ground and in space face increasingly high demands for mirror quality, cost and weight. They will feature optical systems that combine several of the lightweighting methods presented here using active control or cored structures in combination with novel materials.

This chapter will examine the available methods for producing lightweight optics. It will outline the requirements for optical materials for both space- and ground-based applications and discuss the candidate materials for astronomical optics. One class of materials, that of carbon fibre composites, will then be discussed in more detail. Finally, the chapter gives an outline of the project presented in this thesis.

1.2 Mirror materials

The essential characteristics of any candidate material for large ground- or space-based optical mirrors are as follows (Enard *et al.*, 1996):

- manufacturability in large pieces;
- good polishability;
- good mechanical strength;
- good thermal conductivity; and
- very low thermal expansion.

For space applications, the materials' behaviour at cryogenic temperatures is often an important factor, as well as the CTE profile over large thermal gradients. This is illustrated in figure 1.1, which shows the CTE profile of several materials at cryogenic temperatures.

Material experimentation has been ongoing for more than a century, but only since the 1970s has serious research into non-glass materials been carried out. Problems with the manufacture and polishing of the new 8-10 m class mirrors was foreseen at the time, and this sparked developments using alternative materials. This section will give an

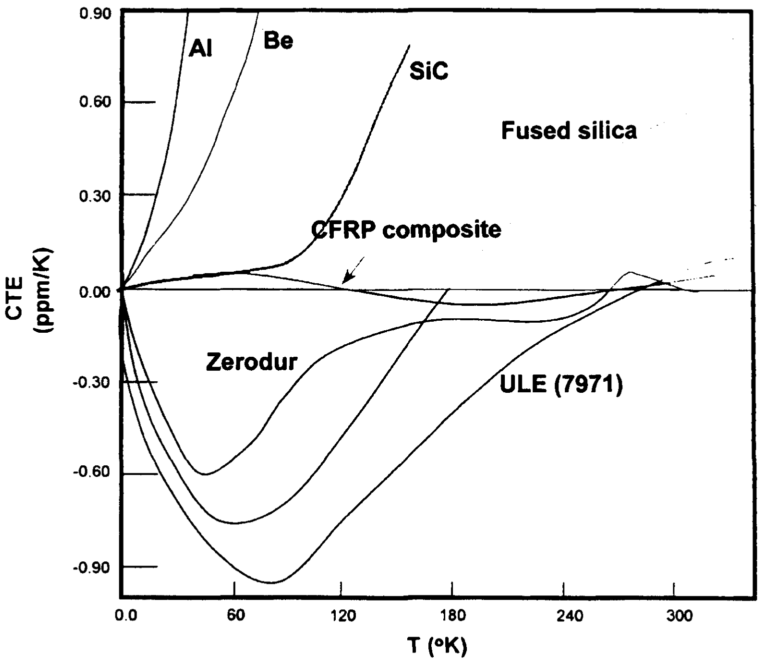

Figure 1.1: Thermal expansion profiles of candidate lightweight mirror materials (Abusafieh *et al.*, 2001).

overview of the three categories of materials that are currently used in telescope optics or under investigation for such purposes: glasses and ceramics, metals, and composites. Table 1.1 at the end of the section shows a summary of these materials and their properties.

1.2.1 Glasses and ceramics

Until the mid-20th century, glasses and ceramics were the materials of choice for telescope mirrors. The main constituents of this category include borosilicate crown glass (also known as Pyrex or BK7 glass), fused silica and ultra low-expansion fused silica (ULE), Zerodur ceramic glass and silicon carbide. The main advantages of glasses are that they are relatively easy to grind and polish, and from their long tradition of use in telescope mirrors the largest amount of experience is available. This is however a large class of materials and properties can vary quite significantly between the different types.

Traditional glasses such as borosilicate glass have relatively high CTEs (around $3 \times 10^{-6}/^{o}C$) and low thermal conductivity, which makes it less than ideal for making large mirror blanks, as thermal gradients will spread very slowly through the volume. Fused silica has a much lower CTE of around $1 \times 10^{-8}/^{o}C$ (Rozelot, 1995). The intrinsic variation of these materials' CTE can however be of the same magnitude as the CTE value itself, which can affect the system's optics.

An additional complication is the intrinsic inhomogeneity of the material. Large thick substrates can have a high number of cracks, fissures or bubbles which can cause polishing and grinding difficulties. However, low expansion glasses are still good candidates for many optical applications, and manufacturers continue to publish promising results for producing ultra-lightweight glass mirrors (see for example Hobbs *et al.* (2003)).

To overcome these problems novel glass and glass ceramic materials such as Zerodur and silicon carbide (SiC) were developed. Zerodur was developed at Schott in Germany in the late 1960s. Its near-zero thermal expansion at ambient temperature and excellent homogeneity properties have made it the material of choice for primary mirrors of large ground-based telescopes; using the spin-casting technique described in the previous section, Zerodur was used to fabricate the lightweight primary mirrors of the VLT measuring 8.4 m in diameter. At cryogenic temperatures, however, its CTE shows a marked increase in magnitude, making it unsuitable for many space applications. The CTE profile of Zerodur is shown in figure 1.2.

The ceramic SiC is one of the newest members of this category. With its high stiffness, low thermal expansion, high thermal conductivity and excellent environmental stability, it is one of the best candidates for high-precision astronomical optics (Wilson, 1999, vol 2). As its CTE remains constant at cryogenic temperatures, SiC technology is being increasingly taken up by future space and airborne observatories, such as Herschel, which will have a 3.5 m primary, and the Stratospheric Observatory for Infrared Astronomy (SOFIA), whose secondary mirror was made from SiC.

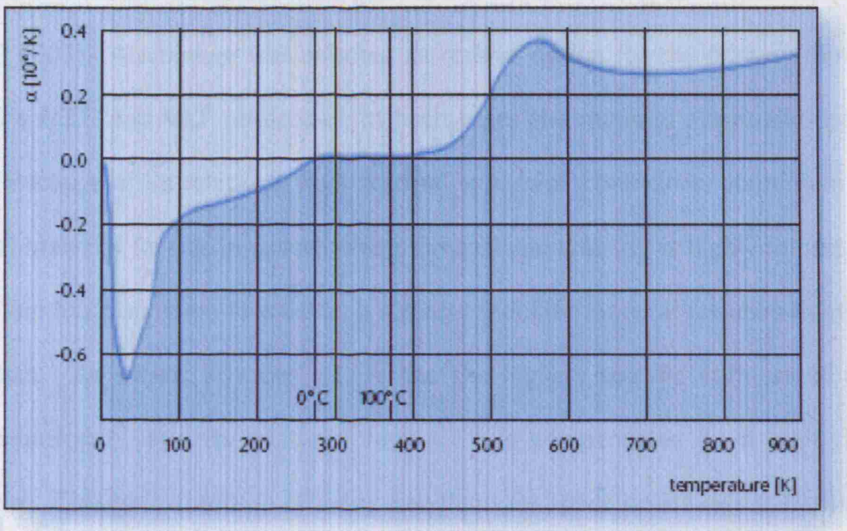

Figure 1.2: Plot of the thermal expansion profile of the glass ceramic Zerodur (Glaswerke, 2006).

1.2.2 Metallic materials

Two metallic materials, aluminium and beryllium, have especially promising properties for the manufacture of astronomical mirrors.

First, aluminium is a very well-known and -characterized material. Its lower stiffness and higher thermal expansion are compensated by a high thermal conductivity, which allows the mirror to reach a thermal equilibrium very rapidly. Aluminium blanks are also relatively easy to manufacture, figure and coat with nickel, whose CTE it closely matches, minimizing any bimetallic effects. In addition, for active control actuators can be screwed directly into the faceplate, foregoing the need for cemented bonds; its high conductivity eliminates the occurrence of high spatial frequency distortions with temperature variations. Manufacture is also fast, relatively simple and cost-effective, and aluminium's resistance to fracture makes it easier to handle than glass.

Wilson (1999, vol. 2) and Rozelot (1995) amongst others argue that the barriers to the use of aluminium for ground-based telescope mirrors are not technical but due to conservatism, although questions have been raised about its long-term stability (Andersen *et al.*, 2003). Aluminium was selected as reserve option for the primary mirrors of both ESO's NTT and VLT telescopes; in both cases the material eventually used was Zerodur. Because of its relatively high thermal expansion coefficient, aluminium is not an optimal material for use in space, where dimensional stability is highly important.

Beryllium has also come forward as a strong candidate material for ultra-lightweight space optics. As shown in table 1.1, it has the highest specific stiffness of all the candidate materials, and its relatively high CTE is compensated by a high thermal conductivity. Though a tradition of using beryllium for space optics exists, dating back to the 1983 InfraRed Astronomical Satellite (IRAS) mirror, use of the material has been limited because of its high cost and the toxic nature of the powder residues from figuring. Advances in manufacturing techniques have, however, increased the safety aspects of working with beryllium, and the material has been used in several high-profile projects in space and on the ground with good results.

The four secondary mirrors for the VLT telescope are made from beryllium. The most recent high-profile space mission to employ the material for its optics is the 0.85 m Spitzer infrared observatory, launched in 2003. Following a rigorous selection process by NASA, it was also selected as material for the 6.5 m lightweight deployable primary for JWST. Parsonage (2004) reports on the details of the beryllium grade to be used and manufacturing techniques for these optics.

1.2.3 Composite materials

Matthews *et al.* (2003) defines composite materials as "any material that is a combination of two or more distinct constituents". This definition covers a wide variety of materials, including concrete and plywood, as well as modern man-made composites such as fibre-reinforced plastics. The main advantage of these materials is that the best properties of each of the constituents are combined in the composite to produce a material with appropriate physical properties for a given application. Section 1.3 will provide a very detailed description of the structure and properties of composite materials; few details will therefore be presented here of the mechanical and thermal behaviour or manufacturing methods.

Several types of composite materials have been identified as candidates for astronomical optics. They can roughly be categorized according to their matrix element, which can be a ceramic, polymer or metal. Several hybrid mirror designs featuring both traditional materials and composites have also been reported in the literature.

The most common type of composite used for optics are the carbon fibre-reinforced polymers (CFRP). These materials exist in many fibre-matrix combinations and are commonly used in the aerospace industry for ultra-lightweight heat resistant structures. Table 1.1 shows the basic material properties for a typical CFRP. These materials especially are discussed in great length in the next section, so their properties will not be discussed here.

Much research into CFRP optics has been presented in the literature in the last 20 years, originally driven by the need for lightweight optics for space applications (Chen *et al.*, 1998; Chen *et al.*, 2000), but more recently focusing on the manufacture of large lightweight deformable mirrors for ground-based telescopes (Bennett *et al.*, 2004; Ozaki and Hahn, 2003). Hybrid designs featuring low-expansion glass on a composite support for space applications have also been proposed (Burge *et al.*, 2000). CFRP technology for optics lies at the basis of the work presented throughout this thesis, and other work in this field will be discussed at length in chapter 2. So far no ground- or space-based observatories have made use of CFRP mirrors as questions remain over the long-term stability of these materials.

Carbon fibre-reinforced silicon carbide, also known as C/SiC or Cesic, is a composite consisting of a SiC matrix reinforced with randomly oriented carbon fibres. Contrary to the traditional lay up manufacturing process, which is explained in more detail in section 1.3.2, C/SiC is produced by chemical liquid silicon infiltration of a carbon/carbon greenbody - a porous high-strength, low-density material that can be precisely machined into complex shapes (Krödel, 2004). The infiltration method incurs a very low post-cure dimensional change (0.2%) and the resulting material displays the a similar specific stiffness to CFRP but with higher thermal conductivity and zero moisture uptake (Devilliers and Krödel, 2004). The mirror blank can then be coated with a variety of materials for polishing (Bauereisen *et al.*, 1995). Krödel (2004) presents test results of the thermal expansion of C/SiC, showing a strongly decreasing CTE from 300 to 20 K, but below 120 K it remains highly stable, making it suitable for cryogenic applications.

1.2.4 Summary

Table 1.1 below shows an overview of material properties of the mirror substrate materials discussed in this section.

In summary, the low expansion glasses traditionally used for telescope mirrors still hold a strong position in the industry, mainly because of their well-characterized behaviour and manufacturing methods. The zero-expansion glass ceramic Zerodur remains for the time being the preferred material for large monolithic or segmented substrates for ground-based applications following good results with existing telescopes such as VLT. However, the development of new manufacturing and coating techniques has brought several other promising candidates, most notably silicon carbide, beryllium and a large class of composites.

In space material experimentation has a longer history, with research driven to a large extent by the two major optical space observatory projects, HST and JWST. Whereas conservatism in the industry has so far retained low-expansion glasses and Zerodur as the materials of choice, the new generation of space observatories looks likely to adopt new technologies such as beryllium and C/SiC to accommodate increasingly large optics in advanced deployable architectures. For operation at IR wavelengths, the material's

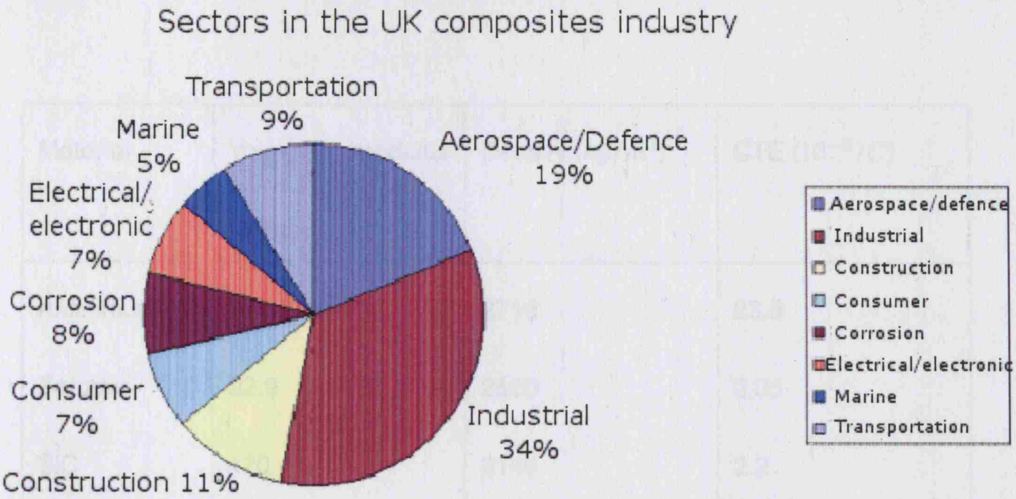

Figure 1.3: Market share of various sectors of the UK composites industry, year 2000 (data from Sims and Bishop (2001)).

stability at cryogenic temperatures is of high importance (see figure 1.1).

The next section will examine the class of composite materials in more detail as CFRP forms the basis of the work presented here. Special emphasis is placed on their use for the manufacture of optics and aerospace structures.

1.3 Carbon fibre composites

Fibre-reinforced composites can be found in a huge variety of commercial applications: from tennis rackets, skis and bicycles through automobile and aviation components to bridges. A study carried out by the National Physical Laboratory (NPL) and NetComposites for the UK Department for Trade and Industry (DTI) in 2001 (Sims and Bishop, 2001) showed that the UK composites industry in 2000 generated an annual revenue of £510 million against shipments of 240,000 tonnes, and comprises of roughly 1000 companies, mostly small- to medium-sized enterprises (SMEs). Figure 1.3 shows the breakdown of sectors served by the UK industry.

The composites discussed in the context of the research detailed in this thesis are

Material	Young's modulus (GPa)	Density (kg/m^3)	CTE ($10^{-6}/C$)
Aluminium	71	2710	23.9
Zerodur	92.9	2520	0.05
SiC	420	3140	2.2
Cesic	220	2650	2
CFRP	101	1170	0.2
Beryllium	300	1850	11.5
Material (ctd.)	CME @ 35% RH (10^{-6})	Thermal conductivity (W/mK)	Specific stiffness ($N.m/kg$)
Aluminium	0	167	26.2
Zerodur	0	1.6	36.9
SiC	0	180	133.8
Cesic	0	125	83
CFRP	9-25	14	83
Beryllium	0	200	162.2

Table 1.1: Summary of properties of the main mirror candidate materials at room temperature.CME @ 35%RH is the coefficient of moisture expansion at 35% relative humidity, usually expressed as parts per million.

of the latter type of materials, namely composites of synthetic materials, as these offer the best advantages for astronomy applications.

Fibre-reinforced polymers (FRP) display properties useful to a huge range of applications. The most commonly cited are low density, a high modulus and high strength. However, the advantages of this material class stretch far further: versatility, low thermal expansion, dielectric properties and corrosion resistance are other reasons for their popularity in industry. Within the category of FRPs many different materials have been developed. This section will examine this class of materials, their macro- and micromechanical properties, and issues with and techniques in modelling their behaviour.

1.3.1 Fibre and matrix materials

The class of composite materials is exceedingly large due to the many types of fibres, matrices and composite configurations. New materials are continually being developed with properties tailor-made to specific applications. Many different manufacturing techniques also exist, for the production of fibres as well as laying up the composite. This section will summarize the different types of materials used in the three main constituents of a composite structure - the matrix, fibre reinforcement and the core material - and compare their typical properties. The aim is to give an overview of the broad categories of materials, their strengths and applications, rather than a comprehensive list.

1.3.1.1 Matrix systems

The property requirements for matrix materials fall into 4 categories (Cripps, 2005):

Mechanical behaviour. A good matrix should have a high stiffness (Young's modulus) and a high strain to failure to prevent if from being overly brittle.

Adhesive properties. Good adhesion between the fibres and the surrounding matrix is essential to prevent cracking or debonding.

Toughness properties.[2] A low toughness will make the matrix more prone to cracking or, when cracks occur, allow the cracks to propagate more easily.

Environmental properties. A composite matrix should provide good resistance to the environment and any aggressive substances it is likely to come into contact with.

Figure 1.4 shows a summary of these materials and their uses.

Three main classes of materials are used as matrices in composites. First, metal matrix composites use materials such as aluminium with fibre reinforcements. These materials are most commonly used in the automotive industry. Materials such as graphite or boron fibre-reinforced aluminium, because of their good thermal stability and high stiffness, have also found application in spacecraft such as the Hubble Space Telescope and the Space Shuttle Orbiter (Rawal, 2001).

Second, ceramic matrices are used specifically in extreme temperature environments, such as aircraft fuel tanks or cryogenically cooled instruments. Silicon carbide, discussed in section 1.2, is an important member of this class, as well as its reinforced version, carbon fibre-reinforced SiC, C/SiC or Cesic.

The largest category of matrix materials used in composites is that of the polymers or resins. All materials in this large class are composed of long chain-like molecules consisting of many repeating units. Thermoplastic resins, such as nylon, can repeatedly be melted by heating and re-hardened, without any loss of material properties. This attribute clearly eliminates applications involving high-temperature environments. Conversely, thermoset resins, once hardened, will not melt again at raised temperature. Beyond a critical temperature, however, called the glass transition temperature T_g, their properties will degrade significantly but reversibly (Cripps, 2005). Matthews *et al.* (2003) estimate that around three quarters of all polymer matrices used are thermosets. Rubbers form another large family of polymers.

One class of thermosets is the polyesters. Incorporating a wide range of materials, polyesters are the cheapest resins on the market with moderate strength properties compared with other resins. Several additives are required to allow polyesters to cure, or harden. They are the most common matrix material in the marine industry (Cripps, 2005). Stiffer than polyesters are vinyl esters. These are similar in molecular structure to polyesters but display a better resistance to water and chemical agents. Typical applications include pipelines, chemical storage tanks, and protective coatings for polyester resin composites.

The polymer class favoured by the aerospace industry is that of the epoxies. Out of all the common polymer types epoxies display the best mechanical properties, resistance to environmental degradation, adhesion and water resistance. They also display much less shrinkage post-cure, giving a better surface finish. For precision applications, however, questions remain over the long-term dimensional stability of these materials because of their non-trivial moisture absorption which can lead to hygrothermal strain and loss of stiffness properties. Figure 1.5 shows the moisture absorption profiles of some common resins. Quantification of this effect is important when designing composite structures.

An advanced resin type, cyanate ester, displays a higher stiffness, better temperature stability and low moisture uptake (see figure 1.5) and is fast becoming the new matrix material of choice for space applications (Abusafieh *et al.*, 2001).

1.3.1.2 Reinforcement materials

The role of the reinforcing fibres is to improve the mechanical properties of the matrix. This section will list some of the most common materials used for reinforcing matrices in composites, as well as the forms they come in. Each different type of fibre affects the composite's properties in its own way. The main factors therein are:

1. the fibre's individual mechanical properties;
2. the interface interaction between fibre and matrix material;
3. the amount of fibre in the laminate (the fibre volume fraction, FVF);

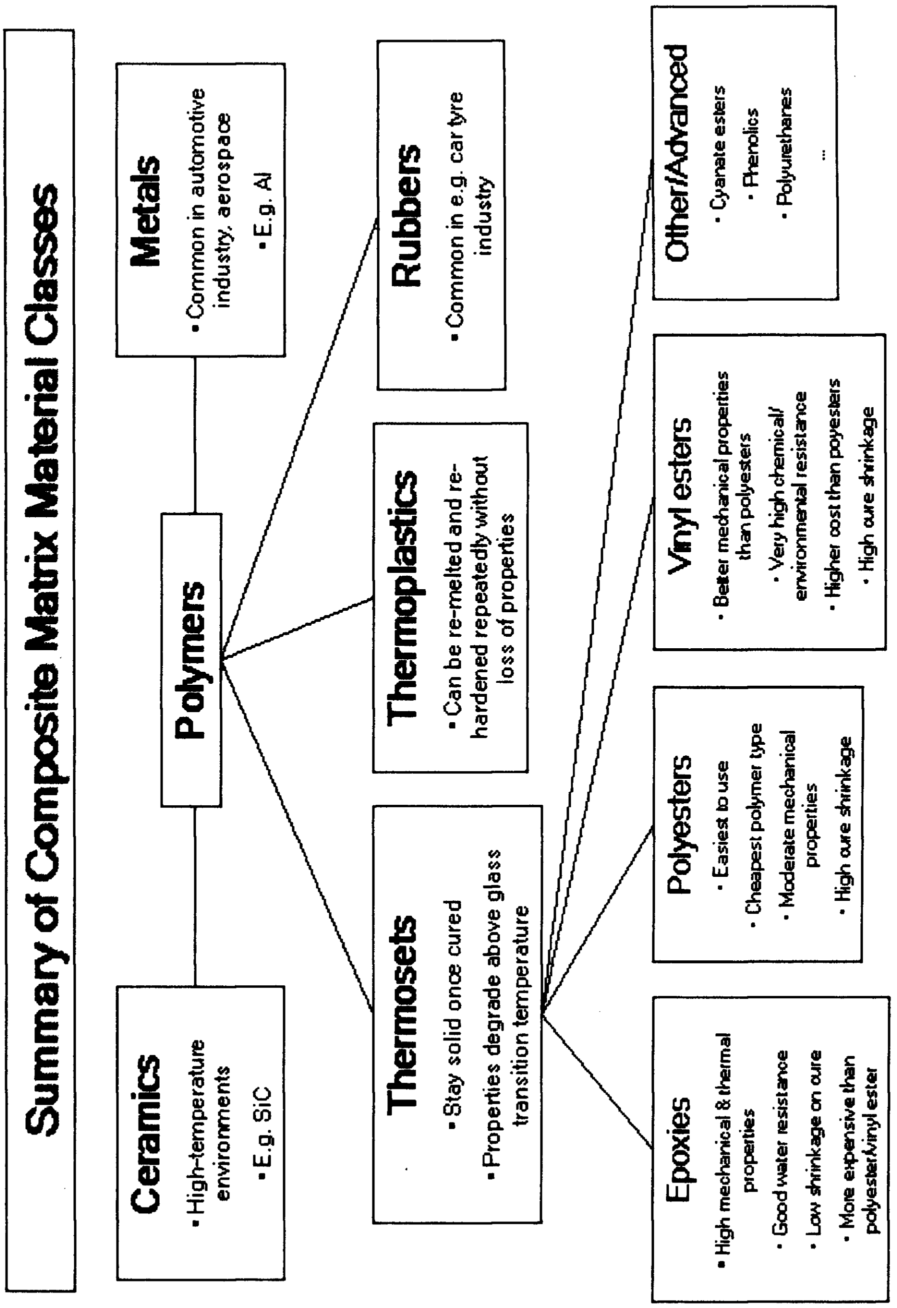

Figure 1.4: Schematic summary of matrix materials used in composites.

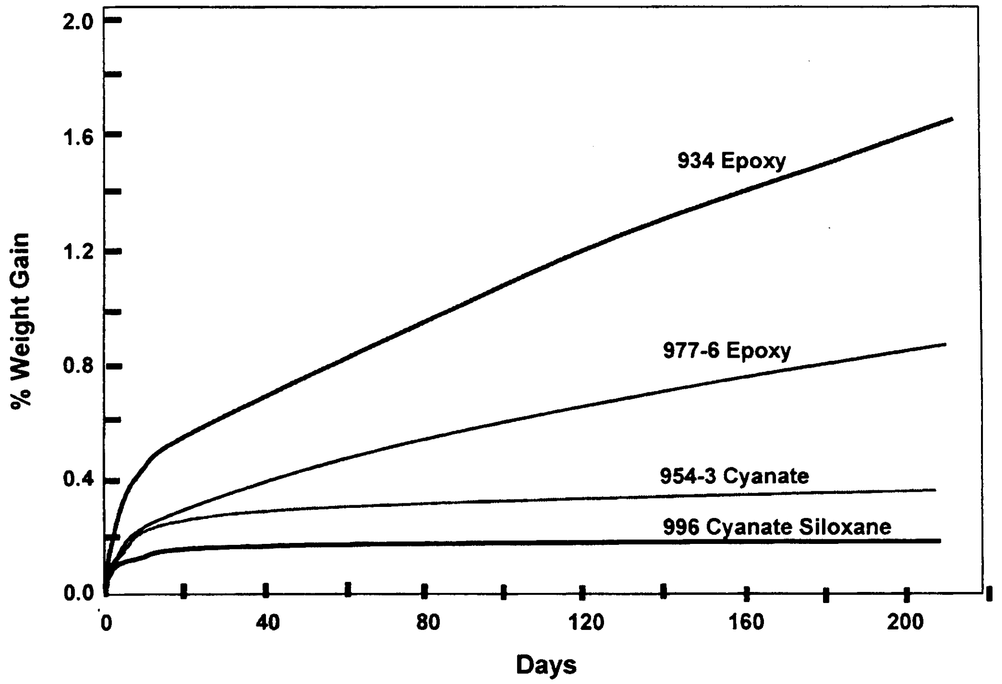

Figure 1.5: Moisture absorption curves for selected resins at room temperature and 50% relative humidity (Abusafieh *et al.*, 2001). 934 epoxy is an early space-qualified epoxy; 977-6 epoxy is toughened and more versatile; 954-3 cyanate is a typical cyanate ester; and 996 cyanate siloxane belongs to a recently developed class of ultra-low absorption cyanates.

4. the orientation of fibres in the matrix.

Points 2 and 3 are largely influenced or determined by the particular manufacturing process and surface finish of the fibre used. Details of these are beyond the scope of this thesis. The effect of fibre orientations within the laminate, however, was investigated as part of the work presented here. The directional aspect of fibres in a composite introduces a non-isotropy in the material's mechanical behaviour. This effect will be discussed in more detail in section 1.3.2.

The most common materials used as fibre reinforcements are glass, aramid and carbon. Table 1.2 shows a relative comparison of the three types for some important properties in composites mechanics.

Glass fibre. These fibres are made from a blend of quarry products, such as sand, kaolin and limestone. Several types of glass fibre exist for different applications, e.g. E-glass, an alkali-free alumino-borosilicate glass, for electrical applications and C-glass, which was developed for chemically corrosive environments.

Aramid fibre. Aramid fibres are man-made organic polymers. They are usually referred to by the ubiquitous proprietary term Kevlar. They have a high specific strength and excellent impact resistance, and are best known for their use in ballistic applications.

Carbon fibre. Carbon fibres are the best known of the reinforcing materials and can be manufactured from a variety of organic precursors, e.g. polyacrylonitrile (PAN), pitch or cellulose. They have the highest specific stiffness of the commercially available fibres as well as excellent resistance against corrosion and fatigue. They are more brittle than aramid fibres.

1.3.1.3 Core materials

Sandwich structures are widely used in composites manufacturing. The inclusion of a lightweight core effectively increases the laminate's bending stiffness without adding significant weight. The most important property for core materials is their shear strength and stiffness. The following list shows some of the most common materials (Cripps, 2005; Hile, 2005).

Rigid polyurethane foams. This is a very broad category incorporating many different types of core materials. Many polyurethanes, however, are brittle and tend to shed dust, which limits their usefulness.

Polyvinyl chloride (PVC) foam. These foams are popular in marine applications because of their moisture resistance. They also have a good fatigue life, bond strength with many types of resins, and are resistant to solvents such as fuels.

Property	Aramid	Carbon	Glass
High tensile strength	B	A	B
High tensile modulus	B	A	C
High compressive strength	C	A	B
High compressive modulus	B	A	C
High flexural strength	C	A	B
High impact strength	A	C	B
Low density	A	B	C
High fatigue resistance	B	A	C
Low thermal expansion	A	A	A
Low cost	C	C	A

Table 1.2: Comparison of different fibre types (from Cripps (2005)), where A represents optimal performance.

Honeycomb structures. Honeycomb panels can easily be manufactured and processed into flat or curved sheets. They require high-performance resins because of the smaller bonding surface. Aluminium honeycombs have the highest strength to weight ratios but display irreversible deformations on impact. Nomex, a Kevlar-based paper, is very expensive but highly popular for its good mechanical properties, low density and long-term stability. Thermoplastic materials, such as polypropylenes and polycarbonates are also used for honeycomb cores.

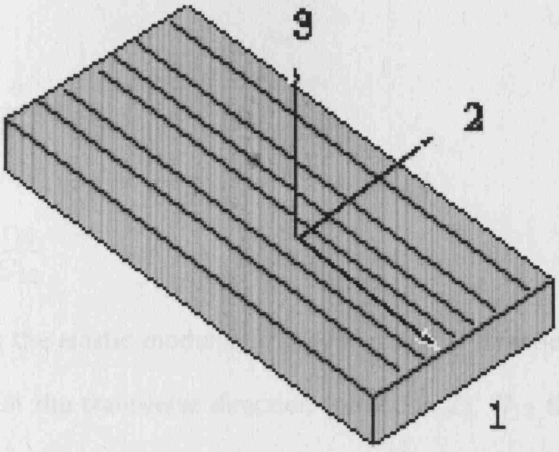

Figure 1.6: Diagram of a UD composite showing axes convention (from UGSPLM (2002)).

1.3.2 Fundamentals of composites

The simplest way of representing a fibre-reinforced composite is as a single sheet with fibres running continuously and parallel in one direction. This is termed a *unidirectional* (UD) composite. In characterizing the material it is convenient in the first instance to employ a macro-mechanical approach, i.e. to disregard the properties of the constituent materials and their interactions and consider the sheet as a material in itself. The key point with this UD composite is that it is not isotropic. The stiffness in the direction along the fibres, the longitudinal direction, is distinctly different from that in the transverse directions. The UD composite is said to be *transversely isotropic* or *orthotropic*. Figure 1.6 shows a diagram of the axes labelling convention used in the rest of this section. Axes 1, 2 and 3 are called the *principal axes*.

Whereas an isotropic material can be fully defined by just two quantities, the Young's modulus E and Poisson's ratio ν, an orthotropic material requires four elastic constants: the moduli in longitudinal and transverse direction E_{11} and E_{22}, Poisson's ratio ν_{12} and shear modulus G_{12}. For stresses applied to the UD composite along the principal axes, the stress-strain relation reads as follows:

$$\begin{aligned} \epsilon_1 &= \frac{\sigma}{E_{11}} - \nu_{21}\frac{\sigma_2}{E_{22}} && (1.5) \\ \epsilon_2 &= -\nu_{12}\frac{\sigma_1}{E_{11}} + \frac{\sigma_2}{E_{22}} && (1.6) \\ \gamma_{12} &= \frac{\tau_{12}}{G_{12}} && (1.7) \end{aligned}$$

where E_{11} is the elastic modulus in the longitudinal direction (direction 1), E_{22} the elastic modulus in the transverse direction (direction 2), G_{12} the shear modulus in the 1-2 axes and ν_{12} and ν_{21} the major and minor Poisson's ratios respectively. ϵ represents strain, γ the shear strain, and σ the stress components. In matrix form these relations become:

$$\boldsymbol{\epsilon_{12}} = \mathbf{S}.\boldsymbol{\sigma_{12}} \tag{1.8}$$

where

$$\mathbf{S} = \begin{bmatrix} \frac{1}{E_{11}} & \frac{-\nu_{21}}{E_{22}} & 0 \\ \frac{-\nu_{12}}{E_{11}} & \frac{1}{E_{22}} & 0 \\ 0 & 0 & \frac{1}{G_{12}} \end{bmatrix} \tag{1.9}$$

which is known as the compliance matrix.

When the load is applied at an angle to the material's principal axes, a transformation matrix must be included in the calculations to account for the coordinate system rotation. If the orientation of the load, as well as the composite's UD properties, are known the lamina's rotated stiffness can be calculated.

Composite structures are usually fabricated from multilayer composites known as laminates. These are composed of a stack of individual layers ordered in a given sequence, called the *lay-up*. The UD type is but one of many. In the case of fibre-reinforced polymers these layer types are referred to as fabrics. The most common types are listed below (Cripps, 2005).

Unidirectional. Fabrics are termed unidirectional if at least 90% of their fibres run in the same direction. Some fibres may be included in the transverse direction to hold the others in place.

Woven. Woven fabrics have fibres woven together at right angles, usually 0 and 90 degrees. The style of weave can affect the composite's porosity, stability and ability to be adjusted into complex shapes ('drape').

Hybrid. In thin structures where the properties of more than one fibre type are required, multiple fibre types can be combined into one fabric. The fibres in these hybrid fabrics are usually woven.

Multiaxial. Multiaxial fabrics contain one or more layers of fibres held in place by a stitching thread, often polyester. By combining several fibre angles within one sheet this configuration can reduce the number of required plies in a laminate, thus reducing costs. However, their manufacture is lengthier and more expensive.

Other configurations. Several other fabric types exist, either with random orientations or styles developed for specific applications, e.g. braided fibres.

Very common are also sandwich structures, where a core material is inserted between two composite layers or skins. Some common materials used in sandwich structure cores were discussed in section 1.3.1.

The best mechanical results are obtained if the fibre orientation angle through a composite laminate varies regularly through the sequence. Common sequences are $0/90/0^\circ$ (cross-ply) or $0/45/90/-45^\circ$ (quasi-isotropic). The number of layers in a laminate can vary from 4 to several hundred, and the layer thickness from tens of nanometers to a few millimeters.

Through extension of the stress-strain matrix formalism to include more than one layer, Matthews *et al.* (2003) show how the stacking sequence affects the laminate's mechanical behaviour. They conclude that imbalances or asymmetries in a laminate result in complex couplings between the stiffness matrix terms, giving rise to anisotropic bending moments on loads.

The macro-mechanical approach provides a useful starting point in the analysis of composite material structural mechanics. As these materials are heterogeneous in nature, however, a more valuable description of their properties comes from including the elastic properties of both fibre and matrix materials in the analysis. This approach is called micro-mechanical analysis.

Using the properties of the constituent materials, it can be shown (Matthews *et al.*, 2003) that the moduli of a UD composite are given by:

$$\begin{aligned} E_{11} &= E_f v_f + E_m v_m && (1.10)\\ \frac{1}{E_{22}} &= \frac{v_f}{E_f} + \frac{v_m}{E_m} && (1.11)\\ \frac{1}{G_{12}} &= \frac{v_f}{G_f} + v_m G_m && (1.12)\\ \nu_{12} &= \nu_f v_f + \nu_m v_m && (1.13) \end{aligned}$$

where the subscripts f and m refer to fibres and matrix, respectively and E_{11}, E_{22}, G_{12} and ν_{12} as defined previously in this section. Experimental results indicate an agreement to 5% for the longitudinal modulus E_{11} in tension; equations 1.11 and 1.12 are less accurate because of simplifications made in the derivation.

To obtain the strength of the material through micro-mechanics analysis, i.e. its resistance to failure, is more difficult still than the stiffness derivation. A composite can fail in several different ways: at the fibres, in the matrix or at the interface. This complexity means that a failure criterion based on assumptions must be employed.

The thermal expansion coefficient of a composite is another very important property, especially in applications where the material is exposed to extreme temperature regimes, such as in aerospace components. The longitudinal and transverse CTEs can be defined in terms of fibre and matrix CTE:

$$\alpha_1 = \frac{1}{E_{11}}(\alpha_f E_f v_f + \alpha_m E_m v_m) \tag{1.14}$$

$$\alpha_2 = (1+\nu_f)\alpha_f \nu_f + (1+\nu_m)\alpha_m \nu_m - \alpha_1 \nu_{12} \tag{1.15}$$

1.3.3 Composites in space applications

Composites have a long history in aerospace applications; Soutis (2005) gives an in-depth account of the history of their use in this industry. Following the development of the earliest carbon fibre composites, the new materials were implemented in military aircraft on a demonstration basis, for example in rudders, spoilers and doors. With continued advancements in fibre and matrix materials and manufacturing processes, in particular the development of toughened epoxies, composites slowly began to displace the more traditional materials, such as aluminium and titanium alloys, for primary structures. Improved analysis methods, especially progress in finite element analysis software, enabled a more sophisticated performance prediction for the anisotropies of the materials.

A major challenge for using composites in space applications is the need for operation at cryogenic temperatures. Schutz (1998) gives an overview of composite material properties for cryogenic applications. Material selection from the large number of available constituents for these applications is determined by the intended application, and further complicated by:

- unique operating environment, including extremes of temperature;
- close dimensional tolerances;
- radiation exposures;
- difficult fabrication processes;
- challenging reliability requirements.

Material properties such as thermal conductivity, tensile and compressive properties are largely determined by the reinforcing fibres; matrix properties affect the composite's fatigue resistance, radiation effects and fabrication concerns. The popular carbon and graphite fibres are ruled out for electrical insulation purposes because of their conductivity.

Examples of the use of composites in space applications are given in Bansemir and Haider (1998) for the Infrared Space Observatory (ISO) and the Dong Fang Hong (DFH3) communication satellite; in Stute *et al.* (2003) for the Planck satellite reflectors and an optical bench breadboard for the JWST's Near InfraRed Spectrometer (NIRSpec); and in Pauschinger *et al.* (1994) for the X-ray spectroscopy mission XMM. Numerous further examples are available in the literature.

1.4 Project outline and aims

The work presented here formed part of a joint project of University College London (UCL) and industrial partners QinetiQ and Cobham Composites in carbon fibre composites for lightweight deformable space optics. From the long history of CFRP in space applications, the production of CFRP optics is a natural step though experience with this technology is limited.

The primary aim of the project was to produce a prototype active mirror in nickel-coated CFRP. Past work at UCL in active mirrors comes from a program in the 1990s which culminated in the production of a 27 cm aluminium deformable mirror whose shape is controlled by seven actuators. As demonstrated in this chapter, technologies for producing ultra-lightweight and thermally stable mirrors with a high optical form and surface quality are of great value. Adaptive optics theory and techniques are discussed in chapter 2, as well as an overview of the history and technology of active control.

A second question addressed in this thesis is how finite element analysis can contribute in the design and characterization of active and adaptive optics systems; in particular in material selection and overall optical design, but also in integrated adaptive optical simulations for large telescopes.

Extensive finite element analysis was carried out over the course of the project to investigate the effect of material stiffness and lay-up on the mirror's mechanical performance. The thermal effects of a nickel coating were modelled in order to optimize the mirror design. In a first manufacturing phase, a passive mirror was produced to test manufacturing and coating techniques and substrate stability. This work will be documented in chapter 3.

Using the results and lessons learnt from this exercise, a thin substrate was produced and fitted with seven actuators for shape control. A mechanism for coupling the actuators to the faceplate was designed and a software programme written for driving the actuators. This mirror too was subjected to extensive dynamical testing; results are presented in chapter 4. The test results are compared in detail with finite element predictions.

An alternative application for such mirrors lies in adaptive optics for the next generation of ground-based telescopes (the so-called extremely large telescopes, or ELTs). Chapter 5 will look at this application of lightweight CFRP more closely, as this is a high-profile and fast-growing area of research.

CHAPTER 2

Active and adaptive optics

"A good idea is worth more than a large telescope."

- R.O. Redman

Active optics is an important method of reducing the primary mirror and overall mass of a telescope. Wilson (1999, vol. 2) describes the purpose of active optics as "the improvement of the quality of a telescope image ... by some systematic process involving the relative positioning of the mirrors and the modification of their form by their supports". Traditionally the term *active optics* is employed where low temporal frequency errors are being corrected, such as:

- optical design and manufacturing errors;
- theoretical errors of mirror supports and structures;
- thermal distortions of mirrors and structures;
- mirror mechanical warping;
- local turbulence (dome seeing).

Active optics does not describe any techniques used to correct for higher temporal frequency error sources, such as atmospheric turbulence.

The main benefits of active optics over other lightweighting methods (Wilson *et al.*, 1987) can be summarized as follows:

- tolerance relaxation on mirror form as low spatial frequency aberrations can be corrected;
- avoiding material removal processes can lead to a more cost-effective manufacturing process;
- has allowed the introduction of segmentation for large mirrors, an essential technology for the new generation of ground- and space-based observatories;
- simplifies the maintenance of the mirror figure as its shape may be continually monitored in operation;
- offers an alternative method for reduction of the mirror's thermal inertia compared with passive lightweighting methods; and
- cans allow novel materials with higher thermal expansions to be considered for large mirrors.

The aim of this chapter is to look at the theory of active optics and the technological requirements to implement it on an astronomical telescope. For ground-based telescopes active optics has been well researched and demonstrated, and a brief history of past work will be given. Actuation methods for mirror shape control will also be discussed. In space active optics have not yet been used, although space observatories arguably stand to gain the most from low spatial frequency corrections due to the absence of an atmosphere. Research into the technology for space use is presented.

The second part of the chapter will examine another interesting application of lightweight deformable mirrors, namely adaptive secondary mirrors for adaptive optics.

Correcting the effects of atmospheric turbulence, whilst relying on many of the same principles as active optics, is more technologically demanding than active optics. The history and theory of adaptive optics will be discussed, as well as its importance in the context of the work presented here. The use of adaptive secondaries is a very important area of research in view of the advent of the next generation of ground-based telescopes, which all aim to use such a system architecture.

2.1 History and principles of active optics

2.1.1 History of active optics

The idea of active wavefront control was first suggested by two important telescope builders of the early 20th century, Couder and Maksutov. They independently undertook simple experiments with counterweights and spring blades, but neither carried out any systematic research into the technology.

The first real efforts into developing active control systems was commenced in the late 1960s by NASA for its first space telescope. In 1969 the United States National Academy of Sciences gave the green light to a series of hearings and feasibility studies for a Large Space Telescope (LST). The work culminated in a successful demonstration of the technique on a 30 inch model mirror (Wilson, 1999, vol. 2). The technology was eventually rejected for the project, which was to become the Hubble Space Telescope (HST) project, as it was considered to carry too high a risk. Following the successful introduction of active optics in the European Southern Observatory (ESO)'s New Technology Telescope (NTT) in 1989, the technology became widely accepted in many major ground-based observatories, such as the Very Large Telescope (VLT) and the American 10 m Keck telescopes.

2.1.2 Active control principles

Active optics systems operate on a simple premise: the reflected wavefront is measured using an image analyser, and a correction is applied to the mirror faceplate. The correction takes the form of a distribution of forces applied by actuators attached to the mirror. The practical implementation, however, is far from trivial and precise calibration of the system is crucial to its performance. Several control methods have been tested and are extensively reported in the literature.

The simplest approach is to relate the mirror shape directly to the wavefront changes induced by the actuators. However, such an algorithm involves lengthy matrix computations and produces a solution with poor accuracy and unrealistically high forces (Wilson *et al.*, 1987). Most active control systems currently in use utilize a modal approach. This is the method used in the NTT and the system has acted as the blueprint for subsequent telescope projects. Wilson (1999, vol. 2) describes this technique extensively.

Three fundamental laws of physics lie at the basis of modal control (Wilson *et al.*, 1987):

Hooke's law of elasticity. Hooke's law states that in an elastic material strain is proportional to stress. In mathematical terms this can be expressed as:

$$\vec{\sigma} = C \cdot \vec{\epsilon} \tag{2.1}$$

where $\vec{\sigma}$ and $\vec{\epsilon}$ are the strain and stress vectors, respectively, and C is known as the material's stiffness matrix. This stress-strain relation and the stiffness matrix is important and will be used further in later sections.

A glass mirror will obey this linearity law up to the point of fracture; in the case of a metal mirror, up to the elastic limit. The implication for an active optics system is that the system's dynamic range must be no more than a fraction of these limits to prevent material failure.

Convergence principle. This principle dictates that the strain produced in an elastic body by a system of forces in equilibrium decreases rapidly with increasing distance from the loaded region. For active optics this implies that correction of higher spatial frequency distortions requires increasing amounts of force. Active optics will thus be most efficient at correcting low spatial frequency distortions, such as tip, tilt, astigmatism or coma.

Law of orthogonality. The modes used in the active control loop should ideally be both mathematically and physically orthogonal and statistically independent, so that they can be controlled without "cross-talk".

Noethe (1991) identified and compared two types of modes for decomposition of the wavefront: modes based on optical aberrations, such as Zernike polynomials; and modes based on mechanical properties, such as free-vibration modes. Both these types are of the general form $f_n(r, \phi) cos(n\phi + \phi_n)$, where n is the rotational symmetry of the mode and r and ϕ are the radial and azimuthal coordinates on the entrance pupil, respectively.

For both types, the modes should be linearly independent to avoid cross-talk. Original work into active wavefront control at NASA used a mirror's natural vibration modes, which can easily be computed by numerical calculation and modelling for relating the wavefront to actuator controls.

Because of their straightforward analytic representation and correlation to classical optical aberrations, Zernikes can be useful in representing aberrations not resulting from a mirror's natural elasticity, such as polishing errors or errors introduced in the mirror environment. The NTT's active optics system, for example, uses a mixed approach of Zernikes and natural modes for different stages of the correction.

The required operation frequency of an active optics system is determined by the variation timescales of the error sources being corrected. The limit of operation for conventional active optics systems is approximately 1 Hz - error sources varying over

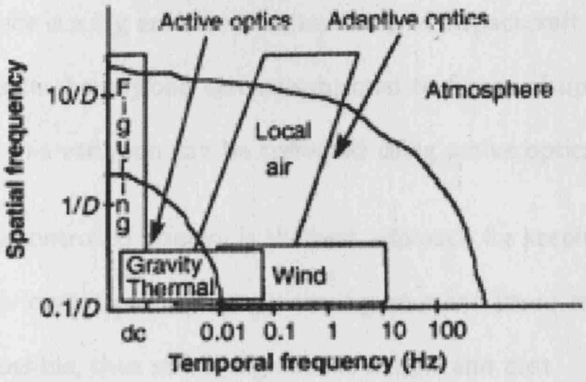

Figure 2.1: Diagram of the spatial and temporal frequencies of some of the major error sources in telescope imaging systems (Wilson, 1999).

faster timescales cannot be corrected with such systems. Fig. 2.1 shows some of these errors diagrammatically.

There are currently no actively controlled space-based imaging systems. With improved experience with the technology on the ground, however, interest is growing in the space community.

2.1.3 Active optics in space

In the absence of an atmosphere and removed from the Earth's gravitational field, optical alignment and mirror figure are easier to maintain. Space optics, however, still face challenges that warrant the inclusion of active optics. The main reasons can be summarized as follows (Wilson, 1999; Bely, 2000):

- diffraction-limited imaging can only be achieved if the tolerances on low spatial frequency errors can be relaxed;
- space systems can face extreme thermal regimes throughout their orbit. Active optics can help compensate where varying temperatures introduce figure errors in the optics;

- though space is a 0 g environment, assembly of a spacecraft takes place at 1 g and during launch the payload can be subjected to forces of up to 5 g. Any changes caused by this variation can be corrected using active optics;
- an actively controlled primary is the best approach for keeping space observatories affordable: lower tolerances on mirror figure mean lower areal density substrates become possible, thus saving significant weight and cost.

The technological requirements for active wavefront control in space will be discussed in section 2.2.

2.2 Active mirror support technology

This section will describe the current state of the art in active mirror control and discuss the technological challenges in applying the technique to future ground- and space-based observatories. On the ground, somewhat different technologies are used for monolithic and segmented mirrors, albeit based on the same support principles. Segmented mirror active optics faces two extra challenges:

1. maintaining the correct radius of curvature at the level of individual segments, as well as over the entire mirror;
2. keeping the segments aligned with respect to each other, to which end edge sensors are usually required in the system setup.

Edge sensors will not be discussed in this thesis but their presence is an important feature of segmented mirror design. Segment alignment techniques and algorithms also fall outside the remit of the work presented here. Some of the actuators described in this section are also used in adaptive optics; their use for this application will be discussed in the next section.

For modern monolithic or segmented telescopes, the main requirements for actuators, in terms of stroke, axial and transverse stiffness, response time and operating temperature, are determined by the optical design. In addition, the following factors must be considered (Schier, 2001):

- Lifetime and reliability. Actuators must remain in operation for several years so risk of failure must be minimal.
- Environmental suitability. The actuator must be resistant to the following conditions:

  accumulated grit and dust;

  exposure to magnetic fields from motors and transformers;

  exposure to electric fields generated by high voltage devices;

  exposure to other sources of radiation, for example generated by digital equipment.

  and must not generate interference objectionable to other instruments.
- Ease of installation, maintenance and removal. Installing or replacing an actuator should not result in significant downtime of the system. Ideally, the actuators should not require any maintenance on short timescales.

Actuators can be classified into two categories (Hardy, 1998):

Force or 'soft' actuators. These have near-zero intrinsic stiffness and must therefore be powered to provide support. The most common types are hydraulic, pneumatic or electromagnetic (e.g. voice coils, stepper motors). Their main disadvantage is that the displacement they produce depends on the faceplate stiffness, requiring an accurate feedback circuit and calibration. They are most often used in active optics for large monolithic mirrors.

Displacement or 'rigid' actuators. Displacement actuators possess a very high intrinsic stiffness. Common types are ferroic devices, such as piezoelectric, electrostrictive or magnetostrictive actuators. Displacement actuators are mostly used for smaller mirrors, such as primary segments.

Numerous actuator types have been developed and programmes are ongoing with the advent of a new generation of large ground-based telescopes, as well as the development of active systems for space.

The earliest active optics experiments for ground-based astronomy are extensively described in the literature (Wilson *et al.*, 1984, 1987, 1989; Noethe *et al.*, 1988). Active mirror control was achieved using astatic levers. In the astatic principle the support 'floats' the mirror against the force of gravity as the telescope changes its angle; the weight of the mirror is carried at each support point by the reaction forces. A mechanical drawing of the active supports used in the NTT active optics system is shown in figure 2.2. It uses a two-stage lever mechanism to provide the counterweight required to correct the aberrations; the spring generates negative force modulation, providing tension for first-level (d.c.) active correction. Other low frequency errors are corrected by the moveable counterweights.

This method relies heavily on analytical or numerical (i.e. finite element analysis) methods for precalibration of the force constants at each support point. The method used in the NTT and VLT telescopes was devised and described in detail by Schwesinger (1988). The NTT active optics system produced a great improvement in image quality; figure 2.3 shows a set of images obtained from astronomical first light in 1989, reported in Wilson *et al.* (1991).

The effective stiffness of motor-based supports can be greatly increased when used in conjunction with a screw mechanism, as used in the 10 m segmented Keck Telescopes, which contain 3 such actuators on each of their 36 primary segments. These designs are very versatile and many different variations are in use (see for example Schier (2001)).

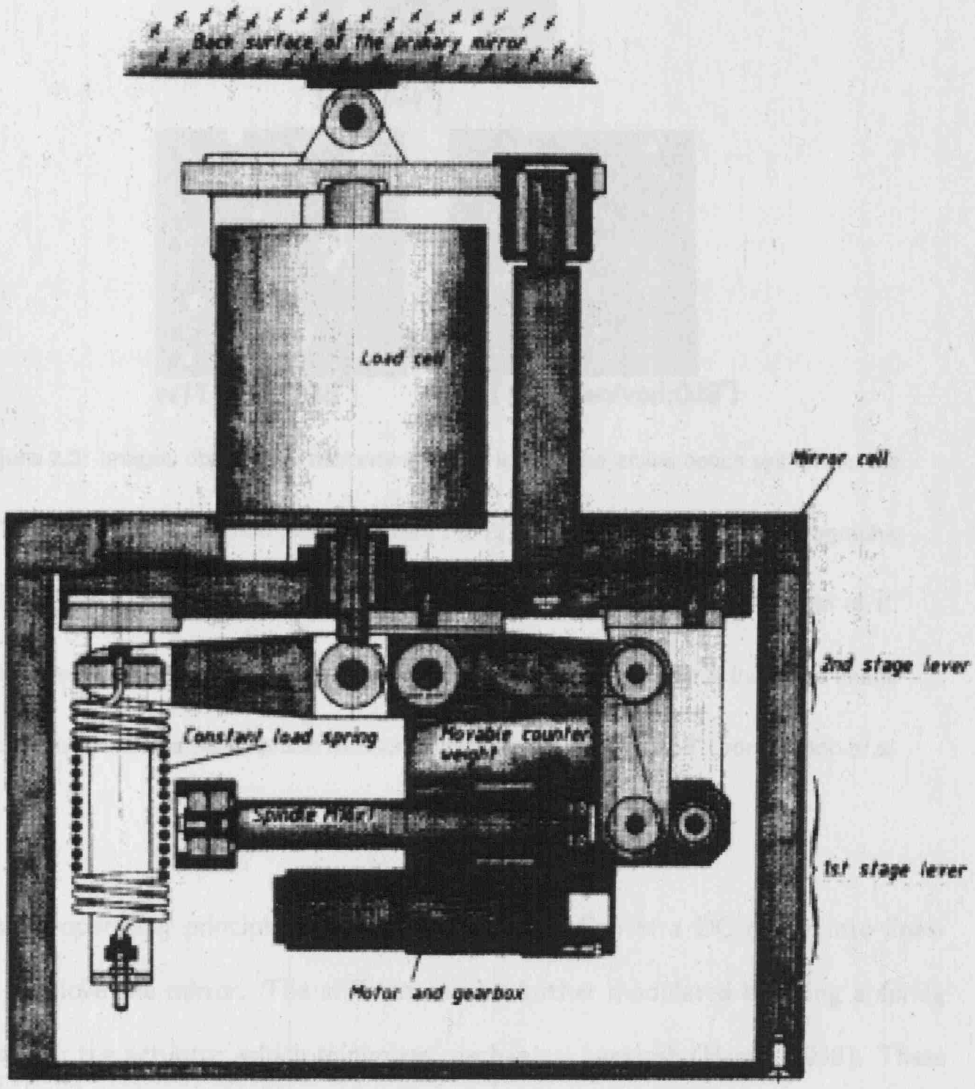

Figure 2.2: Mechanical drawing of the active supports used in the NTT primary mirror. These actuators contain a double astatic lever mechanism to 'float' the mirror against gravity.

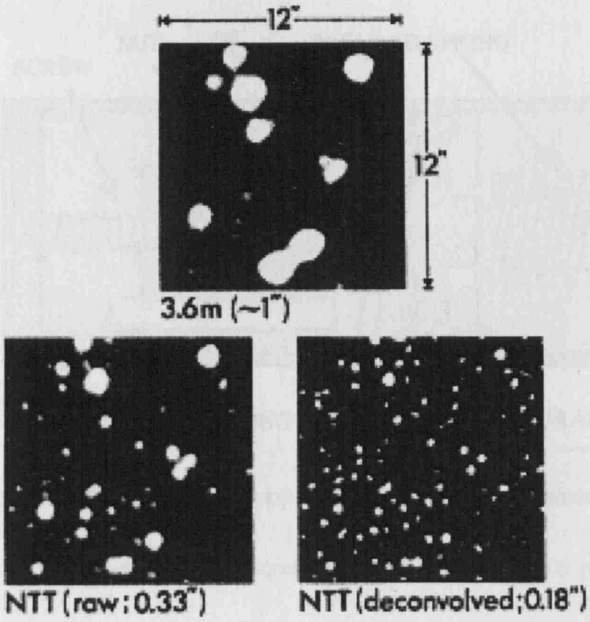

Figure 2.3: Images obtained at astronomical first light of the active optics system on the NTT. The top image shows a picture of the 12×12" region obtained with a photographic plate on the ESO 3.6 m telescope on the same site in 1977, achieving a FWHM of 1". Bottom left is the raw NTT image with a FWHM of 0.33". Bottom right is the same image deconvolved with the point spread function, achieving a FWHM of 0.18" (from Wilson *et al.* (1991)).

Their basic operating principle is to convert rotary motion of a DC motor into linear motion to move the mirror. The stiffness can be further modulated by using a spring in series with the actuator, which minimizes mechanical backlash (Hardy, 1998). These actuators have proved reliable and able to meet high performance requirements (Lorell *et al.*, 2003). Because of their high intrinsic axial stiffness they are very simple to operate, and resemble static supports.

However, their stiffness also has negative consequences. Any forces are transferred via the actuators from the mirror cell structure to the load-spreading whiffletree (a multi-layered system of mirror supports built atop three adjusting points) and segments, and vice versa, leading to excitations. Also, they have no means of dissipating energy, which

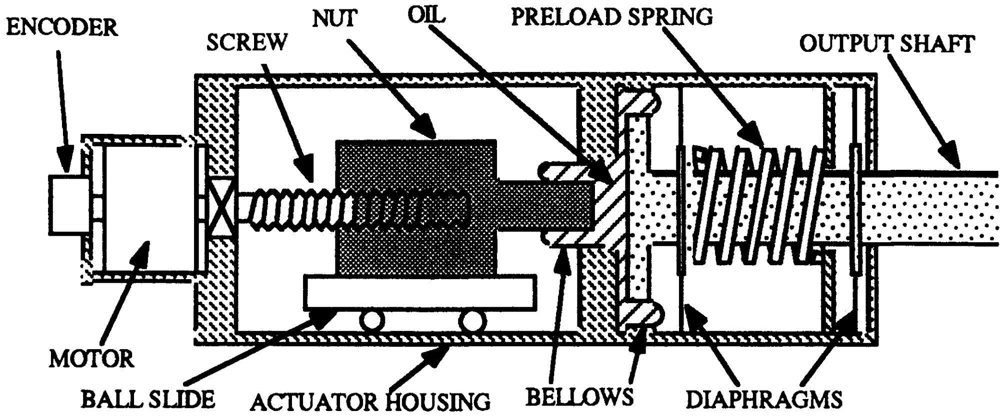

Figure 2.4: Diagram of the rigid axial supports used in the Keck telescopes, showing the internal parts. The actuator uses a screw drive mechanism with a preload to avoid mechanical backlash.

can add to the system's vibrational energy and cause instability. At the Keck observatory this is currently dealt with by keeping the maximum operational bandwidth around 0.25 Hz. In addition, rigid actuators are expensive, with the Keck actuators reported to cost 10,000USD each in the early 1990s. Figure 2.4 shows a diagram of the axial support actuators used in the Keck telescopes.

An alternative for the mechanical soft supports described above are electro-magnetic voice coils, which are mainly used in mirrors for adaptive optics (see section 2.4). Consisting essentially of two simple parts, a coil and a magnet, they are lightweight, compact and relatively cheap; contain few moving parts; require no lubrication and can produce large forces in a short time.

A limitation of voice coils is that they use part of their stroke for supporting the mirror, which compromises their ability to correct distortions. Lorell *et al.* (2003) suggest a 'gravity offloading' mechanism to remove the static force using a counterweighted lever. Schier (2001) presents a voice coil actuator where the load reaction is provided by a pneumatic chamber below the voice coil.

Several large telescopes with monolithic lightweighted primaries, such as the Very Large Telescope (4×8.2 m), Gemini (2×8.1 m) and Large Binocular Telescope (2×8.4 m) observatories, use pneumatic soft supports for active control. In all of these telescopes, passive support is provided axially and laterally by hydraulic support cylinders (European Southern Observatory, 1998; MacLean, 2000; Martin *et al.*, 2004), mounted on top of the pneumatic actuator. Each hydraulic cylinder is connected in 3 sectors to the back of the primary via a whiffletree.

Figure 2.5 shows a drawing of a pneumatic actuator. This particular model is proposed for the 4 m Visible and Infrared Survey Telescope for Astronomy (VISTA), construction of which is in process at the time of writing; its working is described in detail by Bennett and Baine (2004). Figure 2.6 shows a picture of the mirror support cell of one VLT unit telescope, showing the tripod structure at each support point.

The most common types of 'hard' displacement actuators are magnetostrictive (MS), electrostrictive and piezoelectric actuators. Magnetostriction is the property that causes certain ferromagnetic materials to change shape under the influence of a magnetic field (Etrema Products Inc., 2002). Magnetostrictive (MS) actuators are composed of a rod of ferromagnetic material surrounded by a coil. An electrical current generates a magnetic field which causes a strain in the ferromagnet; the strain is proportional to the square of the magnetic field, and can be increased by preloading the magnetic rod. The most commonly used material is Terfenol-D, an alloy of terbium, dysprosium and iron metals, which has the largest known magnetostriction at room temperature. MS actuators have a wide operating temperature range (-20 to 100°C). Their main disadvantage is a relatively high level of hysteresis (around 20%).

In piezoelectric actuators a strain-inducing stress is produced in the actuator material by applying an electric field. In their baseline 'natural' state, the molecules in the lattice are oriented randomly and no macroscopic piezoelectric behaviour is observed. Because of the materials' ferroelectric properties, a permanent alignment of the molecular cells

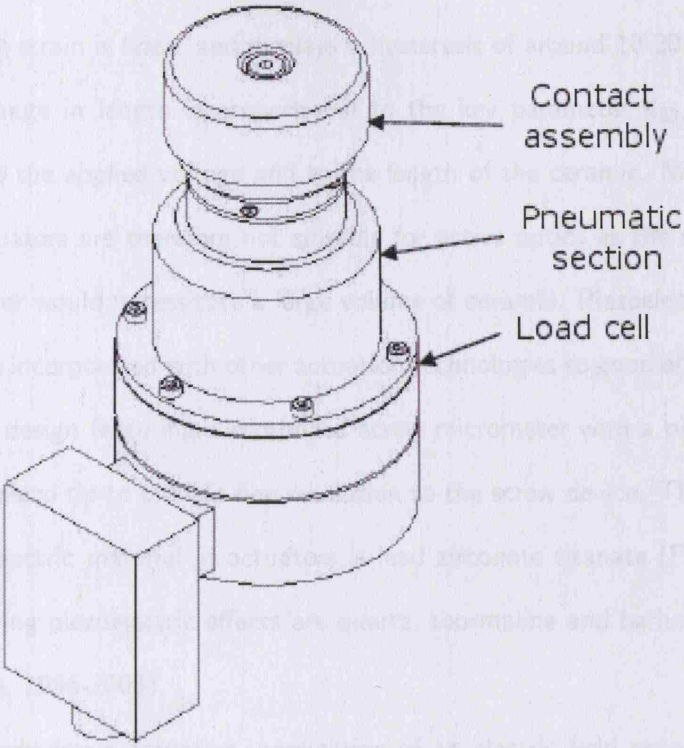

Figure 2.5: Drawing of a pneumatic actuators for active optics (Bennett and Baine, 2004). This particular model is suggested for the Visible and Infrared Survey Telescope for Astronomy (VISTA).

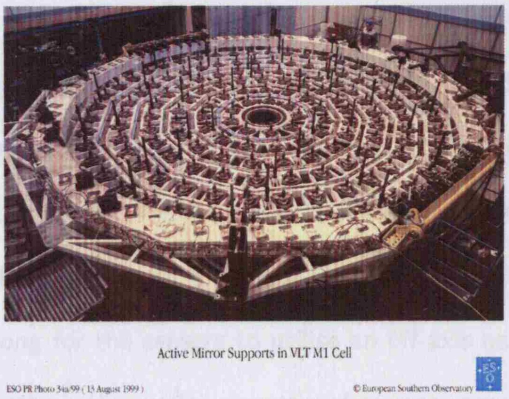

Figure 2.6: Picture of the primary mirror cell of one of the VLT unit telescopes, showing the combined active and passive support structure (picture courtesy of ESO).

can be forced using a strong electric field; this process is called 'poling'. After poling, the piezoelectric strain is linear and displays a hysteresis of around 10-20% (Hardy, 1998).

The change in length is proportional to the key parameter d_{33}, the piezoelectric constant, to the applied voltage and to the length of the ceramic. Normal linear piezoelectric actuators are therefore not suitable for active optics as the required stroke for a large mirror would necessitate a large volume of ceramic. Piezoelectric materials can, however, be incorporated with other actuation technologies to good effect; Schier (2001) describes a design featuring a motorized screw micrometer with a piezoelectric tip, allowing the piezo tip to provide fine resolution to the screw device. The most commonly used piezoelectric material in actuators is lead zirconate titanate (PZT). Other materials displaying piezoelectric effects are quartz, tourmaline and barium titanate (Physik Instrumente, 1996-2006).

In electrostrictive actuators, application of an electric field generates a strain proportional to the square of the applied field. The most commonly used material is the ferroelectric lead magnesium niobate (PMN), which displays low hysteresis, high tensile strength and nanometer precision (Ealey *et al.*, 1996). Their main drawbacks are its nonlinear response, which can be controlled with a position feedback system, and its temperature sensitivity (Hardy, 1998). PMN's hysteresis and strain response is strongly temperature dependent, which necessitates more complicated drive circuitry.

The actuator design and configuration must be closely co-ordinated with the wavefront sensing and image analysis architectures. Because of the slow timescales on which active corrections are carried out, the demands on the wavefront sensor are not as stringent as in adaptive optics systems for correcting for atmospheric turbulence. Integration times are sufficiently long for the sensors to utilise an off-axis natural guide star in the field of view. Limits on the active optics correction frequency are usually imposed by the image analysis process, as separating out the effects of the atmosphere is not a trivial process.

2.2.1 Active mirrors in space

As optical aberrations in space arise from different sources than on the ground, the technological requirements for active mirror control are distinct from those for ground-based active optics. No active space systems are currently in operation; experience is therefore limited to prototypes and laboratory-based testing. Whilst several research projects have examined the possibility of having a fully actively controlled space telescope (e.g. Burge *et al.* (1998, 2000), largely in the framework of the next-generation James Webb Space Telescope (JWST), these designs were rejected in favour of a more traditional approach.

A three-year program was carried out at Ball Aerospace & Technologies Corp. in the framework of the JWST to develop a nano-positioning actuator suitable for use in space. Results from this research are reported extensively by Streetman and Kingsbury (2003). The following qualitative requirements were identified:

- Low weight
- Sub-10 nm position resolution
- Minimum stroke of 20 mm
- Operational at ambient and cryogenic temperatures
- High axial stiffness
- Capability to maintain position without power
- Simple control system
- Single fault tolerant
- Cost-effective

Most existing actuators used for ground-based active control, as described in this section, do not fit all the above criteria. The resulting design features a two-stage positioning system with a coarse and linear stage of motion provided by a simple stepper

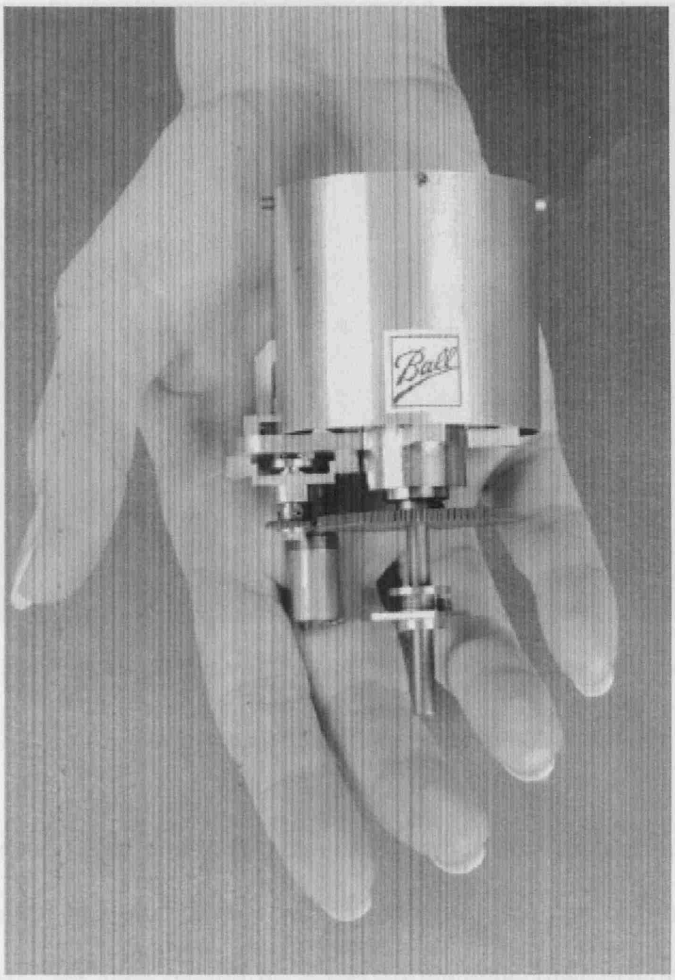

Figure 2.7: Picture of the nano-positioning actuator developed by Ball Aerospace & Technologies Corp. in the framework of JWST research (Streetman and Kingsbury, 2003).

motor. Operation at the required temperatures was demonstrated by the authors and the actuator weighs just 288 g. A picture of the actuator is shown in figure 2.7; a detailed description is unavailable because of patenting restrictions.

In the chosen architecture for JWST each of 18 hexagonal segments is controlled by three such actuators providing rigid body motion for alignment of the segments. A fourth actuator adjusts the radius of curvature. The segments are to be made from beryllium each measuring 1.6 m in size.

Burge *et al.* (2000) propose an alternative mirror design based on the ground-based active/adaptive optics model, featured a 2 mm thick polished glass membrane measuring

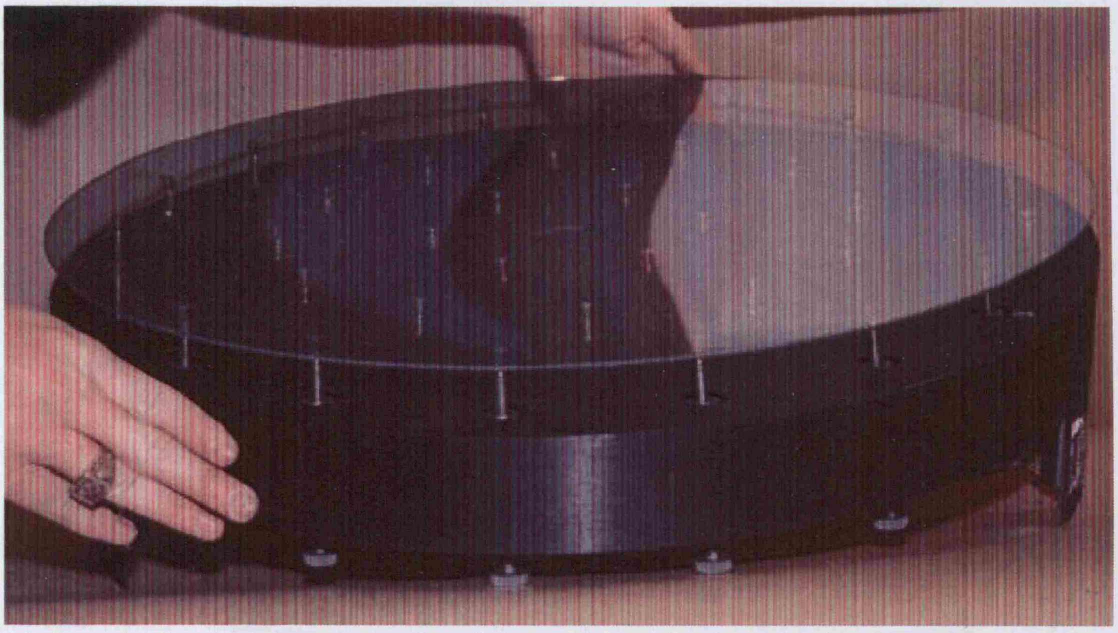

Figure 2.8: 53 cm prototype mirror with 2 mm thick glass membrane, proposed as a solution for the JWST by Burge *et al.* (1998).

2 m in diameter supported over a rigid laminated carbon fibre composite. The actuators are remotely driven fine pitch screws with a reported resolution of 6 nm. Because of their intrinsic stiffness they require no power to maintain their position, and a cable mechanism is included to withstand the launch load. The actuators in the demonstrator system were however not optimized for use at cryogenic temperatures. Figures 2.8 and 2.9 show a picture of a 53 cm prototype and a diagram of the proposed actuators, respectively.

2.3 Atmospheric turbulence compensation: adaptive optics

Whilst the ability to produce seeing limited images with an actively controlled ground-based telescope is a useful result, the image quality often remains unsatisfactory for detailed scientific research. At the best observing sites, the median seeing is of the order of 0.5 - 1 arcsecond at a wavelength of 500 nm, the equivalent diffraction limit of a 25 cm telescope. For comparison, 4 and 10 m telescopes are capable of 0.03" and 0.01"

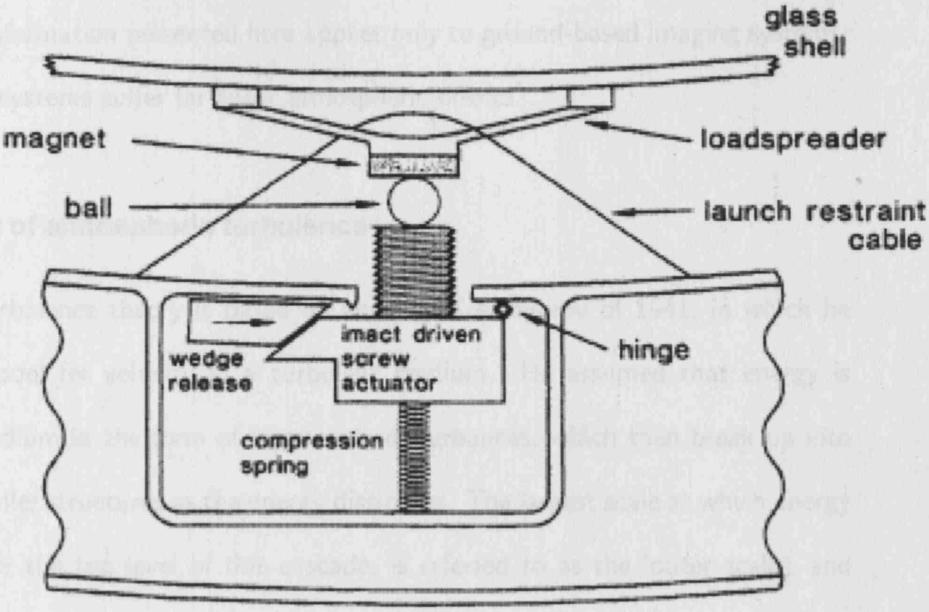

Figure 2.9: Conceptual design of actuators coupling to the glass membrane in the active mirror system suggested by Burge *et al.* (2000).

resolution respectively. Only in the latter half of the 20th century did the understanding of thermodynamics of large air masses become sufficient to begin efforts to model and correct this effect using an advanced optical technique derived from the active optics principle, adaptive optics.

The atmosphere's influence on astronomical images can be categorized in three areas (Wilson, 1999, vol 2):

1. Extinction (atmospheric absorption)

2. Seeing (atmospheric turbulence)

3. Refraction (including atmospheric dispersion)

Of these categories, atmospheric seeing or the effects of atmospheric turbulence degrade images to the greatest extent. It is also the most complex and poorest understood. This section will describe the basic theory of atmospheric turbulence, its limitations and effects on astronomical images. The final subsections will deal with adaptive optics in practice. The information presented here applies only to ground-based imaging systems, as space-based systems suffer far fewer atmospheric effects[1].

2.3.1 Theory of atmospheric turbulence

Atmospheric turbulence theory is based on work by Kolmogorov of 1941, in which he developed a model for velocity in a turbulent medium. He assumed that energy is fed into the medium in the form of large scale disturbances, which then break up into smaller and smaller structures as the energy dissipates. The largest scale at which energy is introduced, or the top level of this cascade, is referred to as the 'outer scale', and the smallest scale, beyond which the kinetic energy is dissipated into heat by molecular friction, is called the 'inner scale'. Kolmogorov derived the following power law for the turbulence power spectrum in one dimension (Hardy, 1998):

$$\Phi(\kappa) \propto \kappa^{-5/3} \tag{2.2}$$

where κ is defined as $2\pi/l$ with l the spatial scale size.

Further work by Obukhov and Yaglom (Hardy, 1998) showed that Kolmogorov's theory also applies to refractive index variations in the atmosphere, which give rise to the degradation of astronomical images. Expanding this to 3 dimensions, the power spectrum becomes (Noll, 1976):

$$\Phi_N(\kappa, z) = 0.00969 C_N^2(z) \kappa^{-11/3} \tag{2.3}$$

The parameter $C_N^2(z)$ is known as the refractive index structure function coefficient, which varies with altitude and time and is usually described with empirical models for

---

[1] Space-based astronomical imaging systems of course suffer no atmospheric degradation but Earth-observation satellites can.

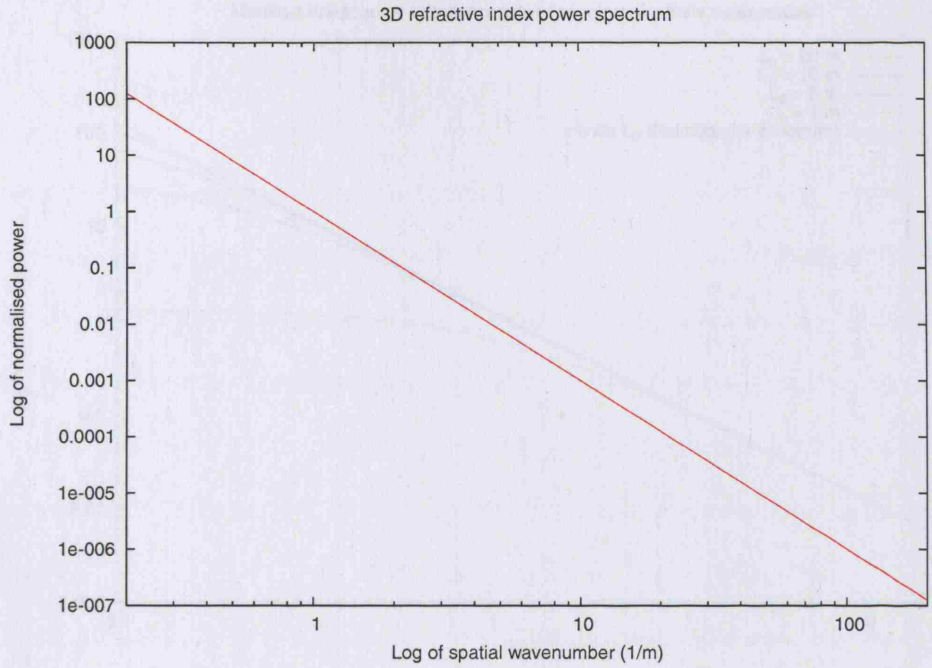

Figure 2.10: Log plot of the 3D Kolmogorov turbulent power spectrum, with infinite outer scale and zero inner scale.

a given site. Its integral over the optical propagation path is a measure of the total amount of wavefront degradation. Fig. 2.10 shows a plot of the Kolmogorov power spectrum.

For application to astronomical imaging through the atmosphere, Kolmogorov's theory has limitations. First, he assumes that the cascade-like process of energy transfer to smaller scale sizes is isotropic and homogeneous. Experimental work (Hardy, 1998) has shown that turbulence does experience sudden discrete bursts. These bursts are significant in astronomy as a sudden and brief deterioration of seeing during a long exposure can degrade the image substantially. Also, Kolmogorov's theory only holds between the inner and outer scales - the so-called *inertial range*. The size of the outer scale, in particular, has been the subject of some debate, and only since the 1990s have substantial studies to measure and characterize this quantity been undertaken (see for example Abahamid *et al.* (2004), Martin *et al.* (2000), Lukin *et al.* (2003)).

To include the effects of a finite outer scale in the model of atmospheric turbulence,

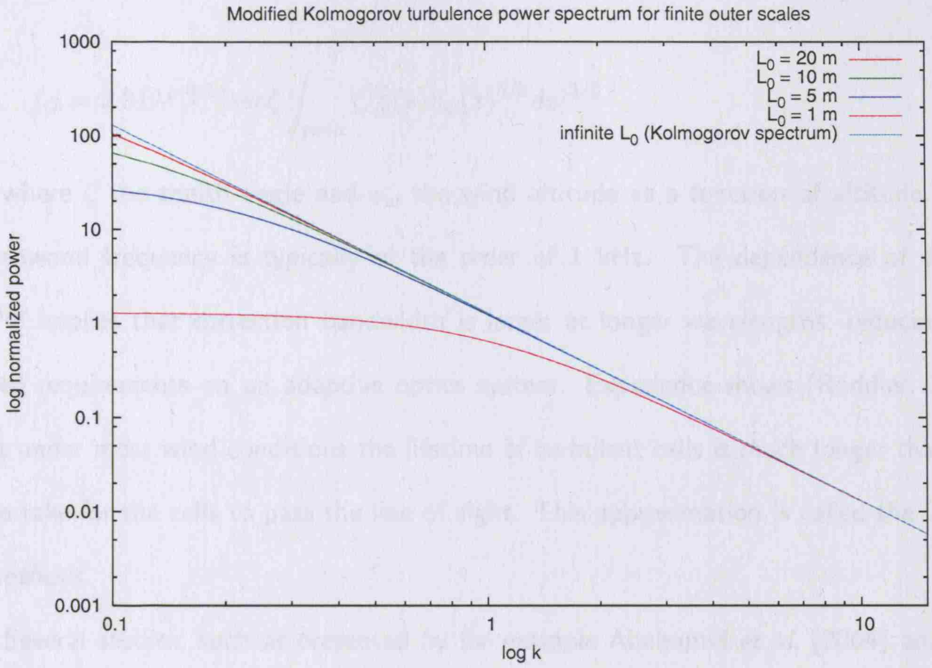

Figure 2.11: Plot of the modified Kolmogorov spectrum as defined by Winker (1991) for several outer scale sizes.

a constant $\kappa_0 = 1/L_0$, where L_0 is the outer scale, is added in quadrature with the spatial wavenumber κ (Winker, 1991):

$$\Phi_n(\kappa, z) = 0.00969 C_N^2(z)(\kappa^2 + \kappa_0^2)^{-11/6} \tag{2.4}$$

Figure 2.11 shows how the addition of this term modifies the turbulence power spectrum.

Wind velocity also has a strong effect on atmospheric turbulence, with C_N^2 showing a proportionality to the square of wind velocity. Strong wind shear often exists in the atmosphere around altitudes of 5 and 10 km (Hardy, 1998), with the layer estimated to be several tens of meters thick. Greenwood (1977) assumed a Gaussian wind profile from which he derived a characteristic timescale, the Greenwood frequency, over which Kolmogorov turbulence varies:

$$f_G = 2.31\lambda^{-6/5}[sec\zeta \int_{path} C_N^2(z)v_w(z)^{5/3}dz]^{3/5} \tag{2.5}$$

where ζ the zenith angle and v_w the wind altitude as a function of altitude. The Greenwood frequency is typically of the order of 1 kHz. The dependence of f_G on $\lambda^{-6/5}$ implies that correction bandwidth is larger at longer wavelengths, reducing the speed requirements on an adaptive optics system. Experience shows (Roddier, 1999) that under most wind conditions the lifetime of turbulent cells is much longer than the time take for the cells to pass the line of sight. This approximation is called the *Taylor hypothesis.*

Several studies, such as presented by for example Abahamid *et al.* (2004) and Devaney and Owner-Petersen (2001), show a very strong contribution to the overall turbulence profile from the surface layer, i.e. altitudes of 0-50 m. Based on such observations, it has been suggested that correcting for only the turbulence from this layer can result in significant improvement in image quality.

2.3.2 Imaging through the atmosphere

This section will describe the background theory for adaptive optics technology: how turbulence in the atmosphere affects incoming light, and the mathematical tools used to describe these effects.

2.3.2.1 Structure functions

To characterize the effect of atmospheric turbulence on an imaging system, the difference in phase of the wavefront is studied at two different points in the aperture. Structure functions, first introduced by Kolmogorov in 1941 to describe non-stationary random functions, represent the variance of the difference between the two values. The phase structure function is thus given as:

$$D_\phi(\xi) = \langle |\phi(\vec{x}) - \phi(\vec{x} + \vec{\xi})|^2 \rangle \tag{2.6}$$

where $\vec{x}$ and $\vec{\xi}$ are two-dimensional vectors and $\langle x \rangle$ denotes the ensemble average. Roddier (1981) derived an expression for D_ϕ in terms of the refractive index structure constant:

$$D_\phi(\xi) = 2.91\kappa^2 \int C_N^2(z)dz\xi^{5/3} \tag{2.7}$$

This equation describes the spatial distribution of wavefront distortions. A more common notation for the phase structure function is:

$$D_\phi(\xi) = 6.88(\xi/r_0)^{5/3} \tag{2.8}$$

where r_0 is the Fried parameter (Fried, 1965), also referred to as the coherence length. It is a convenient measure of the strength of turbulence as it represents its integrated effect over the entire atmosphere. For a known C_N^2 profile r_0 is defined by (Tyson and Frazier, 2004):

$$r_0 = \left[0.423k^2 \sec\zeta \int_{path} C_N^2(z)dz \right]^{-3/5} \tag{2.9}$$

where ζ is the zenith angle and k is defined as $2\pi/\lambda$. Equation 2.9 thus shows that r_0 varies as the $6/5$ power of wavelength, making adaptive optics easier at longer wavelengths.

Knowledge of r_0 alone is insufficient to determine the required characteristics for an adaptive optics system. An expression for the temporal dependence of turbulence is needed to dictate how fast corrections must be carried out. This property can be described using the following structure function (Roddier, 1999):

$$D_\phi(\tau) = \langle|\phi(\vec{x},t) - \phi(\vec{x},t+\tau)|^2\rangle \tag{2.10}$$

The required operating frequency for an AO system is determined by a number of factors, such as the average wind speed, and is typically of the order of milliseconds.

2.3.2.2 Modal decomposition of atmospheric turbulence

Distorted wavefronts at an aperture, as produced by Kolmogorov turbulence, can as with active optics be represented by two-dimensional Zernike polynomials, which enable complex wavefront shapes to be decomposed into a set of basis functions. Noll (1976) provided a convenient definition of Zernikes for characterization of turbulence-degraded wavefronts in polar coordinates on a unit circle, normalized such that each polynomial has a root mean square (rms) value of 1 over the unit disk.

$$\begin{aligned} Z_{even} &= \sqrt{n+1}R_n^m(r)\sqrt{2}\cos(m\theta) & (2.11)\\ Z_{odd} &= \sqrt{(n+1)}R_n^m(r)\sqrt{2}\sin(m\theta) & (2.12)\\ R_n^m(r) &= \sum_{S=0}^{(n-m)/2} \frac{(-1)^S(n-S)!r^{n-2S}}{S![(n+m)/2-S]![(n-m)/2-S]!} & (2.13)\end{aligned}$$

where n is radial degree, m azimuthal frequency, with $m \leq n$ and $n-m$ even.

A phase function over a unit-sized aperture can thus be written as:

$$\phi(r,\theta) = \sum_{0}^{\infty} a_j Z_j(r,\theta) \tag{2.14}$$

where a_j are the mode coefficients, representing their relative strengths. Figure 2.12 shows a plot of the variance of the first 25 Zernike coefficients showing their relative strengths in Kolmogorov turbulence with an infinite outer scale. The plot illustrates how the lowest order modes representing tip and tilt are the dominant aberrations in the

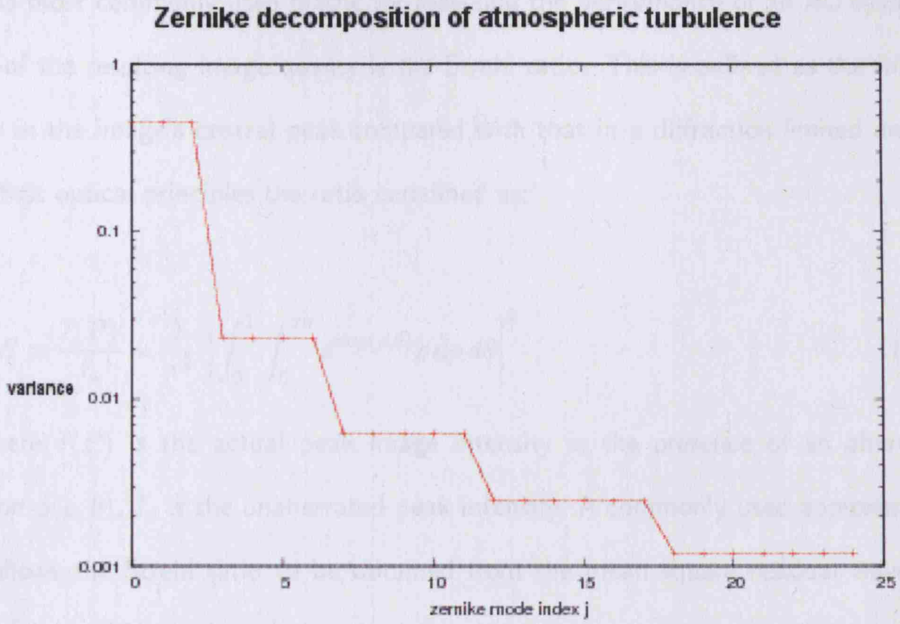

Figure 2.12: Plot of the Zernike decomposition of Kolmogorov turbulence for infinite outer scale.

wavefront. The first Zernike term, with $n = m = 0$, represents piston; its coefficient has infinite variance and is therefore excluded from the graph. The Zernike coefficients a_j of an aberrated wavefront are computed by matrix multiplication techniques. Winker (1991) derived the Zernike decomposition for a finite outer scale turbulence spectrum, as described in equation 2.4. The effect of a finite outer scale is to attenuate the low-order modes, whilst the high-order terms remain relatively unchanged.

As in active optics, an optimal modal wavefront representation has both orthogonal and statistically independent modes. Calculation of the covariance matrix of Zernike modes (Noll, 1976) reveals that cross-talk exists between several of the modes. A more accurate fit to the wavefront for a given number of terms can be obtained using Karhunen-Loève (K-L) modes. These functions have no straightforward analytical forms and must be calculated with the characteristics of a particular system. In the lowest order modes, K-L modes are very similar to Zernikes; they can in turn be expressed in terms of Zernike terms by diagonalizing the Zernike covariance matrix.

The most commonly used metric for assessing the performance of an AO system in terms of the resulting image quality is the Strehl ratio. This is defined as the ratio of energy in the image's central peak compared with that in a diffraction-limited image[2]. From first optical principles the ratio is defined as:

$$S = \frac{I(P)}{I_\star} = \frac{1}{\pi^2}\left|\int_0^1\int_0^{2\pi} e^{ik\phi(\rho,\theta)}\rho\,d\rho\,d\theta\right|^2 \qquad (2.15)$$

where $I(P)$ is the actual peak image intensity in the presence of an aberration function $\phi(\rho,\theta)$, $I_\star$ is the unaberrated peak intensity. A commonly used approximation that allows the Strehl ratio to be obtained from the mean square residual wavefront error σ_p^2 is the Maréchal approximation:

$$S = \exp(-\sigma_p^2) \qquad (2.16)$$

This approximation is valid for wavefront errors up to 2 radians; it is not suitable for characterizing uncompensated images.

2.3.3 Adaptive optics in practice

A typical adaptive optics (AO) system contains three key subsystems: a wavefront sensor, a deformable mirror, and a control system.

Wavefront sensor (WFS). The function of the WFS is to sample the aberrations in the incoming wavefront. Several different approaches have been developed to this end. The three most popular types are the Shack-Hartmann WFS, the curvature sensor and the shearing interferometer. In recent years the pyramid WFS has also gained increasing popularity, in particular for high-contrast applications and

---

[2] the central disk of a diffraction-limited image contains 84% of the total energy; the rest is diffracted into concentric rings.

multi-conjugate systems. Irrespective of the type of sensor, the accuracy for measuring the wavefront will increase with the number of subapertures over which the wavefront is sampled. For Kolmogorov turbulence, the variance of the wavefront measurement error is proportional to $(d/r_0)^{5/3}$ for subapertures of size d (Tyson and Frazier, 2004).

Deformable mirror (DM). The function of the DM is to carry out the necessary corrections on the incoming wavefront. Its shape is controlled by actuators, which push the mirror faceplate into the required shape. Deformable mirror technology is discussed in detail in section 2.4.

Control computer. Adaptive optics in practice is complicated by the fact that a very fast closed-loop operation is required for effective wavefront correction. First the control computer builds an *influence matrix* characterizing the mirror shape functions. Inversion of this matrix allows it to directly translate the measured aberrations to the required DM commands. A detailed description of this procedure can be found in Tyson and Frazier (2004), Madec (1999) and Hardy (1998).

A fourth element is the reference source, the light from which is used to sense the wavefront and compute the required DM commands. The area around the source within which an object can in theory be corrected perfectly is known as the isoplanatic patch. The size of this patch is determined by turbulence statistics, generally of the order of arcseconds. Because of the scarcity of sufficiently bright reference stars, this effect, in combination with the limited available integration times, results in current AO systems being severely limited in sky coverage. The size of the isoplanatic patch is given by:

$$\theta_0 = 0.341(\cos\zeta)\frac{r_0}{h} \tag{2.17}$$

where ζ is the zenith distance, r_0 the atmospheric coherence parameter and h the turbulence height. For example, if $r_0 = 0.16m$ and the mean turbulence height is

$5km$, the resultant isoplanatic angle is just 2 arcseconds. This definition is however very simplistic and only holds where very high Strehl ratios are desired; it does not take into consideration the dependence of anisoplanatism on aperture diameter and detailed vertical turbulence profile.

Several methods have been developed to combat isoplanatic effects in AO-assisted imaging. Artificial laser beacons (Foy and Labeyrie, 1985) can be projected close to the source of interest in the absence of a suitable guide star; several such systems are currently in operation or under development. Second, detailed modelling of the AO point spread function over a wide field can allow algorithms to be formulated that overcome anisoplanatic effects. Britton (2006) presents a detailed investigation of anisoplanatic effects on the AO PSF; the author's analytical model shows good agreement with AO observations.

Several different types of WFS and DM exist, and all three subsystems must be finely tuned to each other to deliver optimal performance. Figure 2.13 shows a typical adaptive optics system optical layout, including the most common error sources which are discussed in the next section.

2.3.3.1 Sources of error

Because of the short correction timescales and the complexity of AO systems, errors arise at various stages within and outside the system. The most important error sources are shown in figure 2.13 (Max, 2003).

Anisoplanatism error. Because of small coherence length in atmospheric turbulence, light from the reference source should ideally pass through the same region of turbulence as the source. The size of the isoplanatic patch can be increased by implementing several deformable mirrors, each conjugated to a given turbulent layer. This method is called multi-conjugate adaptive optics (MCAO).

Deformable mirror fitting error. The DM fitting error arises from the DM's inability

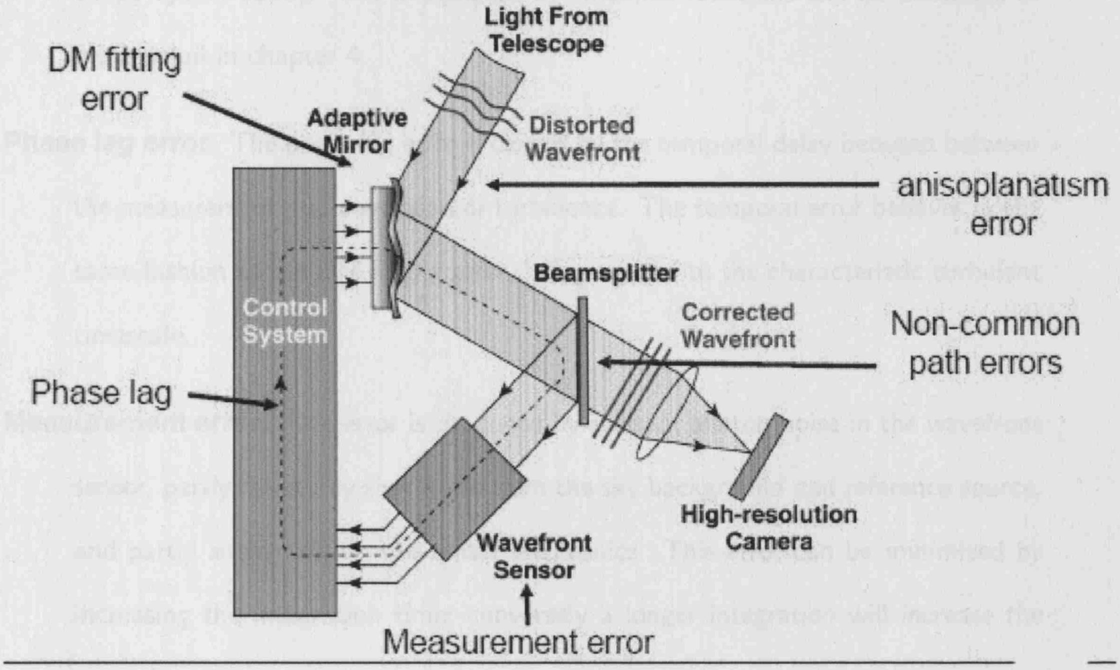

Figure 2.13: Basic optical layout of the key components of a typical adaptive optics system. Also marked are the most common sources of error and the stage at which they arise (adapted from Max (2003)).

to correct the turbulence-degraded wavefront exactly. This is due to the impracticality of correcting for errors at all spatial frequencies occurring in Kolmogorov-type turbulence. The fitting error can be reduced by increasing the number of subapertures for a given pupil size (Hardy, 1998). The general form of the mean-square fitting error is:

$$\sigma_F^2 = a_F \left(\frac{a}{r_0}\right)^{5/3} \tag{2.18}$$

where a_F is the fitting error coefficient, dependent on the shape of the influence functions on the DM, a the subaperture size and r_0 the atmospheric coherence length. A plot of this expression for various values of a_F, corresponding to different influence function shapes and DM geometries, is shown in figure 2.14 (Hardy, 1998; Tyson, 1990). The importance of influence functions will be discussed in more detail in chapter 4.

Phase lag error. The phase lag error is caused by the temporal delay between between the measurement and correction of turbulence. The temporal error behaves in the same fashion as the DM fitting error, being related to the characteristic turbulent timescale.

Measurement error. This error is produced by random photon noise in the wavefront sensor, partly caused by shot noise from the sky background and reference source, and partly arising within the sensor electronics. This error can be minimized by increasing the integration time; conversely a longer integration will increase the phase lag error.

Non-common path errors. These errors, randomly arising from variations in the optical paths going to the science instrument and to the wavefront sensor, can be minimized by accurate calibration (Max, 2003).

In error budget analysis for real AO systems, the contributions from each source are generally added linearly. The disadvantage of this is that the statistics of the error sources are not taken into account. More detailed performance predictions are carried out using Monte Carlo techniques where non-linearities and propagation of errors can be taken into account (Northcott, 1999).

The deformable mirror's fitting error is an important contributor to the overall error budget as it poses a fundamental limit to the performance of an AO system. Implementing a new mirror technology, such as novel faceplate materials, must be preceded by extensive laboratory testing and modelling to ensure the optimal quality of adaptive correction. The following section will discuss aspects of DM design, such as faceplate architectures and actuation techniques, which are very important and relevant to the work presented here.

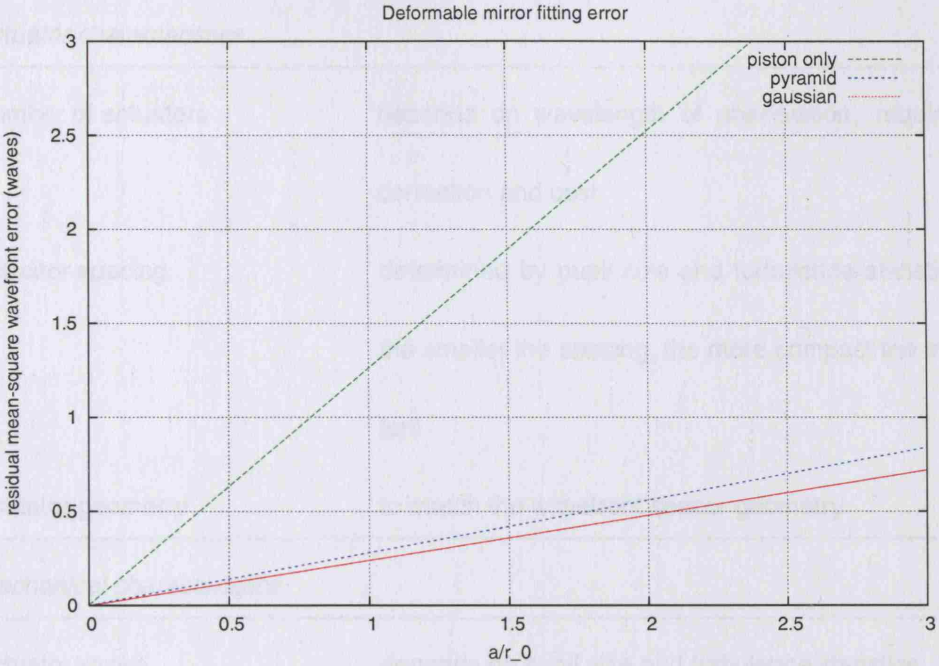

Figure 2.14: Plot of the mean-square residual wavefront error due to the imperfect fit of the deformable mirror shape to the wavefront aberration.

2.4 Deformable mirrors for adaptive optics

Whilst the principle of an adaptive mirror is essentially the same as that of an active primary, the nature of the aberrations to be corrected dictate a very different method of operation. As the aberrations in AO arise from the environment outside the telescope, as opposed to from within the telescope itself, the system must be tailored to the spatial and temporal frequency properties of the phase fluctuations at the observing site, as well as to the required degree of correction. The fast timescales on which the corrections are required to be carried out also place important challenges on the system architecture.

Table 2.1 lists the most important actuator, mechanical and optical characteristics for deformable mirrors (Séchaud, 1999). This section will describe the system architecture for the 'traditional' adaptive optics systems which are currently in operation on many large telescopes; the concept of adaptive secondary mirrors; and the need for lightweight deformable mirrors. The first section will examine actuation methods for AO.

Actuator characteristics	
Number of actuators	depends on wavelength of observation, required correction and cost
Actuator spacing	determined by pupil size and turbulence statistics; the smaller the spacing, the more compact the system
Actuator geometry	to match the wavefront sensor geometry
Mechanical characteristics	
Actuator stroke	depends on pupil size and turbulence statistics
Fitting error	calculated from the actuator influence functions
Actuator mechanical coupling	the size of the influence function with respect to the actuator separation
Faceplate mechanical frequency	should be much higher than the operation frequency
Failure probability	must be kept as low as possible
Optical characteristics	
Pupil diameter	depends on the number of actuators and actuator spacing; determines the system size
Optical quality	requirements for static aberrations, residuals after closed-loop correction, and surface roughness
Spectral reflectivity	depends on the sensing and imaging bandwidths

Table 2.1: Required actuator, mechanical and optical characteristics for an adaptive mirror, showing the complexity involved in the design of an AO system (Séchaud, 1999).

2.4.1 Actuators for adaptive optics

The actuator array controlling the DM shape is fundamental to the system's operation. Whilst there is an overlap in technologies used, actuators for adaptive optics have distinct operational requirements from those used in active mirror control (Ealey and Wellman, 1989):

- adequate stroke in push and pull direction;
- fast response time;
- high position resolution;
- inherent stability;
- higher resonant frequency than the operational frequency; and
- low power dissipation.

The correction timescale especially is unique to adaptive optics and places very high demands on actuators and their drive circuits. Certain types of actuators used frequently in active optics, such as the Keck-type stiff screw mechanism, are unsuitable for AO because of their slower response time, lower position resolution and size. Pneumatic systems are unsuitable because of their inability to easily provide push and pull forces. Because of the small size of deformable mirrors in traditional AO systems the actuators must also be simpler and more compact in design.

Most AO systems currently in operation, using small adaptive mirrors, feature electrostrictive or piezoelectric actuators for deformable mirror control. Their main advantages are availability in a wide range of sizes, good push-pull ability, fast response time and relatively low hysteresis. These actuators are well-known and tested, and commercially widely available.

Magnetostrictive actuators were identified to be promising candidates for adaptive optics systems using large (> 0.5 m) adaptive mirrors, such as adaptive secondary mirrors (Bigelow *et al.*, 1997). Especially attractive were their good lifetime and failure rates, and commercial availability in a variety of stroke and sizes. Bigelow *et al.* (1997) subjected an MS actuator to substantial testing and found a linear frequency response to 3 kHz and power dissipation of approximately 0.5 W over a 10 μm stroke from 100 to 1000 Hz. Their relatively high hysteresis can be compensated by displacement sensors for closed-loop operation.

The only such large adaptive systems in operation, however, use soft voice coil actuators, which were identified to be the most suitable in an early study by Salinari *et al.* (1993), in terms of accuracy, frequency response, reliability, size and cost. Conversely, in a paper discussing the deformable mirror for the MMT Observatory, which uses 336 voice coil actuators, Lloyd-Hart *et al.* (2003) report the loss of 13 actuators in the first year of operation. A distinct advantage of voice coils over stiff actuators is the ability to operate the mirror on failure of a small number of actuators. Whereas a failed stiff actuator would create a hard point in the faceplate, a broken soft support will allow local mirror bending (Wildi *et al.*, 2003). Their main disadvantage is non-trivial power dissipation, which necessitates a cooling mechanism to remove heat. Salinari *et al.* (1993) gives the total power dissipation from a voice coil-actuated mirror as:

$$W_{total} = (R/G^2)N\sigma_F^2 \tag{2.19}$$

where R is the voice coil impedance, G is the ratio of force to current (F/I), N is the number of actuators and σ_F is the rms actuator force.

2.4.2 System architectures

Current AO systems, with very few exceptions, were developed as 'add-ons' to existing telescopes and are thus poorly integrated into the telescope's operation. The correction of wavefront aberrations is often split over two stages: image motion is removed by a simple tip-tilt mirror and a deformable mirror corrects for higher-order modes. Tip-tilt mirrors are usually several centimeters in diameter and tilt on two orthogonal axes. Deformable mirrors can be found in several faceplate configurations, discussed in this section, measuring between some 5 and 50 cm in size.

Where the turbulence is concentrated in a single atmospheric layer, the aberrations can in theory be corrected perfectly by a DM placed at the optical conjugate of the layer. This principle of optical conjugation maintains the spatial relationship between the turbulence and the DM (Hardy, 1998). As much of atmospheric turbulence is concentrated in the surface layer, i.e. the layer directly above the primary mirror, the pupil plane offers a method of conjugating the DM to this layer.

DMs for the earliest adaptive optics systems used segmented faceplates with either one or three actuators per segment, corresponding to piston-only and piston plus tip-tilt correction, respectively. Figure 2.15 shows a picture of the segmented adaptive mirror for NAOMI on the 4.2 m William Herschel Telescope. It is comprised of 76 segments, each measuring 7.6 mm^2 in area. Three actuators move each segment with a stroke of 6 μm each (Myers *et al.*, 2003). The advantage of a segmented faceplate is their simpler designs and lower cost. Because of the discontinuous faceplate no cross-talk exists between the subapertures, thereby simplifying control strategies (Pearson and Hansen, 1977). The main problems with segmented faceplates arise from the segment edges, which cause a direct loss of energy and substantial scattering which lowers the attainable image quality. The gaps between the segments also act as infrared emitters.

Adaptive mirrors using continuous faceplates again come in several different types, the most common of which, and the type of interest in this thesis, uses a continuous faceplate with an array of discrete actuators. The actuators are connected onto a stiff baseplate which acts as position reference. A coupling mechanism between the actuator and faceplate provides compliance to faceplate tilt and to any shear stresses. The shape of the mechanism also determines the shape of the influence function created by the

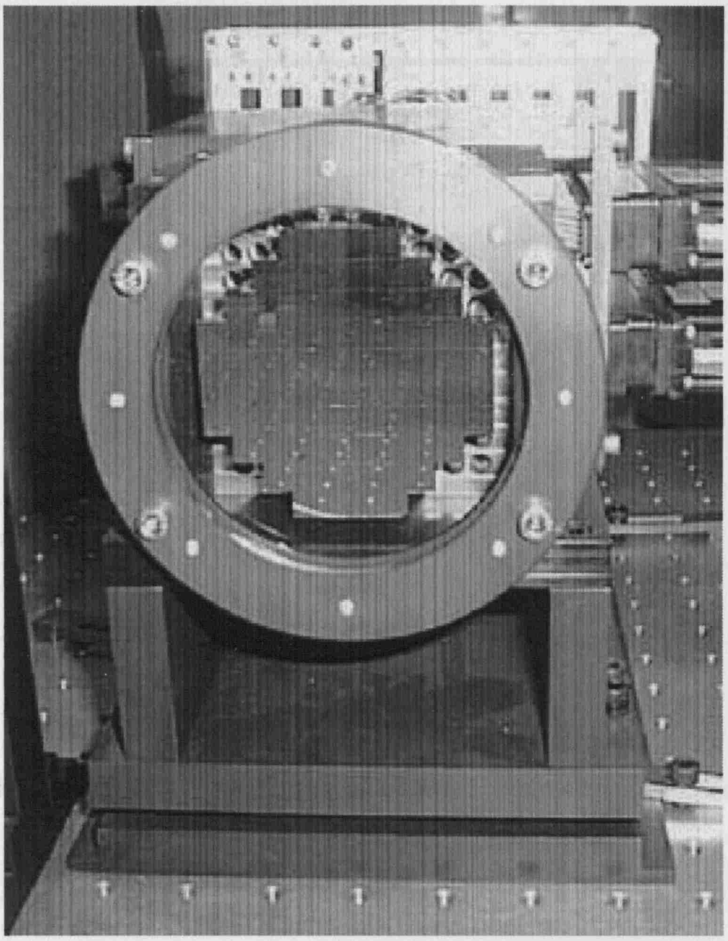

Figure 2.15: Segmented deformable mirror for the Nasmyth Adaptive Optics system for Multi-purpose Instrumentation (NAOMI) on the William Herschel Telescope. The faceplate consists of 76 segments, each controlled by 3 actuators.

actuator, which is very important to the mirror's performance. The importance of this, and the theory of influence function shapes, will be discussed in chapter 4.

The continuity of the faceplate allows for a degree of coupling between adjacent actuators. Whilst this complicates the mirror control algorithms, it allows for an improved accuracy with which a random wavefront can be compensated.

The design of these DMs is a complex process because of the many parameters to be traded against each other, such as faceplate thickness and stiffness, actuator stiffness and flexure mechanism; Ealey and Wellman (1989) outlined the process of optimization

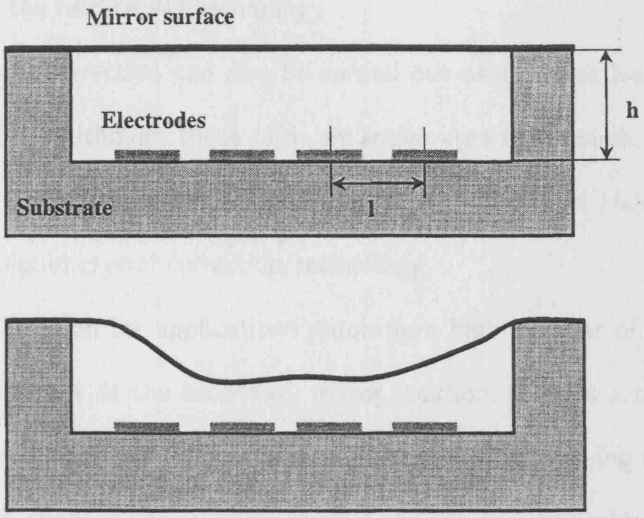

Figure 2.16: Schematic of a MEMS continuous-membrane deformable mirror, in the rest position (top) and activated (bottom) (from Zamkotsian *et al.* (2000)), showing how the thin membrane is deformed by underlying electrodes.

of DM design.

An important area of development in continuous facesheet adaptive mirrors is micro-electro-mechanical (MEMS) systems. MEMS technology is closely linked to the micro-electronics fabrication process, where various materials are deposited onto the surface of a substrate, and, using masks, their localization on the substrate is very precisely defined in order to ensure their specific tasks (Zamkotsian *et al.*, 2000). The facesheet of the mirror is in the form of an ultra-thin membrane without inherent stiffness. Figure 2.16 shows an example diagram of a MEMS DM architecture.

The micro-machining allows for very close packing of the actuators, with typical separations of 200-500 μm and total size of a few tens of millimetres; they thus offer a solution for adaptive optics applications requiring a high number of actuators at a lower cost than with conventional actuators. Wallace *et al.* (2003) reports a cost of $1,000 per actuator for piezoelectric designs compared with $20 in a MEMS-based mirror. No MEMS DM has been used in a working adaptive optics system but this is a significant area of research in the field of AO technology.

Finally, wavefront correction can also be carried out using refractive optics such as liquid crystal devices. Although these form an active area of research, they have not been implemented on any working systems. Séchaud (1999) and Hardy (1998) give good overviews of liquid crystal correction technology.

An alternative solution for applications requiring a high number of actuators is to place the adaptive mirror at the secondary mirror location. This is a technology with limited practical experience but a major area of research. The following section will discuss the advantages of adaptive secondary mirrors and the specific problems in designing such systems.

2.4.3 Adaptive secondary mirrors

The need for lightweight deformable mirrors in astronomy is related to the use of adaptive secondary mirrors (ASMs) in advanced adaptive optics (AO) systems. The use of a telescope's secondary mirror as adaptive correction element was first suggested in the early 1990's with early studies carried out by Salinari *et al.* (1993) and Bigelow *et al.* (1993). Adaptive secondary mirrors form an attractive solution to the problem of providing integrated adaptive optics to all telescope instruments, which is essential as telescope primary mirror diameters are set to increase dramatically in the next decades (Andersen *et al.*, 2003; Dierickx, 2002).

Bigelow (1996) studied the impact of using adaptive secondary mirrors on the performance of an AO system. The improved integration has the following beneficial consequences:

- greater efficiency and throughput by using an existing mirror surface for adaptive corrections;
- reduced emissivity in IR observations;

- simpler optical layout; and
- the capability to provide atmospheric compensation directly to the Cassegrain and Nasmyth foci.

The design of these mirrors, however, presents some unique problems. An important factor is the added weight to the secondary structure from the actuators and control system, which places higher stresses on the support structures. Because of its location above the primary mirror, risk of mechanical failure can be costly. Constraints on heat dissipation from the actuators are very tight because of the location in the telescope's entrance pupil, an area very sensitive to turbulence. Because of their larger size, typically up to 1 m, and hence large actuator spacing, the resonant frequency can lie below the AO operating frequency.

More fundamentally, the use of an adaptive secondary mirror in Cassegrain telescopes prevents the AO system's correcting devices from being conjugated to the height of turbulence. This causes a non-trivial reduction in isoplanatic patch size (Hardy, 1998). However, Bigelow (1996) studied the shear and pupil vignetting arising from the deformable optics being conjugated to the entrance pupil instead of the turbulence height for telescopes in the 4-8 m size range, and found no significant deterioration in performance with the adaptive secondary system. Use of multiple deformable mirrors is complicated by the use of an adaptive secondary.

The actuator stroke must be large enough to incorporate the chopping requirements of the secondary mirror when used in the infrared. Whereas traditional deformable mirrors require a stroke of up to 10 μm, chopping ability can require a stroke of an order of magnitude higher. Bigelow *et al.* (1993) derives a stroke of up to 145 μm for an adaptive secondary for the Gemini telescopes, corresponding to mirror tilts of 60 arcsec on the sky.

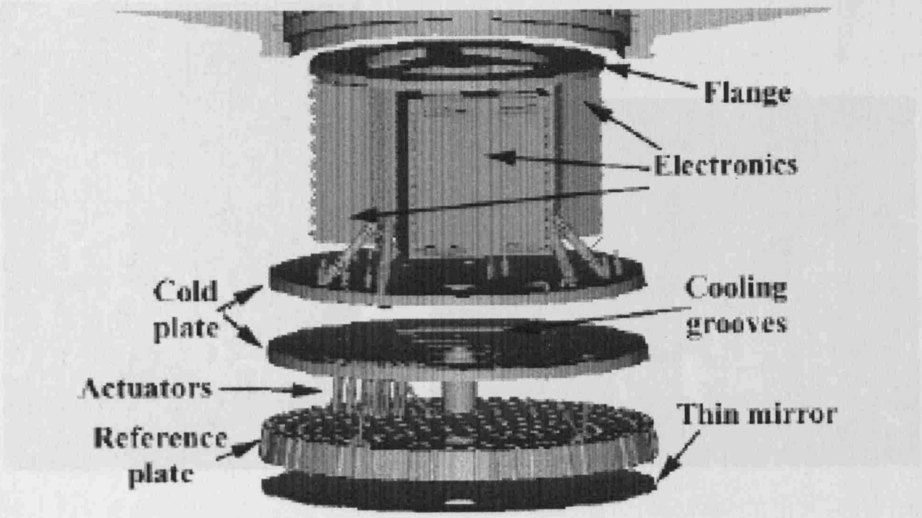

Figure 2.17: Schematic layout of the deformable secondary system on the 6.5 m MMT telescope (Riccardi *et al.*, 2001).

2.4.3.1 The MMT and LBT adaptive secondary systems

The MMT observatory is currently the only optical/IR facility employing an adaptive secondary mirror. It consists of a 2 mm thin faceplate in Zerodur measuring 640 mm in diameter, and is controlled by 336 voice coil actuators. Position reference is provided by a stiff Zerodur reference plate. Figures 2.17 and 2.18 illustrate this system.

Wildi *et al.* (2003) discuss two major problems with operation of the mirror, which illustrate the difficulties of such a complex system:

- leaking of the cooling mechanism, necessitating a shut-down of the cooling system and allowing the actuators to dissipate heat into the system;
- dust contamination of the gap between facesheet and reference plate. The air gap is necessary to provide vibrational damping at the highest correction frequency (550 HZ).

In addition, the authors report on the extreme delicacy of handling the thin glass shell, which is a non-trivial problem as size increase. In fact, handling requirements

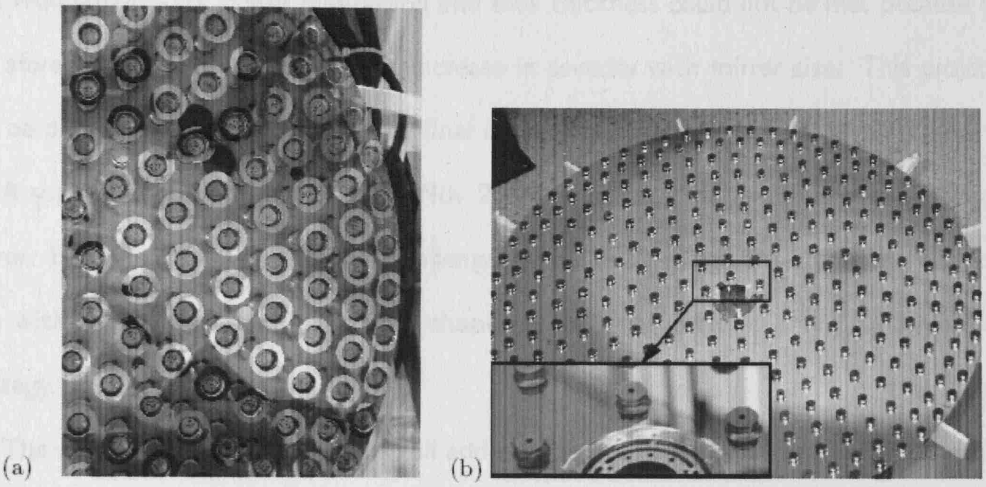

Figure 2.18: (a) Reference plate of the MMT deformable secondary mirror, showing the actuator holes. Around each hole is the armature of the position sensors. (b) Back surface of the thin mirror, showing the magnets glued onto the shell (Riccardi *et al.*, 2001).

dictated the minimum thickness of 2 mm for the shell.

Currently under construction, the twin 8.4 m LBT telescopes will use adaptive secondary mirrors measuring 911 mm in diameter and 1.6 mm in thickness, using essentially the same design as the MMT model. 672 voice coil actuators control each mirror's shape.

2.4.3.2 Future developments

Adaptive secondary mirrors are included in the designs of the European extremely large telescope projects (Andersen *et al.*, 2003). These telescopes' primary mirrors will measure 30 to 100 m in diameter, with secondary sizes of several meters. There is evidence that the MMT/LBT technology will reach an upper size limit around 1 m in diameter - beyond that size a trade-off will be needed between shell thickness and power requirements to drive the mirror (see chapter 5).

This was the finding in an important precursor project to the ELT designs (Gallieni and Biasi, Sep 2004), an adaptive secondary mirror for one of the VLT unit telescopes (Arsenault *et al.*, 2004*b*), measuring 1120 mm in diameter, where initial research found that requirements for power dissipation and shell thickness could not be met because of the aforementioned problems, which increase in severity with mirror size. This project will be discussed in more detail in the final chapter of this thesis.

A suggested solution (Ragazzoni, Nov 2004) is to segment the adaptive secondary mirror. However, the technological challenges of combining high-order adaptive correction with issues of segmentation and shape control, suggest this is not an advisable strategy.

The work presented in this thesis will address the possibility of using a novel material, carbon fibre reinforced polymer (CFRP), to solve some of these issues. With its high stiffness and excellent thermal stability CFRP could offer an alternative to traditional material choices. Problems with handling of the thin shell would be largely avoided because of the material's higher fracture strength.

2.5 Conclusions

This chapter has presented two important technologies, active and adaptive optics, in ground- and space-based optical/IR astronomy.

It was demonstrated that active optics, the 'live' correction of primary mirror aberrations due to slow-varying disturbances, has now become an essential part of ground-based observatories, allowing for a relaxation of tolerances on low spatial frequency aberrations and lightweighting of large primary mirrors. It has also enabled the introduction of large segmented mirrors; a technology which is well suited to a scaling up of mirror sizes.

In space active optics, where experience with optical observatories is limited to the Hubble Space Telescope, active optics can also play an important role in allowing mirrors to become lightweighted. Segmentation of mirrors for space also allows aperture sizes to increase without compromise to launch vehicles; this is the chosen approach for Hubble's successor JWST. While not accommodating active optics in the same fashion as ground-based telescopes, limited active control will ensure proper segment alignment after deployment in space.

In adaptive optics ultra-lightweight mirror technology offers an attractive solution to problems encountered with integration of AO systems in the form of adaptive secondary mirrors. The use of an existing optical surface for carrying out high-order wavefront corrections presents some unique design challenges which are currently being met by a thin-shell approach using Zerodur. However, with telescope sizes looking to increase in the next decade, this technology may not be viable at larger sizes. A more robust material such as CFRP could offer an alternative.

The following two chapters will discuss a project to build and characterise a prototype active/adaptive mirror in nickel-coated CFRP to investigate issues such as coating methods and adhesion and stability with this attractive technology. Conclusions will be drawn on the problems likely to be encountered and suggestions for further work are made.

CHAPTER 3

CFRP mirrors: initial modelling and investigations

"Experience is simply the name we give our mistakes."

– Oscar Wilde

The initial aim of the project was to investigate material properties, manufacturing processes and coating effects, to specify the optical design and define operational parameters. After comprehensive discussions with Cobham Composites, extensive preliminary finite element analysis (FEA) of the various possible laminate configurations of the faceplate was carried out in collaboration with QinetiQ. Following this, it was decided to produce a test mirror, not intended for active control, to test the manufacturing, coating, grinding and polishing processes, to carry out initial stability checks and thus validate the finite element modelling results. This chapter will discuss this extensive body of preliminary work: other past and ongoing projects in CFRP optics, the production of a stainless steel mold for the lay-up process, design considerations for the passive test piece, and a presentation of the relevant FEA results. Experimental results are also shown for the passive mirror, leading to useful lessons learned for the second stage of the project, the development of a deformable composite mirror.

3.1 CFRP for space- and ground-based optics

Previous efforts into CFRP materials for lightweight optics have been carried out in the context of the James Webb Space Telescope (JWST) for space applications, and of Extremely Large Telescope (ELTs) on the ground. In addition, composite reflectors have been developed for far IR/submillimetre observatories in space.

The next generation of large optical/IR space observatories such as JWST have highlighted the need for large ultra-lightweight optics; this was previously discussed in chapter 2. Research efforts into CFRP have focused on achieving an ultra-low surface roughness, performance at cryogenic temperatures, and stability on changing temperature and humidity.

Results of research into lightweight composite mirror technologies at Composite Mirror Applications Inc. are presented in Chen *et al.* (1998), Chen *et al.* (2000) and Chen and Romeo (2004). Experiments with replication of graphite reinforced cyanate ester test pieces yield an aerial density of <5 kg/m^2. An rms surface accuracy of a fractional wave is achieved in curved mirrors over 90% of the pupil, with the edges showing severe edge roll-off and several waves of astigmatism, coma and third-order spherical aberration; flat mirrors show surfaces of $\lambda/20$ at optical wavelengths. An optically reflective coating is applied in a vacuum process but no information is given regarding materials.

This technology is applied to the specific case of the Euro50 extremely large telescope design, which features a 4 m class adaptive mirror (Bennett *et al.*, 2004). The authors report results from a prototype telescope mirror faceplate in a graphite-reinforced cyanate ester resin with a surface roughness of < 10 $\mathring{A}$. Novel ultra-lightweight actuators are also developed weighing just 30 g each.

Research at Mitsubishi Electric Corp., the University of Tokyo and the National Astronomical Observatory of Japan into ultra lightweight carbon/carbon composite mirrors for astronomy is reported by Takeya *et al.* (2004). The authors describe the design and manufacture of a 150 mm diameter, 1000 mm radius of curvature prototype for optical/IR applications. Carbon matrices form an alternative to cyanate esters for a low moisture absorption matrix, but are hard to grind because of their porous nature. The manufacturing process is also significantly more complex than for epoxies or esters. Electroless plating was used to apply a 100 μm nickel coating. A final surface accuracy of 0.175 waves is reported.

Abusafieh (2003) described a process developed at ATK Composite Optics Inc. to produce ultra-smooth surfaces using diamond turning. A composite substrate was plated with a copper coating which was then diamond turned to a surface roughness of 2.5 nm rms without requiring further polishing. The copper also provides a moisture barrier to prevent dimensional changes from moisture ingress. The author suggests that further polishing could reduce the roughness to the level required for optical imaging.

An alternative to segmentation for large deployable space-based mirrors is the use of shape memory composites (SMC). These are polymer-based thermoset materials based on epoxy or cyanate ester chemistries. They differ from traditional composites in their ability to "store" mechanically induced strain and recover it when subjected to a specific thermo-mechanical cycle (Arzberger *et al.*, 2003). Thin lightweight SMC optics can thus be rolled and redeployed in orbit.

Research into this technology at Northwestern University (USA), Ball Aerospace and Technologies Corp. and Cornerstone Research Group is described in the literature by Arzberger *et al.* (2003), Ulmer *et al.* (2005) and Varlese *et al.* (2005). An in-mold nickel coating process on these SMC optics is described and several methods of improving the adhesion between the nickel and composite are tested, to prevent the nickel from creasing or detaching on rolling of the composite.

The main focus in these research projects worldwide is the production of an ultra-smooth surface roughness. This is a very important goal for reducing scattering, which is crucial for science drivers requiring extremely high PSF control such as planet detection. As well as surface roughness, the aim of the project presented here was to obtain a good form, which reduces the required actuator stroke for flattening the mirror and facilitates optical testing.

3.2 Initial design considerations

This section will examine some of the initial considerations in the design of the mirror.

Mirror size and form. The mirror size and form followed the design of a previous demonstrator system, carried out at UCL in the late 1990s featuring an aluminium faceplate. As this system was still available in the lab, its design was adopted for the CFRP mirror as this would eliminate the need for a new set of actuators. Details of this aluminium system will be discussed in this section and the next chapter, and comparisons with previous results from it referenced throughout.

Material specifications. FEA results were used to determine the optimal laminate configuration and thickness. The findings of these models will be presented in section 3.4.

Coating method and thickness. The mirror was coated using a novel process developed at Cobham Composites. The mirror's thermal stability was thought to be strongly influenced by the thickness of the metallic coating, and FEA was carried out to attempt characterizing the coating's behaviour under varying temperature. These results are also discussed in section 3.4.

Surface form accuracy and roughness. Whilst surface form is not of the highest priority for an active mirror, the aim here was to get the best possible baseline form to maximize the actuators' stroke range. Surface roughness is of high importance for precision optical systems as it affects the amount of stray scattered light in a system. The passive test mirror was largely produced to investigate these properties. Results are presented in section 3.5.

Actuator connections. The connection between the actuators and the mirror faceplate affect the shape of the actuators' influence function, the amount of inter-actuator coupling and the system's eigenfrequencies. The design of the connectors will be discussed in chapter 4.

3.2.1 The UCL adaptive secondary demonstrator

The aluminium adaptive secondary demonstrator, whose architecture was adopted for the CFRP active mirror, is discussed in detail in Walker *et al.* (1998); Lee (1999); Lee *et al.* (1999*b*,*a*, 2000), and formed the culmination of several years of research into metal deformable mirror technology.

The design of the aluminium demonstrator was innovative in several areas. First, it used aluminium as faceplate material with matched actuator connectors and backing structure to make a thermally homogeneous structure. A 100 μm electroless nickel coating was applied to the faceplate. The final mirror form after polishing by Dr. D. Brooks (Lee, 1999) showed a radius of curvature of 2944 mm and an rms surface error of 0.148 μm. Second, the system was one of the first to use magnetostrictive actuation in a deformable mirror experiment. Finally, a design feature of the mirror was that the mirror faceplate was supported solely by the actuators without radial support, which at the time was unusual. The flexure couplings designed for the aluminium adaptive secondary were extensively modelled and tested, and allow a satisfactory relaxation of the system's overall stiffness.

Table 3.1 shows the basic specifications of the aluminium active mirror system. Figure 3.2 shows a schematic layout of the setup. Figure 3.1 shows a picture of the finished system.

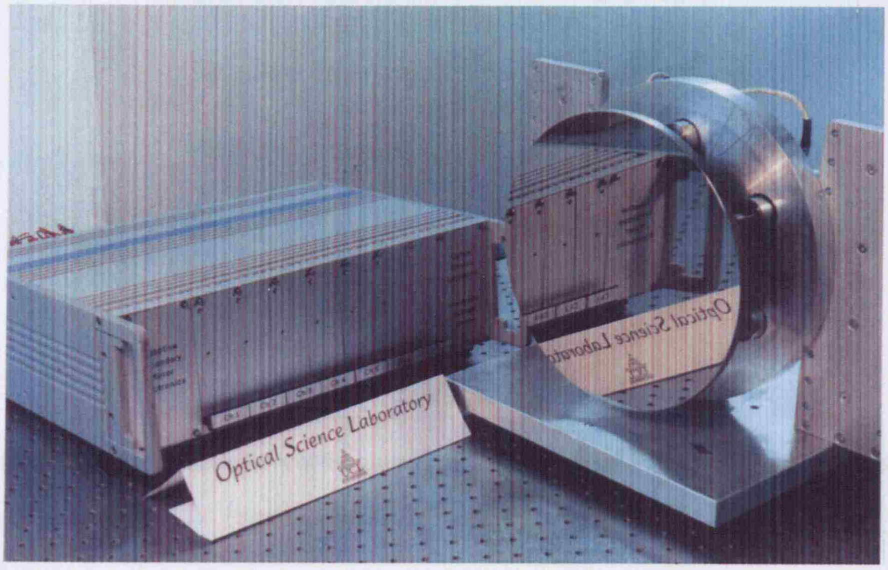

Figure 3.1: Picture of the aluminium active mirror system.

Before proceeding to a discussion of finite element results, the following section will provide an introduction to the finite element method, its uses, advantages and limitations. Section 3.4 will then discuss the basics of finite element analysis for composite materials using I-DEAS, and how this method was used to investigate the properties of the composite deformable mirror. Based on these results, a laminate thickness and configuration was decided upon.

3.3 The finite element method for deformable mirror analysis

Finite element analysis (FEA) is a method of analyzing the displacements, stresses and strains in complex structures by dividing it into a finite number of geometric regions, or 'elements' (Matthews *et al.*, 2003). Many finite element results are presented in this thesis. The aim of this section is to present the fundamentals of finite element theory, an overview of solution methods. The final subsection will examine the specific case of

Diameter	270 mm
Faceplate thickness	10 mm
Radius of curvature	2955 mm
Shape	spherical, concave
Number of actuators	7
Inter-actuator spacing	100 mm

Table 3.1: Basic specifications of the aluminium active mirror produced at UCL (Lee, 1999).

composite materials FEA.

3.3.1 History and development

Since early developments in the 1950s and 1960s, finite element analysis has grown into a very powerful tool in many branches of engineering. This section will describe the historical context that led to the formulation of the finite element method, and the basic concepts that govern its use.

Until the early 1950s, structural analysis consisted of computing the solution to a set of differential equations, into which the principles of equilibrium, Newtonian gravity, potential energy, strain energy, conservation of total energy, virtual work, thermodynamics and many more had been distilled. With the tools available at the time, this meant that only simple problems with regular geometry and simple boundary conditions could be accurately solved. In many industries, most notably the aircraft, automotive and nuclear sectors, the resulting oversimplification of models and calculations represented unacceptable risks where large amounts of money and human lives were at stake.

In the finite element method, complex structures are approximated by a number of finite simple geometric regions, or elements, for which approximate displacement

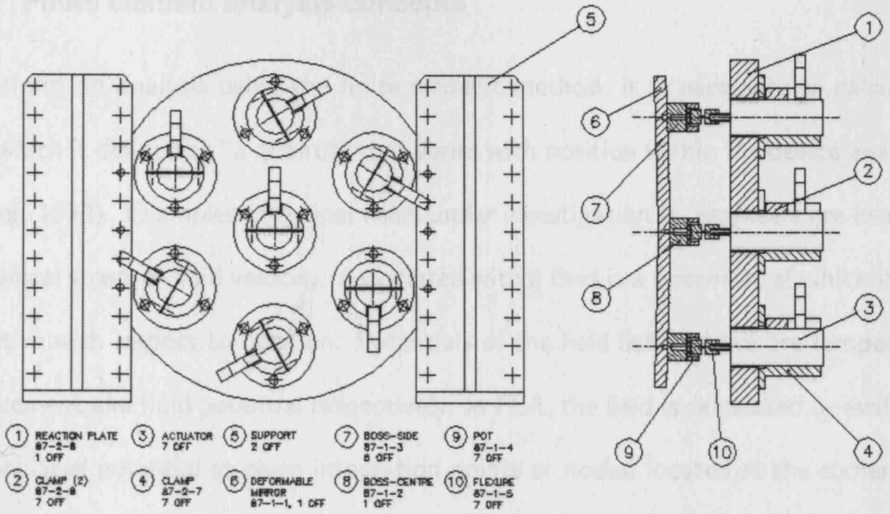

Figure 3.2: Drawing of the aluminium active mirror setup showing the faceplate, actuators and backing structure.

functions can be assumed. Stress and strain can then be computed using these functions. Section 3.3 will elaborate on the mathematical methods used in the analysis. The strength of FEA is that it transforms structural analysis from a differential equation approach into an algebraic problem. For the companies developing the early FEA codes [1], the possibility of carrying out stress analysis in the early stages of product development, made it easy to make changes to the design and recompute the stresses.

The value of the finite element method lies in its elegance and simplicity. Highly sophisticated software packages have been developed that can "assemble" the elements in a mesh and their stiffness matrices and carry out large numbers of matrix computations. They allow engineers to predict the behaviour of a structure to a degree which was previously only achievable from experimental analysis. The finite element method can also be used for heat transfer, electromagnetics and fluid flow analyses. A more recent advance is to use the method for electromechanical and magnetic work.

---

[1] Many of the best established codes today, such as NASTRAN, were developed by NASA or in aerospace companies

3.3.2 Finite element analysis concepts

To perform an analysis using the finite element method, it is necessary to calculate a *field*, which is defined as "a quantity that varies with position within the device analyzed" (Brauer, 1993). Examples of typical fields under investigation by engineers are heat flux, mechanical stress or fluid velocity. Associated with a field is a *potential*, of which it is the derivative with respect to position. Potentials of the field listed above are temperature, displacement and fluid potential respectively. In FEA, the field is calculated by evaluating its associated potential at given integration points or *nodes*, located at the corners (and sometimes midpoints) of each element. In a linear structural analysis, the mechanical stress is calculated from the displacement of each node.

The potential has a given number of degrees of freedom at each node. Temperature, for example, is a scalar quantity with thus only one degree of freedom, whilst the displacement potential may have 6 degrees of freedom - 3 in translation and 3 in rotation. The degrees of freedom in FEA can be left unconstrained or constrained. By applying constraints at the nodes, *boundary conditions* are specified on the model. These principles will be illustrated with a simple example, taken from Shih (2000).

Consider a one-dimensional truss - a uniform slender bar with length L much bigger than the cross-sectional dimensions (figure 3.3), cross-sectional area A and elastic modulus E. A node is located at each end of the bar. Forces are applied to the nodes only and along the direction of the truss's length.

If equal and opposite forces of magnitude F are applied to the end nodes, the material will undergo a change in length of magnitude:

$$\delta = \frac{FL}{EA} \tag{3.1}$$

in accordance with Hooke's law for linear springs, where the equivalent spring constant for the truss, K, is EA/L. By analyzing the relative motion of the two nodes, a general expression for the forces can be derived.

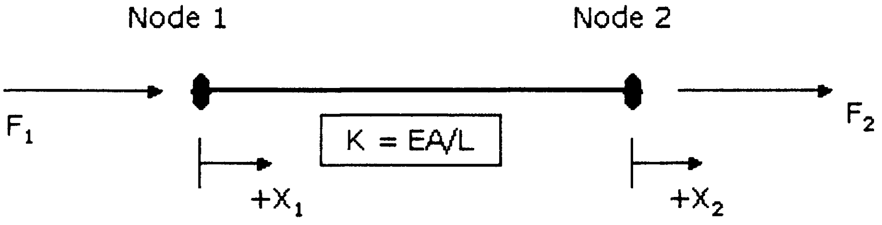

Figure 3.3: Example layout for demonstrating the finite element stiffness method.

First, let $X_1 = 0$. Based on Hooke's law F_1 and F_2 can be expressed as:

$$\begin{cases} F_2 = KX_2 \\ F_1 = -KX_2 \end{cases} \tag{3.2}$$

Then, put $X_2 = 0$. Using the same arguments:

$$\begin{cases} F_1 = KX_1 \\ F_2 = -F_1 = -KX_1 \end{cases} . \tag{3.3}$$

Combining equations 3.2 and 3.3:

$$F_1 = KX_1 - KX_2 \tag{3.4}$$

$$F_2 = -KX_1 + KX_2 \tag{3.5}$$

or in matrix notation:

$$\begin{pmatrix} F_1 \\ F_2 \end{pmatrix} = \begin{pmatrix} +K & -K \\ -K & +K \end{pmatrix} \begin{pmatrix} X_1 \\ X_2 \end{pmatrix} \tag{3.6}$$

In general terms:

$$\mathbf{F} = \mathbf{K} \cdot \mathbf{X} \tag{3.7}$$

where $\mathbf{X}$ represents the matrix of unknowns, such as displacement in the above example. Matrix $\mathbf{K}$ in equation 3.7 is the global stiffness matrix, which relates the node displacement to the applied forces. In two- and three-dimensional space, co-ordinate transformations are also needed as part of the calculations. Boundary conditions can then be applied for the known quantities and the equations solved for the unknowns. In structural analysis, either a load on or a displacement at a node must be specified as a boundary condition. The process is equivalent to a minimization of the potential energy in the system in terms of a prescribed displacement field (Zienkiewicz and Taylor, 2000, vol.1).

For complex structures the method is effectively the same as for this simple example. The size of the stiffness matrix, however, grows rapidly in size, and the number of equations in the set can often run into the hundred thousands, demanding increasing amounts of processing power and memory. Fortunately, these large matrices are both sparse and symmetrical, requiring storage for approximately half the non-zero elements. The availability of cheap and powerful hardware has enabled the development of very sophisticated and user-friendly FEA software packages.

The main limitation of the finite element method is that the displacement-based formulation overestimates the true elemental stiffness. As a result, the displacements tend to be *underestimated* (Becker, 2004). Figure 3.4 demonstrates this effect graphically.

Users now have access to a large family of elements to enable finite element modelling of both simple and highly complex structures. Elements with two dimensions much

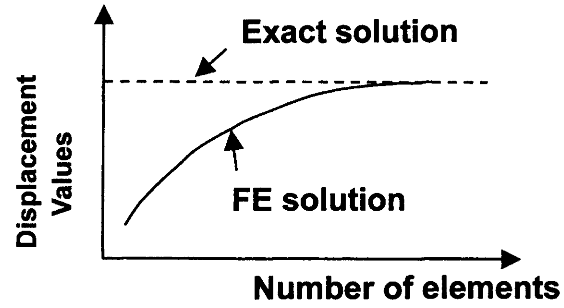

Figure 3.4: Graph demonstrating the accuracy of the finite element method, showing how the displacement error is always negative due to the intrinsic over-stiffness of the elements (adapted from Becker (2004)).

smaller than the third define the 1D elements, such as beams, rods and springs. Those with one such dimension define 2D elements such as plates and shells. Table 3.2 shows a summary of the types of elements offered by typical modern FEA pre-processors. In addition, many packages provide specialist element types, for example for multiphysics modelling of piezoelectric or magnetic materials. Naming of element types is very much software-dependent; many texts even use the elements' proprietary name and 'generic' element descriptions are rare. The element names listed in table 3.2 are taken from the software package I-DEAS. In general for structural analysis parabolic element types give better results than linear ones because of the higher number of integration points per element, and quadrilateral or hexahedral elements give more accurate stress results than triangular or tetrahedral ones respectively (UGSPLM, 2002).

3.3.3 Modern FEA solvers

Access to cheap powerful workstations has allowed huge modernization of FEA software interfaces since its inception in the 1950s. Many different packages exist, some have a very broad spectrum catering for many different kinds of analysis, whilst others are smaller and specially designed for a given application, such as crash test analysis, heat

Summary of FEA element types in I-DEAS					
1D	Beam	Exist in linear, curved, parabolic or tapered geometry. 2 (linear, curved, tapered) or 3 (parabolic) nodes.	3D	Tetrahedral	Can be linear (4 nodes) or parabolic (10 nodes).
	Rod	2 nodes with 3 translational degrees of freedom (DOF) each.		Brick	Can be linear (8 nodes) or parabolic (20 nodes). More computationally efficient than tetrahedrals.
	Axisymmetric thin shell	To model structures which are symmetric about an axis of rotation and are subject to axisymmetric boundary conditions. Can be linear (2 nodes) or parabolic (3 nodes).	Other	Constraint	Constrains up to 2000 nodes to an independent node in one or more DOF, using a least squares minimization technique. Has no material properties.
2D	Thin shell	Can be linear or parabolic, triangular or quadrilateral with 3, 6, 4 or 8 nodes respectively. Supports laminate material types.		Gap	A node-to-ground gap limits the motion of the node and can be used to simulate the presence of a rigid obstacle. Node-to-node gaps limit the relative nodal motion.
	Axisymmetric solid	To model structures which are symmetric about an axis of rotation and subject to axisymmetric boundary conditions. Can be linear, parabolic and triangular (3, 6 nodes) or quadrilateral (4 or 8 nodes).		Rigid	Connect 2-2000 nodes. A rigid link implies that the connected nodes move together as if connected by an infinitely rigid massless beam.
	Plane stress/strain	Assume zero stress/strain in the out-of-plane direction. Exist in linear or parabolic, triangular (3 or 6 nodes) or quadrilateral (4 or 8 nodes) shape.		Spring	Can be translational or rotational and connect nodes to other nodes or nodes to ground. Contain no material properties.

Table 3.2: Summary of the most common element types using the naming conventions of FEA software I-DEAS (UGSPLM, 2002).

flow, or multiphysics problems.

Graphical user interfaces (GUIs) fall into two categories (MacNeal, 1993). A first and cheaper type are dedicated processors that provide a single interface to one given solver engine. If one particular analysis is needed, such a program can be adequate. Many modern packages however serve a number of solvers with state of the art capabilities, catering for many analysis types.

Most FEA software also provides an interface with computer aided design (CAD) programs, which is important where complicated structures are being modelled. A careful balance between design and modelling setup must be found when performing FEA, as there exists a conflict between the needs of CAD and FEA programs. A CAD representation will include all the structure's fine details, whereas these details are not necessary for, and can indeed complicate, FEA models.

Numerous methods have been developed for solving the large matrices described in section 3.3.2, broadly falling into the three broad categories of direct, iterative or eigenvalue solutions. While the solution should be independent of the solver method, the algorithm can have a significant effect on solve time, and complex models can fail to converge with a given solver. Care must be taken to ensure that the applied loads and resulting stresses do not result in non-linear material effects such as breaking or cracking, and that the material does not suffer from creep or hysteresis.

The software package used for the work presented in this thesis is I-DEAS versions 8 and 11. It offers the following analysis types:

- Linear statics (normal and adaptive)
- Nonlinear statics
- Normal mode dynamics
- Response dynamics
- Frequency dynamics

- Linear buckling
- Heat transfer
- Potential flow

All the work presented here was carried out with normal linear statics analysis, which is defined by the assumption of a linear strain-displacement relationship. I-DEAS features two different solver methods for linear statics analysis, one direct and one iterative, and support for linking to the external solver NX NASTRAN. A two-way exchange of models and results with other solvers such as ANSYS, NASTRAN or ABAQUS, is also supported. I-DEAS main strength lies in its excellent CAD modelling and drafting toolboxes, as well as a comprehensive add-on for modelling composite structures.

3.4 Finite element analysis results of composite mirror substrates

Composite materials form a special case for FEA. Due to the abundance of different fibre and matrix materials, as demonstrated in chapter 1, experimental testing of every possible combination in different laminate configurations is not practically possible for users or manufacturers. Engineers therefore rely on analytical calculations, and more importantly on modelling tools such as FEA, for predicting the mechanical behaviour of these materials.

This section will present results from FEA of composite substrates, used to determine the optimal laminate configuration and thickness for the CFRP deformable mirror. First, section 3.4.1 will describe the method used for modelling composite materials in I-DEAS, the package used throughout this work unless indicated otherwise. Thermal models were also carried out to check the stability under varying temperature regimes of the nickel-coated substrate.

3.4.1 Finite element analysis of composite materials using I-DEAS

All major software packages have special element families or toolboxes to deal with orthotropic materials, laminates, and sandwich structures. This section will discuss some of the issues in modelling specific to composites and how these can be dealt with.

Not all element types are suitable for use with composite materials. Neither one-dimensional beams nor tetrahedrons support laminate materials. Two-dimensional shell elements are most commonly used; these are modelled in terms of their mid-plane surface instead of the whole volume. Some software packages offer specific element families for modelling laminated materials. In I-DEAS, composites are modelled using the same shell meshes as are used for isotropic materials, with the laminate assigned as its material. These elements generally come in two varieties: the 4-node linear shell and the 8 or 9-node parabolic shell. In a comparison by Matthews *et al.* (2003) between the performance of the 9-node shell and that of the 18-node 3D layered brick element for laminate FEA both element types give the same results. The 9-node element, however, is more efficient to use as there are fewer integration points.

From its very nature the finite element method is an approximate solution, guaranteeing equilibrium only on the scale of the element size. A fine mesh is therefore more accurate than a coarse one, and the parabolic element types with mid-nodes increase the accuracy further. To guarantee the best solution, experimentation with different element types and mesh densities is recommended (UGSPLM, 2002; Matthews *et al.*, 2003). The mesh density should always be highest where the stress gradient is the greatest.

Three methods are available in I-DEAS for creating laminate materials. Firstly, a tool exists for creating plies from the individual material properties of fibre and matrix materials, and the fibre volume fraction. Several micro-mechanics theories are available for the computation of elastic properties; the default is as outlined in section 1.3.2. The software supports five reinforcement systems: continuous fibres, discontinuous fibres, continuous ribbons, discontinuous ribbons, particulate, and user-defined. Second, the ply properties can also be entered directly into a new orthotropic (or isotropic) material definition. Finally, the user can hand-calculate the laminate elastic properties using micro-mechanics equations and create a laminate material. The preferred method is largely determined by the set of material properties available to the user. Some composites manufacturers provide properties for the raw materials, whereas others give properties for UD plies of a given fibre-matrix combination.

Before the laminate is applied to the model, tools exist within I-DEAS to *validate* the laminate, i.e. check that it performs as expected. Stress-strain graphs and ply failure envelopes can be plotted for given plies in the laminate (see figure 3.5 for examples of these plots).

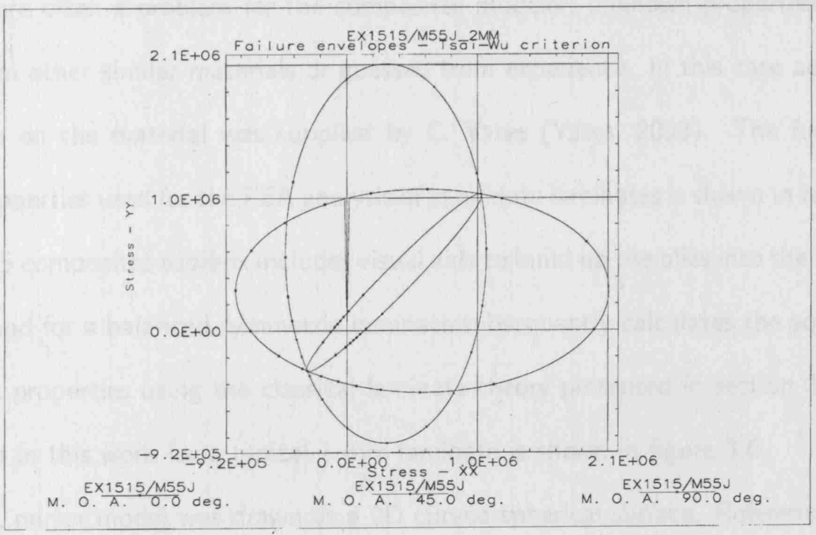

Figure 3.5: Example of a typical ply failure envelope plotted in I-DEAS for laminate validation.

Following satisfactory validation the laminate can then be applied to the model. In post-processing the stresses and strains in individual plies can be calculated from the overall laminate stress state.

3.4.2 Gravitational sag models of composite substrates

The first step in modelling candidate laminates was to create a ply material to form the basis. Following discussion with the QinetiQ and Cobham Composites teams, the ideal candidate material was chosen to be a high modulus carbon fibre-reinforced cyanate ester such as the commercially available EX1515/M55J. The highest strength is obtained using unidirectional plies stacked in a balanced symmetric sequence. The cyanate ester has the lowest moisture expansion coefficient of the polymer matrices whilst maintaining a high strength.

A partial set of material properties for this fibre-matrix combination at a typical fibre volume fraction of 0.60 was available from the cyanate ester EX1515's manufacturer, Bryte Technologies Inc. (Bryte Technologies Inc., Jan 2003). Incomplete sets of material properties are often a problem for the composites modeler; unknown properties can be derived from other similar materials or guessed from experience. In this case additional information on the material was supplied by C. Yates (Yates, 2003). The full set of material properties used for the FEA analysis of candidate laminates is shown in table 3.3. The I-DEAS composites toolbox includes visual aids to build up the plies into the required laminate, and for a balanced symmetric laminate subsequently calculates the equivalent orthotropic properties using the classical laminate theory presented in section 3.3. The lay-up used in this work for a typical 1 mm laminate is shown in figure 3.6.

A basic mirror model was drawn as a 2D curved spherical surface. Reference points were created at the actuator locations to simulate the support points. Several laminates were applied to the meshed surface and a gravity load vector applied in both the in-plane direction (simulating the deformation in the horizon-pointing position) and the out-of-plane direction (representing the zenith-pointing deflections). To simulate the pads connecting the actuators to the faceplate, nodes within a circle of 12.5 mm radius were constrained together - this will underestimate the gravitational sag as in reality the pads will be waisted to avoid a top-hat effect in the influence function. This approximation

Property	*Value*	*Source*	*Property*	*Value*	*Source*
Density	1800 kg/mm^2	(1)			
Elastic moduli			Coefficients of thermal expansion		
E_x	327.5 GPa	(1)*	α_x	-1 ppm/K	(2)
E_y	7 GPa	(2)	α_y	21 ppm/K	(2)
E_z	7 GPa	(2)	α_z	0 ppm/K	(2)
Shear moduli			Allowable strength in tension		
G_{xy}	3.774 GPa	(1)	x	1.893 GPa	(1)
G_{xz}	3.774 GPa	(1)	y	1 GPa	(2)
G_{yz}	1.14 GPa	(1)			
Poisson's ratios			Allowable strength in compression		
ν_{xy}, ν_{xz}, νyz	0.342	(2)	x	0.731 GPa	(1)
			y	0.4 GPa	(2)

Table 3.3: EX1515/M55J material properties as used in the laminates FEA. Source (1) is the manufacturer's datasheet (Bryte Technologies Inc., Jan 2003), (2) is from Yates (2003).

* denotes an averaged value of elastic moduli in tension and compression.

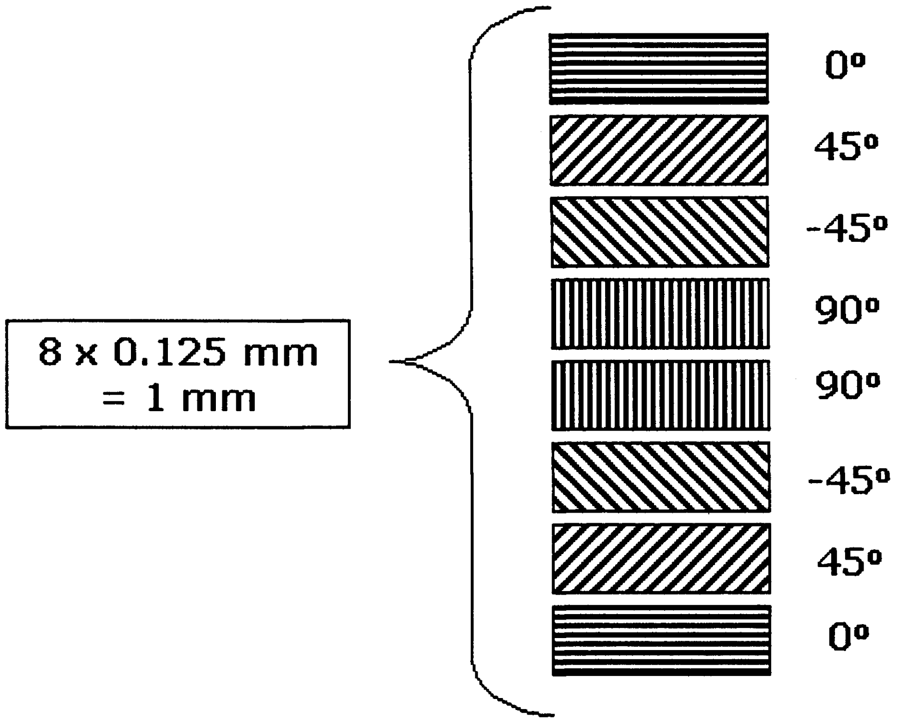

Figure 3.6: Schematic drawing of the typical base 1 mm laminate used in the FEA models. The angle values denote the fibre orientation angle within the ply. Thicker laminates are built up of symmetric copies of the 1 mm lay-up.

was used to save on computation time; for detailed analysis a full three-dimensional model would be more appropriate.

As a first step models of the candidate laminates for the passive mirror were produced, which has a "thick" design. These laminates are all stiffer than were likely to be used for the active mirror, and include aluminium honeycomb cores. The main issue for the passive mirror was the required core thickness, and three thicknesses were modelled: 5, 10 and 15 mm. The core is modelled as a thick ply in the laminate. The CFRP skins measure 1 mm each. As the 7-point support is an unlikely configuration for a real passive mirror, two more supports were included in the models: a full edge support and a three-point edge support. A brief test was carried out to check for the effect of a thin nickel coating on the overall stiffness and its contribution was found to be negligible;

Core thickness	Rms gravitational sag		
	3-point edge support	7-point support (pads)	full edge support
5 mm	895.5 nm	34.3 nm	75.9 nm
10 mm	522.7 nm	20.6 nm	43.3 nm
15 mm	378.3 nm	15.1 nm	31.2 nm

Table 3.4: FEA results for rms gravitational sag of the passive CFRP test mirror for various core thicknesses. The 7-point support used 25 mm diameter pad-shaped restraints to simulate actuation pads.

the nickel coating was therefore omitted for the gravitational models. Table 3.4 shows the results of these models.

Results from a similar model carried out by Lee (1999) for the aluminium deformable mirror using ANSYS showed a maximum sag of 31.9 nm using a 7-point support scheme. This was very closely matched by the results of the 10 mm cored model, where the maximum sag was 33.4 nm, and this configuration was subsequently chosen for the passive test mirror.

Sagging in the horizon-pointing position was found to be approximately one order of magnitude smaller and hence not of major importance compared with zenith-pointing sag and thermal effects. Figure 3.7 shows a plot of the sag under an in-plane gravity load, showing a maximum distortion of 2.06 nm.

Prior to proceeding with the passive mirror manufacture, finite element models were also carried out to predict the level of stress and deformation resulting from variations in ambient temperature. These results are presented in the next section.

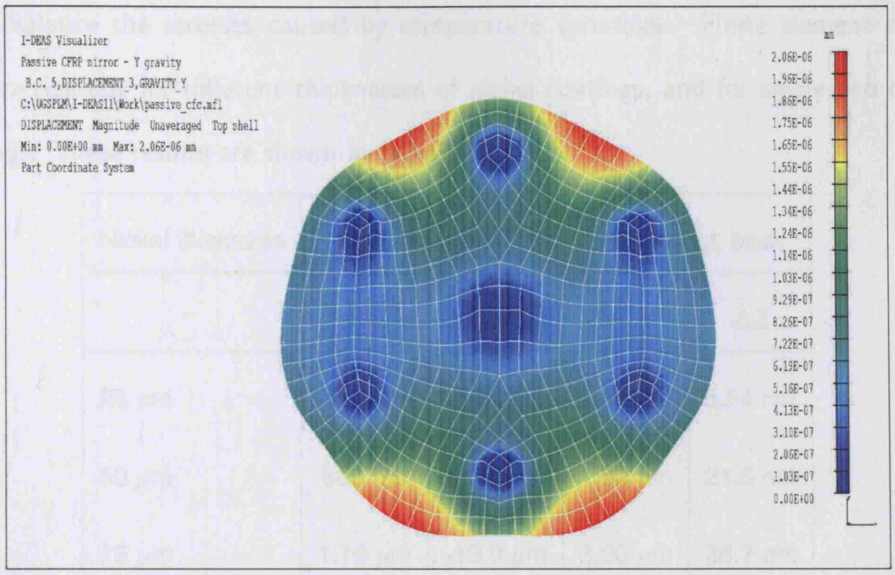

Figure 3.7: FEA plot showing deformation of a thick composite mirror design under in-plane gravity. The laminate modelled here uses a 10 mm aluminium honeycomb core and 1 mm skins. The maximum deformation is 2.06 nm.

3.4.3 Thermal models of a nickel-coated composite substrate

Thermal stability of the mirror was identified in the early stages of the project as one of the most important issues to address. Whilst the composite substrate has excellent thermal properties with a near-zero thermal expansion coefficient and a higher thermal conductivity than many glasses, albeit lower than that of aluminium, beryllium or silicon carbide, the bimetallic effect caused by the presence of a nickel layer is likely to introduce stresses and deformations. Modelling was carried out to attempt predicting the magnitude of these problems and to allow modifications to the design to minimize them. The results are also important in judging how material removal during grinding and polishing will affect the mirror form with changing temperatures.

A model of the proposed thick design for the passive laminate, restrained at the centre point confirmed this. With an increase in temperature of $10°C$, the uncoated laminate in fact shows a slight shrinkage, as the equivalent laminate CTE is negative. It was suggested early on that a matching nickel layer on the mirror's back surface could balance the stresses caused by temperature variations. Finite element models were carried out for different thicknesses of nickel coatings, and for single and double coatings. These results are shown in table 3.5.

Nickel thickness	Nickel front		Nickel front, back	
	ΔD	ΔZ	ΔD	ΔZ
25 μm	-154 nm	-5.04 μm	0.48 μm	5.54 nm
50 μm	860 nm	-9.63 μm	1.90 μm	21.8 nm
75 μm	1.70 μm	-13.9 μm	3.20 μm	36.7 nm
100 μm	2.48 μm	-17.7 μm	4.4 μm	50.5 nm

Table 3.5: FEA results of thermal stability models for the chosen laminate for the passive test mirror, featuring 1 mm CFRP skins and a 10 mm aluminium honeycomb core. The modelled variation is $\Delta T = +10^oC$. ΔD is the change in diameter resulting from the expansion or contraction in the XY direction, and ΔZ is the out-of-plane bending of the mirror edges.

The results in table 3.5 are broken down into two components. The first is the change of mirror size in the XY direction, shown in the ΔD column. These values represent the trade-off between the negative CTE of the composite laminate and the positive thermal expansion of the nickel. The second is the out-of-plane motion of the edges ΔZ; this is thought to be caused by the stress arising from the bimetallic effect. The figures show that:

1. ΔD increases with the nickel layer thickness. Between 25 and 50 μm there exists a turning point beyond which the nickel's thermal expansion becomes dominant, resulting in a dimensional increase of the mirror size with increasing temperature;
2. the ΔZ motion in the presence of just one nickel layer show a pulling back of the

mirror edges, which would in practice result in a lengthening of the mirror focus;

3. the effect of the matching nickel layer on the back surface is twofold:
   - an increase in the size change of the mirror is seen, thought to be caused by the increased stress from the second nickel layer;
   - a reduction of the ΔZ motion and a reversal of its direction (i.e. the mirror's concavity is seen to increase, and the focus shortened).

The out-of-plane motion of the edges can be explained from laminate theory: the addition of a single nickel layer unbalances the laminate, causing it to deviate from quasi-isotropic behaviour. Coupling terms arise in the material stiffness matrices, giving rise to the observed bending motions. The distortion varies greatly with variations in nickel thickness and the addition of a second matching nickel layer. Figure 3.8 shows a comparison of ΔZ for the 4 modelled thicknesses with one single coating; the figures are plotted on the same scale for ease of comparison. With the levels of bending predicted in these models, the amount of stress the expansion causes should also be examined. Figures 3.9 and 3.10 show plots of the 4 modelled thicknesses comparing the out-of-plane movement for a single and front-and-back nickel configuration.

These results imply that the nickel coating is likely to prove crucial to the success of the active mirror design. Whilst a thicker nickel coating strengthens the bond, decreasing the likelihood of delamination, it also significantly increases the level of defocus to be expected on temperature changes. Whilst low spatial frequency terms can be corrected with the actuators, this reduces the level of correction that can be achieved during operation.

The models presented here use a simple central constraint; with a more complicated support system this distortion could give rise to uncorrectable high spatial frequency errors.

The addition of a matching nickel layer on the mirror's back surface redresses the laminate balance and symmetry and greatly reduces the amount of out-of-plane bending, as well as the resulting defocus. It does, however, cause a bigger dimensional change on changing temperatures. The stresses caused by such changes, at the levels predicted in these models, can be relieved by a flexure mechanism in the support structure.

Figure 3.11 shows the stresses in the first 4 plies of the mirror on ΔT of 10^oC. The magnitude of the interlaminar stresses is of the order of a few MPa for a single 100 μm nickel layer. Such levels of stress are not insignificant and the thermal stability requirements must be balanced against the strength of the nickel bond. This is largely affected by the coating method used and work into an optimal coating strategy will be highly important for the mirror's stability.

3.4.4 Passive mirror FEA results: conclusions

Several conclusions can be made from the FEA results presented in this section:

1. Laminates are considerably stiffened by the addition of an aluminium honeycomb core. This does not affect the thermal properties of the mirror and the added weight is negligible.

2. The rms gravitational sag for a passive mirror in a zenith-pointing position, using a 10 mm core and 1 mm CFRP skins is 20.6 nm using a 6-point hexagonal support around a central actuator. This is comparable to the results obtained for the UCL aluminium mirror system, and this configuration was selected for the CFRP test mirror.

3. The nickel coating is a crucial part of the mirror's design, affecting to a high degree the mirror's behaviour under varying temperatures. A single nickel coating on the mirror's front surface creates an unbalanced laminate, causing it to deviate from quasi-isotropic behaviour. A nickel layer of 100 μm, whilst providing a stronger bond, is predicted to cause an out-of-plane distortion of around 17 μm. For a 25

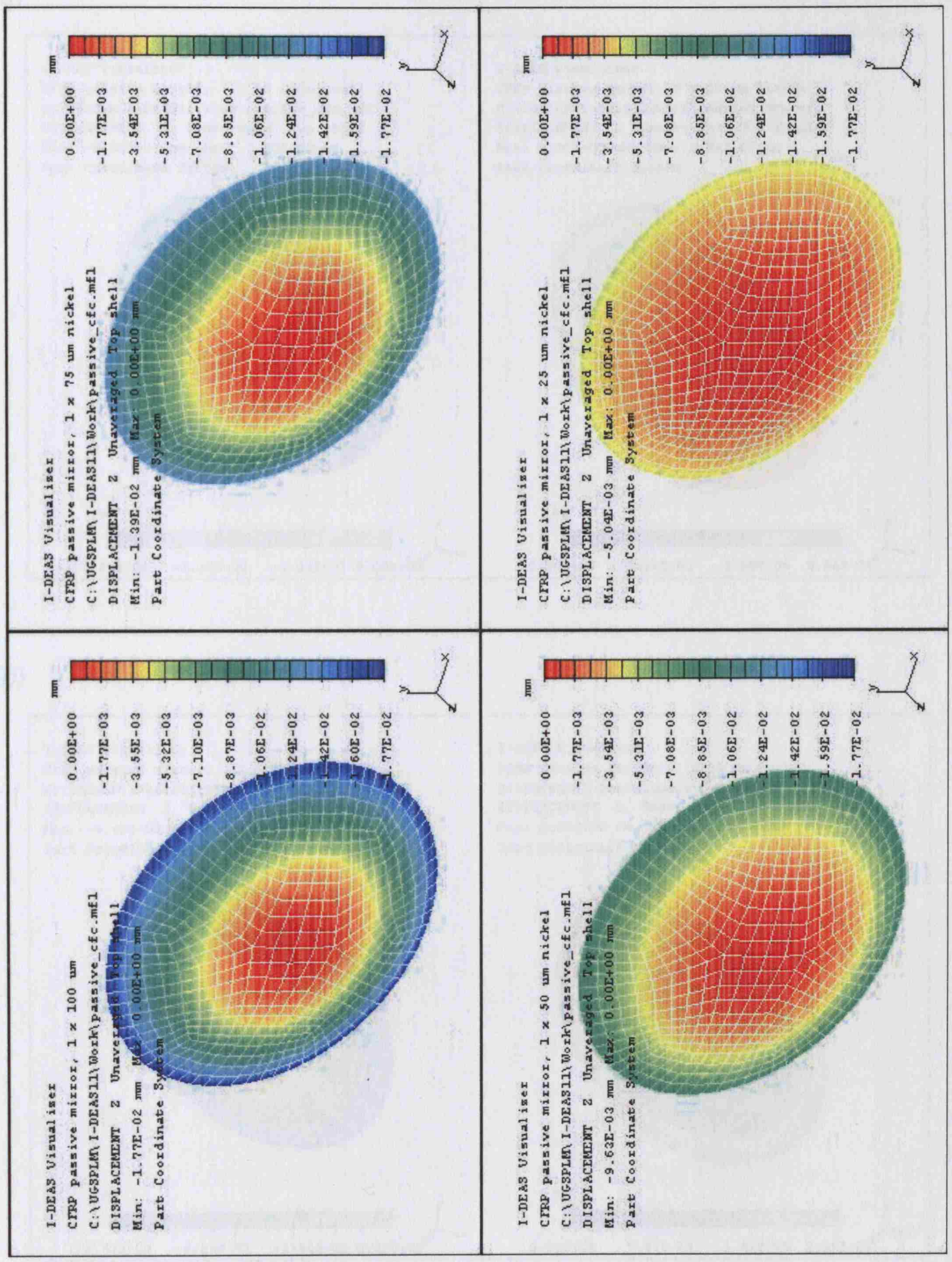

Figure 3.8: Comparison of the out-of-plane edge bending resulting from $\Delta T = +10^oC$ for nickel coatings of 25, 50, 75 and 100 μm thickness.

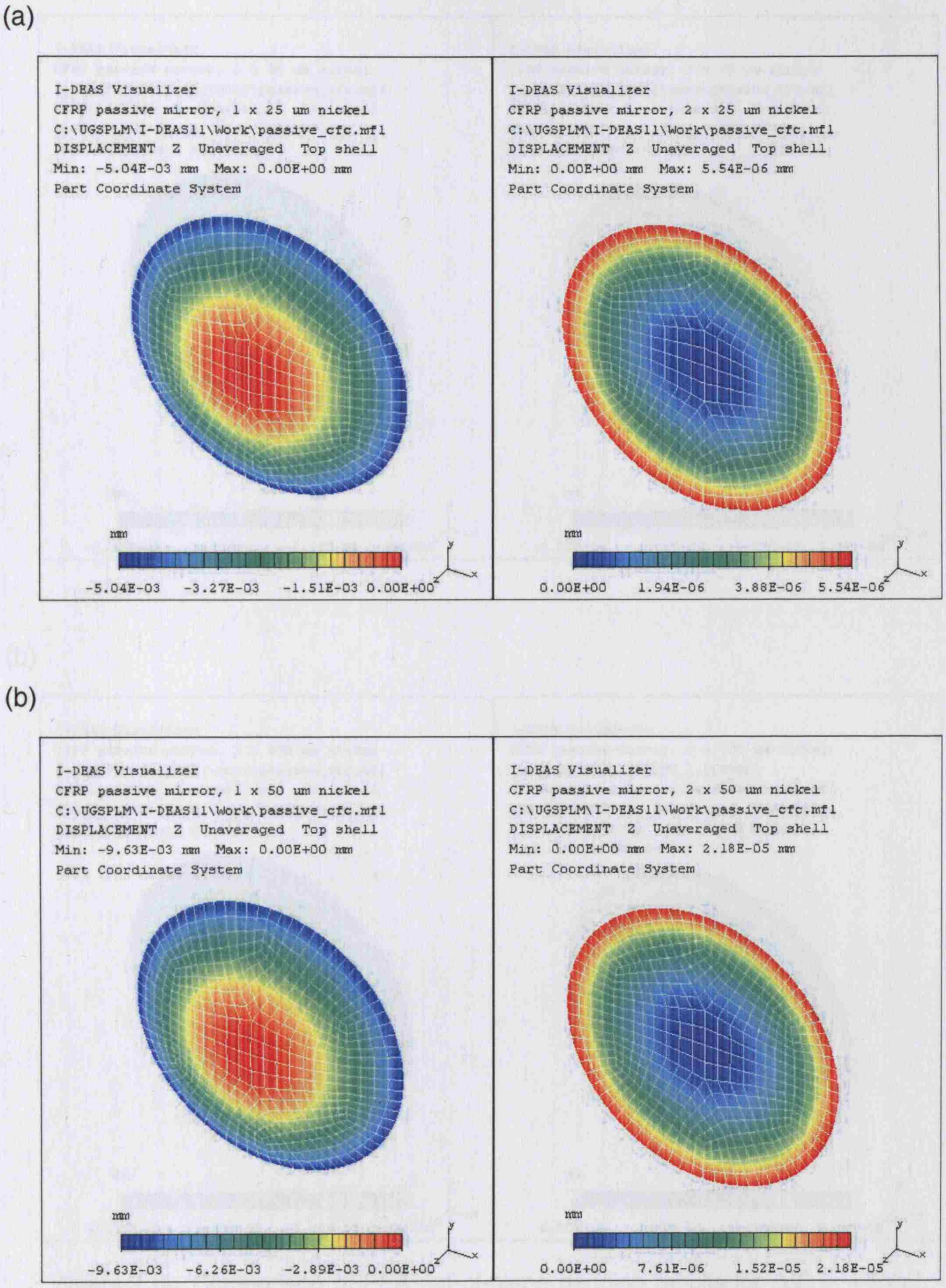

Figure 3.9: Comparison of the effect of a single nickel layer and of a matching back nickel layer for $\Delta T = +10°C$. Nickel thicknesses modelled are (a) 25 μm and (b) 50 μm.

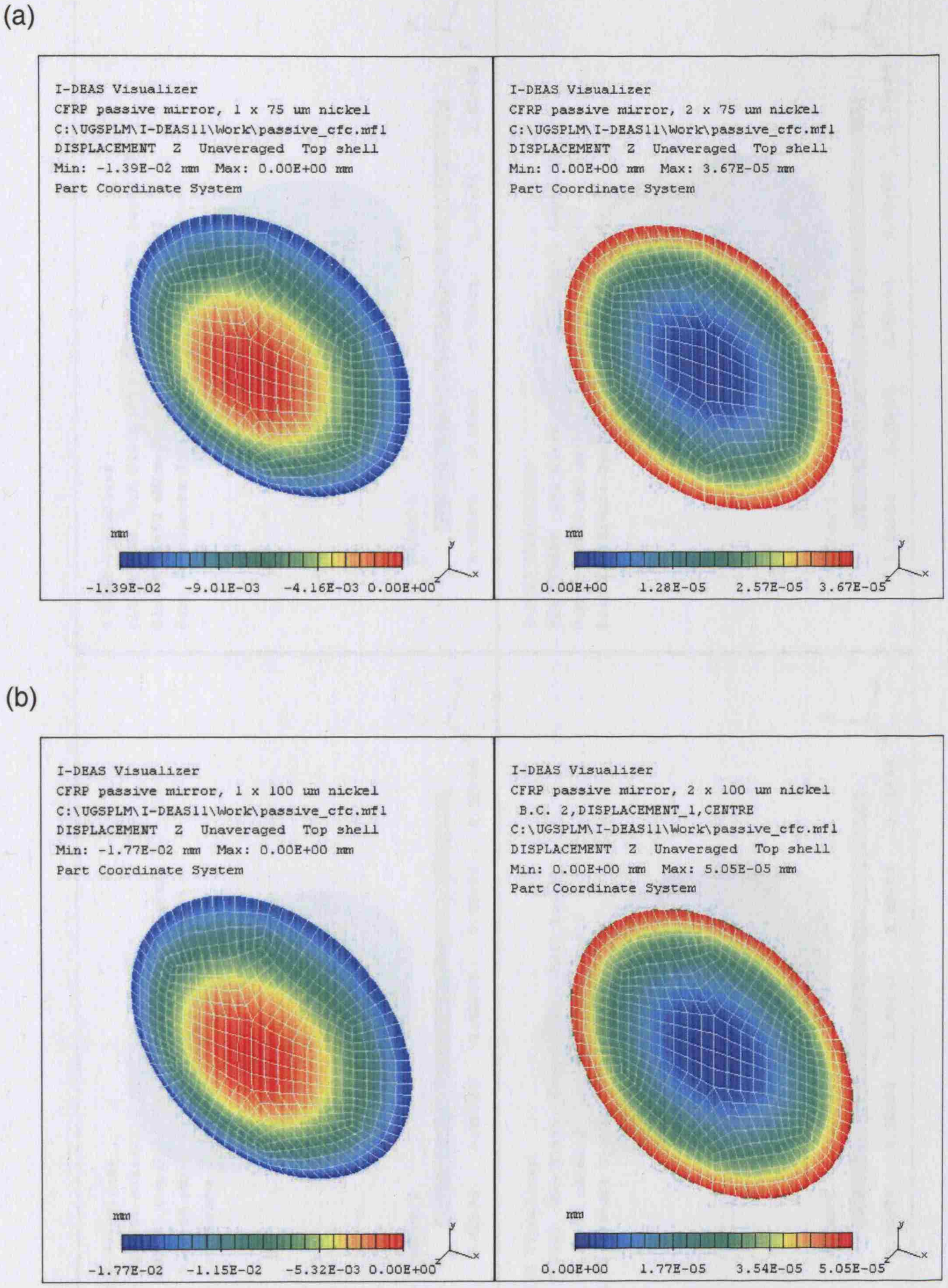

Figure 3.10: Comparison of FEA out-of-plane bending results for $\Delta T = +10°C$, showing the effect of a single nickel layer and of a matching back nickel layer on thermal stability. Nickel thicknesses modelled are (a) 75 μm and (b) 100 μm.

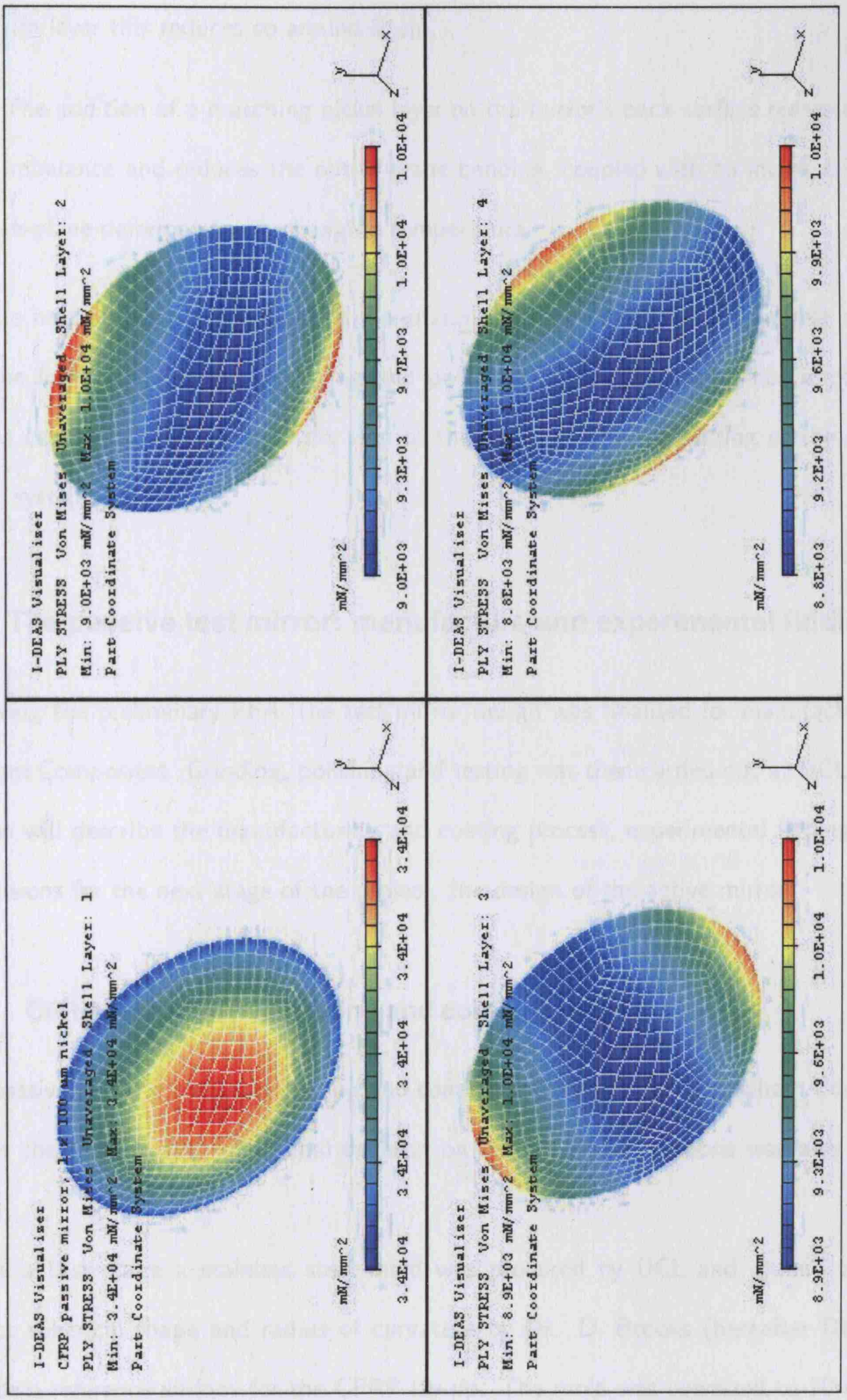

Figure 3.11: Stress plots for the first 4 plies of the passive mirror laminate with one 100 μm nickel coating on temperature variation, clearly showing the directionality of the individual plies. The first ply is the nickel layer, showing a uniform radial stress profile with maximum stress around the edge.

μm layer this reduces to around 5 μm.

4. The addition of a matching nickel layer on the mirror's back surface redresses the imbalance and reduces the out-of-plane bending, coupled with an increase in the in-plane deformation on changing temperature.

The next section will discuss the manufacturing process for the passive test mirror and the form achieved after grinding and polishing. From this experience important lessons can be learned for the next step of the work, design and testing of the active mirror system.

3.5 The passive test mirror: manufacture and experimental findings

Following the preliminary FEA, the test mirror design was finalised for manufacture at Cobham Composites. Grinding, polishing and testing was then carried out at UCL. This section will describe the manufacturing and coating process, experimental findings and conclusions for the next stage of the project, the design of the active mirror.

3.5.1 CFRP mirror manufacturing and coating process

The passive mirror's composite lay-up and coating was carried out by Cobham Composites at their UK facility. The final decision on materials and methods was also made there.

As a first stage a stainless steel mold was procured by UCL and ground to the correct spherical shape and radius of curvature by Dr. D. Brooks (hereafter DB), to provide a reference surface for the CFRP lay-up. The mold was oversized to 30 cm to avoid the transferral of any polishing edge effects to the mirror surface, and produced by turning and grinding a blank close to the required form. The final form was then achieved through polishing. The final radius of curvature was 2946 mm with a departure

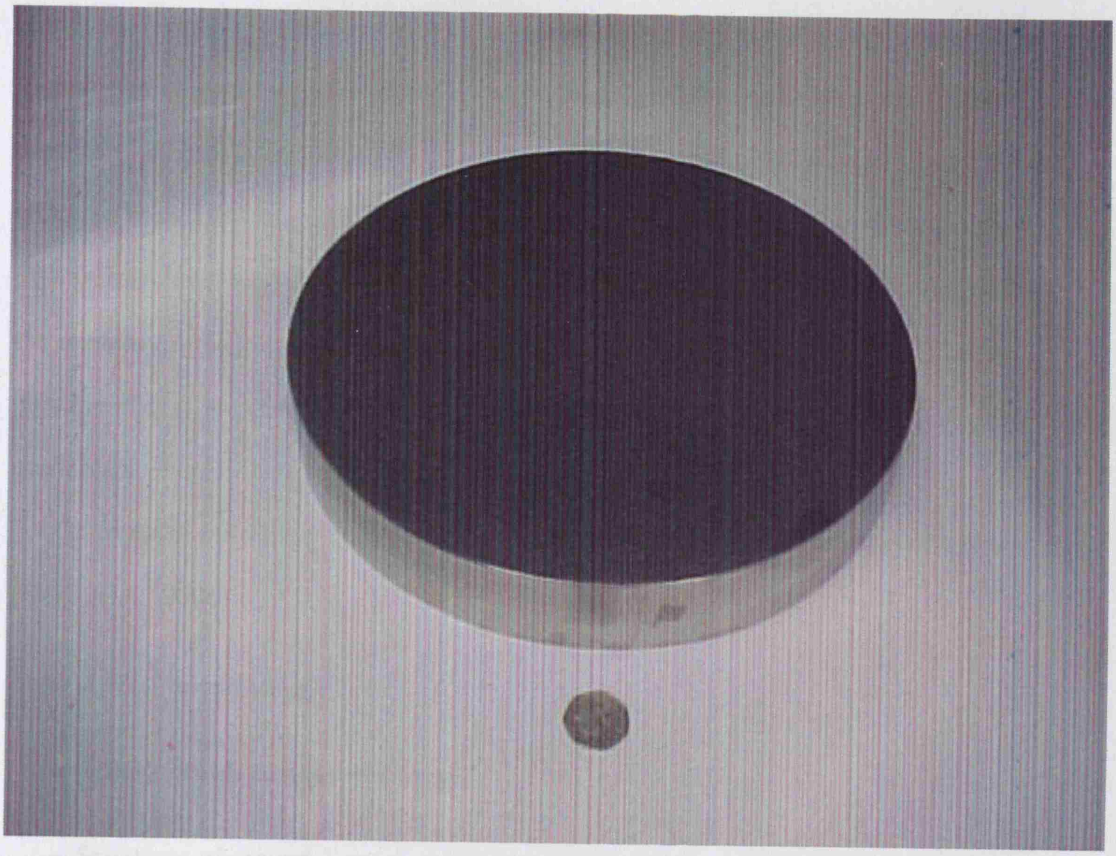

Figure 3.12: Stainless steel mold used for laying up of the composite mirrors.

from spherical form of less than 1 μm. The surface texture was approximately 4 nm. Figure 3.12 shows a picture of the final mold.

For reasons of cost and availability the matrix material was chosen to be a regular epoxy, MTM49, instead of the more suitable cyanate ester resin EX1515. As discussed in chapter 1, cyanate esters have a lower moisture expansion coefficient and a higher elastic modulus. The reinforcing fibres were the commonly used high-modulus graphite M55J. A woven $[0°/45°/-45°/90°]_s$ lay-up was used in 0.125 mm plies. The plies in this case were 'prepreg' sheets, where the materials manufacturer pre-impregnates the fibres and resin under heat and pressure or with a solvent, and a pre-catalysed resin.

The coating process involved a 100 μm layer of pure nickel being deposited on the stainless steel mold via an electroforming process. In electroforming, an electrolytic bath is used to deposit the nickel onto the conductive surface of the mold. The advantage of this process is that accurate replication of the mold surface can be achieved. Following deposition of the CFRP/aluminium laminate, including an adhesive layer to bond the nickel to the CFRP, and curing, the coated substrate is then removed from the mold. FEA results have shown that a nickel coating on the mirror's back surface would reduce the stresses on temperature variation; this would however necessitate a non-trivial modification of the manufacturing process, for which neither the budget or timescales were available.

On removal from the mold, the following features were visible on the mirror's surface (Doel *et al.*, 2004):

- A fibre print-through;
- A honeycomb core print-through;
- Striations of around 1 cm in width running across the mirror surface in one direction; and
- A depressed ring just inside the mirror.

Of these effects, the fibre print-through was the most marked. The cause of this feature was initially unknown as the fibres were not expected to be visible through a 100 μm thick layer of metal. Following discussion with the manufacturing team it was suggested that the print-through was due to post-cure shrinkage of the adhesive layer between composite and nickel, that 'pulled' the nickel round the underlying fibres. The cause of the edge depression was identified as a filler material that had been used to protect the honeycomb core around the edges to prevent it from being crushed by the vacuum bag pressure during the lay-up process. Figure 3.13 shows a profilometry measurement with a Mark 1 Form Talysurf of this feature prior to grinding and polishing. The cause of the unidirectional striations was not conclusively identified. The mirror's weight was 497 g.

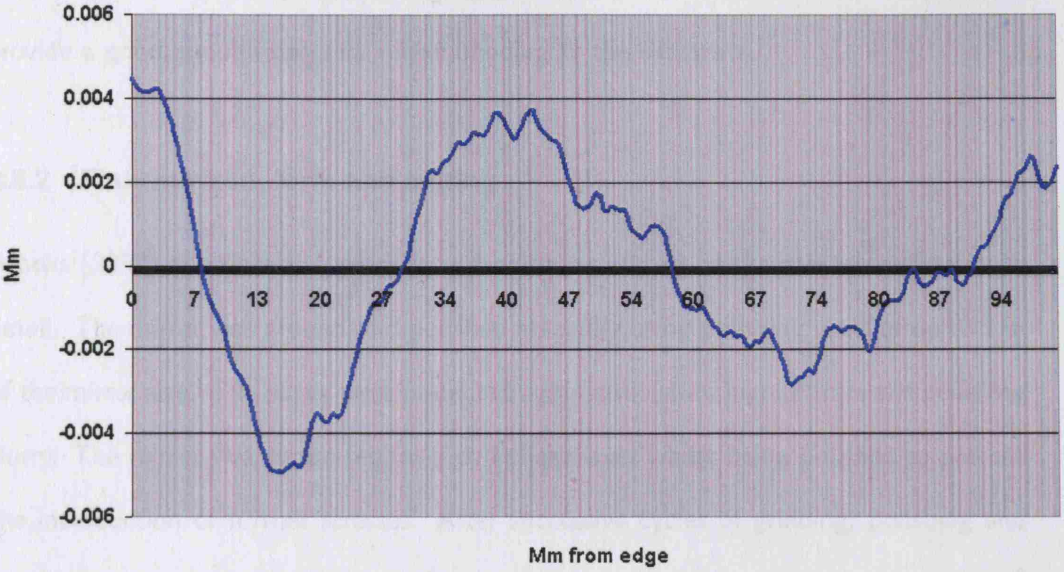

Figure 3.13: Profilometry measurement of the outer 10 cm of the passive test mirror, showing the depressed ring feature around 20 mm inside the edge, with a magnitude of around 10 μm.

Surface measurement with a 10.3 μm Wyko phase-shifting interferometer revealed a radius of curvature of 2910 mm - 35 mm shorter that that of the mold - indicating that residual stresses on release from the mold had increased the mirror's concavity. This can almost certainly be attributed to the stresses caused by the thermal expansion mismatch between the nickel and the composite on cooling. Tests with a composite-only sample did not show this level of radius of curvature shrinkage.

Ulmer *et al.* (2005) report results using the same coating process for a 12 inch thin shape memory composite for deployable space optics, using a much thinner coating of just 20 μm. They report similar findings of CTE mismatching and surface features such as wrinkles and bubbles. An added challenge for monolithic deployable space optics is to avoid creasing of the nickel while the mirror is stowed during launch. The authors investigate methods of improving the nickel-composite bond, and found that plasma ion etching of the nickel surface before lay-up improves the adhesion between the metal and composite substrate; acid etching, meshed masks and mechanical abrasion did not provide a good enough basis for nickel bonding to the substrate.

3.5.2 Final surface, form and testing

Brooks (2003) describes the grinding and polishing process of the passive test mirror in detail. The mirror was ground and polished manually using polishing tools of up to 7/8 of the mirror size. The edges were protected against moisture ingress from the polishing slurry. The mirror was supported on a compliant layer whilst being polished to prevent the introduction of further stresses. After successive cycles of grinding, polishing and measurement, a surface roughness of 4 nm rms was obtained, measured over a 1 mm^2 square (see figure 3.14). This value is no absolute limit and can be improved on with experience. The striations and fibre print-through observed after the lay-up process were removed in polishing.

Figure 3.15 shows the final mirror form. The interferogram shows a residual edge depression that was not removed by the grinding process. The overall surface form was approximately 1 μm P-V, the edge ring accounting for a large part of this. The central 24 cm displayed a form of 517 nm P-V. Apart from the bimetallic effect, another possible cause of these form errors is a slight misalignment of ply angle within the composite laminate, which could affect its stability. On measuring the surface with the mirror in the horizon-pointing position, there was no observable change in form due to gravitational sagging, confirming the FEA result that the magnitude of this deformation is smaller than the interferometer resolution. A small amount of delamination of the nickel coating occurred along the mirror edge after substantial working of the surface. Figure 3.16 shows a picture of the passive mirror after polishing.

The mirror displayed no measurable form changes over one month at constant temperature and relative humidity. A thermal stability test carried out in 2004 showed a defocus of 6 mm for $\Delta T = 5°C$ (see figure 3.17). The magnitude of this is in good agreement with the FEA results shown in section 3.4.3.

3.5.3 Passive test mirror: conclusions

The following conclusions can be made from the experience with a passive nickel-coated CFRP test mirror:

1. A spherical surface can be produced with form errors of the order of 1 μm for a 'thick' CFRP design. Grinding and polishing can remove a large part of these errors, providing enough coating material is applied for removal;
2. A very good surface quality ($<$ 5 nm) was achieved with conventional manual polishing, and this can be improved on with experience;
3. Print-through effects can be removed in the polishing process;
4. The laminate was shown to be lightweight (497 g) and robust, with minimal nickel delamination occurring after substantial working;
5. Stability testing confirmed that stresses from the bimetallic interaction between the composite and the nickel coating gives rise to stresses and form errors, particularly in the form of defocus.

These lessons from the first stage of the project were taken on board for the manufacture and testing of the active mirror. The next section will show preliminary modelling results for the choice of laminate using the same methods as for the passive mirror, as well as a report of the manufacturing process and final form.

3.6 A CFRP thin active mirror: manufacture and form

The design and manufacture of a deformable CFRP mirror was the ultimate aim of the project presented here. This section will show the preliminary modelling results

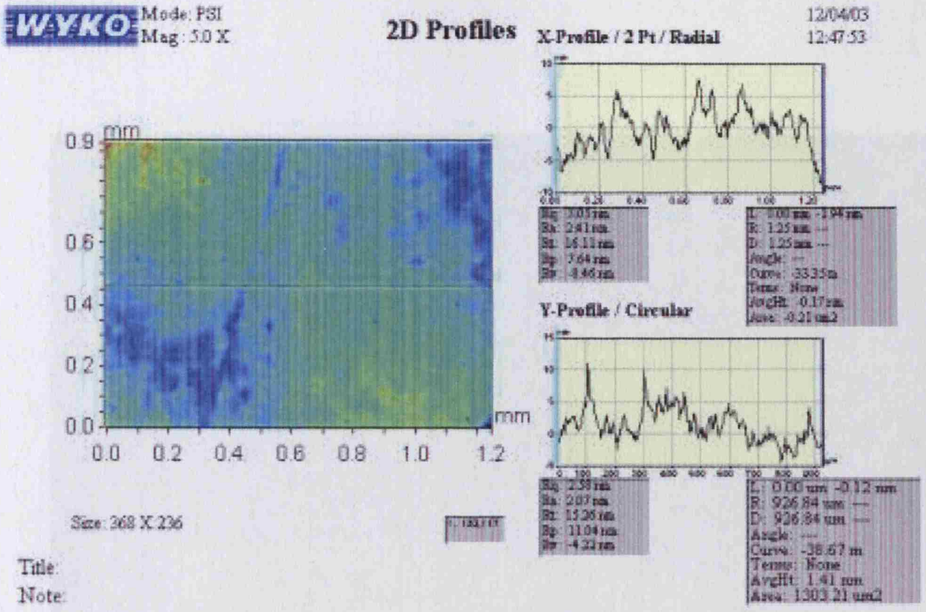
Mode: PSI
Mag: 5.0 X

2D Profiles

12/04/03
12:47:53

X-Profile / 2 Pt / Radial

Rq: 3.05 nm
Ra: 2.41 nm
Rt: 16.11 nm
Rp: 7.64 nm
Rv: -8.46 nm

L: 0.00 mm -1.94 nm
R: 1.25 mm ---
D: 1.25 mm ---
Angle: ---
Curve: 33.35 m
Terms: None
AvgHt: 0.17 nm
Area: -0.21 um2

Y-Profile / Circular

Rq: 2.58 nm
Ra: 2.07 nm
Rt: 15.26 nm
Rp: 11.04 nm
Rv: -4.22 nm

L: 0.00 um -0.12 nm
R: 926.84 um ---
D: 926.84 um ---
Angle: ---
Curve: -38.67 m
Terms: None
AvgHt: 1.41 nm
Area: 1303.21 um2

Size: 368 X 236

Title:
Note:

Figure 3.14: Interferometry measurement used to determine the passive mirror's surface roughness.

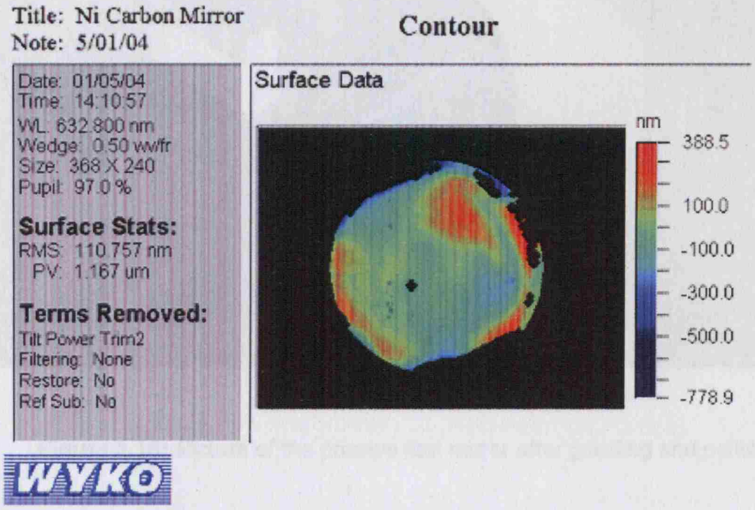
Title: Ni Carbon Mirror
Note: 5/01/04

Contour

Date: 01/05/04
Time: 14:10:57
WL: 632.800 nm
Wedge: 0.50 wv/fr
Size: 368 X 240
Pupil: 97.0 %

Surface Stats:
RMS: 110.757 nm
PV: 1.167 um

Terms Removed:
Tilt Power Trim2
Filtering: None
Restore: No
Ref Sub: No

Figure 3.15: Interferogram of the final passive mirror surface form. The residual edge depression is clearly visible.

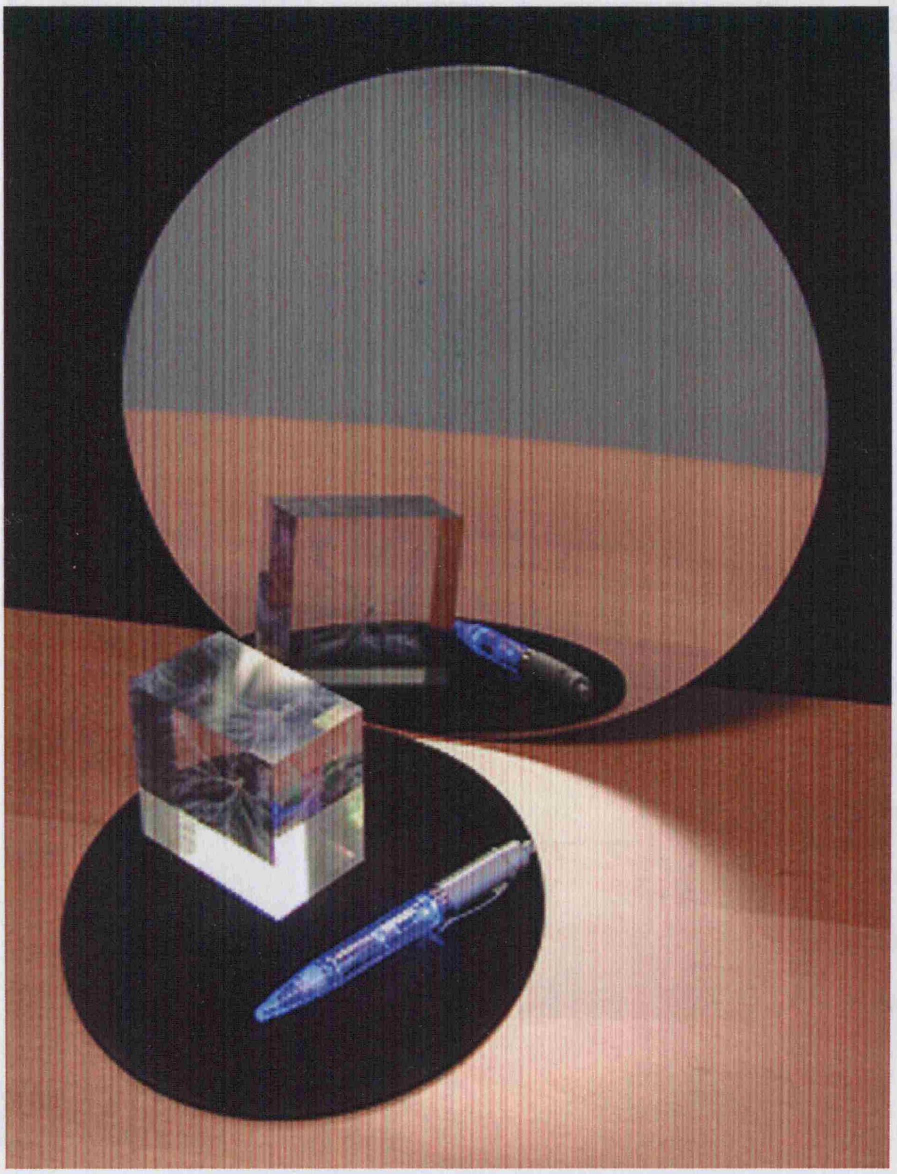

Figure 3.16: Picture of the passive test mirror after grinding and polishing.

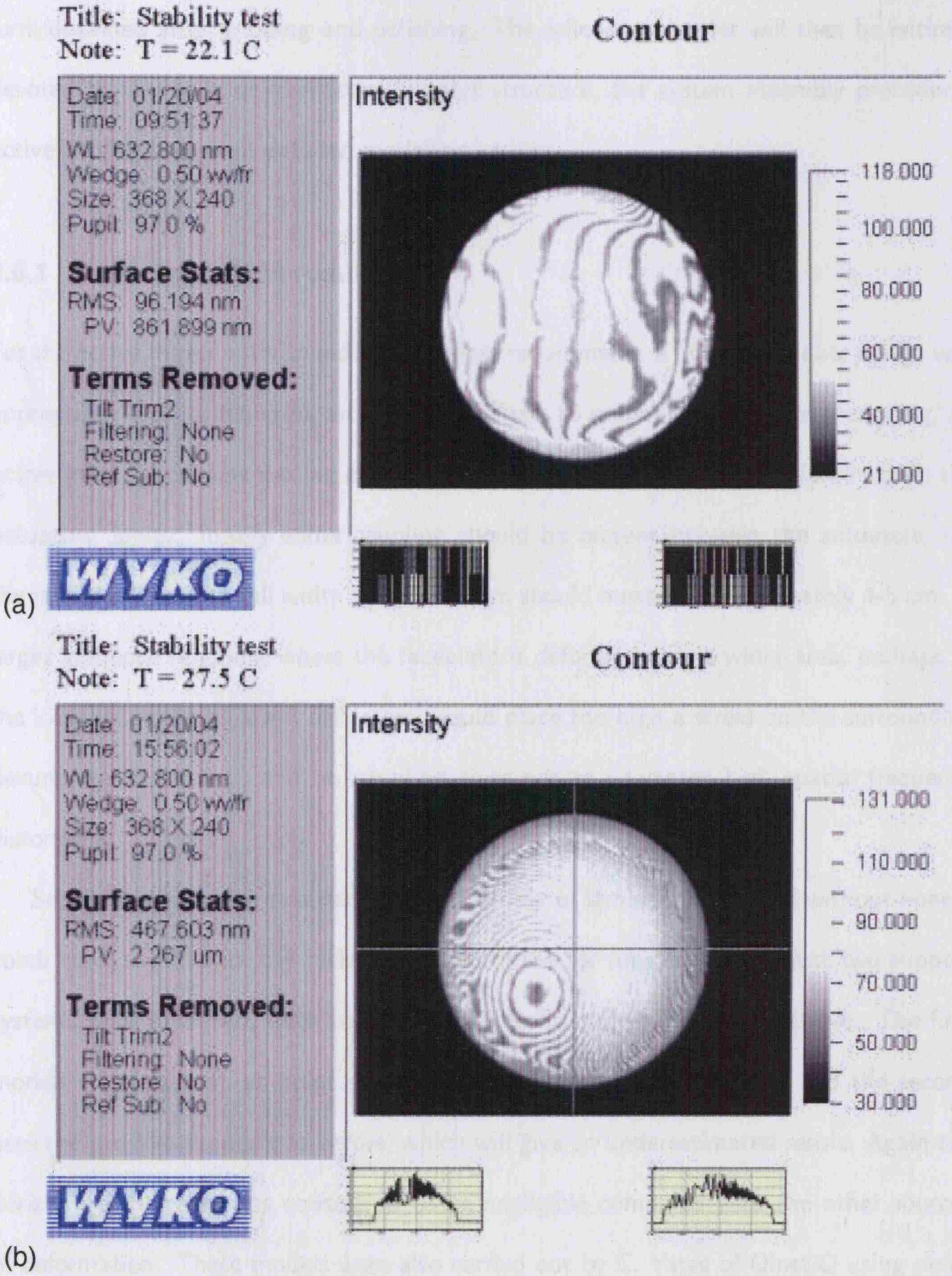

Title: Stability test
Note: T = 22.1 C
Date: 01/20/04
Time: 09:51:37
WL: 632.800 nm
Wedge: 0.50 wv/fr
Size: 368 X 240
Pupil: 97.0 %

Surface Stats:
RMS: 96.194 nm
PV: 861.899 nm

Terms Removed:
Tilt Trim2
Filtering: None
Restore: No
Ref Sub: No

Title: Stability test
Note: T = 27.5 C
Date: 01/20/04
Time: 15:56:02
WL: 632.800 nm
Wedge: 0.50 wv/fr
Size: 368 X 240
Pupil: 97.0 %

Surface Stats:
RMS: 467.603 nm
PV: 2.267 um

Terms Removed:
Tilt Trim2
Filtering: None
Restore: No
Ref Sub: No

Figure 3.17: Passive mirror interferometry measurements at 2 different temperatures to investigate stability. (a) $T = 22.1^\circ C$, (b) $T = 27.5^\circ C$. These measurements show the defocus of approximately 6 mm introduced by heating, confirming the predicted thermal instability of a CFRP mirror with one-sided nickel coating.

carried out for the choice of laminates, and report on the manufacturing process and form obtained after grinding and polishing. The following chapter will then be entirely devoted to the work on the active support structure, the system assembly procedure, active testing and more detailed modelling results.

3.6.1 Preliminary FEA results

For the active mirror with its reduced stiffness requirement, a "thin" laminate design was appropriate. Whilst requiring an intrinsic stiffness to minimize gravitational sagging, an active mirror should be flexible enough to be deformed with reasonable force within the actuators' limits. Ideally some coupling should be present between the actuators, i.e. the influence function full width half maximum should measure approximately 4-5 cm. A larger influence function, where the faceplate is deformed over a wider area, perhaps at the location of the adjacent actuators, would place too high a stress on the surrounding flexures and actuators, and no coupling gives rise to unwanted high spatial frequency distortions.

Separate models were carried out for a variety of laminates with and without honeycomb cores, again with the nickel coating omitted for simplicity. Here just two support systems were modelled, both based on the 7-point support discussed above. The first models the actuators as point supports, thus overestimating the sag, and the second uses the pad-like supports as before, which will give an underestimated result. Again the horizon-pointing sag was considered to be negligible compared with the other sources of deformation. These models were also carried out by C. Yates of QinetiQ using point supports, and the results are included in the plot for comparison labeled QQ (Yates, 2004). The sag values of the QQ models are significantly higher - the reasons for this are an increased mirror diameter of 30 cm instead of 27 cm, increasing the edge sag, and a lower (by approximately 6 %) elastic modulus used for the composite.

Taking these factors into consideration, in addition to the subtle differences between

FEA solvers and meshes, the QQ results show a reasonable agreement with the UCL models. Figure 3.18 shows a graphical and tabular representation of these results. As with the passive mirror modelling results, the cored models display a better stiffness.

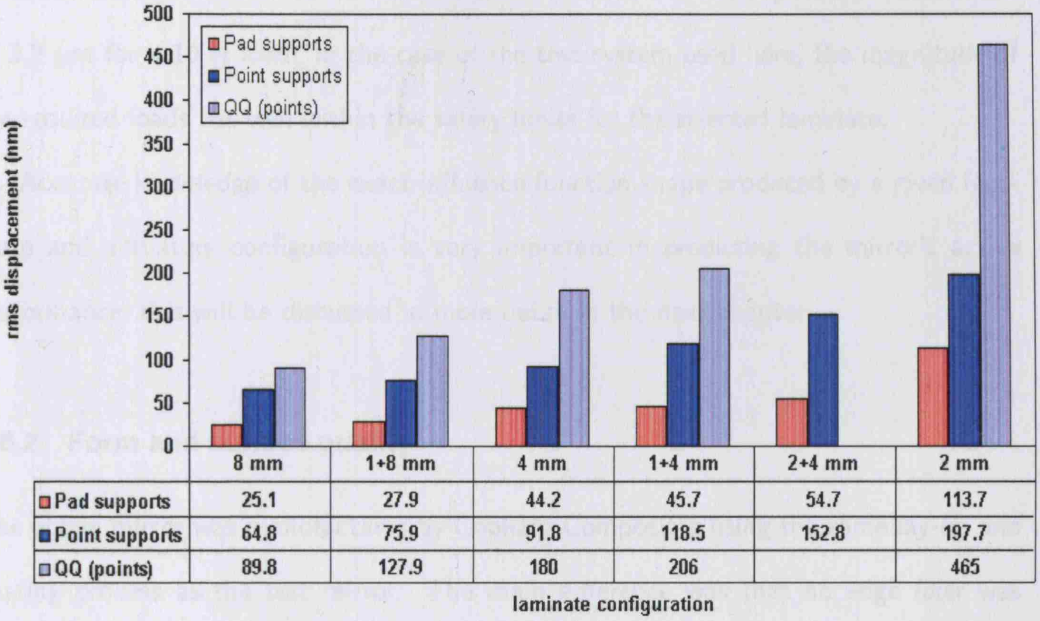

	8 mm	1+8 mm	4 mm	1+4 mm	2+4 mm	2 mm
🟥 Pad supports	25.1	27.9	44.2	45.7	54.7	113.7
🟦 Point supports	64.8	75.9	91.8	118.5	152.8	197.7
▨ QQ (points)	89.8	127.9	180	206		465

Figure 3.18: Combined graphical and tabular representation of out-of-plane gravitational sag results for thin mirror laminates. Notation for laminate thicknesses x + y mm signifies x mm thick faceskins and y mm thick core. The points models represent a pessimistic value, whilst the pad models underestimate the realistic value as they produce a rigid displacement shape.

Models at QinetiQ also examined to a first approximation the actuator influence function on a gravity load, using pads as well as point supports. These showed that both a 4 mm and a 6 mm core gave FWHM of around 8 cm, which suggests that these laminates would give the right amount of coupling in combination with adequate stiffness. The 4 mm cored laminate was eventually selected as the force requirements would be lower than with a 6 mm core.

The worst case loading for the actuator pads occurs when the actuator pulls back from the faceplate. Delamination is most likely thought to occur at the CFRP-to-core bond as the honeycomb structure reduces the bond area. Yates (2004) calculated the maximum load capacity from a 25 mm pad, connected to the faceplate with an adhesive of tensile strength 5 MPa to be 610 N. For the 4 mm core, Yates predicts a movement of 3.2 μm for a 10 N load. In the case of the test system used here, the magnitude of the required loads lies well within the safety limits for the selected laminate.

Accurate knowledge of the exact influence function shape produced by a given faceplate and actuators configuration is very important in predicting the mirror's active performance; this will be discussed in more detail in the next chapter.

3.6.2 Form and surface quality

The active mirror was manufactures by Cobham Composites using the same lay-up and coating process as the test mirror. The main difference was that no edge filler was used around the mirror edge, following the observation that the filler locally modified the substrate hardness in the passive mirror. The mirror was delivered late in 2004 and weighed 312 g. Figure 3.19 shows a picture of the mirror before grinding and polishing, showing the slight ripple caused by the fibre print-through.

Initial interferometry testing by D. Brooks showed a relatively high degree of astigmatism (65 μm) and again a fibre print-through. Figure 3.20 shows an interferometry measurement of the mirror in the early stages of grinding, clearly showing astigmatism.

Successive cycles of grinding and polishing removed the print-through and reduced the astigmatism to approximately 15 μm. This seemed to be the baseline level the faceplate returned to when left to rest, even after initial improvement, suggesting residual stress. The astigmatism is localized in two well-defined areas, giving the appearance of "holes", as shown in figure 3.21. The edge ring observed with the passive mirror was entirely absent, confirming the filler material as the suspected cause.

The residual astigmatism suggests that stresses at the nickel-CFRP interface are

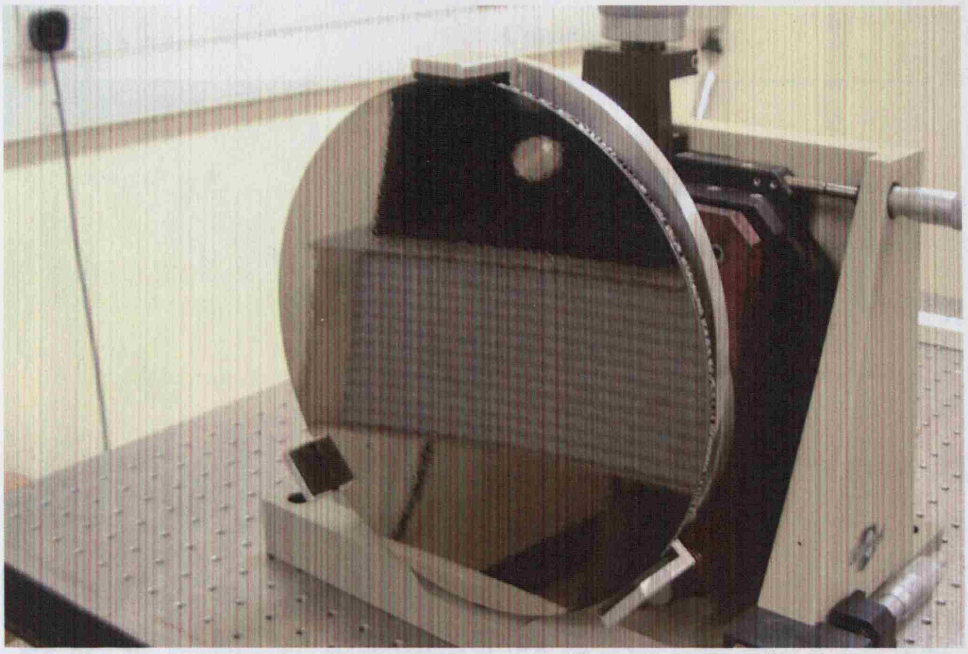

Figure 3.19: Picture of the active mirror faceplate prior to grinding and polishing, showing the fibre print-through.

introduced after removal from the mold. This is most likely due to a differential cooling of the nickel coating and the composite substrate. This suggests again that the coating method used by Cobham Composites is not optimal for the manufacture of precision reflective optics, as was suggested following the initial laminate FEA and experience with the passive test mirror. Also, the aluminium honeycomb core reacts to the changing temperatures experienced during the lay-up process. It is thought that this could introduce localized stresses. This residual astigmatism was not observed in the passive mirror, where the honeycomb core was filled in at the edges with a hard filler material.

Finally, after removal from the mold, material is selectively removed from the mirror surface during grinding and polishing, eventually leaving a nickel layer with non-uniform thickness. This can cause problems with stability in a changing environment during operation.

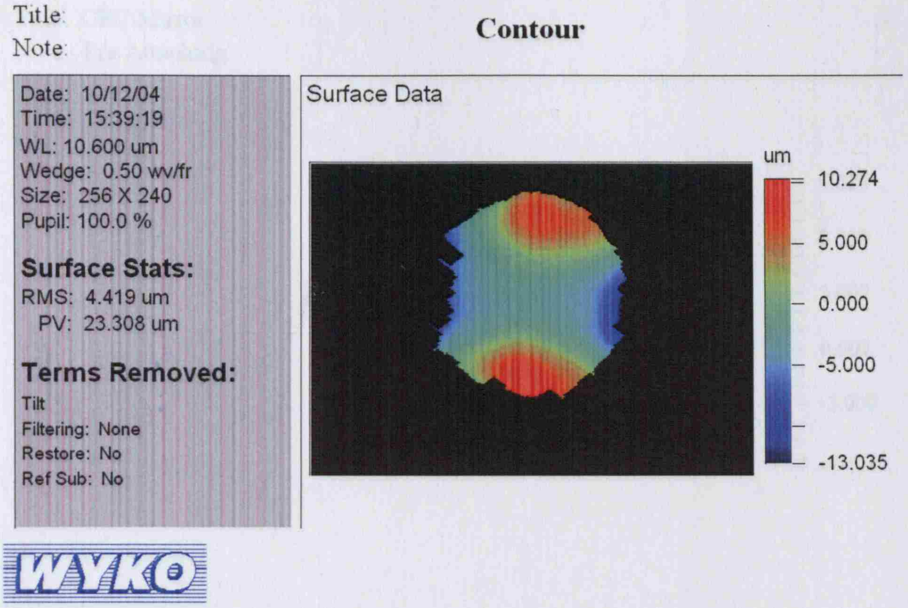

Title:
Note:

Date: 10/12/04
Time: 15:39:19
WL: 10.600 um
Wedge: 0.50 wv/fr
Size: 256 X 240
Pupil: 100.0 %

Surface Stats:
RMS: 4.419 um
PV: 23.308 um

Terms Removed:
Tilt
Filtering: None
Restore: No
Ref Sub: No

Figure 3.20: Interferometry measurement at 10.3 μm of the active mirror surface in the early stages of grinding, showing a significant degree of astigmatism.

3.7 Conclusions from initial modelling and testing of thick and thin composite substrates

From the work presented in this chapter, important conclusions can be made.

1. The mirror prototypes have shown that a spherical surface can be produced with form errors of the order of 10 μm for both thick and thin designs. A very good surface roughness below 5 nm rms was achieved with manual polishing.
2. The in-mold coating technique as used by Cobham Composites is not an optimal method for producing precision reflective optics. After post-cure cooling the substantial difference in thermal expansion coefficients of the nickel and CFRP introduces stresses, causing form changes. These are generally of low spatial frequency, such as defocus and astigmatism, and for an active system should not compromise the ability to flatten the mirror. It does, however, reduce the effectiveness of the actuator stroke in correction aberrations of other sources.

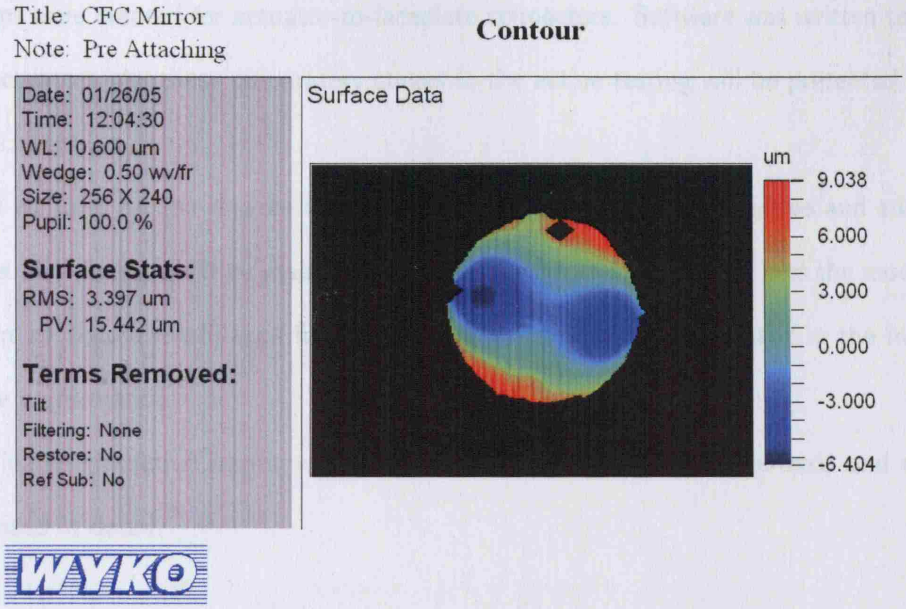

Title: CFC Mirror
Note: Pre Attaching

Contour

Date: 01/26/05
Time: 12:04:30
WL: 10.600 um
Wedge: 0.50 wv/fr
Size: 256 X 240
Pupil: 100.0 %

Surface Stats:
RMS: 3.397 um
PV: 15.442 um

Terms Removed:
Tilt
Filtering: None
Restore: No
Ref Sub: No

Figure 3.21: Interferogram of the active mirror final surface prior to assembly.

3. Sandwich panels with aluminium honeycomb cores are effective ways of stiffening the mirror substrate without adding weight or compromising the CFRP's stability properties. These cores are widely available, cheap, and can be worked into curved shapes to match the composite skins. However, the contribution of the aluminium core to any residual stresses after removal from the mold must be investigated. Cores in other materials are likely to be more stable, albeit perhaps at an increased cost.

4. Finite element analysis can and should play an important role in material selection for and design of deformable optics. It is especially valuable in situations where little-known or exotic materials are involved. Results should, however, be interpreted with care and always compared with experimental results where possible.

After the process of polishing and initial testing of the mirror, the next stage was to complete the active setup by fitting the mirror faceplate to the aluminium support structure and actuators. To facilitate this and optimize the mirror's active performance, designs were created for actuator-to-faceplate connectors. Software was written to drive the actuators. All these preparatory stages to the active testing will be presented in the next chapter.

It will also further explore the use of FEA in optical design for active and adaptive optics. An attempt will be made to include actuators and connectors into the models to obtain an accurate influence function shape, which is highly important in the mirror's active performance.

Finally the active mirror will be extensively tested and characterized, and results discussed in detail.

CHAPTER 4

Dynamical modelling and testing of a CFRP active mirror

The dynamical behaviour of an active or adaptive mirror, and its final performance in a working system, is determined by the interaction of the actuators, drive electronics and faceplate. Some (but not all) of the factors determining a system's performance are (Hardy, 1998):

- the number of actuators and their spatial arrangement;
- the temporal frequency response of the mirror and drive electronics;
- the actuator influence functions;
- hysteresis;
- the power dissipation.

Integrated modelling of the deformable mirror system, including actuator attachments and support structures, can help predicting the overall performance.

This chapter will describe how the active mirror faceplate, whose design and construction was described in detail in the previous chapter, was attached to a set of actuators and support structure and prepared for active testing. This involves the design and manufacture of the required connectors between actuators and faceplate, and development of drive software.

An attempt was made to predict the precise influence function shape from this architecture using finite element analysis. The problems in modelling this and the results obtained are presented in section 4.2. The central actuator influence function was then measured by interferometry and the shape analysed in detail analytically using a custom-written MatLab routine. The modelling and measurement results are extensively compared, in order to assess the value of FEA in influence function shape prediction. Finally, an attempt is made to flatten the mirror and its stability over time investigated.

4.1 Active mirror assembly

Following the completion of grinding, polishing and faceplate testing, planning commenced for the assembly of the mirror system. The architecture was largely determined by the existing aluminium system, which was described in detail in section 3.2.1 of the previous chapter. A new design was made for the connectors, as the existing pieces were damaged in disassembling the aluminium mirror, and the method of connection was different for the CFRP mirror: because of the thinness of the CFRP skins it was not thought possible to screw cups and bosses directly into the mirror as was the case for the aluminium mirror. A design was created using aluminium, largely for reasons of cost and simplicity, to be glued to the back skin.

The following sections will describe the actuators used, the process of mirror assembly, from a summary of the requirements to the electronics and software development.

4.1.1 Actuator specifications

The magnetostrictive actuators used in the project were selected on the basis of availability from the aluminium deformable mirror project (Bigelow, 1996). MS actuators are available in a variety of sizes, capable of a wide range of strokes. The required stroke was calculated by Lee (1999) for the aluminium mirror demonstrator on the basis of the seeing statistics at the William Herschel Telescope. A drawing of the model used in this project is shown in figure 4.1, and its specifications are shown in table 4.1. In addition, the actuator was reported by the manufacturer to have an excellent lifetime, with no measurable loss in performance over 10^{10} cycles. However, their size and weight does not make them suitable for an ultra-lightweight active or adaptive optical system.

Stroke	± 25 μm
Natural frequency	5400 Hz
Maximum dynamic force	$\pm 220N$
Maximum blocked force	$462N$
Axial stiffness	$18.5N/\mu m$
Temperature range	-20 to $100°C$
Input current	$\pm 1.4A$ rms
DC resistance	3.2Ω
Inductance	$2.1mH$

Table 4.1: Specifications of the Etrema magnetostrictive actuator (Etrema Products Inc., 2002).

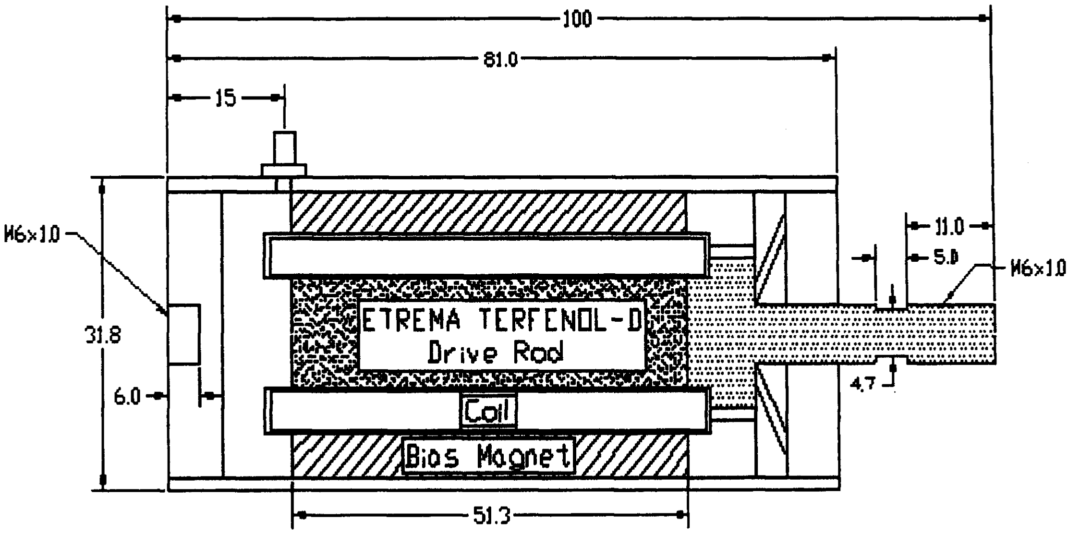

Figure 4.1: Drawing of the magnetostrictive actuators used to control the mirror's shape (Lee, 1999).

Bigelow *et al.* (1997) subjected a single actuator to extensive testing. Hysteresis and frequency response were found to agree with the manufacturer's specifications, with linear amplitude response observed to a frequency of 3 kHz. Hysteresis was high at around 30%. Continuous operation at 500 Hz for over a billion cycles showed no loss in performance, again confirming the manufacturer's data.

The presence of non-linear behaviour and hysteresis necessitate the inclusion of a closed-loop feedback system in the mirror's drive electronics. For this purpose the actuators were modified by Etrema, who fitted a strain gauge to the rod of magnetic material inside the actuator casing. A closed-loop electronics circuit was designed for the aluminium system, but due to a poor understanding of the method in which the modifications were carried out, the feedback loop was removed for this project. The electronics are discussed further in detail in section 4.1.3.

The choice of actuator is very important in a working active system. Equally important, however, is the method by which the actuator is attached to the faceplate. The next section will discuss the designs of clamps, support and mounting structures.

4.1.2 Support structure specifications

The support structure of a deformable mirror system can be divided into the following categories:

1. A backing plate
2. Mirror radial supports
3. Actuator mounts, connecting the actuators to the faceplate
4. Flexures, allowing a relaxation of faceplate stresses.

The requirements for a given system determine the exact architecture. In the case of an adaptive secondary, for example, the design can be simplified by omitting any radial support and having the faceplate supported solely by the actuators. This can save significant weight in the system.

The backing plate acts as a reference for the actuators to react against, and must therefore be stiffer by several orders of magnitude. It should also be thermally matched with the faceplate to avoid any stresses occurring on temperature changes. Differential expansion of backing plate and mirror will cause bending stresses in the actuators, and can compromise their performance.

The actuators mounts should act as connectors between the actuators and the faceplate. Their shape and connection method determines the influence function shape as the actuation force is transmitted. They should ideally be matched thermally to the other structural components.

Flexures are highly important in the mirror's dynamical performance. They allow alleviation of any stresses that occur and decrease the effective bending stiffness of the actuator. This enables coupling between the actuators, which is essential for avoiding high spatial frequency deformations, or ripples, from occurring on actuation.

As described in the previous chapter, most of the components for the CFRP active mirror system were taken from the existing aluminium mirror system. The backing plate, including the actuator attachment clamps, and flexures were designed by Bigelow (1996), and modified by Lee (1999).

4.1.2.1 Backing plate

The original design specifications for the Gemini adaptive secondary mirror demonstrator called for an aluminium honeycomb sandwich construction for the support plate in order to achieve maximum stiffness with minimum weight. To save on time and cost, a simple solid round aluminium plate was used, with clearance holes for the actuators. It was designed to be several orders of magnitude stiffer than the faceplate.

Lee (1999) carried out flexure testing of the assembled aluminium mirror system, with displacement measurements made at the faceplate, the flexure, the backing plate and the back surface of the actuator casing. These showed that on actuation the backing plate displayed a backward movement of 4% of the actuator stroke, confirming the adequate stiffness of the plate.

4.1.2.2 Actuator clamps

A clamping system was developed by Lee (1999) to attach the actuators to the backing plate. As a result of the strain gauge modifications to the actuators, the drive connector exits along the length of the cylindrical casing, and the strain gauge wires from the back of the actuator. To allow for these connections, the actuators are clamped around the body only.

In Lee's flexure tests described in the previous section, the actuators showed a backward movement on actuation with a magnitude of 12.4% of the total stroke magnitude, implying that the clamp designs were not optimal for keeping the actuators in place. Because of the different clamped forces on each actuator, this also resulted in a non-uniformity of influence functions across the mirrors.

As the actuators could not be replaced, a modification of the clamp system was not possible. However, future systems should feature back support of the actuators to prevent the slipping observed here.

4.1.2.3 Flexures

The problem posed by flexure design is to trade off requirements of flexibility for avoiding excessive torque loading to the mirror, and stiffness for maintaining radial support and a high resonant frequency. Bigelow (1996) modelled and tested two flexure designs, a cross-bladed and a waisted cylindrical design. Figure 4.2 shows a CAD drawing of the final flex coupling used in the aluminium mirror system, and also in the CFRP active mirror.

This design was subjected to a fatigue test by Lee (1999), in which a flexure-coupled actuator was cycled at 100 Hz with a $\pm 10\mu m$ stroke. No failure occurred in 800 million cycles over 3 months.

4.1.2.4 Actuator mounts

The actuator mounts provide the coupling between the actuators and the faceplate via the flexures. An important factor in the design of these components is the replaceability in case of actuator failure. The mounts include several parts, and a threaded joint between the faceplate and the connectors to allow an actuator to be removed without causing damage to the system or compromising the optical quality of the faceplate. In order to compensate for any discrepancies in actuator lengths (at a sub-mm level), the flexures were glued into a cup-like component with the epoxy compensating for any length differences. All the components were fabricated from the same aluminium alloy

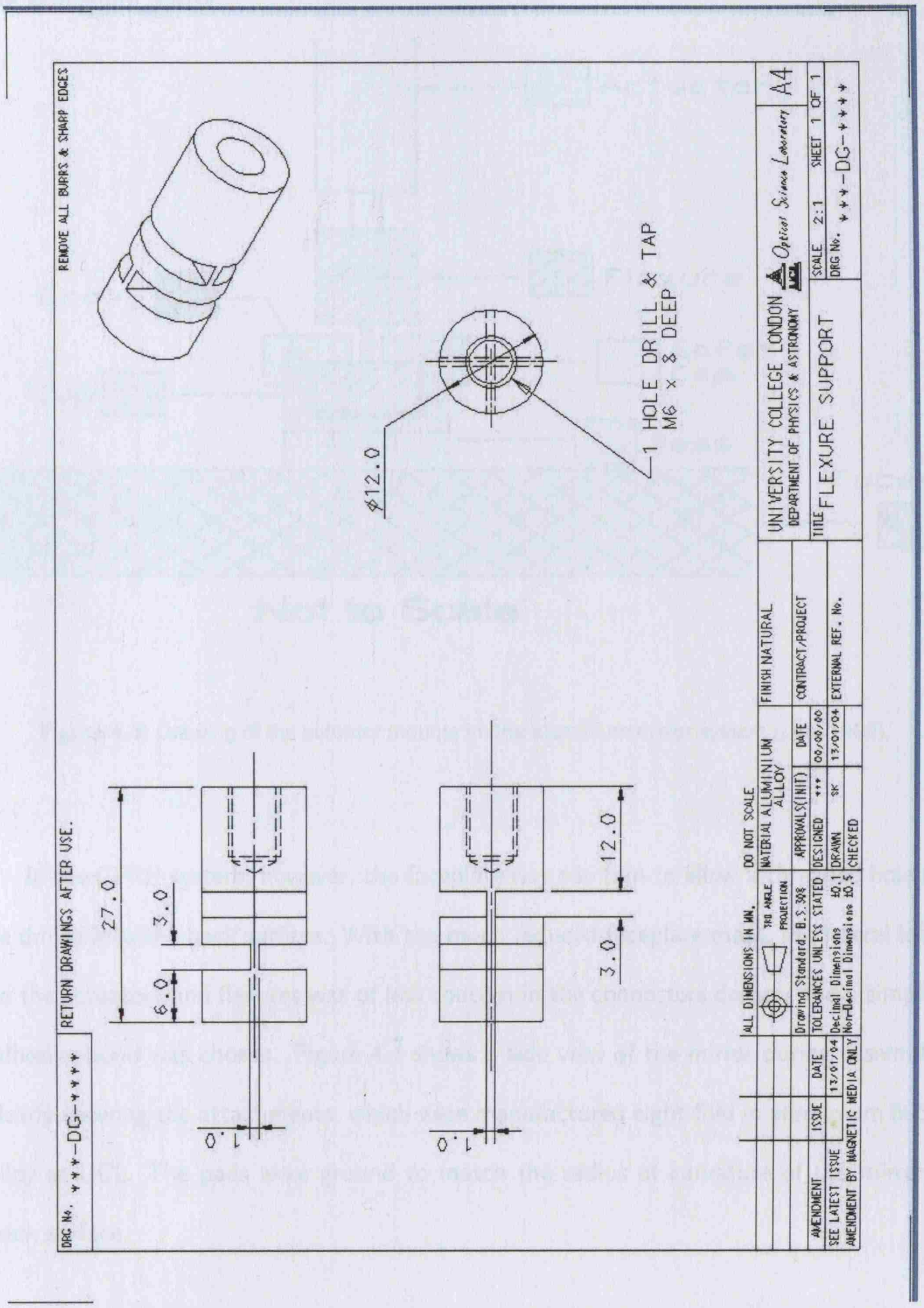

Figure 4.2: Draft of flexure couplings, showing the cross-blade design. The flexures will relax the actuator bending stiffness, preventing the introduction of stresses into the system.

as the faceplate and backing structure. Figure 4.3 shows a drawing of the mounts for the aluminium mirror.

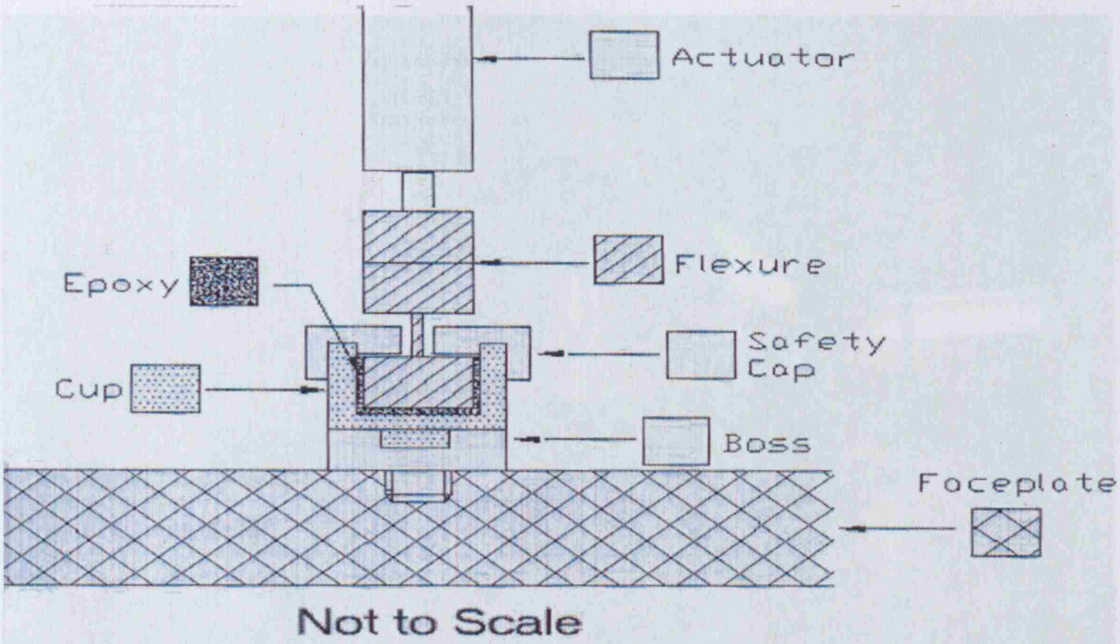

Figure 4.3: Drawing of the actuator mounts for the aluminium mirror system (Lee, 1999).

In the CFRP system, however, the faceplate was too thin to allow a threaded hole to be drilled into the back surface. With the much reduced faceplate mass, the lateral load on the actuators and flexures was of less concern in the connectors design, and a simpler adhesive bond was chosen. Figure 4.4 shows a side view of the mirror during assembly, clearly showing the attachments, which were manufactured eight-fold in aluminium 6062 alloy at UCL. The pads were ground to match the radius of curvature of the mirror's back surface.

4.1.2.5 Mirror assembly

A rig was set up to assemble the mirror without placing any stress on the faceplate from the weight of the backing structure (see figure 4.4). The adhesive used was a two-part epoxy, 3M 2216, which is well suited for use with composite materials (Dando, Jan 2005).

Figure 4.4: Picture of the gluing rig used to assemble the mirror systems. The raised stages stop the backing plate from stressing the faceplate during the cure process. The picture also shows the actuator mounts and flexures.

During assembly an effort was made to place two of the actuators directly over the observed 'holes' in the surface to allow the actuators to correct the distortion. The mirror surface did not show any deterioration of form after assembly and curing (in fact the holes seemed reduced, as shown in figure 4.5), and dynamic testing was commenced.

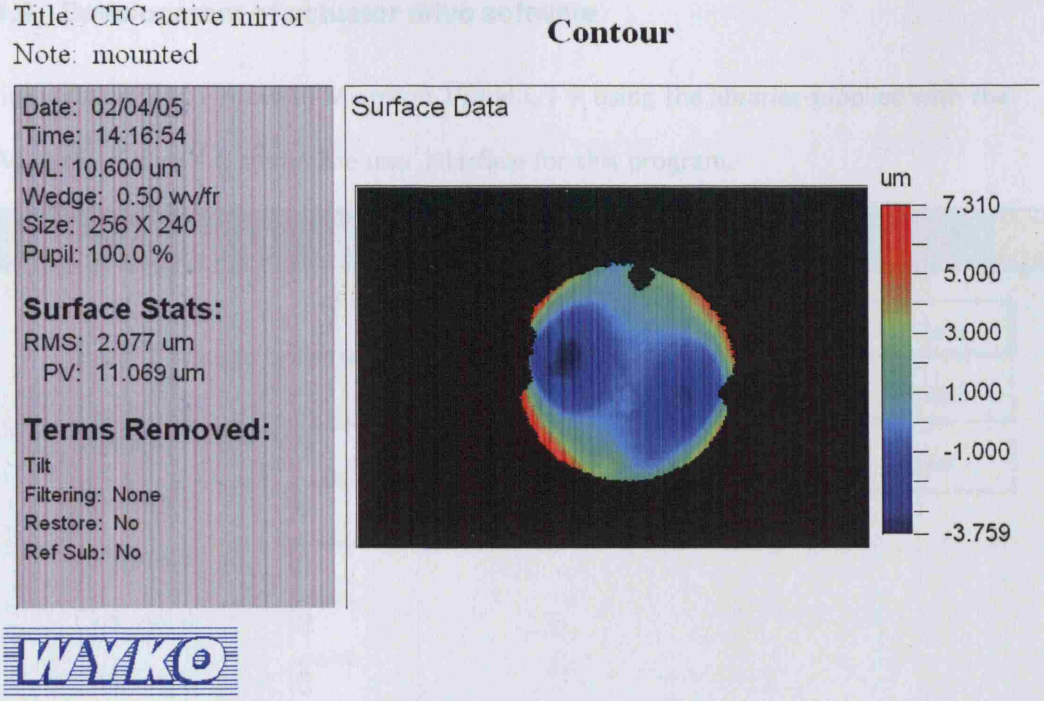

Title: CFC active mirror
Note: mounted

Date: 02/04/05
Time: 14:16:54
WL: 10.600 um
Wedge: 0.50 wv/fr
Size: 256 X 240
Pupil: 100.0 %

Surface Stats:
RMS: 2.077 um
PV: 11.069 um

Terms Removed:
Tilt
Filtering: None
Restore: No
Ref Sub: No

Figure 4.5: Active mirror surface after assembly and curing, showing no significant deterioration of surface form compared with the pre-assembly measurements.

4.1.3 Electronics architecture

The existing circuitry for closed-loop actuator control was designed and manufactured by G. Nixon and J. Lee, and is described in detail in Lee (1999). The closed loop incorporates feedback from the strain gauge sensors to correct for thermal effects and hysteresis. The control processor inputs a given actuator voltage through a digital-to-analog converter (DAC) interface. A power amplifier amplifies this signal so that the range matches the current input for the actuator. Where the actuator does not reach the desired position, the residual error is sensed by the strain gauge, which, when properly calibrated, will differ from the DAC signal by a small amount. A wheatstone bridge configuration is then used to modify the input to the actuator by the desired amount.

However, as closed-loop operation was not envisaged for this project, the feedback loop was deactivated for testing of the CFRP active mirror.

4.1.4 Development of actuator drive software

Drive software was written in Microsoft Visual C++ using the libraries supplied with the DAC card. Figure 4.6 shows the user interface for this program.

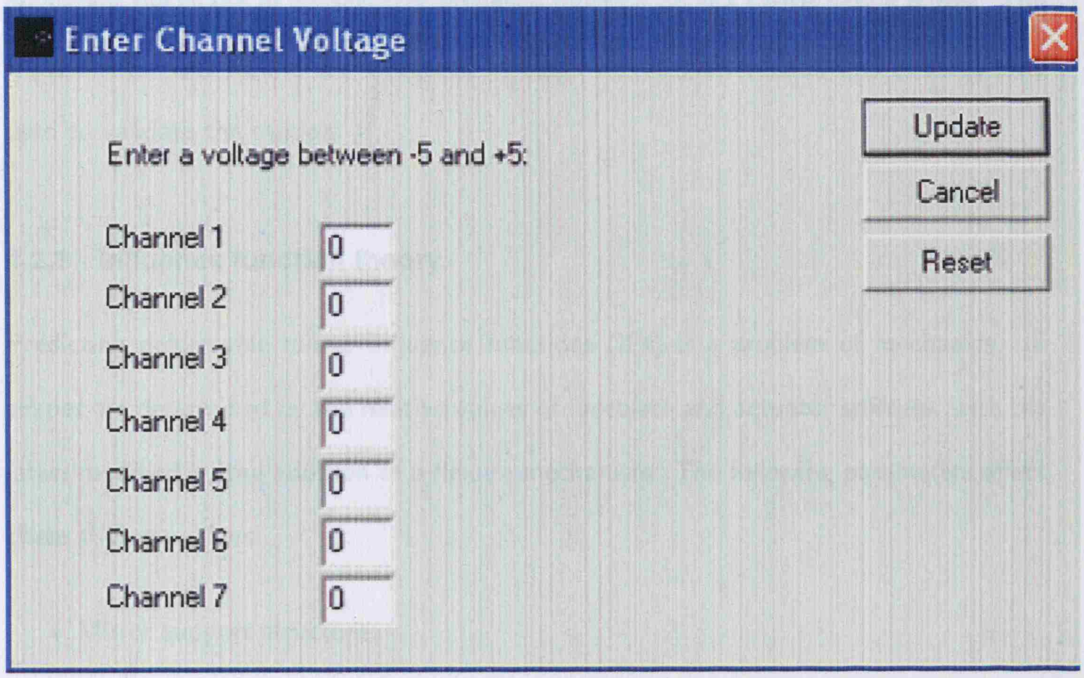

Enter a voltage between -5 and +5:

Channel 1 0
Channel 2 0
Channel 3 0
Channel 4 0
Channel 5 0
Channel 6 0
Channel 7 0

Figure 4.6: Graphical user interface of the mirror drive software.

A more elaborate GUI was also designed for a more recent model of DAC card, but because of problems with the hardware, which failed on several occasions due to short circuits, the original hardware and software were used.

4.2 Finite element prediction of influence function shapes

The elementary deformation caused by one activated actuator is commonly referred to as the actuator's *influence function*. The actuators' influence functions in a deformable mirror system collectively determine the mirror's set of shape eigenmodes, which fundamentally limit the performance of an active or adaptive system. For the case of a deformable mirror correcting for atmospheric turbulence distortions, equation 2.18 defines the mean square fitting error σ_F^2 in terms of fitting coefficient a_F, r_0 and actuator pitch d.

This section will discuss the theory of influence functions and will use FEA to attempt predicting the shape of an actuator influence function on the CFRP active mirror. The experimental test results are discussed in detail in the next section and subsequently used to validate the models.

4.2.1 Influence function theory

Predicting deformable mirror influence functions (IFs) is a problem of mechanics. IF shapes are determined by the relative values of faceplate and actuator stiffness, with the latter modified by the addition of a flexure mechanism. The following parameters affect these stiffness values:

- Mirror support structure;
- Actuator type, layout and density;
- Method of connecting the actuators to the faceplate;
- Faceplate architecture (segmented or continuous):
- Faceplate thickness and modulus.

Deformable mirrors must therefore be designed to produce the best shape of influence function for the required corrections in the particular application. Analytical approximations have been developed to predict IF shapes, in order to optimize designs and for use in optical simulations. Whilst a characterization of mirror shapes is useful in all optical systems using deformable mirrors, it is especially important in adaptive optics, where aberrations of a wide range of spatial frequencies must be corrected over millisecond timescales.

The simplest shape approximations use basic geometrical forms, such as piston-only motion for segmented mirrors or pyramid-shapes IFs for continuous facesheet mirrors. Most commonly used in simulations is an empirical Gaussian-like shape (Tyson and Frazier, 2004):

$$\phi_{gauss} = A\exp(\frac{\ln C_A}{d^2}r^2) \tag{4.1}$$

where r is the polar radial coordinate in the mirror plane, d is the interactuator spacing and C_A is the interactuator coupling, or the movement of the surface at the position of the adjacent actuator, expressed as a value between 0 and 1. A is the amplitude of the IF.

The Gaussian shape equation is easy to manipulate analytically and matches observed IF shapes well in close proximity to the actuator. However, the Gaussian assumption has no basis in physical reality and does not allow for the faceplate to bend to negative values.

Ealey and Wellman (1989), hereafter EW, derived an approximate expression for deformable mirror IF shapes from elementary beam theory, also discussed in detail by Hardy (1998). The advantage of this approach is that is based on the same principles as structural modelling software such as FEA, and the authors report a good agreement with 3D FEA modelling and experimental measurements. They distinguish two extreme cases: the clamped-clamped (C-C) case and the clamped-free (C-F) case. These are illustrated in figure 4.7.

In the C-C setup the beam ends are clamped in all degrees of freedom, corresponding to the case where the actuator bending stiffness is large compared to the faceplate stiffness. The beam deflection on a mid-point load F is given by:

$$y_c = \left(\frac{F}{K_F^c}\right)\left[2\left(\frac{x}{d}\right)^3 - 3\left(\frac{x}{d}\right)^2 + 1\right] \tag{4.2}$$

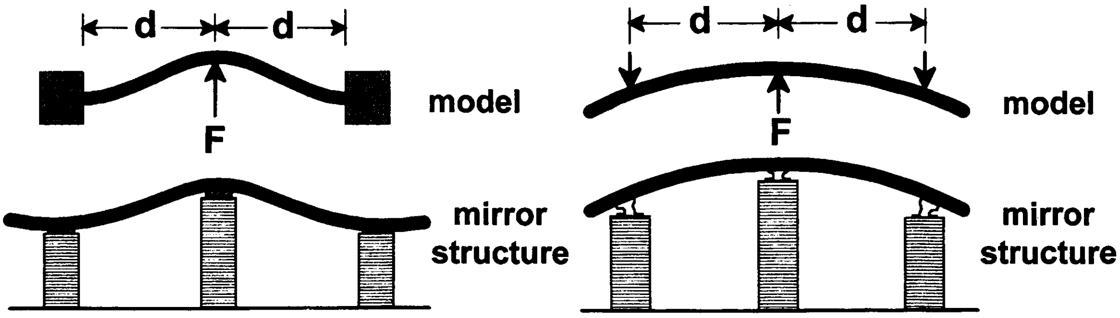

Figure 4.7: Two beam cases used by Ealey and Wellman (1989) to approximate deformable mirror influence function shapes (adapted from Hardy (1998)).

where x is the distance from the central actuator, d the inter-actuator spacing and K_F^c is the clamped faceplate stiffness, given by

$$K_F^c = \frac{24EI}{d^3} \tag{4.3}$$

with E the Young's modulus and I the moment of inertia of the faceplate beam section.

Conversely, the C-F case represents the situation where actuators have zero intrinsic stiffness or flexures are included in the design. The deflection in this case is:

$$y_u = \left(\frac{F}{K_F^u}\right)\left[\frac{1}{2}\left(\frac{x}{d}\right)^3 - \frac{3}{2}\left(\frac{x}{d}\right)^2 + 1\right] \tag{4.4}$$

and:

$$K_F^u = \frac{6EI}{d^3} \tag{4.5}$$

respectively. A real system will represent a trade-off between these two cases. A parameter β can be introduced to specify the ratio of actuator bending stiffness to that

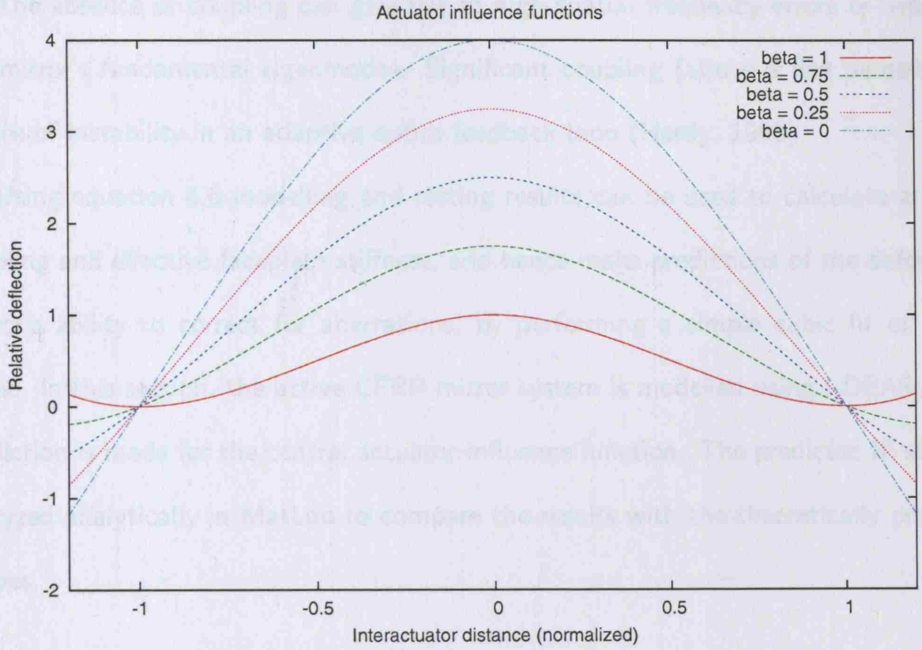

Figure 4.8: Cubic influence function shapes for varying values of β, according to equation 4.6. The shape is purely determined by β, the ratio of actuator to faceplate stiffness.

of the faceplate. $\beta = 1$ thus corresponds to the C-C case, $\beta = 0$ the C-F case. The actual deflection of the beam can be expressed as follows:

$$y_a = \left(\frac{Fd^3}{24EI}\right)\left[2\left(\frac{x}{d}\right)^3 - (6-3\beta)\left(\frac{x}{d}\right)^2 - 3\beta + 4\right] \tag{4.6}$$

Figure 4.8 shows a plot of this influence function shape for different values of β. The effective faceplate stiffness in this case is given by:

$$K_F = \frac{F}{y_{pk}} = \frac{24EI}{d^3(4-3\beta)} \tag{4.7}$$

The actuator coupling can easily be derived from these analytical expressions:

$$C_A = \frac{y_d}{y_{pk}} \tag{4.8}$$

The absence of coupling can give rise to high spatial frequency errors or 'ripple' in the mirror's fundamental eigenmodes. Significant coupling (above a few percent) is a source of instability in an adaptive optics feedback loop (Hardy, 1998).

Using equation 4.6 modelling and testing results can be used to calculate actuator coupling and effective faceplate stiffness, and hence make predictions of the deformable mirror's ability to correct for aberrations, by performing a simple cubic fit of the IF shape. In this section, the active CFRP mirror system is modelled using I-DEAS, and a prediction is made for the central actuator influence function. The predicted IF shape is analyzed analytically in MatLab to compare the results with the theoretically predicted shapes.

4.2.2 Modelling method

A finite element model was created to model the central actuator IF. As the combination of meshes becomes difficult when the model includes small details, such as the flexures, and large structures, such as the faceplate, some approximations can simplify the modelling process. The actuators were therefore modelled as beams with the corresponding cross-sections. Because beam elements cannot be connected to a shell mesh, the faceplate had to be meshed with 3D tetrahedral elements. This causes further problems with I-DEAS' composites toolbox, which only allows laminates to be modelled using 2D shell elements.

As a solution, the I-DEAS Laminates toolbox was used to compute the equivalent orthotropic properties of the active laminate, which were then applied to a 3D mesh. When verifying the results it is important to consider this a potential source of error. However, when the Young's modulus of the material was varied up- and downward by 10% as a test, the effect was an increase or reduction in the amplitude of deformations, respectively, but the IF shape remained unchanged.

As the edge actuators function as restraints for the faceplate on activation of the central actuator, they were modelled as beam elements attached to the faceplate mesh using rigid links. The bending stiffness of the actuator itself is much larger than that of the flexures. The actuators themselves were therefore not included in the model on the assumption that the flexures would provide the bending compliance. The flexure beams were restrained at the back node in all degrees of freedom, simulating a stiff backing structure.

To aid with the analysis of results, a horizontal line of nodes was grouped to provide a 2D cross-section of the IF. The IF shape was assumed to be perfectly axisymmetric as is expected for a central actuator in a real system. A total force of 10 N was then applied uniformly to the back surface of the central pad. Using the central line of nodes the 2D IF was then plotted and exported for analysis.

4.2.3 Modelling and analysis results

The first model corresponds to EW's clamped-clamped case and does not include flexures. This is a very simple case as it considers the actuator bending stiffness to be infinite, and can be easily used to test the theory. Nodes within a circle of radius of 12.5 mm were clamped in all degrees of freedom at the proposed actuator locations. Figure 4.9 shows a plot of the model on application of 10 N to the central actuator pad. The amplitude of the central displacement is $1.71\mu m$. The IF shape shows some irregularity, which is most likely due to the irregular shape of the restrained pad areas on the meshed faceplate.

The coordinates and displacements of the nodes along the central mirror diameter were exported to MatLab, where a polynomial fit of the form $y = ax^3 + bx^2 + c$ was performed to the data in the Curve Fitting Toolbox, where according to equation 4.2 for the clamped case:

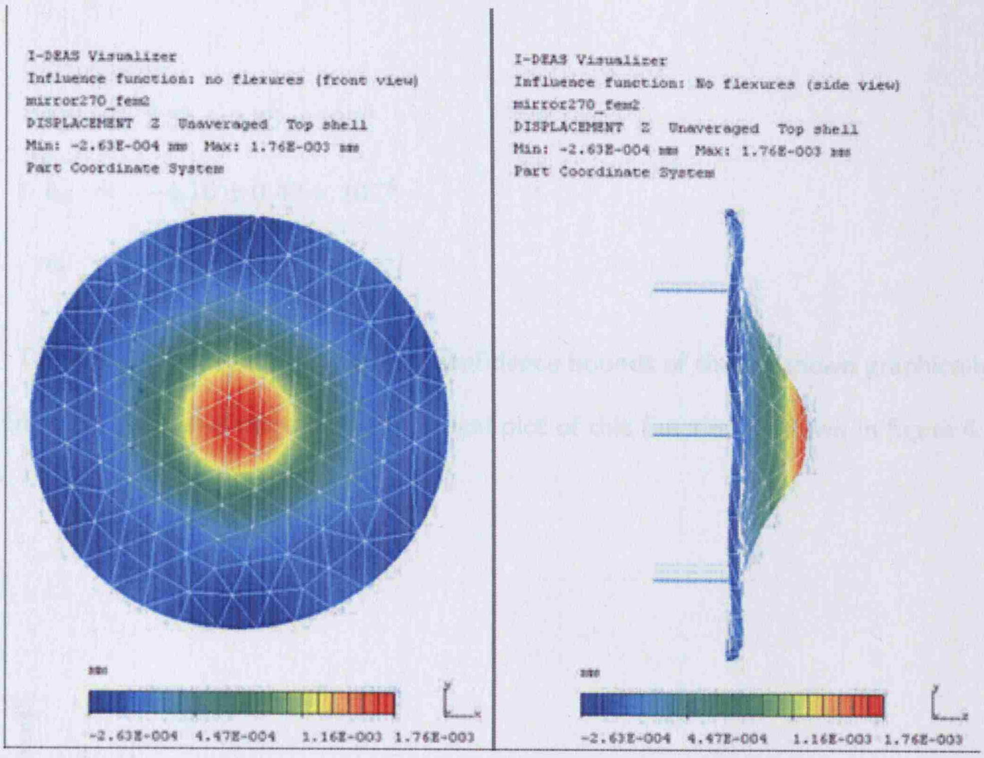

Figure 4.9: FEA influence function of the model with pads clamped (C-C case). The faceplate shows no bending to negative values, as is predicted by the theory. The slight asymmetry of the IF shape is due to mesh shape irregularities.

$$a_c = \frac{2F}{K_F^c d^3} \tag{4.9}$$

$$b_c = -\frac{3F}{K_F^c d^2} \tag{4.10}$$

$$c_c = \frac{F}{K_F^c} \tag{4.11}$$

From equation 4.2 parameter c_c also represents the amplitude of the displacement. The MatLab Curve Fitting toolbox uses a least squares method, which minimizes the summed squares of residuals. A simple linear least squares algorithm was selected, and the polynomial was entered as a custom equation using the Creat Custom Equation GUI in the toolbox. The following values were found for the parameters a_c, b_c and c_c:

$$a_c = 2.33 \pm 0.36 \times 10^{-6}$$

$$b_c = -4.16 \pm 0.42 \times 10^{-4}$$

$$c_c = 1.71 \pm 0.087$$

The errors are taken from the 95% confidence bounds of the fit, shown graphically in figure 4.14. A three-dimensional theoretical plot of this function is shown in figure 4.10.

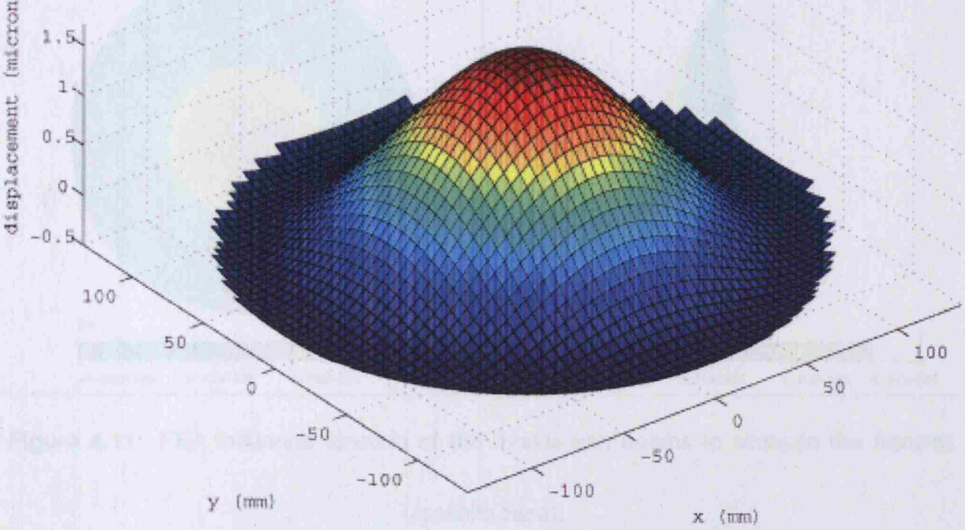

Figure 4.10: Three-dimensional plot of the modelled clamped IF shape, using parameters a_c, b_c and c_c.

Using the same model setup, the flexures were then included in the analysis. Based on equation 4.6, the parameters now include the β factor to account for the presence of flexures. They are defined as follows:

$$a_a = \frac{F}{12EI} \tag{4.12}$$

$$b_a = \frac{Fd}{8EI}(2-\beta) \tag{4.13}$$

$$c_a = \frac{Fd^3}{24EI}(-3\beta+4) \tag{4.14}$$

The beams representing them were restrained at the back node, simulating the presence of a stiff backing plate. Again 10 N were applied to the central actuator pad. Figure 4.11 shows the resulting mirror deformation.

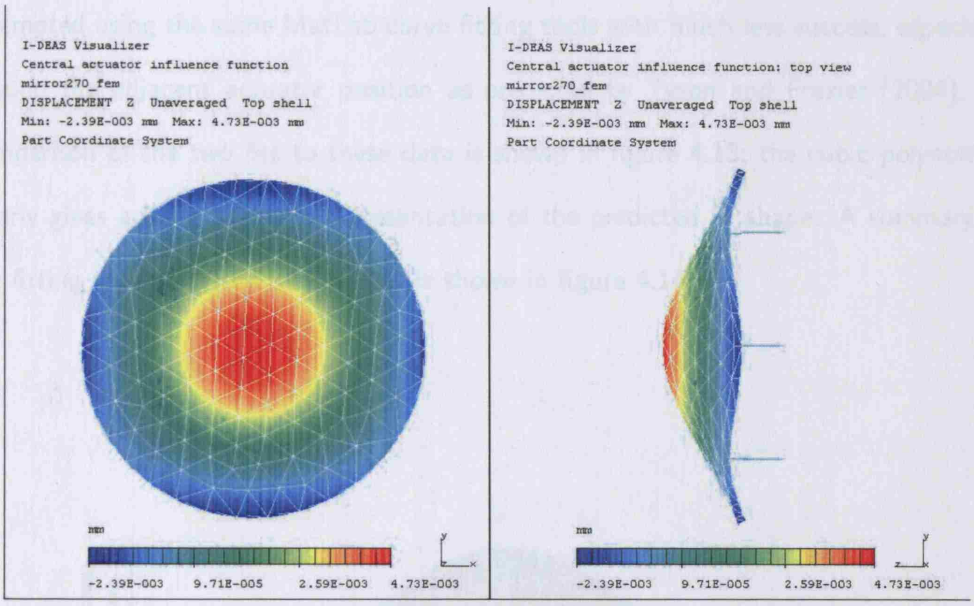

Figure 4.11: FEA influence function of the model with beams to simulate the flexures (realistic case).

The plot clearly shows a wider-shaped influence function due to the flexures allowing the mirror to bend beyond the edge actuators. The squared shape is most likely due to the hexagonal actuator layout. The faceplate also bends below the zero level beyond the edge actuators, which is typical of mirror designs that include flexures.

As with the clamped case, the displacement of the group of nodes along the central diameter was exported to MatLab and the curve fitted to the cubic polynomial $y = ax^3 + bx^2 + c$. The following results were found:

$$a_a = 3.182 \pm 0.218 \times 10^{-6} \tag{4.15}$$

$$b_a = -8.171 \pm 0.281 \times 10^{-4} \tag{4.16}$$

$$c_a = 4.74 \pm 0.054 \tag{4.17}$$

A three-dimensional reconstruction of this function is shown in figure 4.12. Using the coefficients, the predicted coupling factor is $5.3 \pm 1.1\%$. Taking $d = 100mm$ and dividing c_a by a_a, β is found to be 0.34 ± 0.02. A Gaussian fit of this IF was also attempted using the same MatLab curve fitting tools with much less success, especially beyond the adjacent actuator position as predicted by Tyson and Frazier (2004). A comparison of the two fits to these data is shown in figure 4.13; the cubic polynomial clearly gives a more accurate representation of the predicted IF shape. A summary of the fitting results for the two models is shown in figure 4.14.

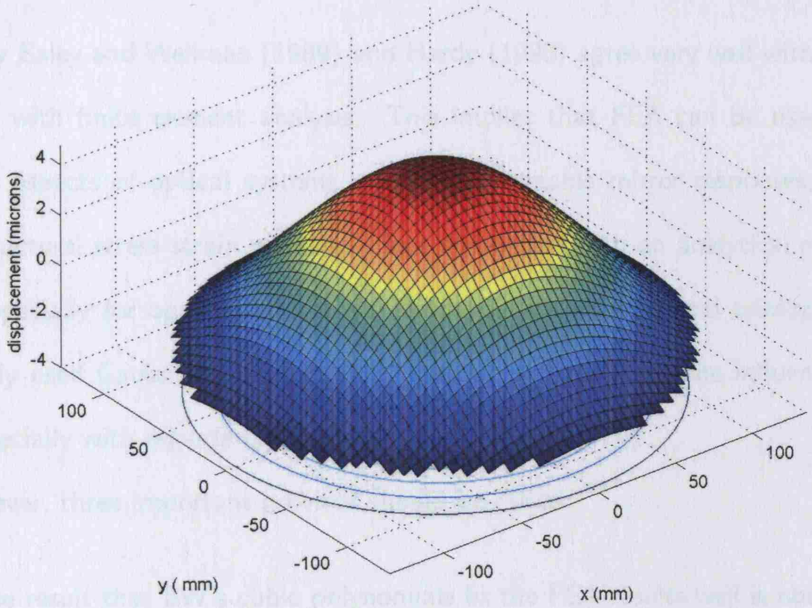

Figure 4.12: Three-dimensional plot of the modelled clamped IF shape, using parameters a_a, b_a and c_a.

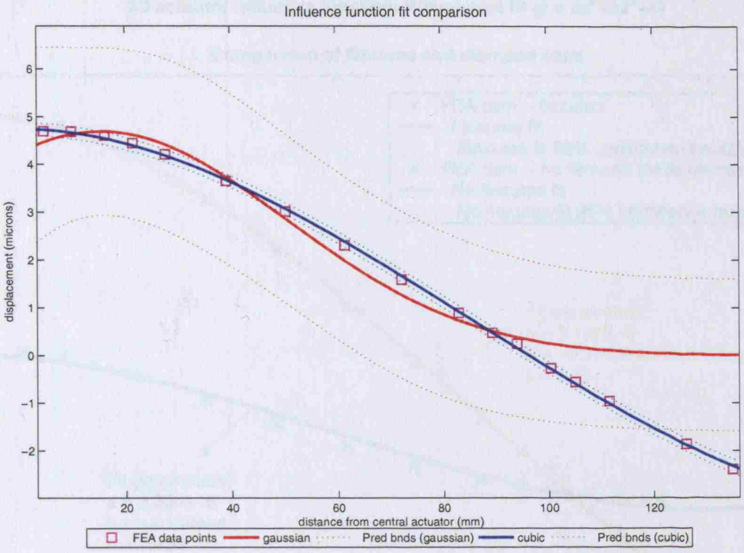

Figure 4.13: FEA data fitted with both a Gaussian and cubic fit, showing the 95% confidence bounds for each. The plot shows the excellent quality of the cubic fit.

4.2.4 Conclusions

These finite element and analytical models have shown that the cubic polynomials suggested by Ealey and Wellman (1989) and Hardy (1998) agree very well with the results obtained with finite element analysis. This implies that FEA can be used to model precision aspects of optical systems, such as deformable mirror responses, as well as other structural stress-strain matters. Close agreement with an analytical expression is useful especially for optical simulations for adaptive optics-assisted telescopes, as the commonly used Gaussian or pyramidal shapes do not represent the influence function well, especially with regards to coupling.

However, three important provisos should be raised:

1. The result that EW's cubic polynomials fit the FEA results well is not surprising, as the finite element method itself is based on the same assumptions that underlie beam theory.
2. Approximations were used in the FEA models. The laminates modelling procedures

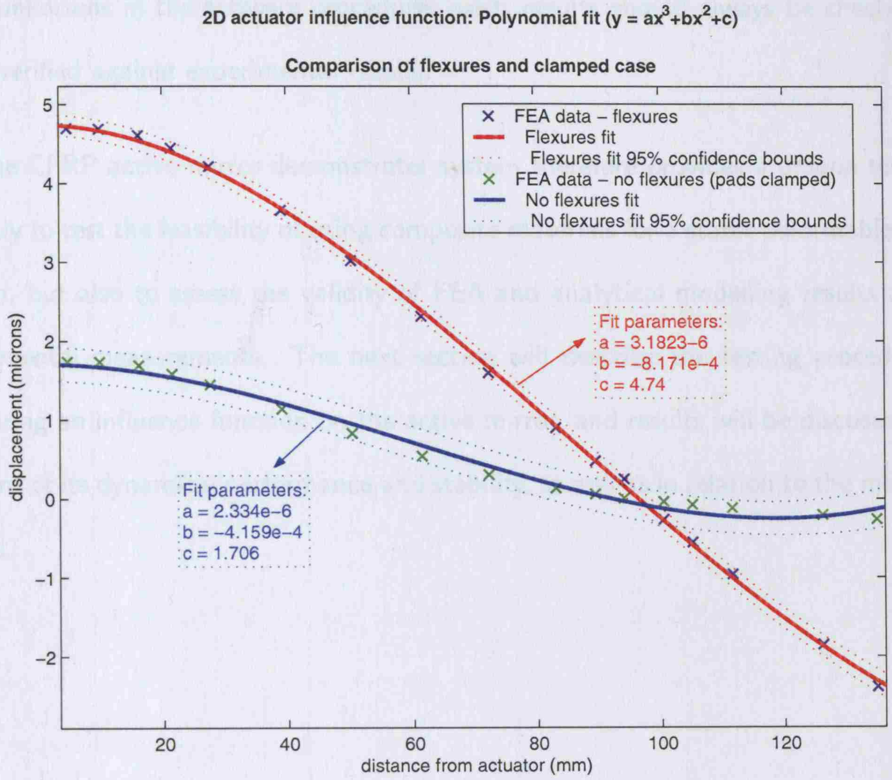

Figure 4.14: Summary plot of the cubic fit results for the two modelled influence functions with the coefficient values for each MatLab linear least squares fit, from the EW polynomial

$$y = ax^3 + bx^2 + c.$$

in I-DEAS are poorly documented and the validity of modelling composite materials with 3D elements should be questioned and investigated further. While the method of modelling the edge actuators with beam elements should in theory be able to produce valid results, further work is needed to check the accuracy. For example, creating a mesh using parabolic hexahedral (brick) elements instead of tetrahedrals would increase the number of integration points per element and allow an easier connection of the beam elements to the faceplate mesh.

3. It should always be borne in mind that FEA itself employs approximations, related to the use of a finite number of integration points and degrees of freedom and assumptions of a linear displacement response. In this case especially, where

unknowns in the software procedures exist, results should always be checked and verified against experimental results.

The CFRP active mirror demonstrator system therefore provides a unique test bed, not only to test the feasibility of using composite materials for a stable deformable mirror system, but also to assess the validity of FEA and analytical modelling results against experimental measurements. The next section will describe the testing procedure for measuring an influence function on the active mirror, and results will be discussed both in terms of its dynamical performance and stability, as well as in relation to the modelling results.

4.3 Dynamical testing of the CFRP active mirror

Following the preliminary work with the passive test mirror and finite element modelling, testing of the active mirror has two major aims:

1. To investigate the dynamical behaviour and stability of the mirror on actuation , and hence draw conclusions about the suitability of CFRP for precision optics in space and on the ground;
2. To validate the FEA results and assess the usefulness of FEA in the design of deformable optical systems.

This section will discuss the procedures used to test the active mirror, and present results of influence function measurements. Problems that arose and observations made throughout testing are discussed.

4.3.1 Initial tests and investigations

The same metrology equipment was used for the dynamical testing as for the initial form measurements of both the active and the passive mirrors. The mirror system was set up with a 10.3 μm infrared Wyko interferometer. The images are initially viewed in Wyko's proprietary interferometry software, Vision, from where the data can be exported into an Optical Path Difference (OPD) file. Vision has however only limited analysis facilities, which are poorly documented, and a MatLab routine developed by Dr. Andrew King was used to import the OPD files into MatLab, where more detailed processing was carried out. This also allowed a straightforward comparison with the FEA data, which were also exported to MatLab.

A description of the routine was provided by King (Feb 2006). The OPD file contains the operator settings together with the surface data in the form of the difference between a reference wavefront and the measured wavefront. The exported OPD file is a binary file with a well-organised directory structure; this makes further data analysis impossible without the aid of bespoke software. The MatLab routine, which uses 4 separate function files, allows the user to process the selected OPD file,and displays 2D slice data of the reconstructed file in a figure, as well as writing the set out to a text file. The data can then be read into other software packages, such as MS Excel, or used in high level languages such as C or Fortran. All results quoted here, however, were produced in MatLab itself.

Some initial investigations were carried out to gain an understanding of the Vision software routines. To allow for statistical variations and random effects, 20 exposures were taken per measurement. In practice this was carried out by setting the software to take the average of 4 snapshots per measurement. Five of these exposures were then averaged manually in Vision using the Average function. To test the routine five test measurements were averaged in varying permutations: 5, 1-4, 2-2-1 and 2-3. The resulting interferograms were checked for variations. The standard deviation between the different averages was found to be $< 0.5\%$. A conservative uncertainty of 1% was assumed on all subsequent averaging results to take any errors into account.

The MatLab routine takes X-Y slices through a surface measurement at a chosen pixel position in order to determine the 2D surface profile. This function is also available in Vision, albeit with fewer options, and tests were carried out to verify the correct working of custom analysis routine and ensure a thorough knowledge of the exporting procedure. The MatLab function also converts the pixel scale to distance units, and writes the data points to a variable as well as to a data file.

Numerical averaging in MatLab was carried out by using simple matrix manipulation functions, such as adding, subtracting and dividing. The results were also compared against the surface averaging in Vision, and a good agreement was found. The only apparent difference is that the Vision averaging results in fewer bad data points, and this was therefore the chosen averaging method. Also, for a MatLab subtraction the data require interpolation onto a regular grid of abscissae using function *interp1*, which complicates the procedure. A plot of these test results is shown in figure 4.15. The test was repeated with another measurement to ensure the result was consistent, with similar results. Numerical subtraction of surfaces was also compared in the same way for both software methods, again with excellent results (see figure 4.16).

At a later stage a scaling error was identified in the software, with the aperture size shown to be a smaller size than in reality. While the software was being debugged, measurement scales were adjusted on an ad hoc basis using the separation of known features on the mirror surface. This was especially important in the comparison of the measurements with the FEA modelling results. Figure 4.17 shows the actuator position marked on the mirror surface measurement used to determine the scaling error, which was found to be $36 \pm 3\%$.

4.3.2 Measurement of the central actuator influence function

At the start of the test session, the actuator drive voltage was set to 0V before switching on the power to the mirror, to prevent any sudden power surge to the actuators. Before each actuator was moved a measurement was always taken of the mirror reference surface. No attempt was made to flatten the mirror before testing the actuator response at this stage. Each actuator was then activated and tested in turn. After testing on one actuator was finished, it was cycled from +5 V to -5 V and back to 0 V to compensate for any hysteresis. A reference surface measurement was taken each time before moving on to the next actuator.

Because of the relatively poor surface quality along the edges the interferometer could often not resolve the edge surface, which resulted in bad data points on the edges. The measured edge actuator influence functions were therefore of lesser quality than the central IF and not as suitable for detailed analysis in the first instance. Figure 4.18 shows surface measurements of a central and edge influence function respectively.

The central actuator IF proved a very suitable measurement target and the reference

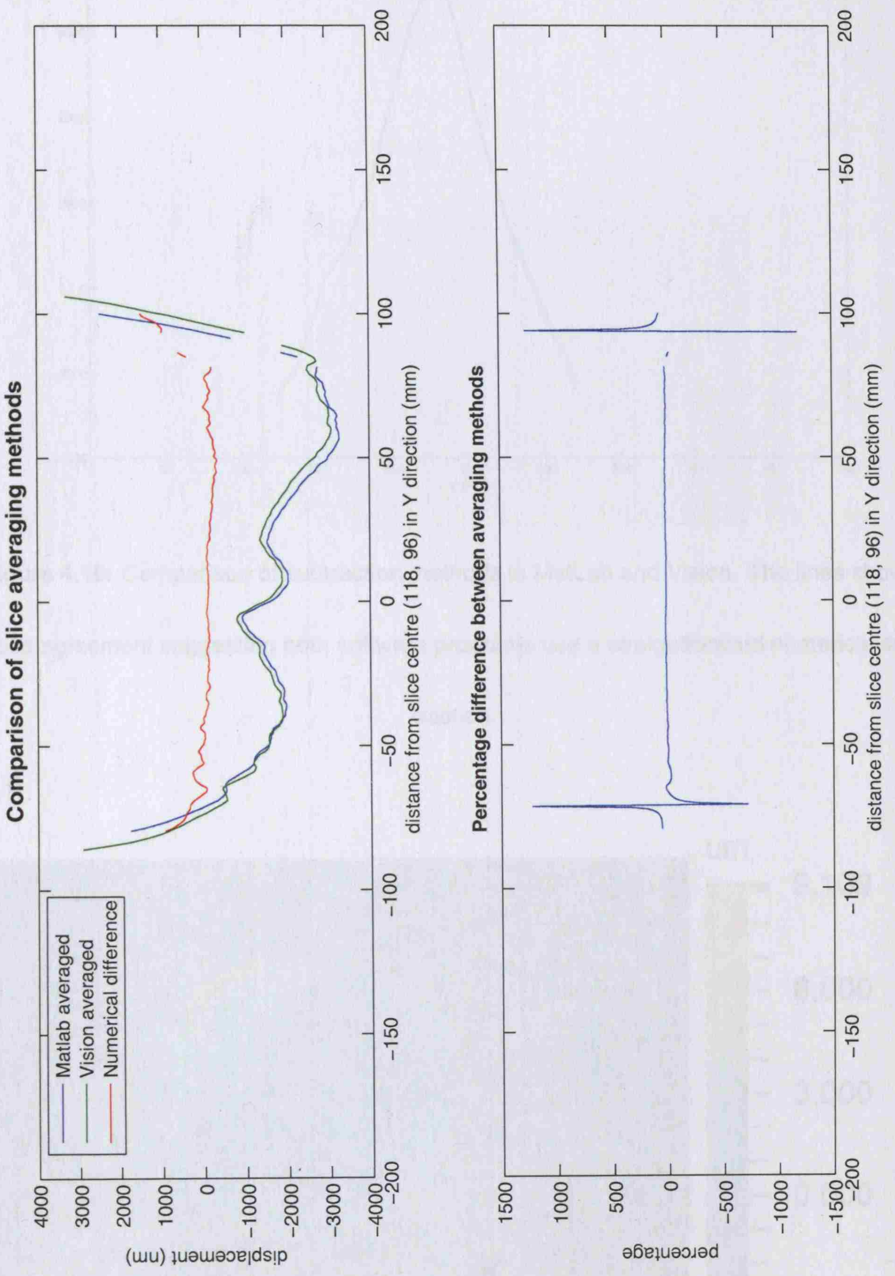

Figure 4.15: 2D plot of averaged slices through the mirror surface at rest. Each line is an average of 20 exposures or 5 measurements comprising of 4 snapshots each. The bottom plot shows the percentage value of the difference, the peaks at the line end being due to non-coinciding bad data points in the measurements.

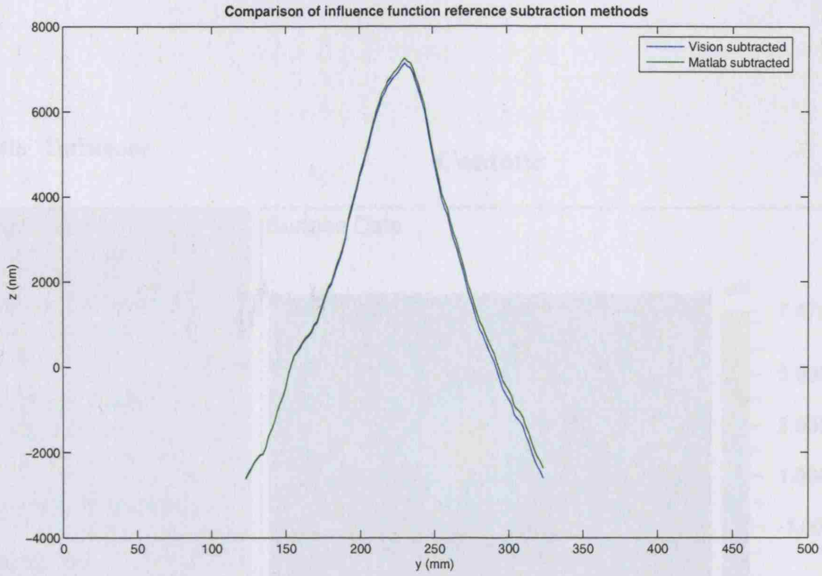

Figure 4.16: Comparison of subtraction methods in MatLab and Vision. The lines show a good agreement suggesting both software programs use a straightforward numerical subtraction.

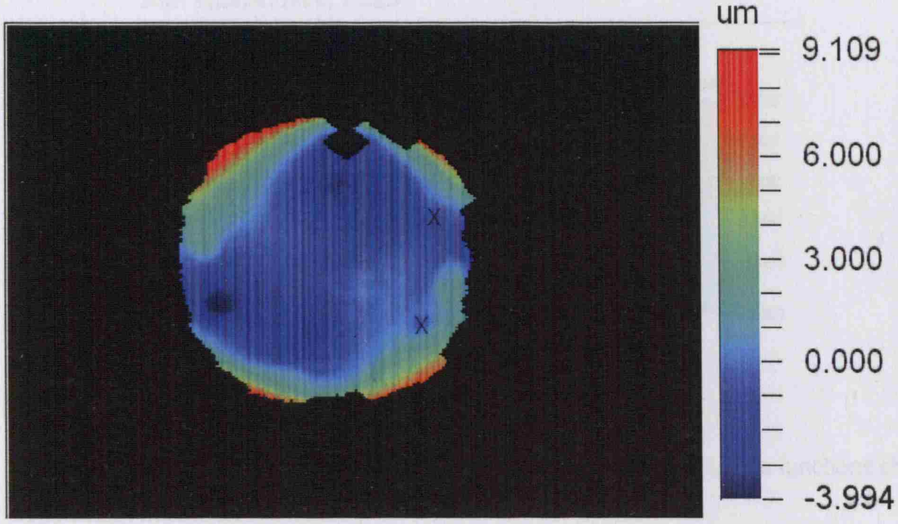

Figure 4.17: Interferogram of the CFRP active mirror showing the locations on the surface used to determine the scaling error in the dataset.

(a)

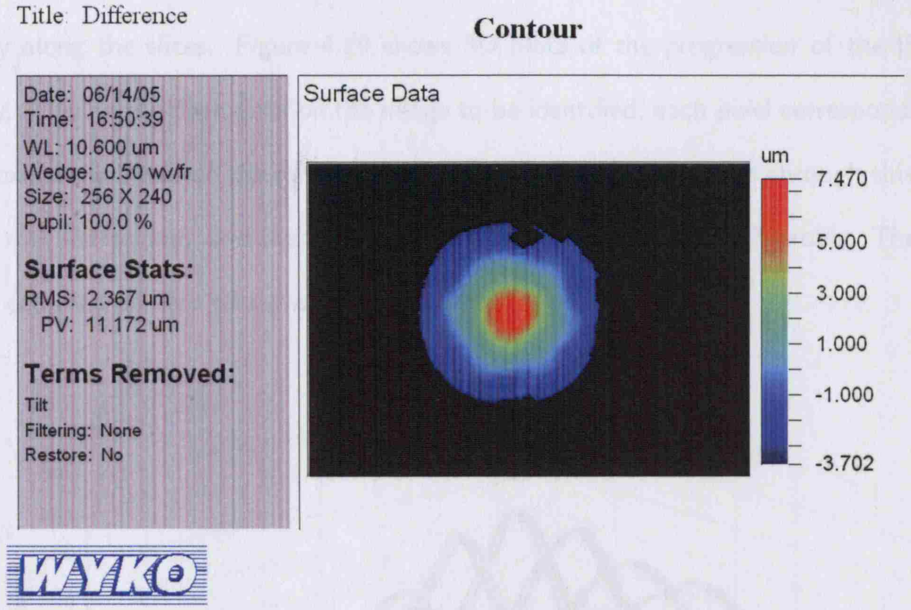

Title: Difference

Date: 06/14/05
Time: 16:50:39
WL: 10.600 um
Wedge: 0.50 wv/fr
Size: 256 X 240
Pupil: 100.0 %

Surface Stats:
RMS: 2.367 um
PV: 11.172 um

Terms Removed:
Tilt
Filtering: None
Restore: No

(b)

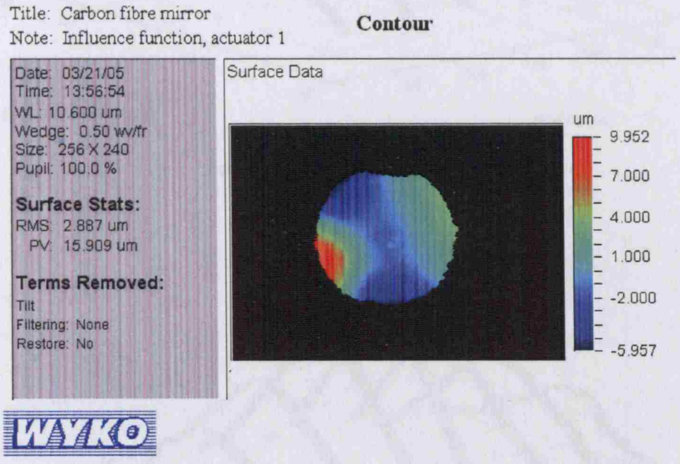

Title: Carbon fibre mirror
Note: Influence function, actuator 1

Date: 03/21/05
Time: 13:56:54
WL: 10.600 um
Wedge: 0.50 wv/fr
Size: 256 X 240
Pupil: 100.0 %

Surface Stats:
RMS: 2.887 um
PV: 15.909 um

Terms Removed:
Tilt
Filtering: None
Restore: No

Figure 4.18: Interferogram of measured (a) central and (b) edge influence functions showing the mirror shape on actuation with a central and edge actuator. A reference surface has been subtracted from these frames.

frames and activated measurements were analysed in detail. A set of 7 slices around the central IF region were taken from both the IF and reference measurement and the data run through the MatLab routine, which creates data files for the 2D profiles in x and y along the slices. Figure 4.19 shows 3D plots of the progression of the IF in x and y, allowing the peak pixel on the image to be identified, each pixel corresponding to approximately 2 mm on the mirror surface. 2D slices were then taken through this peak pixel row and column, and the reference profile subtracted from the IF profile. The data were centered on zero to aid with the data fitting.

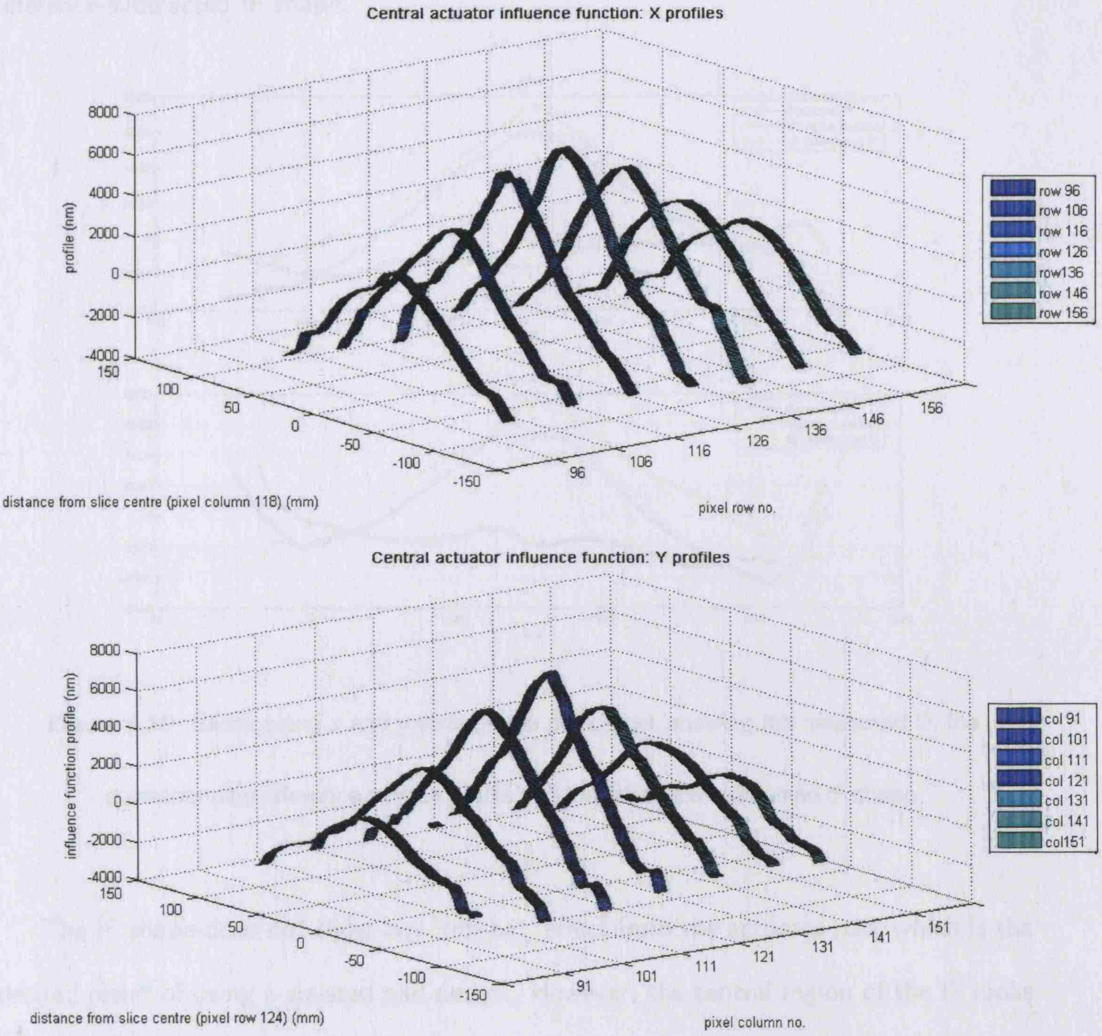
Central actuator influence function: X profiles

Central actuator influence function: Y profiles

Figure 4.19: 3D progression of the IF profiles in the central region of the mirror, (a) in the x direction, and (b) in the y direction, showing the IF profile at different points along the axis.

On inspection one of the reference measurements taken before testing the central actuator showed a displacement with respect to the other 4 frames. Showing a good agreement in shape with the other frames, the outlying measurement appears displaced in the negative x-direction, suggesting a systematic error perhaps resulting from accidental physical movement of the mirror between measurements. This dataset was therefore left out of the average and subsequent analysis, making the reference surface an average of 16 exposures instead of 20. Figure 4.20 shows a plot of the measured IF on the peak pixel in x and y, the corresponding slice through the reference surface, and the reference-subtracted IF shape.

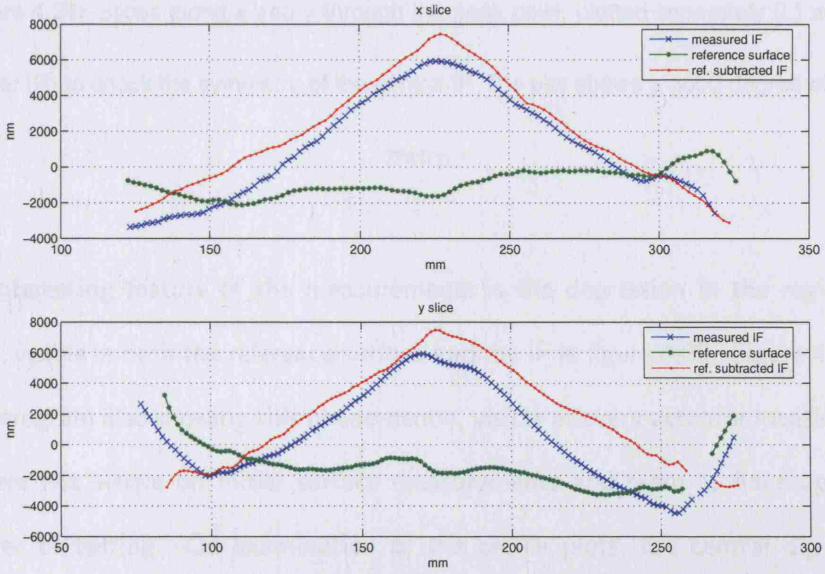

Figure 4.20: Slices along x and y through the peak pixel, showing the measured IF, the corresponding reference surface profile and the reference-subtracted IF shape.

The IF shape does not show any 'top-hat' effect from the actuator pad, which is the desired result of using a waisted pad design. However, the central region of the IF looks more peaked than expected in the presence of a 25 mm pad. When the slices along x and y through the peak pixel are plotted together, they show a good agreement in shape, suggesting that the IF is largely symmetrical (see figure 4.21). The next section will compare these measurements with the FEA results in more detail.

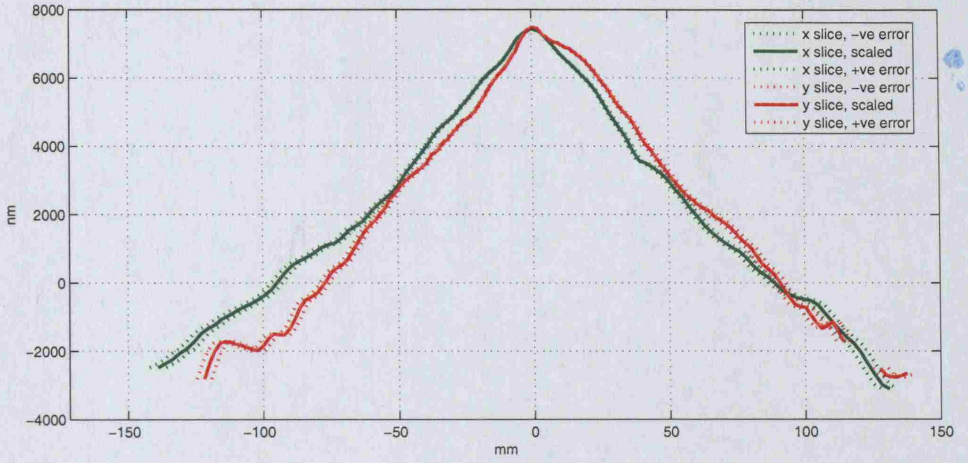

Figure 4.21: Slices along x and y through the peak pixel, plotted separately (L) and together (R) to check the symmetry of the central IF. The plot shows a good degree of symmetry.

An interesting feature of the measurements is the depression in the region of the actuator, visible in both the reference surface and the IF in figure 4.20. Figure 4.22 shows an interferogram also showing this phenomenon, visible at every actuator location. These 'dips' were not visible on initial surface measurements and seem to have appeared in the course of testing. On examination of the profile plots, the central dip measures approximately 25 mm in width, which is the size of the underlying pad.

These 'dips' measure around 1 μm in depth in the reference surfaces, and slightly lower in the measurements with activated actuators. They are thought to be connected to the epoxy used to connect the actuator pads to the CFRP of the faceplate.

One theory is that the epoxy has shrunk over time. Precise figures for the epoxy shrinkage were not available from the manufacturer at the time of purchase, but it is suggested that epoxies can display long-term shrinkage after the initial curing phase. This can cause a small change in local curvature, as observed in the measured surfaces. This effect could potentially introduce errors in an active or adaptive system and warrants

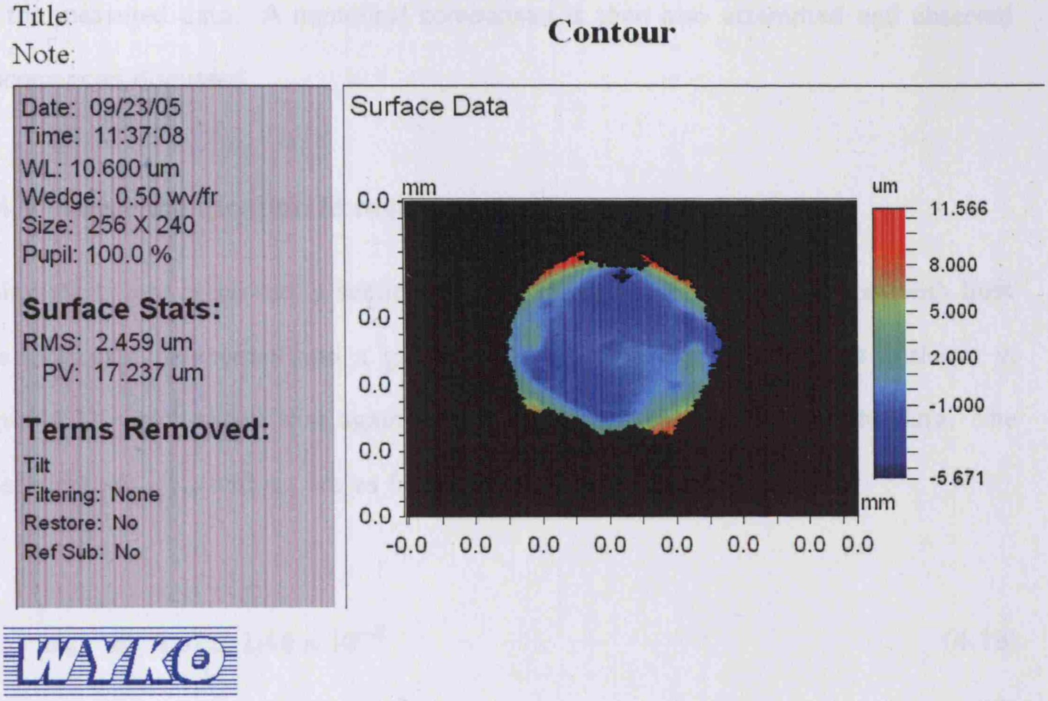

Title:
Note:

Date: 09/23/05
Time: 11:37:08
WL: 10.600 um
Wedge: 0.50 wv/fr
Size: 256 X 240
Pupil: 100.0 %

Surface Stats:
RMS: 2.459 um
PV: 17.237 um

Terms Removed:
Tilt
Filtering: None
Restore: No
Ref Sub: No

Figure 4.22: Mirror interferogram showing marked 'dips' at each actuator location.

further investigations.

Another possibility is that, because of the relative softness of the epoxy compared with aluminium and CFRP, and of the thickness of the epoxy layer used, continuous working of the actuators has caused them to crush the central part of the underlying epoxy layer. On contraction of the actuator, this could give rise to the observed 'dips'.

The measurements and finite element analysis results have yielded two shapes. The next section will discuss how these two sets of data compare, and examine the causes of the discrepancies.

4.4 Comparison of modelling and experimental results

This section will address the second aim of the dynamical testing: to validate the FEA results and assess the usefulness of FEA in the design of deformable optical systems. The first method of comparison is to repeat the least squares fit of the FEA results to the measured data. A numerical comparison is then also attempted and observed discrepancies discussed.

4.4.1 Influence function fit results

Using the theory presented in section 4.2, the measured IF shape was fitted with both the EW cubic polynomial and a gaussian function. A plot of these fits is shown in figure 4.23, which shows that again the cubic fit is the better match to the data. The coefficients a_m, b_m and c_m are as follows:

$$a_m = 8.67 \pm 1.44 \times 10^{-6} \tag{4.18}$$

$$b_m = -1.63 \pm 0.14 \times 10^{-3} \tag{4.19}$$

$$c_m = 6.33 \pm 0.30 \tag{4.20}$$

The 95% prediction bounds on these fit parameters are larger than in the fit of the FEA results, which can be expected, and do not overlap with the FEA fit parameters. They are, however, of the same order of magnitude. The biggest discrepancy lies in the region of the peak. Using $d = 100mm$ and dividing c_m by a_m, β was found to be 0.85 ± 0.15. This is very different to the β value derived from the fit results of the FEA influence function and suggests that the ratio of actuator-to-faceplate stiffness is in fact higher than predicted by the FEA models. The peakiness of the IF shape has also biased the value of the c-parameter upwards. The numerical analysis presented in the next section can examine the differences in more detail.

The cubic fit does not replicate the sharp peak observed in the measured IF. The gaussian fit matches the data better in this region, but breaks down as x approaches 100 mm, the location of the adjacent actuator.

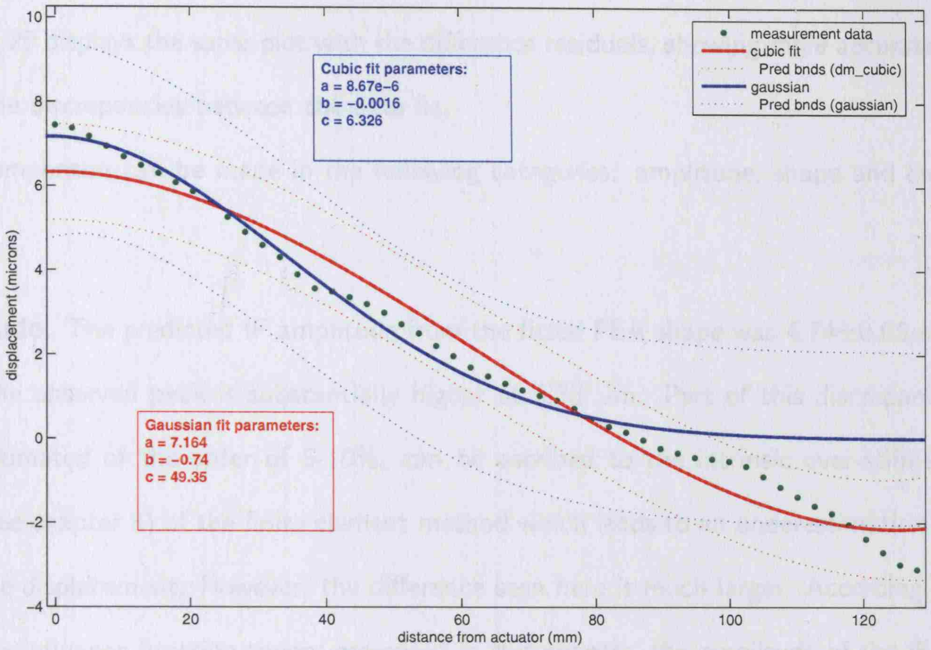

Figure 4.23: Plot of the cubic fit to the measured IF shape. The cubic fit is a better fit to the data, as well as showing narrower 95% confidence bounds. The gaussian function matches the peak region well but diverges from the data points with increasing actuator distance.

4.4.2 Comparison of measurement and FEA data

A direct numerical comparison of the FEA and experimental results required some preparation of the data. First the curve peaks were accurately centred on zero, to compensate for any difference in array size between the sets. In order to calculate the difference between the datasets, the curves were interpolated onto a regular abscissa using the MatLab interpolation function *interp1*. Several algorithms are available with this function, and a test was carried out to identify the most suitable method. The default linear interpolation gave the most accurate replication of the data sequence. The software scaling error discussed in this chapter was also corrected for in this comparison.

Figure 4.24 shows a plot of the centred and scaled slice through the peak pixel in the x direction, together with two FEA profiles, one with flexures and one clamped. Figure 4.25 displays the same plot with the difference residuals, showing more accurately where the discrepancies between the data lie.

A comparison can be made in the following categories: amplitude, shape and coupling.

Amplitude. The predicted IF amplitude from the fitted FEA shape was $4.74 \pm 0.05 \mu m$. The observed peak is substantially higher at 6.33 μm. Part of this discrepancy, estimated of the order of 5-10%, can be ascribed to the intrinsic over-stiffness (see chapter 3) of the finite element method which leads to an underestimation of the displacement. However, the difference seen here is much larger. According to the influence function theory presented in this chapter, the amplitude of the IF is determined by the Young's modulus of the faceplate material. However, the good level of agreement seen in the rest of the profile suggests that there is another cause to this sharpness in the peak. One explanation is that the epoxy, which was found to be relatively soft compared with the CFRP and the aluminium, has yielded in the centre of the pad, allowing it to flex more than predicted. This is an important problem to address, as any sharp peaks in the IFs will give rise to high spatial frequency components in the mirror shape eigenmodes, and compromise its ability to correct for aberrations. The explanation is in keeping with the observed 'dips' that developed in the faceplate over the actuator positions, which were suggested to originate through the same process.

Shape. There is a very good agreement in shape of the profile along the IF flanks. The measured data show a slight inflection not predicted by FEA, which suggests that the actuators (with flexures) are over-stiff relative to the faceplate. This is consistent with the observed variation in value of β based on the fit parameters of modelled and measured data. Because of the approximate method used to simulate the flexures and attachments in the finite element models, some error in the resulting relative actuator-to-faceplate stiffness relation was expected. Refining the finite element models, using a better approximation for the flexure mechanism, should reduce this discrepancy.

Coupling. The displacement of the faceplate at the location of the nearest actuator, at $x = -100$mm and $x = 100$mm, is matched to within 0.5 μm between the datasets. On the negative side, the discrepancy is 276 nm, and on the positive side 268 nm. This again highlights the good level of symmetry seen in the measured IF. The observed discrepancy, again, can most likely be ascribed to the approximate modelling method of the actuator connection pieces. Revisiting and improving this strategy should improve the accuracy of the FEA results.

4.4.3 Conclusion of data comparison

The measured influence function shape of the CFRP active mirror shows a good agreement with the modelling results presented in section 4.2 of this chapter. A scaling error was present in the custom-written MatLab analysis routine and this was corrected on an ad hoc basis in the measurements presented in this section.

The first method of comparison, the polynomial fitting, yielded mixed results. In both cases the cubic polynomial derived by EW and Hardy (1998) provided the best fit results over more traditional approximations such as the Gaussian shape. The value of the fit parameters derived from equation 4.6, whilst being of similar order of magnitude, varied by approximately 35%, in the case of the a parameter, to 75%, in the case of c. The large discrepancy in c can be explained from the peakiness of the IF shape which is thought to be caused by crushing of the adhesive used to attach the actuator pad to the back of the faceplate.

The calculated value of β also varied significantly between the datasets, with $\beta(FEA) = 0.34 \pm 0.02$ and $\beta(measured) = 0.85 \pm 0.15$. Whilst the measured value is biased by the high value of c_m, this suggests a higher actuator-to-faceplate stiffness ratio than in the FEA model.

The cubic polynomial provides a good fit to both the FEA results and the measured data. As this expression provides a convenient way of relating physical parameters, such as the faceplate stiffness, applied force and actuator separation, to the IF shape, it could potentially be used in active and adaptive optics models, which are important in the design of real deformable systems. This warrants further FEA work to optimize the modelling method, and to gain an understanding of how this theory can be used with real systems.

The second comparison method, where the profiles were compared numerically, was especially important in addressing the second aim of this chapter: to investigate the usefulness of FEA in modelling of deformable systems. The measured central actuator IF profile matches the modelling results very well with the exception of the region of the IF peak. In future experiments more care should be taken with selection and use of any adhesives, as this experiment has shown that they can have a significant effect on an active mirror's performance.

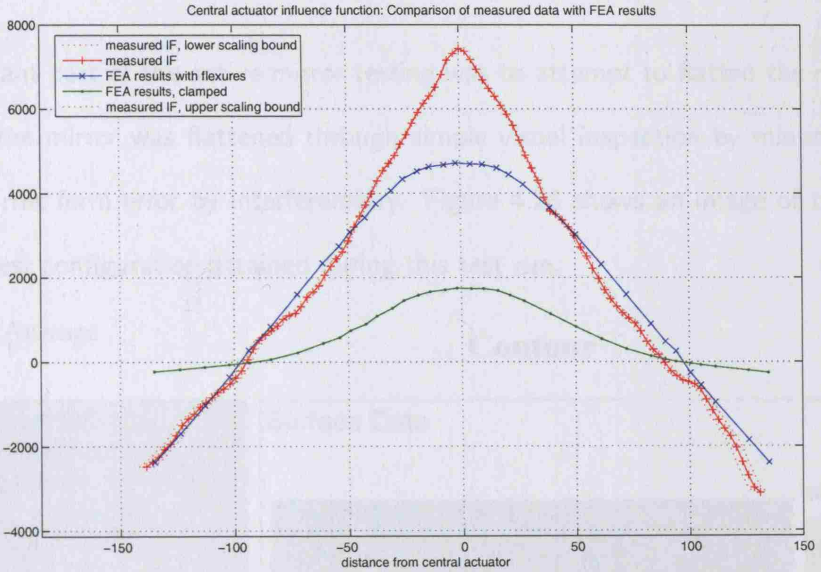

Figure 4.24: Comparison of measured and modelled influence function shapes. The model profile with flexures matches the experimental data to a good degree along the flanks of the profile; the central region of the experimental results is much more peaked than the modelled data.

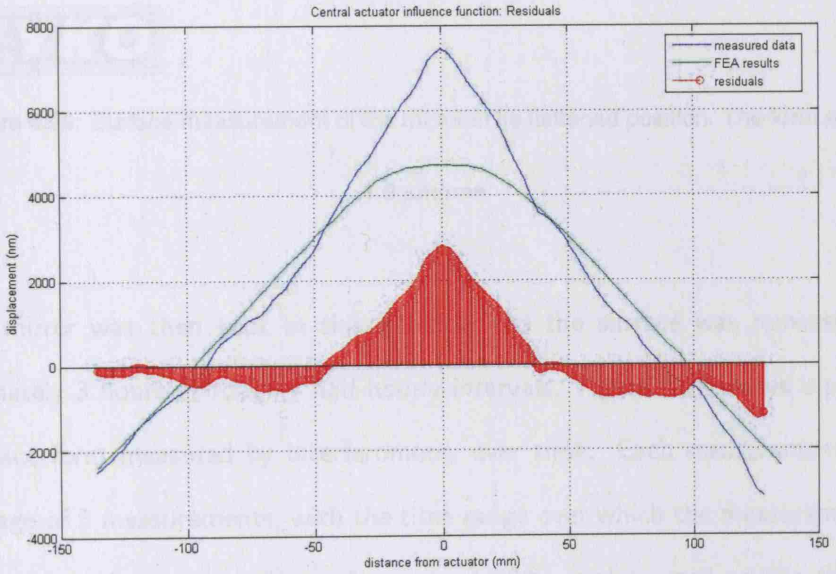

Figure 4.25: Comparison of the measured and FEA IF data with residuals.

4.5 Mirror flattening

An important part of the active mirror testing was to attempt to flatten the mirror. In this case the mirror was flattened through simple visual inspection by minimizing the measured rms form error by interferometry. Figure 4.26 shows an image of the mirror in its flattest configuration attained during this test run.

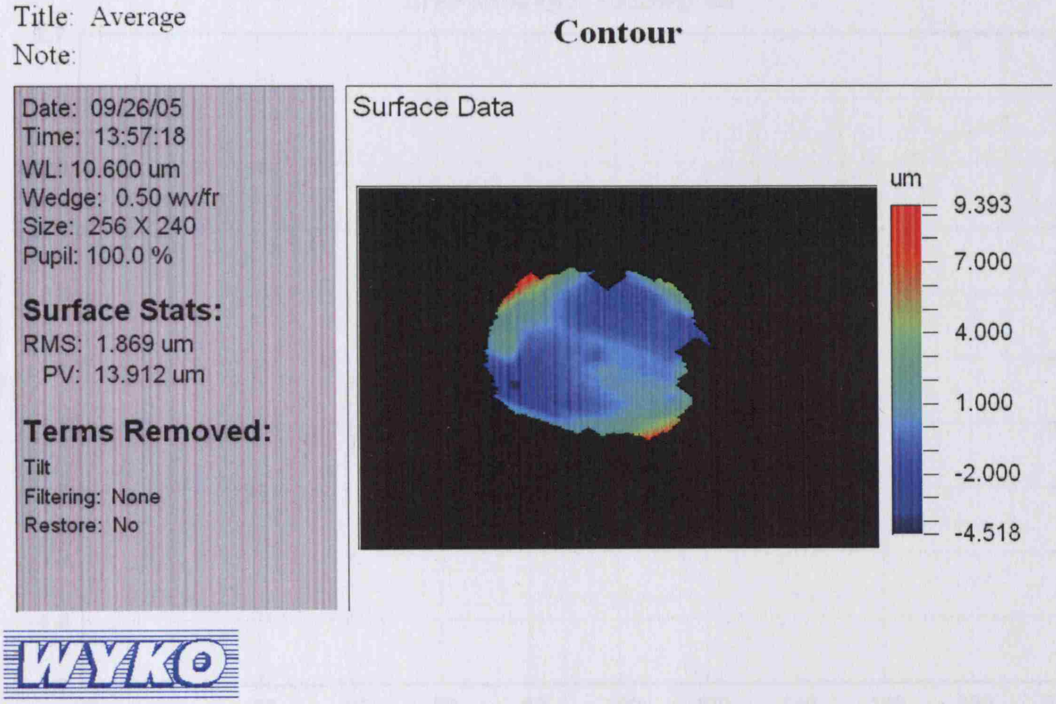

Title: Average
Note:

Contour

Date: 09/26/05
Time: 13:57:18
WL: 10.600 um
Wedge: 0.50 wv/fr
Size: 256 X 240
Pupil: 100.0 %

Surface Stats:
RMS: 1.869 um
PV: 13.912 um

Terms Removed:
Tilt
Filtering: None
Restore: No

Surface Data

Figure 4.26: Surface measurement of the mirror in its flattened position. The form error is 1.9 μm rms.

The mirror was then kept in this position and the surface was remeasured over approximately 3 hours at roughly half-hourly intervals. Figure 4.27 shows a plot of the rms surface form measured by interferometry over time. Each measurement result is the average of 5 measurements, with the time range over which the measurements were taken providing the errorbars in x. An error of 10% was assumed on the rms values. This shows that the surface form deteriorated over the monitored period; the magnitude of the deterioration is of the order of 1 μm rms. This excursion is most likely caused by instability of the electronics or the actuators themselves. In an adaptive optics system where closed-loop operation is required this would not pose a problem, as corrections are carried out on sub-second timescales. In active systems, however, especially in a space environment, a closed-loop feedback system would be essential for the stability of the system.

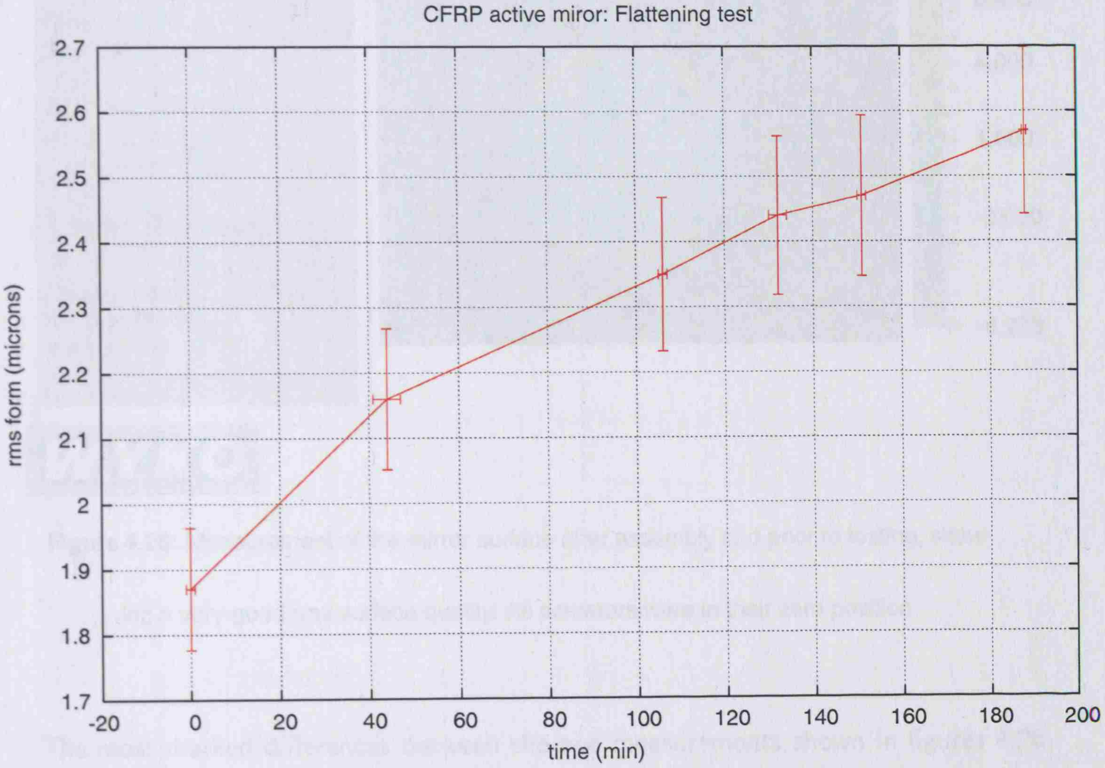

Figure 4.27: Progression of rms surface form over time after flattening, measured with the IR interferometer.

The mirror flattening exercise gave additional information on the long-term evolution of the mirror's surface form. Whilst a good degree of flatness was achieved, as reported above, the surface form has significantly deteriorated over the course of the months during which the mirror was tested; this is thought to be mainly due to the appearance of the dip features over the actuator positions. To illustrate this, figure 4.28 shows a surface measurement taken after the mirror assembly and before any intensive testing was commenced. The mirror was switched on but a zero signal was written out to all actuators. The rms surface error is lower in this measurement than that in which the mirror was actively flattened.

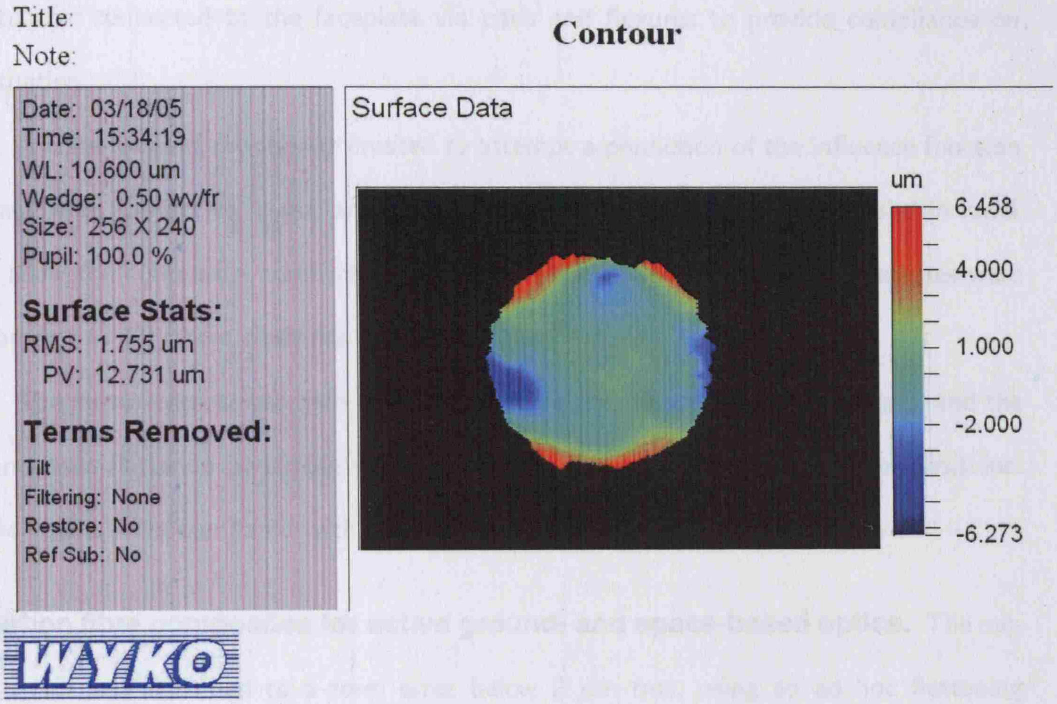
Title:
Note:

Contour

Date: 03/18/05
Time: 15:34:19
WL: 10.600 um
Wedge: 0.50 wv/fr
Size: 256 X 240
Pupil: 100.0 %

Surface Stats:
RMS: 1.755 um
PV: 12.731 um

Terms Removed:
Tilt
Filtering: None
Restore: No
Ref Sub: No

Figure 4.28: Measurement of the mirror surface after assembly and prior to testing, showing a very good rms surface quality. All actuators were in their zero position.

The most marked differences between the two measurements shown in figures 4.26 and 4.28 are the 'dips' that have appeared at the actuator locations.

4.6 Conclusions

This chapter has described in detail the experimental setup for testing the active CFRP mirror and dynamical test results. In addition, influence function theory was presented, and two analytical shapes were fitted to both finite element results and measured data to investigate their validity to real systems.

Carbon fibre reinforced polymers as used for the active mirror have advantages over traditional deformable mirror materials, such as ceramics and metals, especially in their robustness and thermal stability. After grinding and polishing with good results (see chapter 3), the mirror was assembled with a backing structure, seven magnetostrictive actuators connected to the faceplate via pads and flexures to provide compliance on actuation.

A finite element model was created to attempt a prediction of the influence function shape from the active mirror architecture. An approximate method was used in order to allow the composite material to be modelled using 3D elements. The flexures were modelled as 1D beam elements.

The mirror system was then extensively tested for influence function shapes, and the mirror was flattened by simple visual inspection and adjustment of actuator positions. The results were compared with the FEA results.

Carbon fibre composites for active ground- and space-based optics. The mirror was flattened to a form error below 2 μm rms, using an ad hoc flattening method. The actuator positions were adjusted visually to obtain the best surface form. On actuation, the actuator influence functions display a good shape. The faceplate has proved to be light and and robust. One of the main concerns was the issue of long-term stability, and the faceplate did indeed show marked deterioration over the months in which the mirror was dynamically tested: 'dips' of the order of 1 μm in depth appeared over the actuator locations, and the rms surface error was seen to increase over time. However, these effects can most likely be ascribed to problems with the adhesive used to attach the actuator pads to the faceplate, which was crushed by repeated actuator movements. The mirror's excursion over shorter timescales (hours) from its flattened state are a thought to be a manifestation of instability of the electronics rather than any problems with the composite substrate. In a closed-loop system these errors can be corrected.

Analytical influence function expressions. Using influence theory described in the literature, the modelled and measured influence function shapes were fitted with two analytical expressions, a gaussian and a cubic polynomial derived by EW, using the MatLab Curve Fitting toolbox to investigate their validity. Two functions especially were tested: the cubic polynomial described by EW, and a straightforward Gaussian, which is most commonly used in predictions and optical simulations. These tests consistently showed the EW cubic to give the most accurate fit, including beyond the location of the adjacent actuator. However, the resulting fit parameters differed significantly between the measured and modelled data, and the FEA model setup, which in this case used some broad approximations (in particular the unconventional use of a 3D tetrahedral mesh for modelling composites), should be investigated in more detail in order to obtain a better matching shape. However, this is a promising result, as this polynomial relates directly to the system's physical parameters. If further research finds it to match observed IFs to a better degree than gaussian shapes consistently, its use could greatly improve the performance prediction and simulations of active and adaptive systems.

Finite element analysis in active and adaptive optical design. FEA is a valuable tool in the design of structures and instruments for astronomy and beyond. This usefulness could be greatly enhanced if FEA could also be used in optical design of systems using deformable optics. The results presented in this chapter show a good match between modelled and tested IF shape profiles. The main observed discrepancy, in the peak region, is thought to be caused by the use of an unsuitable adhesive to connect the actuator pads to the faceplate - a problem which manifested itself in several ways throughout the testing procedure. Several approximations were used in the FEA method, and these should be investigated further to validate the results. Further research should also focus on a more seamless integration between the FEA process and further design or modelling processes.

In conclusion, the results from the dynamical testing have yielded very interesting and promising results on the use of CFRP materials for deformable optics. Though the work has led to further questions to be addressed in the future, such as long-term stability issues in a changing environment, no fundamental reasons have been identified why this technology is not a viable alternative for the currently used strategies.

Investigating the role of FEA in modelling methods of active and adaptive systems, the results suggest that both numerical techniques such as FEA and finite element-based analytical methods can be used in the optical design and simulation process. This is an area where current methods can be greatly improved in terms of simplicity and speed, and the work presented here makes a strong case for further investigations.

In the following chapter, one particular development is examined in more detail. Designs for the next generation of ground-based observatories, the Extremely Large Telescope, are currently being developed worldwide. Novel technologies for many aspects of these observatories, from the primary mirror segments to the observational procedures and data pipelining, are hugely important in bringing these projects to a successful conclusion. Active and adaptive optics are at the forefront of the preparatory research surrounding ELTs, and much of the work presented here is highly relevant in this context.

CHAPTER 5

Lightweight deformable optics for extremely large telescopes

"Nothing shocks me. I'm a scientist."

– Harrison Ford, as Indiana Jones

Designs for the next generation of ground-based optical/IR observatories are currently under way. These telescopes, with primary mirror diameters of 30 to 100 m, are generally referred to as Extremely Large Telescopes or ELTs. Scaling telescope sizes up three- to tenfold presents enormous challenges in design, manufacture and operation.

It is widely acknowledged (Andersen *et al.*, 2003; Gilmozzi *et al.*, 1998) that fully integrated active and adaptive optics are essential for an optimum scientific return from these projects. With adaptive optics currently reaching maturity on the present generation of 10 m-class telescopes, much work is required to develop strategies for integration into the telescope's operation, user-friendliness, increased sky coverage and optimal corrected field of view.

The carbon fibre composite technology demonstrated in this thesis has possible application in these projects as a candidate solution for the large adaptive optical elements these telescopes require. This is an important and exciting driver for further research. Section 5.1 contains a summary the science case for ELTs. Section 5.2 will then discuss three major ELT projects and their respective proposed optical designs and potential risk areas. None of these projects have yet secured full funding at the time of writing and collaborations are being put together.

Section 5.3 will illustrate how the carbon fibre composite mirror technology could potentially provide a solution to problems with the adaptive optics system operation. The work into an adaptive secondary mirror for a Very Large Telescope forms an important precursor to the ELT designs, and problems will be highlighted and discussed.

5.1 Science with 30-100 m telescopes

This section will give an overview of the scientific advances made possible by ELTs with 30 to 100 m sized apertures. Following the model outlined by Hook and Gilmore (2005), the science case can be broken down into three categories:

1. Detection of exoplanets and study of circumstellar environments;
2. Stellar populations studies and galaxy formation and evolution;
3. Studies of the high-redshift environments.

Whilst an in-depth description of the science drivers for ELTs is beyond the remit of this thesis, a 'highlight' will be described here for each category. These drivers dictate aspects of the ELTs' design and instrumentation packages, especially with regards to the adaptive optics requirements. A final subsection summarizes the results of the extensive European ELT Science Case study with regards to the necessary aperture for aspects of the key science drivers. These results must be carefully weighed up against the technological considerations.

5.1.1 Direct detection of terrestrial exoplanets

At the time of writing some 170 planets have been detected in extrasolar systems (Schneider, 2006). Only one of these has thought to have been successfully imaged by a ground-based observatory using the VLT NACO[1] instrument (Chauvin *et al.*, 2005). The possibility of increasing the catalogue of known exoplanets, and in particular the capability to obtain direct images of Earth-like planets, is one of the most exciting prospects for an ELT.

The difficulty of this task is two-fold: firstly, the close separation of the planet and its host star at large distances from Earth is of the order of milli-arcseconds; and secondly, the brightness of the star makes the reflected light from the planet very challenging to detect. To optimize the possibility of achieving this goal, detailed simulations must be carried out to predict the performance of telescope designs and AO architectures, and to identify the requirements for instrumentation.

Lardiere *et al.* (2004) simulated the photon-noise limited performance of an ELT for exoplanet imaging, taking into account AO parameters such as observation wavelength, phase lag error (see section 2.3), actuator pitch and atmosphere characteristics at 2 sites. Figure 5.1 shows the observable planet-star flux ratio at a signal to noise ratio of 3 over a 10 hour exposure with a variety of aperture sizes in the NIR J-band. A simple coronagraph was also included in the simulations. The actuator pitch is constant at 0.1 m, which the authors identify as the optimal actuator pitch for planet searching from 10 pc for any telescope diameter. The required actuator spacing is an important factor in the AO system design as it dictates a minimum required size for the AO corrector. The star magnitude in the figure is $m_v = 5$, corresponding to a Sun-like star at a distance of 10 pc. The atmospheric statistics are modelled on those of Mauna Kea.

Figure 5.1 illustrates the extreme imaging contrast ($10^6 - 10^{10}$ at optical wavelengths)

---

[1] NACO consists of the Nasmyth Adaptive Optics System (NAOS) and the Near-Infrared imager and spectrograph CONICA

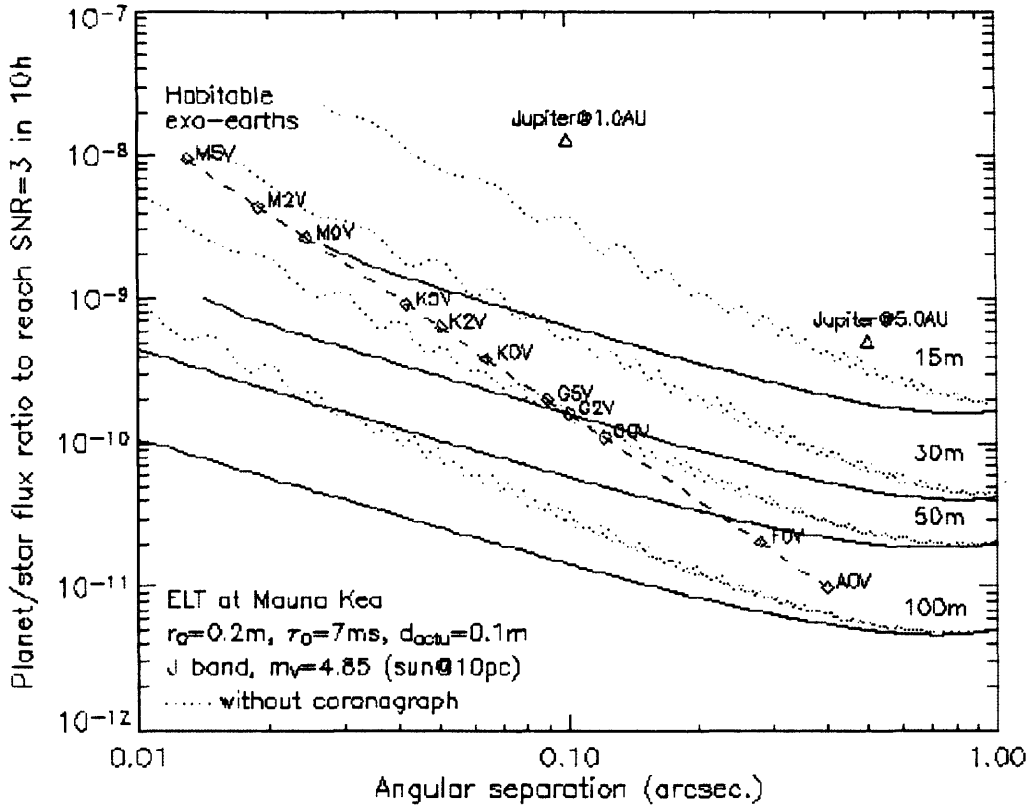

Figure 5.1: Observable planet-star flux ratio at a signal to noise ratio of 3 in a 10 hour exposure in the NIR J-band, as a function of planet-star angular separation. Data are shown for telescope diameters of 15, 30, 50 and 100 m, with and without a coronagraph (Lardiere *et al.*, 2004).

required to detect terrestrial exoplanets. The authors also highlight the importance of site selection for optimal seeing conditions. Further studies (Chelli, 2005; Cavarroc *et al.*, 2005) have identified other important sources of error, such as speckle noise arising from active optical corrections at the primary mirror and static phase aberrations of the instrument. The detectability of exo-Earths was shown to be dependent on the ability to measure or correct segment piston errors to an accuracy of below 1 nm.

5.1.2 Resolved stellar populations in a representative section of the Universe

The chemical composition and evolution of stars in galaxies outside our own is an important source of knowledge on the history of star formation. Because of the distances involved our information on extragalactic stars is however limited; several key questions remain unanswered (Hook and Gilmore, 2005) with regards to stellar evolution, chemical abundances, age distributions and the behaviour of stellar winds in lower-metallicity environments. Characterization of these processes can contribute significantly our understanding of stellar evolution and ultimately the reionization of the Universe.

Properties of extragalactic stellar populations can be derived from spectroscopy and photometry of resolved stars or, where resolution is insufficiently high, from studies of the integrated light from stars within extragalactic clusters. The study of young hot stars is of particular interest because of the significant mass-loss they display throughout their lifetimes, and their ultimate end as core-collapse supernovae, which are important contributors to the chemical enrichment of, and injection of kinetic energy into, the interstellar medium.

Large-scale spectroscopic studies of such young extragalactic stellar populations are currently in progress for the Magellanic Clouds, such as reported in Evans *et al.* (2005), which will add significantly to the body of knowledge surrounding these issues. Figure 5.2 shows the target field in one of the LMC star clusters observed in this study (N11), illustrating the issue of field crowding and the value of multi-object instruments. A recent publication by Crowther (2006) showed a distinct metallicity dependence of the stellar winds from Wolf-Rayet stars, with WR stars in low-metallicity environments displaying lower wind velocities. As high-redshift galaxies are generally metal-poor, this impacts on galactic and cosmological studies of high-redshift galaxies, supernovae and gamma ray bursts.

The alternative method of studying the integrated light of extragalactic stars in

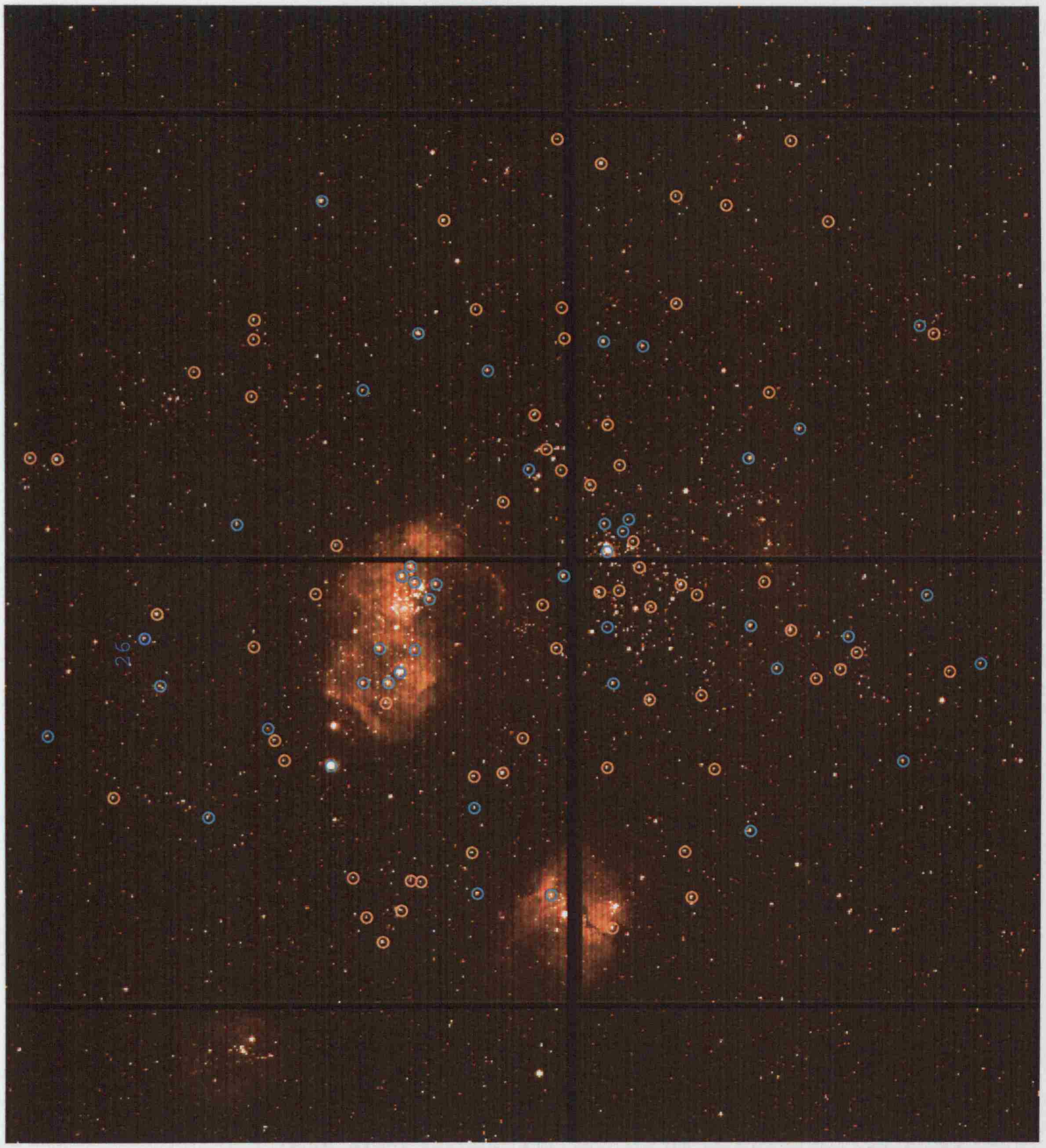

Figure 5.2: V-band image of targets observed by Evans *et al.* (2005) in young star cluster N11 in the LMC for a recent VLT survey of massive galactic and extragalactic stars. The blue and yellow circles indicate O and B-type stars respectively. V-band target magnitudes were of the order of 12-15.5; the image illustrates the challenges of resolving extragalactic stellar populations.

clusters is well illustrated in a recent publication by Bastian *et al.* (2005). The authors use HST broad and narrow band images in conjunction with millimetre observations to derive sizes, intensity profiles, age, mass and star formation history of complexes of young star clusters in spiral galaxy M51. From these results they draw conclusions on the formation of such complexes from their progenitor Giant Molecular Clouds, their evolution and overall star formation efficiency.

For studies of lower mass, older stars, which are equally important in characterizing extragalactic star formation histories, only the latter method is available as current observational facilities do not offer the resolution and sensitivity to resolve these fainter objects.

The nearby Magellanic Clouds and M31 are at the limit of sensitivity and resolution of the current host of ground-based instruments. A larger sample of galaxies, and higher z galaxies, are needed to obtain data on a representative section of the Universe. The Virgo cluster, the distance to whose centre is estimated at 16 MPC, lies approximately 13 times further away than the most distant Local Group members, is currently beyond the reach of ground-based telescopes, but forms an attractive and realistic target for a 30-100 m ELT.

An important factor is the need for near diffraction-limited performance at optical wavelengths; the higher resolution of the diffraction limit in the optical is needed to resolve the crowded fields, which are largely confusion-limited rather than photon- or sky background-limited. With JWST optimized for the mid-IR, an ELT is the only facility able to carry out these observations.

5.1.3 The first galaxies and the ionization state of the early Universe

The formation of the first stars and galaxies, as well as their impact on the surrounding intergalactic medium (IGM) is an important problem in astrophysics and cosmology. The first light from these stars and galaxies ended the 'dark ages' of the Universe and caused the ionization of the IGM. Barkana and Loeb (2001) give a detailed overview of the current state of knowledge on this era. Figure 5.3 shows a schematic diagram of the history of the Universe showing the reionization epoch.

The first stars, formed from the zero-metallicity primordial gas with masses upwards of 100 $M_{\odot}$, are known as Population III stars. Because of their low metallicities, such stars have very short lifetimes before undergoing a thermonuclear explosion or supernova. Population III supernovae are thought to be important contributors to enrichment and ionization of the early Universe (Hook and Gilmore, 2005).

Calculations imply that the Universe was ionized at $z \sim 7-12$, and has remained ionized ever since. The current 8-10 m class of observational facilities have enabled substantial progress in the understanding of the nature of star-forming galaxies at $z \sim 5-6$, but limited information is available at higher redshifts.

To probe to redshifts of 10 and beyond, more sensitive optical/NIR observations are needed with ELTs. Telescopes with apertures of 60-100 m will be able to survey and study spectroscopically the earliest galaxies, their luminosities, mass functions, star formation histories, metallicities, sizes, morphologies, clustering and dynamics, as well as their effect on the surrounding IGM. These sources have an estimated magnitude of approximately 27.5, which lies within the remit of an ELT (Hook and Gilmore, 2005). Blain *et al.* (1999) compiled a plot of star formation rate history as a function of redshift, as inferred from ultraviolet/optical/IR/sub-millimetre observations, which is shown in figure 5.4.

Of interest also are the galaxies and active galactic nuclei (AGN) at the end of the reionization era, at redshifts of 5-6. A 30-100 m telescope could obtain a spatially resolved spectrum at $z = 5-6$, which would yield information on the dynamics and total mass of their stellar populations, and enable the detection of HII regions in these galaxies. With a large enough field of view ($>$ 5 arcmin) and a moderate level of adaptive optical correction, non-contiguous over the field using integral field units (IFUs), it

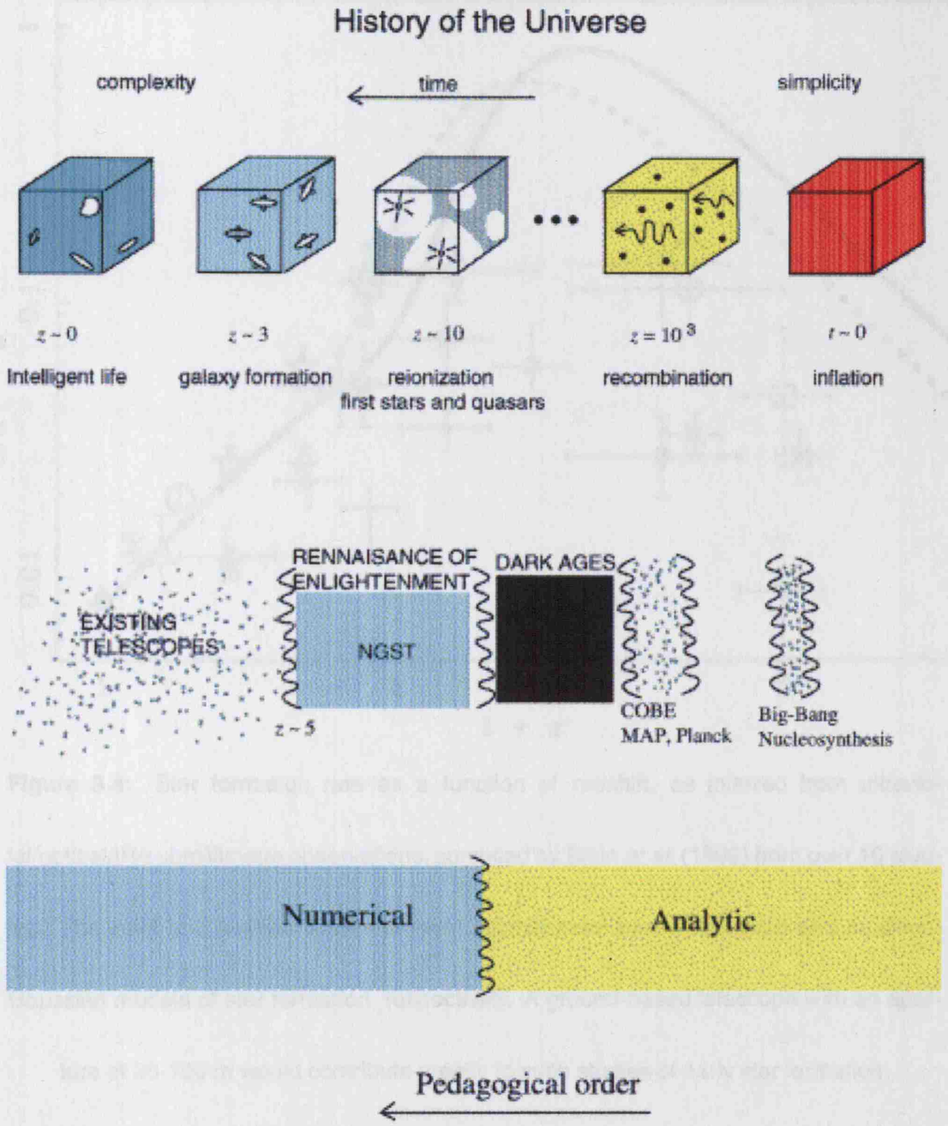

Figure 5.3: Milestones in the evolution of the Universe. The end of the 'dark ages' bridges the recombination era, studied with microwave anisotropy experiments, and the current horizon of observations at $z \sim 5-6$ (Barkana and Loeb, 2001). The figure shows the epochs that are currently reliant on analytical models, as opposed to direct observational data. The era labelled 'Renaissance of enlightenment' is largely that of interest to the new generation of ground-based observatories.

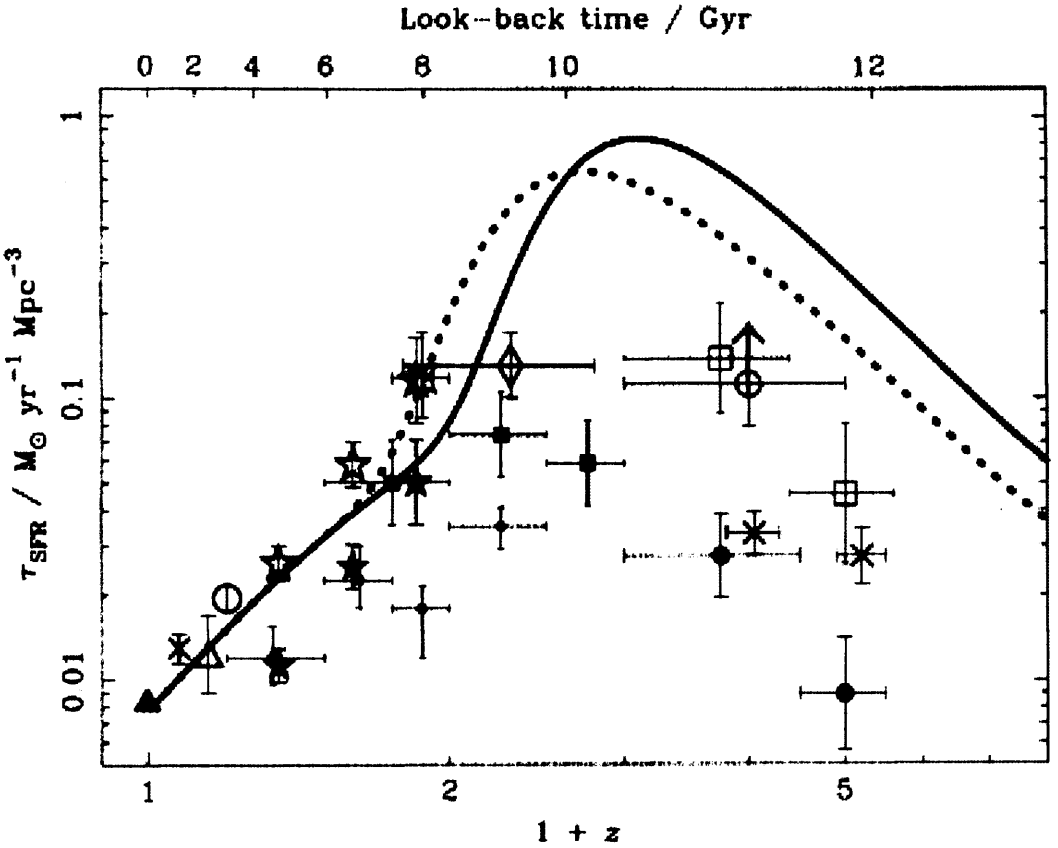

Figure 5.4: Star formation rate as a function of redshift, as inferred from ultraviolet/optical/IR/submillimetre observations, compiled by Blain *et al.* (1999) from over 10 studies. The solid and dashed lines represent submillimetre-based Gaussian and modified-Gaussian models of star formation, respectively. A ground-based telescope with an aperture of 30-100 m would contribute greatly to such studies of early star formation.

would be possible to obtain simultaneous observations of several tens of these sources at once (Hook and Gilmore, 2005). This method is termed multi-object adaptive optics (MOAO); the non-contiguity of the corrected field sets it apart from the more commonly discussed multi-conjugate adaptive optics (MCAO).

The fine diffraction limit of a 60-100 m telescope will enable the detection of the first bright objects of the early reionization epoch: gamma ray bursts (GRB), Population III supernovae and ultra high-redshift quasars. Whilst these objects are all the targets for dedicated space missions in the next decade, most notably the JWST and SPICA missions (Lilly, 2000; Nakagawa *et al.*, 2004) set for launch in 2012 and 2010 respectively, an ELT will deliver superior results shortward of 3 μm because of the more flexible instrumentation opportunities.

5.1.4 Summary of key science goals as a function of aperture

Table 5.1 summarize results of the extensive European ELT Science Case study carried out between 2001 and 2005 (Hook and Gilmore, 2005). Aspects of the key science drivers are listed as a function of the ELT primary aperture.

Aperture	**Planets and stars**	**Stars and Galaxies**	**Galaxies and Cosmology**
20 m	▪ Direct detection of Jovian-mass planets in wide orbits around nearby solar-type stars ▪ Radial velocity search on fainter stars, increasing available volume by a factor of 200	▪ Resolve oldest stellar populations in Magellanic Clouds and Local Group dwarf spheroidals ▪ Resolution of the brightest giant stars in galaxies in the Virgo cluster ▪ Observations of halo giants in LG galaxies (hi-resolution spectroscopy)	▪ Ly a emission line spectroscopy from $6 < z < 10$ ▪ Possible detection of $z\sim10$ objects
30 m	▪ Imaging of young (< 10 Myr) Jovian planets around stars in star-forming regions out to 75 pc ▪ Detection and classification of mature Jovian planets to 10-20 pc. ▪ Possible detection of one Earth-like planet within ~5 pc	▪ Age/metallicity measurement of resolved populations in M31/M32 at ~750 kpc (imaging) ▪Determination of star formation and chemical enrichment histories of galaxies to the nearest active galaxy	▪ Possible detection of $z\sim10$ objects (depending on their nature) ▪ Spectroscopy of the earliest galaxies found by JWST ▪ IGM studies to $z\sim10$ using brightest GRBs as background sources
100 m	▪ Survey of 1000 solar-like stars and direct detection of Earths within 30 pc ▪ Time-resolved photometry of Earth-like planets ▪ Spectroscopy of Earth-like planets and search for 'bio-markers'. ▪ Study of exoplanetary systems	▪ Age/metallicity measurements of resolved populations in M87 (16 Mpc) ▪ Detailed study of galaxy formation in a representative sample of the Universe	▪ Detection of $z > 10$ objects ▪ Spectroscopy of galactic objects to $z\sim20$, possibly resolved ▪ IGM studies at $z > 10$ (GRBs, Pop III supernovae and QSOs as background)

Table 5.1: Summary of key science drivers for ELTs as a function of aperture size (Hook and Gilmore, 2005).

5.2 Overview of ELT projects

This section will give an overview of three major ELT projects currently under way worldwide, in order of increasing aperture size. Optical designs are presented together with proposed adaptive optics architectures.

The optical design problem requires a trade-off of scientific, instrumental and budgetary requirements within a given technological framework. In his study of optical designs for ELTs, Goncharov (2003) finds that diffraction limited imaging over a 1-2' field with fast spherical designs requires complex relay optics, which make the integration of an advanced AO system very demanding, especially in the case of multiple DMs, where each mirror is conjugated to a different height in the atmosphere. Spherical primary mirrors also require larger secondary mirrors to achieve the same performance. Conversely, segment manufacture for aspherical primary mirrors is more demanding and costly.

The optical design of ELTs also affects the chosen adaptive optical system architecture. The science goals for these telecopes have generated a new vocabulary of AO modalities, each requiring extended functionality beyond the experience with current systems (Dekany *et al.*, 2004):

- multi-object adaptive optics (MOAO)
- multi-conjugate adaptive optics (MCAO)
- ground-layer adaptive optics (GLAO)
- extreme contrast adaptive optics (ExAO, XAO)

The integration of these AO modalities into the telescope's operation will prove an important challenge in addition to the problems posed by the development of the aberration control system itself.

5.2.1 Thirty Meter Telescope

The US-led Thirty Meter Project, or TMT, is a collaboration of the Associated Universities for Research in Astronomy (AURA), the Association of Canadian Universities for Research in Astronomy (ACURA), the University of Victoria, the University of California and the California Institute of Technology (Caltech). It features a primary mirror of 30 m in diameter, with a preliminary design review planned in 2007 and first light in 2014. The TMT project is the furthest advanced of all ELTs and forms the synthesis of three early projects, the California Extremely Large Telescope (CELT), the Giant Segmented Mirror Telescope (GSMT) and the Canadian Large Optical Telescope.

Scientific opportunities led to the formulation of the following design requirements (Nelson, 2003):

- Aperture: filled, fully steerable, 30 m diameter
- Field of view: 20 arcmin with 0.5 arcsec seeing (seeing-limited)
- Adaptive optics: low order AO and multi-conjugate AO, rms wavefront error down to 75 nm rms
- Zenith angle for observation: 0° to 65°
- Observing wavelength range: 300 nm to 30 μm
- Instrument support: two 15 x 30 m Nasmyth platforms

Ellerbroek *et al.* (2005) give an overview of the chosen optical design and proposed AO architecture. Figure 5.5 illustrates the proposed configuration. The aplanatic gregorian design features a 30 m f/1 parabolic primary mirror consisting of 738 hexagonal segments, each measuring approximately 1.2 m across. The concave ellipsoid secondary mirror, measuring 3.6 m across, generates an f/15 output focal ration which is optimized for a 20 arcmin field. A flat tertiary mirror directs the beam to either of 2 Nasmyth platforms.

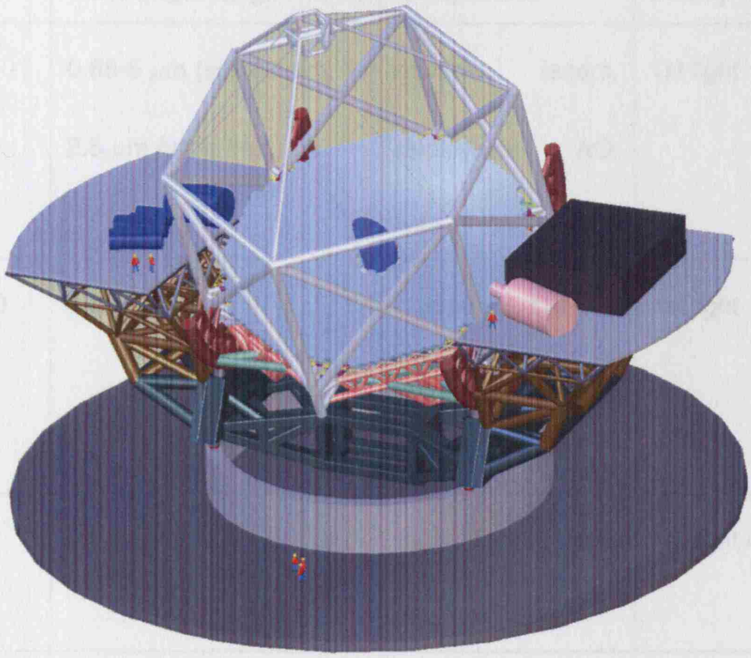

Figure 5.5: Optical design for the 30 m TMT project (Ellerbroek *et al.*, 2005).

An extensive overview of the AO requirements for the TMT design together with a detailed assessment of a number of 'risk areas' are presented by Dekany *et al.* (2004). Table 5.2 shows the envisioned AO modes with their respective components and priorities.

Important risk areas for the implementation of these AO architecture include high-stroke high-order deformable mirrors (including cryogenic); large (2-3 m) adaptive secondaries capable of chopping for mid-IR observations; and computing power and algorithms capable of fast matrix inversions for high order AO control.

An elaborate site testing campaign has been under way for several years (Stepp and Strom, 2004). Activities have included compiling data on site topography, demographic issues, land ownership, environmental regulations, seismic hazards and light pollution; remote sensing studies of cloud cover and precipitable water vapor above candidate sites;

AO mode	Wavelength range	Components	Priority
MOAO	0.65-5 μm (small field), 1-2.5 μm (wide field)	multiple lasers, deployable AO, MEMS DM, IFUs	1st light
Mid-IR AO	7-28 μm	cryogenic DM or ASM, multiple lasers	1st light
GLAO	0.3-1 μm	multi-object spectrograph	1st light optional
ExAO	1-2.5 μm	MEMS DM, coronagraph	unknown
MCAO	0.8-5 μm	multiple lasers, multiple DMs, IFUs	2nd light

Table 5.2: The five AO observing modes proposed for the 30 m TMT together with their priorities (Dekany *et al.*, 2004).

installation of weather stations. A decision with regards to the TMT site is expected in 2006-2007.

5.2.2 Euro50

The Euro50 project is a multi-national European collaboration, led by the University of Lund, of the United Kingdom, Finland, Ireland, Spain and Sweden. An extensive design study was published in 2003 outlining the science case and proposed optical design (Andersen *et al.*, 2003). The Euro50 telescope features a 50 m aspheric segmented

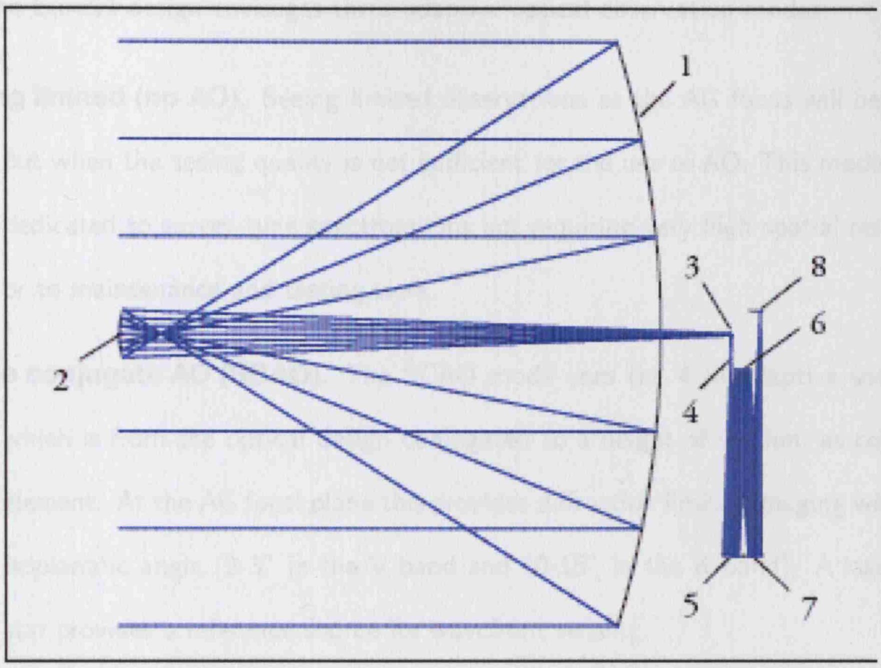

Figure 5.6: Optical design of the Euro50 (Goncharov, 2003): 1 - elliptical segmented primary, 2 - elliptical deformable secondary, 3 - beam splitter, 4 - intermediate focus (AG focus), 5 - collimating mirror, 6 - flat deformable mirror, 7 - focusing mirror, 8 - final focus.

primary mirror in an aplanatic Gregorian design (see figure 5.6). A major advantage of the aplanatic Gregorian design over other aspherical designs, such as the Ritchey-Chrétien favoured for the TMT, is the concavity of the secondary mirror, which facilitates manufacturing and metrology. Should the project secure funding, first light is foreseen for 2014.

An important part of the design is the inclusion from first light of a large adaptive secondary mirror (ASM) to provide AO correction to the Gregorian and Nasmyth foci. A second DM, flat in design, is conjugated to a height of 8 km. The proposed ASM is hexagonal in shape measuring 4.43 m over the corners. Its form is elliptical. A study carried out for the Euro50 project in 2002 (Walker *et al.*, 2002) identified CFRP as a promising candidate material for this deformable mirror. The use of CFRP material for large adaptive mirrors in ELTs will be discussed in more detail in section 5.3.

The Euro50 design envisages three adaptive optical observation modes:

Seeing limited (no AO). Seeing limited observations at the AG focus will be carried out when the seeing quality is not sufficient for the use of AO. This mode can be dedicated to survey-type spectrographs not requiring very high spatial resolution, or to maintenance and testing work.

Single conjugate AO (SCAO). The SCAO mode uses the 4 m adaptive secondary, which is from the optical design conjugated to a height of 0.6 km, as correcting element. At the AG focal plane this provides diffraction limited imaging within the isoplanatic angle (2-3" in the V band and 10-15" in the K band). A laser guide star provides a reference source for wavefront sensing.

Dual conjugate AO (DCAO). The addition of an extra DM to the SCAO architecture for Euro50 was first suggested by Goncharov *et al.* (2002). The second mirror is conjugated to a height of approximately 10 km. Two laser guide stars provide reference sources.

The critical design issues identified in Andersen *et al.* (2003) include firstly the dynamical control of the correct optical form and and position of the surfaces on a 50 m scale (Riewaldt *et al.*, 2004). Secondly, MCAO and AO with multiple laser guide stars are at present an unproven technology. Finally, experience with the use of large adaptive secondaries is very limited and the use of novel materials, such as CFRP, for such applications unproven.

5.2.3 OverWhelmingly Large Telescope

The third, largest and most ambitious ELT project is the ESO project for a 100 m OverWhelmingly Large Telescope (OWL). A substantial document (European Southern Observatory, 2006) was recently published outlining the body of work dedicated to the design of this telescope; because of the enormous challenges of building and operating a

Baseline specifications of the OWL telescope	
Pupil size	100 m
Collecting area	> 6000 m^2
Multi-conjugate adaptive optics	
Diffraction-limited field of view:	
Visible (0.5 μm)	> 30"
Infrared (2 μm)	> 2'
Strehl ratio (at 0.5 μm):	
Requirement	20%
Goal	30%
Seeing limited field of view	10'
Wavelength range	0.32-12 μm
Max. cost	1000M

Table 5.3: Baseline specifications for the OWL telescope (Dierickx *et al.*, 2004).

100 m telescope, this project faces the longest development timescale of those presented here. The first stage of operation is envisaged to commence in 2016 with an aperture of 60 m, after which the aperture and instrumentation suite will be added to incrementally. Table 5.3 summarizes the overall design characteristics.

The proposed OWL design differs fundamentally from the TMT and Euro50 projects in that it features a spherical primary mirror. The following advantages justify the choice (European Southern Observatory, 2006):

- more suited to mass production and mirror maintenance because of identical segments;

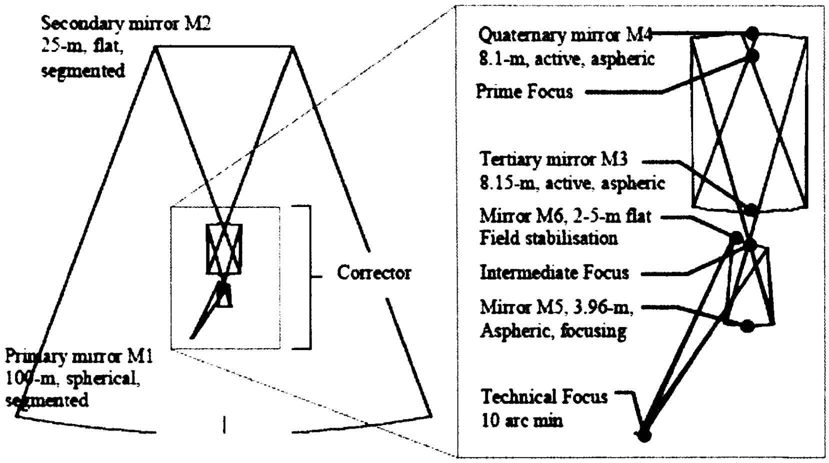

Figure 5.7: OWL 6-mirror baseline optical design (Dierickx *et al.*, 2004).

- enables testing against a unique reference matrix and easier matching of segments;
- requires fewer numbers of spares;
- faster polishing process using full-sized rigid tools;
- no post-polishing cutting to shape required;
- use of full-sized rigid polishing tools more favorable in relation to high spatial frequency errors;
- compatible with lightweight segments technology.

The chosen baseline design is based on a 6-mirror solution (see figure 5.7) with spherical primary (M1), flat secondary (M2) and a four-element corrector. The corrector features two 8 m-class active mirrors (M3, M4), with M4 being conjugated to the entrance pupil. M5 and M6 measure 4 and 2.4 m and are concave aspherical and flat, respectively. The flat M6 mirror can be rotated about the telescope axis in order to feed any of the 6 focal stations. M6 is envisaged to be upgraded to an adaptive mirror following initial commissioning (Dierickx *et al.*, 2004).

The adaptive optics architecture for OWL is designed to grow in stages with the aperture. For the first stage, a visual/NIR AO facility is foreseen designed to operate with natural guide stars, giving a Strehl ratio of 50-60%; the telescope at this time will have an aperture of 60 m. This is essentially an extension of the present systems on 8-10 m class telescopes. This SCAO system will use the M6 adaptive mirror as corrector. Provisional design plans for this large adaptive mirror is discussed in more detail in the next section.

In a second stage, with the primary mirror measuring 80 m, the M5 mirror will be replaced by a 3.5 m adaptive mirror, providing DCAO at IR wavelengths. In the latest stages the addition of a very high order post-focus AO system, most likely featuring a MEMS-based corrector, to provide correction at visible wavelengths (V band). Laser guide stars will be used for wavefront sensing reference to provide adequate sky coverage (Dierickx, 2001; Dierickx *et al.*, 2004).

This section has shown how large adaptive mirrors feature as important parts of at least two, if not all three, of the major ELT projects under way at the present time. They are invariably identified as a risk area because of the limited experience with such optics, especially as all large adaptive systems under construction or in operation use the same design principle. The Euro50 project team, in particular, have highlighted this issue by selecting an alternative based on a thin metal-coated CFRP design. In this context the work presented in this thesis becomes highly relevant.

The next section will examine in more detail the need for large adaptive optics in ELTs and the issues likely to arise with the current thin ceramic shell technology.

5.3 The need for large lightweight deformable optics

The benefits and problems of designing a telescope with a large adaptive corrector in the main optical path were discussed in chapter 2. On the scales of ELTs, for which fully integrated AO has been highlighted as an essential aspect of the design, these mirrors become a very challenging risk area. Whilst the TMT design does not include an adaptive secondary mirror (ASM)[2], both Euro50 and OWL have included one or several such optics from the outset.

The OWL project envisages using the existing ASM technology, as demonstrated on the MMT and LBT observatories, which is felt to be the most promising in the field of marge adaptive mirrors (European Southern Observatory, 2006). The team acknowledge a weight issue with large adaptive mirrors and put forward the idea of lightweighting the support structure by means of material removal. However, they do not consider alternative designs to be acceptably mature for implementation on OWL.

For the large adaptive OWL mirrors (M5 and M6 in figure 5.7), a shell thickness of the order of 1 mm is envisaged. Industrial connections involved in the production of thin glass plates for flat display screens and digital televisions are cited to be capable of producing sub-mm thickness glass shells. A double-sided coating of the shell acts as a capacitive sensor for position feedback, forming a closed servo loop with the actuators operating at a frequency of 80 kHz. It is acknowledged that thin glass shells are currently, and will remain, a high-technology, high-cost and high-risk area, especially for aspheric optics.

The solution suggested in this thesis, of using a CFRP material for the thin shell and its support structure, was first put forward in a study commissioned by the Euro50 project (Walker *et al.*, 2002). For the 4 m deformable secondary mirror, the authors identify the superior resilience of CFRP as a significant advantage over more traditional materials such as Zerodur, which are essentially brittle. The absence of stringent requirements for handling and transportation will make the use of CFRP overall more cost-effective and lower-risk. With regards to problems with stability against environmental conditions, they argue that dedicated research can address the issues and produce feasible and

---

[2] the abbreviation 'ASM' will be used for simplicity, referring to any large adaptive mirror, secondary, tertiary or quaternary, in the main optical path of the telescope.

cost-effective solutions.

An FEA study of this mirror was carried out (Riewaldt, 2003) to compare the performance of different classes of CFRP for different plate thicknesses. A thickness of 2.1 mm was found to be suitable for a high-modulus composite. The author also concluded that:

- a composite based on high-modulus fibres is more attractive as it allows for a thinner shell, which in turn enables closer packing of the actuators and lower force requirements for a given stroke;
- further work is required in the following areas:
    identifying the optimal resin/fibre combination;
    - which lay-up sequence is optimal;
    - the possibility and cost of an experimental demonstrator;
    - characterization of edge effects;
- a new type of support for the centre of the mirror is necessary.

A feasibility study is currently under way for an adaptive secondary mirror for a VLT unit telescope (see chapter 2), using the MMT/LBT/OWL design. This is an important precursor project to the ELT designs which will reveal if the technology is reliable and mature enough for scaling up to 4 m class adaptive mirrors. The following section will discuss some preliminary results from this study, and show that CFRP mirror technology could indeed prove a viable alternative technology.

5.3.1 Case study: FE analysis of an adaptive secondary mirror for VLT

The work presented in this section is based on results which have not been officially published but appear in a number of presentations to the EU-funded Opticon programme[3], in particular in Gallieni and Biasi (Sep 2004) (hereafter GB04), which are supplemented by additional original models to demonstrate the potential use of CFRP for large adaptive mirrors. The G04 presentation addressed the feasibility of the ASM design as proposed by ESO in Arsenault *et al.* (2004*a*). The project is a collaboration between ESO (D), Arcetri Observatory (I), ADS International (I), Microgate (I) and the Ecole d'Ingénieurs du Canton de Vaud (CH). The design is based on the technology used for the MMT ASM. Table 5.4 summarizes the basic design specifications. Additional constraints are dictated by handling and maintenance requirements, coating and re-coating processes and full compatibility with the existing M2 environment. The maximum allowable weight was set to 390 kg. The adaptive optical requirements are shown in table 5.5.

The aim of this section is to test the findings of GB04 with original models set up at UCL, and investigate if the CFRP technology tested in this thesis could offer superior performance. The work will focus mainly on gravitational sagging, local stiffness and power dissipation. Figure 5.8 shows a computer rendering of the proposed system. All FEA data presented in this section, unless labeled otherwise, are the result of original work carried out at UCL.

Following finite element analysis and analytical studies, it was found that the mass and outer size requirements were within the present capabilities; several other parameters, however, could not be met:

Shell thickness. A minimum thickness of 2 mm is suggested for the Zerodur shell, as handling, installation and maintenance procedures on a thinner shell would cause stresses in excess of the recommended 5 MPa for Zerodur (Glaswerke, Oct 2004;

---

[3] The VLT ASM feasibility study forms part of the Joint Research Activity (JRA) on enabling technologies for adaptive optics

VLT ASM faceplate specifications	
Mirror shape	convex hyperboloid
Radius of curvature	-4553.57±10 mm
Conic constant	-1.669±0.003
Maximum external diameter	1120 mm
Maximum internal diameter	50 mm
Optical quality:	
passive mode	< 0.7” rms slope error
adaptive mode	wavefront error ¡ 15 nm rms
Micro-roughness	< 2 nm rms

Table 5.4: Basic design specifications for the proposed VLT adaptive secondary as outlined by ESO (Arsenault *et al.*, 2004*a*).

Wilson, 1999).

Inner diameter. Handling issues also require the central hole diameter to be significantly bigger than proposed, at 96 mm.

Number of actuators. The design proposed in GB04 features 1170 actuators instead of the specified 1300, corresponding to an actuator spacing of $28.5 < d < 29.6$ mm.

Maximum power dissipation. Calculations predict a power budget of 3535 W for a 2 mm shell at median seeing, which is significantly higher than the specified 1200 W. Approximately 12% of this provides power to the actuators.

Adaptive optical specifications for the VLT ASM	
Number of actuators	1300 (1500 goal)
Actuator geometry	radial or squared
Total actuator stroke	±40-50 μm P-V without tip-tilt
Total interactuator stroke	1.3 μm P-V
Stroke resolution	1-3 nm
Response time (stroke ±) 1 μm	0.5 ms @ 90%
Actuator response time (full stroke)	TBD
Actuator hysteresis	< 1% (full stroke)
Influence function coupling	20±2%
DM surface temperature	Active cooling with monitoring of temperature
Less than 10% of maximum stroke shall be used to correct static aberrations and differential gravitational load	

Table 5.5: Adaptive optical specifications for the proposed VLT ASM (Arsenault *et al.*, 2004*a*).

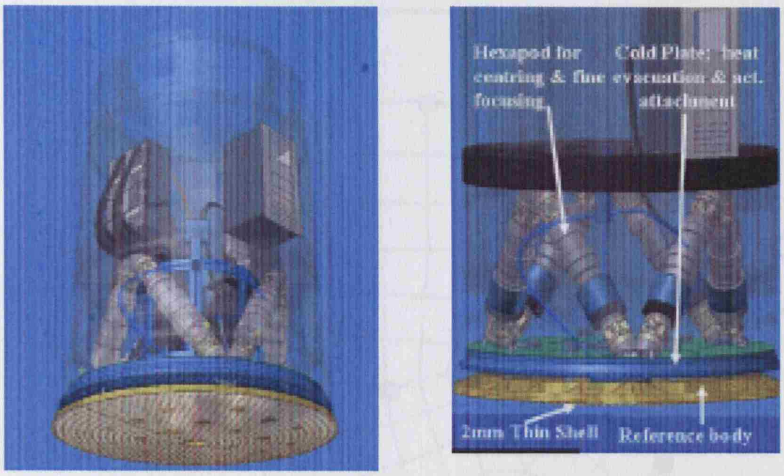

Figure 5.8: CAD drawing of the proposed VLT ASM configuration, showing the thin shell, support structure and hexapod for rigid body control (European Southern Observatory, 2006).

The minimum thickness and actuator spacing requirements in particular will prove difficult to circumvent in this and future ELT projects as they are caused by the material's fundamental properties. Even with improved handling and maintenance procedures it seems that excess stresses on the thin shell will prove an issue.

A finite element model of the VLT ASM design was created in I-DEAS to test the performance of CFRP on some of these points. The results presented in GB04 were verified and repeated with a CFRP material. A segment of the mirror was isolated for investigation of gravitational sagging and local stiffness. Figure 5.9 shows this segment with the actuators, which are placed in a radial arrangement.

The average spacing over this section was $d = 28.3mm$ and $27.5 < d < 28.6mm$; the GB04 model states a separation of $28.5 < d_G < 29.6mm$. Taking respective median values of 28 and 29 mm, this represents a 3.5% reduction in d. The effect of this on the gravitational sag results can be calculated from equation 1.2, which states that a mirror's gravitational sag is proportional to d^4, where d is the distance between supports. Hence:

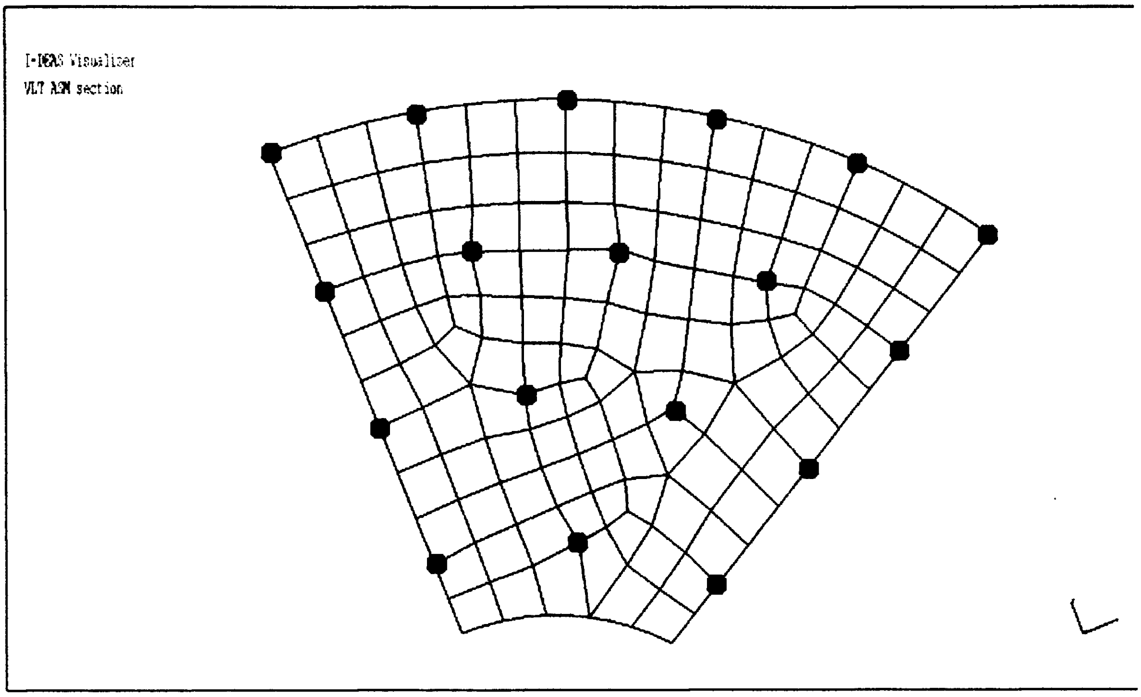

Figure 5.9: Plot of meshed ASM section used for the FEA in I-DEAS, showing the mesh geometry and actuator locations used for the specification of the model boundary conditions.

$$\begin{aligned} (sag) &\propto (0.97 d_G)^4 \\ sag &\propto 0.87 d_G^4 \end{aligned}$$

suggesting that the gravitational sag observed in the new UCL models will be reduced by approximately 13%.

The radius of curvature was set to be infinite for simplicity as the curvature has no significant influence on the gravitational sag or stiffness. In the CFRP models no coating was included for the same reason (see also chapter 2). The CFRP material was created as an isotropic material with the equivalent properties produced by the software for a balanced quasi-isotropic lay-up. This method provides perfect agreement between the algorithms used by the software.

Material	t (mm)	m (kg)
Zerodur	2	19.8
Zerodur	1.6	15.8
CFRP	2	14.08
CFRP	1.6	11.27
CFRP	1	7.04

Table 5.6: Details of materials and thicknesses modelled in the VLT ASM finite element analysis.

Table 5.6 shows the shell materials and thicknesses modelled together with the shell's projected weight for each, using:

$$m = \rho \times \pi t(r_{outer}^2 - r_{inner}^2) \tag{5.1}$$

where ρ is the material's density ($\rho_{Zer} = 2.52 \times 10^{-6} kg/mm^3$ and $\rho_{CFRP} = 1.8 \times 10^{-6} kg/mm^3$), r_{outer} and r_{inner} the outer and inner diameters, respectively, and t the shell thickness.

The same mesh of 2D shells was used for all the models in table 5.6. The results are discussed in the next sections.

5.3.2 Gravity results

An acceleration of 9810 mm/s^2 was applied to the mirror section in the negative z direction, normal to the mirror plane. The mirror was restrained at its 18 actuator locations, which were modelled as anchor points. This overestimated the sag to some extent as the actuators do not have any physical size in the model. The mirror will in practice also be supported with a hexapod structure so the results are only locally representa-

Material	Thickness (mm)	Rms quilting (nm)
Zerodur	2	2.90
Zerodur	1.6	4.31
CFRP	2	1.57
CFRP	1.6	2.33
CFRP	1	5.55
Zerodur (GB04)	2	3.4*

Table 5.7: Rms quilting results from FEA. * the GB04 results exclude edge effects, however, the calculation method is unknown.

tive. The results quoted in GB04 act as a reference and verification for the method. Table 5.7 shows the rms quilting over the modelled section for the 5 configurations, and figures 5.10 and 5.11 show comparison plots of the 2 mm and 1.6 mm results for Zerodur and CFRP. The result for the 2 mm Zerodur shell at 2.9 nm is 15% lower than the G04 figure of 3.4 nm, which is roughly consistent with the predicted reduction from the smaller actuator separation.

These results show that the quilting for CFRP is significantly reduced from Zerodur for a given thickness. Though no detailed studies are available on this topic, it is felt that thin CFRP shells carry a reduced risk of fracture on handling, transportation and maintenance because of CFRP's excellent resilience and robustness.

Another consequence of the increased stiffness of CFRP is the possibility of significant weight saving where the material is used for the thin shell as well as for the backing plate. Although weight is not as high a priority in ground-based applications as in space missions, reduced weight can allow for a relaxation of tolerances on support structures.

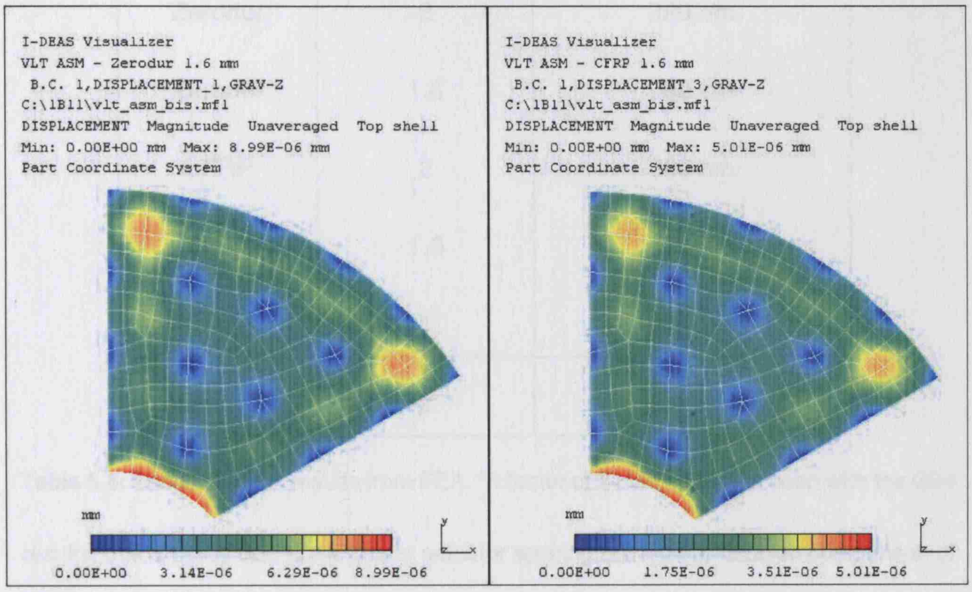

```
I-DEAS Visualizer
VLT ASM - Zerodur 1.6 mm
 B.C. 1,DISPLACEMENT_1,GRAV-Z
C:\1B11\vlt_asm_bis.mf1
DISPLACEMENT  Magnitude  Unaveraged  Top shell
Min: 0.00E+00 mm  Max: 8.99E-06 mm
Part Coordinate System
```

```
I-DEAS Visualizer
VLT ASM - CFRP 1.6 mm
 B.C. 1,DISPLACEMENT_3,GRAV-Z
C:\1B11\vlt_asm_bis.mf1
DISPLACEMENT  Magnitude  Unaveraged  Top shell
Min: 0.00E+00 mm  Max: 5.01E-06 mm
Part Coordinate System
```

Figure 5.10: Gravitational sag results for the 1.6 mm shells: left - Zerodur, right - CFRP. The models show a maximum sag of 8.99 nm for Zerodur and 5.01 nm for CFRP.

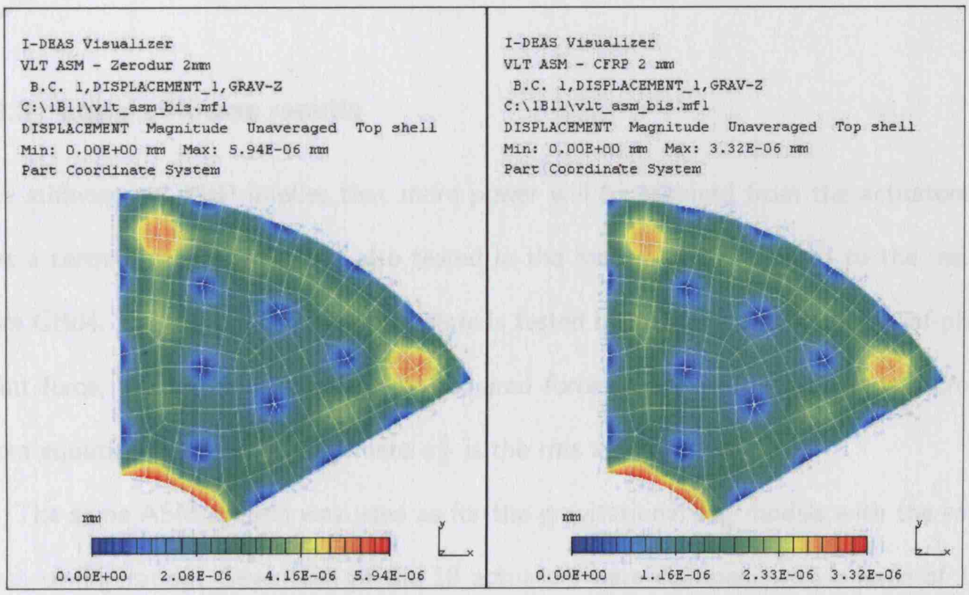

```
I-DEAS Visualizer
VLT ASM - Zerodur 2mm
 B.C. 1,DISPLACEMENT_1,GRAV-Z
C:\1B11\vlt_asm_bis.mf1
DISPLACEMENT  Magnitude  Unaveraged  Top shell
Min: 0.00E+00 mm  Max: 5.94E-06 mm
Part Coordinate System
```

```
I-DEAS Visualizer
VLT ASM - CFRP 2 mm
 B.C. 1,DISPLACEMENT_1,GRAV-Z
C:\1B11\vlt_asm_bis.mf1
DISPLACEMENT  Magnitude  Unaveraged  Top shell
Min: 0.00E+00 mm  Max: 3.32E-06 mm
Part Coordinate System
```

Figure 5.11: Gravitational sag results for the 2 mm shells: left - Zerodur, right - CFRP. The models show a maximum sag of 5.94 nm for Zerodur and 3.32 nm for CFRP.

Material	Thickness (mm)	Max displacement on 1N
Zerodur	2	399 nm
Zerodur	1.6	760 nm
CFRP	2	300 nm
CFRP	1.6	571 nm
CFRP	1	2.26 μm
Zerodur (G04)	2	0.8 μm*

Table 5.8: Local stiffness results from FEA. *A factor of 2 discrepancy is seen with the G04 results; this is partly due to the closer actuator spacing but a more detailed comparison of modelling methods is required for a better understanding.

A lighter shell requires less power to the actuators to provide differential gravity support.

5.3.3 Local stiffness results

The stiffness of CFRP implies that more power will be required from the actuators to give a certain stroke. This was also tested in the models and compared to the results from GB04. Local stiffness of the faceplate is tested by applying a nominal out-of-plane point force, giving information on the required force to achieve a given mirror stroke. From equation 2.4.1, $W \propto \sigma_F^2$ where σ_F^2 is the rms actuator force.

The same ASM section was used as for the gravitational sag models with the same mesh configuration. Seventeen of the 18 actuators were clamped, with a force of 1 N in the out-of-plane direction applied to the remaining actuator. The resulting maximum mirror displacement is shown in table 5.8. Figures 5.12 and 5.13 show FEA plots of these results comparing the 2 mm and 1.6 mm thickness results for Zerodur and CFRP.

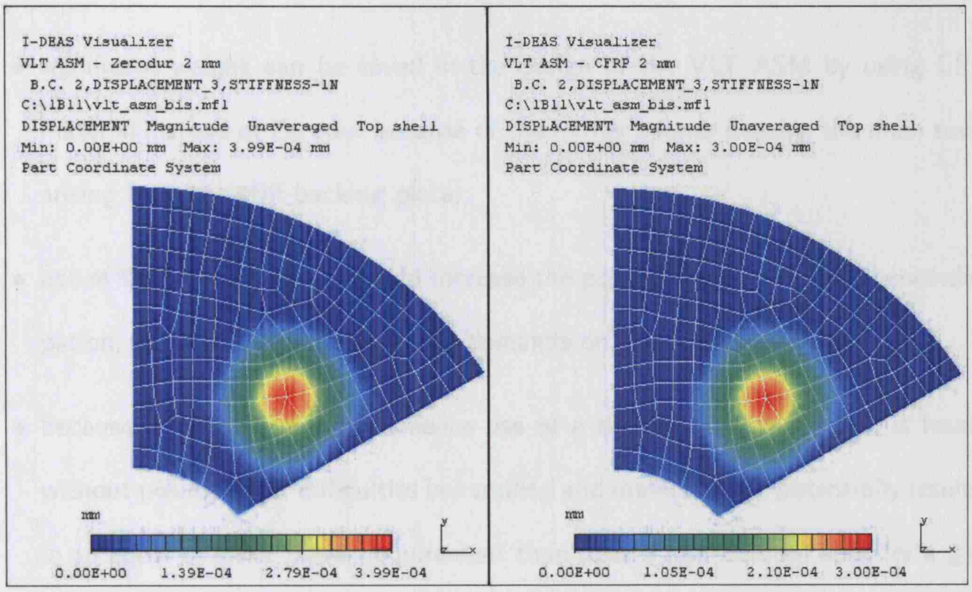

Figure 5.12: Local stiffness results from FEA for 2 mm shells. Left - Zerodur, right - CFRP.

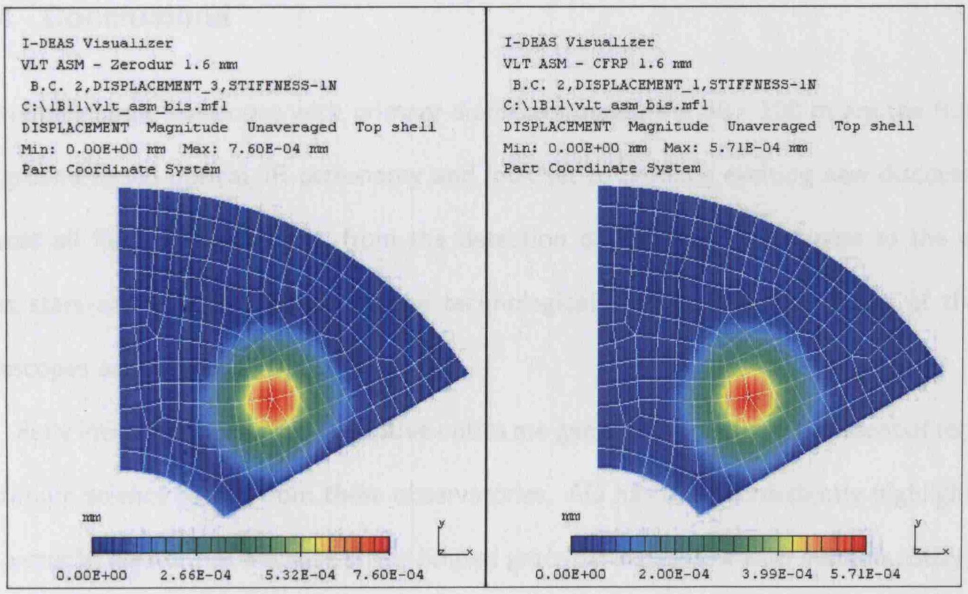

Figure 5.13: Local stiffness results from FEA for 1.6 mm shells. Left - Zerodur, right - CFRP.

5.3.4 Model comparison conclusions

The results presented in this section have shown that:

- significant weight can be saved in the design of the VLT ASM by using CFRP material instead of Zerodur because of the former's lower density, the main saving arising from the stiff backing plate;
- use of CFRP for the shell would increase the power requirement, and hence dissipation, which could pose increased demands on the cooling system;
- because of CFRP's higher resilience use of a thinner (< 2 mm) shell is feasible without posing major difficulties in handling and maintenance, potentially resulting in an equal or lower power requirement than for a 2 mm Zerodur shell for a given stroke, and the possibility of decreasing the actuator spacing on the mirror.

5.4 Conclusions

Extremely large telescopes with primary diameters measuring 30 - 100 m are the future of ground-based optical/IR astronomy and look set to produce exciting new discoveries across all fields of astronomy, from the detection of Earth-like exoplanets to the earliest stars and galaxies. However, the technological challenges in the design of these telescopes are substantial.

Fully integrated active and adaptive optics are generally thought to be essential for an optimum science return from these observatories. AO has been consistently highlighted as a crucial area of risk because of the limited practical experience with systems today; in addition ELTs will require advanced AO observing modes featuring multiple deformable mirrors, integral field units and artificial reference stars.

At least two of the most advanced ELT projects in the world feature large (> 1 m) adaptive mirrors in their baseline optical design; a technology with which experience is limited to just one design, used on the 6.5 m MMT observatory. To investigate the scaleability of thin shell Zerodur design to the sizes required for ELTs, ESO commissioned a feasibility study to implement a 1.1 m deformable secondary mirror for a VLT unit telescope. Preliminary results from this study indicate a potential upper size limit to the technology because of the delicate nature of a mm-class Zerodur shell.

The models from this study were partially repeated to examine the advantages of using CFRP for these large ASMs. The key result from these FEA models, keeping in mind also the experimental results presented in the previous chapters, is that there is no indication that CFRP cannot be a candidate material for these optics. The use of Zerodur, equally, is not a priori excluded but this first suggestion of scaling problems should not be ignored. Because of the increased resilience of CFRP fewer complications with handling and maintenance are expected. The ability to reduce the shell thickness also allows closer packing of the actuators and reduces the force requirements for a given stroke. This has been acknowledged by the Euro50 design study, which highlights CFRP as a promising material for large deformable optics.

These results do not represent an in-depth study of CFRP technology for large ASMs. The final choice of material and system design should be a result of a detailed performance requirements study, the choice of technology for other system components (the telescope optical design, actuator specifications), as well as an in-depth risk analysis.

CHAPTER 6

Summary and future work

Research in carbon fibre composite materials for lightweight optics has been ongoing worldwide for some years. The main advantages of this diverse materials class is their low weight, high strength-to-weight ratio, low thermal expansion and robustness. Although these properties are especially beneficial in space-based applications, interest has grown in the ground-based community in the context of extremely large telescopes (ELTs) - the next generation of ground-based observatories with primary mirror sizes of 30 to 100 m.

Although no space missions have yet implemented active optics for imaging systems, it is widely thought that this step is required to continue the trend towards lighter optics; a first step towards this development has been taken by the introduction of segmented deployable optics for the James Webb Space Telescope (JWST), which require position sensors to ensure alignment of the segments. With CFRP's long history of use in structures for satellites, the evolution towards CFRP optics also seems natural as more research is carried out.

The key conclusion of the project presented is that no fundamental reason has been identified why CFRP is an unsuitable material for active and adaptive mirrors. Indeed, they are likely to form an attractive alternative to traditional materials such as low-expansion glasses and ceramics with the ever-increasing need for lightweight components in space, and the future demand for large adaptive mirrors on ground-based telescopes. However, much research is needed to address the main problems of instability arising from changes in temperature and humidity, in particular in the presence of a reflective coating with different thermal expansion properties.

This chapter will summarize the results from the work presented here and draw conclusions on two main aims of the work: (1) the feasibility of using CFRP materials for active and adaptive mirrors; and (2) the value of finite element analysis (FEA) in optical design and simulations. A third section will summarize the conclusions from chapter 5 and possible future work will be discussed.

6.1 CFRP for deformable optics in space and on the ground

Work on the design, manufacture and testing of the passive test mirror (chapter 3 showed that the traditional replication technique and Cobham Composite's in-mold nickel coating process can produce spherical mirrors with form errors of the order of 10 μm. Whilst this is insufficient for a passive optic, the magnitude of this error lies within the likely stroke range of shape control actuator. Good mirror form is however very valuable for metrology and testing purposes, and to optimize active and adaptive control.

Manual polishing resulted in a surface roughness below 5 nm; this can certainly be improved upon with experience. Sandwich cores are an effective way of stiffening a laminate without adding extra weight. Further research is necessary to examine the contribution to residual stresses of these cores.

The nickel coating method was shown not be optimal for the manufacture of precision optics because of the CTE mismatch between nickel and the composite substrate, which introduces significant stresses on post-cure cooling, as well as instabilities on temperature variations in operation. This was predicted by finite element analysis and confirmed by simple stability tests. It was shown that a matching nickel coating on the mirror's back surface can redress the balance in the laminate and minimize the stresses on heating or cooling; however, more research is needed to investigate the effect of variation in coating thickness.

Development of an active mirror requires connection of the faceplate to shape control actuators, of which many types and designs are available; in most cases a support structure is required to act as a position reference for the actuators. The design chosen in this project followed from an earlier project at UCL which was not designed for low weight. The faceplate was produced using the same manufacturing and coating process as the passive test mirror, and proved to be lightweight and robust.

The influence functions showed a good shape and symmetry, and detailed analysis of the central actuator IF revealed a high level of agreement with finite element predictions and theoretical predictions. Coupling between the actuators validated the inclusion of flexures to allow bending of the faceplate beyond the adjacent actuator position and relieve stresses.

Dynamical testing of the active mirror resulted in a deterioration of the faceplate form. The main observation was the appearance of marked dips over the actuator locations, which was attributed to compression of the adhesive layer between actuator pads and faceplate. This highlights the importance of adhesive selection, and of the importance of preliminary research and testing in materials and components selection in general. An observed increase in the rms surface form over time also indicates the need for further detailed studies with such composite prototypes to characterize the material's behaviour under varying conditions.

6.2 Finite element analysis for optical design and simulations

FEA results presented in chapter 3 have highlighted the value of this powerful modelling method in the material selection for and design of optical components. In particular where novel or little-known materials are involved, it provides an excellent starting point for predicting material behaviour under varying environmental or load conditions. FEA, being an approximate method, should however not replace or supersede experimental findings.

Actuator influence functions are of high importance in the design of deformable mirrors, especially in adaptive optics. A finite element-based theory developed over a decade ago by Ealey and Wellman (1989) is tested against experimental and modelling results from the active mirror. The theory provides a means of predicting IF shapes from basic parameters of the mirror, the faceplate material and the coupling geometry. A better agreement was found with both the FEA and the test results than for the more traditionally used Gaussian shape. Although the work here is too limited in scope to draw definitive conclusions, its application to large scale integrated adaptive optical simulations can improve the accuracy of results, and hence the accuracy of performance predictions.

The finite element IF shape prediction also agreed well with the observed central actuator shape, despite several assumptions made in the modelling process. This agreement proves that the usefulness of FEA in optical design can be extended to precision shape predictions for applications such as adaptive optics. This can aid greatly in the design of active and adaptive optical systems, support structures and connecting elements such as flexures. Integration of FEA results into optical design is currently carried out on an ad hoc basis; a platform for seamless integration is felt to be a valuable area of research.

6.3 CFRP optics for extremely large telescopes

Chapter 5 discussed the huge scientific promise of ELTs with primary mirror diameters of 30-100m, as well as the immense challenge of providing the necessary fully integrated active and adaptive control for these telescopes. Key science goals include the detection of extrasolar planetary systems with Earth-like planets; the resolution and spectroscopic study of stellar populations in galaxies to the Virgo cluster; and probing the history of the earliest stars and galaxies.

At least two of the three major projects presented in the chapter include at least one large (4-8 m) adaptive mirror in the baseline optical design, and experience with these optics is very limited. A case study of the proposed VLT adaptive secondary mirror highlights some of the potential problems of scaling up the existing thin shell technology to such sizes.

Initial finite element results show that, again, no fundamental reason is present why CFRP is not a viable alternative. Indeed, the use of composites materials for thin shell as well as support structure would lead to significant weight saving and allow for a thinner shell without increased risk of failure as compared with the Zerodur design. The promise of composite materials has been recognized in the 50 m Euro50 design, which plans to use CFRP for its adaptive secondary mirror.

6.4 Future work

Compared with glasses, ceramics and metals, experience with CFRP optics is minimal. This thesis, and several other publications referenced in chapter 3, have demonstrated the promise of the technology for ground- and space-based applications. Several avenues for future work have been identified.

Further experimental work with CFRP optics. Because of the numerous possible fibre-matrix combinations an immense variety in material specifications within the composites class is available. More experimental research is needed with CFRP optics to gain a better understanding of different materials' behaviour under varying conditions on a micrometer-nanometer scale. This is particularly important for progress in precision CFRP optics. Testing of composites cited in the literature is often carried out in an industrial setting and these results are not always applicable to the conditions required for space- or ground-based astronomy.

Coating technologies. Processes for applying an optically reflective coating to a curved composite substrate are of crucial importance to the technology. The method used in this project has proved to be sub-optimal because of the CTE mismatch between the nickel and the substrate combined with the in-mold coating process; a cold coating process would avoid the introduction of stresses from the outset. The ability to deposit a coating on the mirror's back surface would also allow the laminate to remain balanced, thus reducing the stresses on varying temperatures.

Finite element analysis for active and adaptive optics. FEA was shown to be a powerful tool in performance prediction of deformable mirrors, even in the case of a complex non-isotropic material such as CFRP. This suggests that FEA could and should form an integral part of the optical design process. This is currently implemented on an ad hoc level; the development of integration platforms, in the form of dedicated software or algorithms, would provide a valuable tool to the optical designer as it would allow gravitational, thermal or vibrational effects to be directly taken into account in a user-friendly fashion at the design stage.

Finite element-based influence function shape prediction. Results in this thesis tentatively suggest that the Guassian IF shape currently used in the majority of adaptive optical performance simulations can be replaced by a finite element-based metric. The cubic polynomials from Ealey and Wellman (1989), whose coefficients are directly based on the deformable mirror's baseline parameters, provide a better fit to the measure shape. Though the use of these parameters should be further tested against known systems, their use could provide a means of improving the accuracy of simulation results without compromising on computation time or load. In the framework of ELT research, where precise characterization of AO systems is necessary and simulations place huge demands on computational power, this could prove a highly valuable development.

LIST OF PUBLICATIONS

The following papers are based on work described in this thesis.

Kendrew, Doel, Brooks, Dorn, Yates, Dwan, Richardson and Evans (2006) (in press)

Kendrew and Doel (2004)

Doel, Kendrew, Brooks, Dorn, Yates, Dwan, Richardson and Evans (2004)

Acknowledgements

Without the help and support I've received in the last four years from a huge number of people this thesis might not have come into existence. So here is my long list - thanks guys.

First of all on a professional level I am indebted to my supervisor, Peter Doel, who relentlessly pushed me through the work whether I liked it or not, and encouraged me to pursue my own side-avenues. David Brooks was always an invaluable source of knowledge on optics, always willing to lend an ear or a hand. I also benefited lots from working with our industrial collaborators Chris Dorn, Richard Dwan, Glyn Dando and Chris Yates at QinetiQ and Ian Richardson and Glynn Evans at Cobham Composites. A special thanks to Chris Yates for his patience in getting me started in FEA and making time to see me, to Andrew King in OSL for helping me with software issues, and to Jeremy Yates, my second supervisor, for providing very useful feedback on my thesis in its final stages.

Various people at the University of Durham and the UK Astronomy Technology Centre in Edinburgh have supported me in my work over the years, and given me excellent advice and encouragement on occasions when I was in need of a morale booster.

My research would of course never happened without the kind people who funded me throughout my PhD - the Group A and Perren funds. Thanks also to Steve Welch who got me signed up as a Faraday Associate; I met lots of interesting people through the Faraday Partnerships, who will undoubtedly prove to be useful contacts in the future.

I am very grateful to everyone else in OSL for moral and professional support, in particular Sam Thompson, Chris King, Matt Callender and Matt Cassie. I am very thankful for the support and advice I received on many occasions from Richard Bingham, whom we were very sad to lose as a colleague and friend in 2005.

Several people in the department helped me out in the final stages of my PhD with LaTeX or proofing parts of my thesis - in particular Nate Bastian, Adam Burnley, Anais Rassat and Chris Lintott, as well as Tammay Nguyen who helped me set up the thesis style files. Group A has been good to me these last few years and the support I've had from all the other students and postdocs, too many to list but you know who you are, has been fantastic. My fabulous friends and flatmates have played a great part in helping me keep my sanity throughout this long-winded process so lots of love and kisses to you all (don't be shy now!). An extra-special mention also to my family in Belgium who have been with me all the time, you're the best.

A final big thanks to Chris Evans, my most excellent companion in life and travels for the most part of this PhD. You've had a huge part in every aspect of this thesis, more than you know. Big hugs, h.s.

Bibliography

Abahamid, A., Vernin, J., Benkhaldoun, Z., Jabiri, A., Azouit, M. and Agabi, A., 2004, *Astron. Astrophys.*, **422**, 1123

Abusafieh, A., 2003, in W. A. Goodman (ed.), *Proc. SPIE vol. 5179, Optical materials and structures technologies*, pp. 303–310

Abusafieh, A., Federico, D., Connell, S., Cohen, E. I. and Willis, P. B., 2001, in A. E. Hatheway (ed.), *Proc. SPIE vol. 4444, Optomechanical design and engineering*, pp. 9–16

Andersen, T., Ardeberg, A. and Owner-Petersen, M. (eds.), 2003, *Euro50: Design study of a 50 m adaptive optics telescope* (Lund Observatory)

Angel, R. and Woolf, N., 1998, in E. Smith and A. Koratkar (eds.), *Science with the NGST* (ASP), volume 133 of *ASP Conference Series*, pp. 172–187

Arsenault, R., Hubin, N. and Conzelman, R., 2004*a*, *Development of an adaptive secondary mirror for the VLT*, Presentation to the Opticon JRA1

Arsenault, R., Hubin, N., Le Louarn, M., Monnet, G. and Sarazin, M., 2004*b*, *The Messenger*, **115**

Arzberger, S. C., Munshi, N. A., Lake, M. S., Wintergest, J., Varlese, S. and Ulmer, M. P., 2003, in W. A. Goodman (ed.), *Proc. SPIE vol. 5179, Optical materials and structures technologies*, pp. 143–154

Bansemir, H. and Haider, O., 1998, *Cryogenics*, **38**, 51

Barkana, R. and Loeb, A., 2001, *Physics Reports*, **349**(2), 125

Bastian, N., Gieles, M., Efremov, Y. N. and Lamers, H. J. G. L. M., 2005, *Astron. Astrophys.*

Bauereisen, S., Deyerler, M., Harnisch, B. and Papenburg, U., 1995, in J. P. Rozelot and W. Livingston (eds.), *Proceedings of the international workshop on mirror substrate alternatives* (OCA/CERGA), pp. 75–80

Becker, A. A., 2004, *An introductory guide to finite element analysis* (Professional Engineering Publishing Ltd.)

Bely, P. Y., 2000, in E. P. Smith and K. S. Long (eds.), *Astronomical Society of the Pacific Conference Series vol. 207, NGST science and technology exposition*, pp. 25–36

Bennett, H. E., Romeo, R. C., Shaffer, J. J. and Chen, P. C., 2004, in A. L. Ardeberg and T. Andersen (eds.), *Proc. SPIE vol. 5382, Second Bqckqskog workshop on extremely large telescopes*, pp. 526–532

Bennett, R. J. and Baine, F., 2004, in S. C. Craig and M. J. Cullum (eds.), *Proc. SPIE vol. 5497, Modeling and systems engineering for astronomy*, pp. 91–102

Bigelow, B. C., 1996, *Deformable secondary mirrors for adaptive optics*, Ph.D. thesis, University of London

Bigelow, B. C., Walker, D. and Nixon, G., 1997, in A. Ardeberg (ed.), *Proc. SPIE vol. 2871, Optical telescopes of today and tomorrow*, pp. 910–919

Bigelow, B. C., Walker, D. D., Bingham, R. G. and D'Arrigo, P., 1993, *Feasibility of deformable secondary mirrors for adaptive optics and IR chopping*, Technical report, Optical Science Laboratory, University College London

Blain, A. W., Jameson, A., Smail, I., Longair, M. S., Kneib, J. P. and Ivison, R. J., 1999, *Mon. Not. R. Astron. Soc.*, **309**, 715

Brauer, J. R., 1993, in J. R. Brauer (ed.), *What every engineer should know about finite element analysis* (Marcel Dekker Inc.), chapter 2, pp. 9–24

Britton, M. C., 2006, *Pub. Astron. Soc. Pac.*, **118**, 885

Brooks, D., 2003, *Report on polishing the passive carbon fibre mirror*, Technical report, UCL

Bryte Technologies Inc., Jan 2003, *Technical datasheet: EX1515 resin system*

Burge, J. H., Angel, J. R. P., Cuerden, B., Martin, H. M., Miller, S. M. and Sandler, D. G., 1998, in *Proc. SPIE vol. 3356, Space Telescopes and Instruments V*, pp. 690–701

Burge, J. H., Cuerden, B. and Angel, J. R. P., 2000, in J. B. Breckinridge and P. Jakobsen (eds.), *Proc. SPIE vol. 4013, UV, optical and IR space telescopes and instruments*, pp. 640–648

Cavarroc, C., Boccaletti, A., Baudoz, P., Fusco, T. and Rouan, D., 2005, *Astron. Astrophys.*, **in press**

Chauvin, G., Lagrange, A., Dumas, C., Zuckerman, B., Mouillet, D., Song, I., Beuzit, J. and Lowrance, P., 2005, *Astron. Astrophys.*, **438**, L25

Chelli, A., 2005, *Astron. Astrophys.*, **441**, 1205

Chen, P., Bowers, C., Content, D., Marzouk, M. and Romeo, R., 2000, *Optical Engineering*, **39**(9), 2329

Chen, P. C. and Romeo, R. C., 2004, in A. L. Ardeberg and T. Andersen (eds.), *Proc. SPIE vol. 5382, Second Backaskog Workshop in Extremely Large Telescopes*, pp. 397–403

Chen, P. C., Saha, T. T., Smith, A. M. and Romeo, R., 1998, *Optical Engineering*, **37**(2), 666

Cripps, D., 2005, *in Guide to Composites*, online, www.netcomposites.com/education.asp

Crowther, P. A., 2006, in Lamers, Langer and Nugis (eds.), *Stellar evolution at low metallicity: mass loss, explosions, cosmology*, ASP Conference Series (in press)

Dando, G., Jan 2005, Private communication

Dekany, R., Britton, M., Gavel, D., Ellerbroek, B., Herriot, G., Max, C. and Veran, J., 2004, in D. Bonaccini Calia, B. Ellerbroek and Ragazzoni (eds.), *Proc. SPIE vol. 5490, Advancements in adaptive optics*, pp. 879–890

Devaney, N. and Owner-Petersen, M., 2001, *The ORM seven layer standard atmosphere*, Technical report, Lund Observatory, Instituto Astrofisica de Canarias

Devilliers, C. and Krödel, M., 2004, in E. Atad-Ettedgui and P. Dierickx (eds.), *Proc. SPIE vol. 5494, Optical fabrication, metrology and material advancements for telescopes*, pp. 285–296

Dierickx, P., 2001, in R. Ragazzoni, S. Esposito and N. Hubin (eds.), *Proc. of the ESO Workshop, Beyond Conventional Adaptive Optics*, pp. 65–73

Dierickx, P., 2002, in *Beyond conventional adaptive optics : a conference devoted to the development of adaptive optics for extremely large telescopes. Proceedings of the Topical Meeting held May 7-10, 2001, Venice, Italy. Edited by E. Vernet, R. Ragazzoni, S. Esposito, and N. Hubin. Garching, Germany: European Southern Observatory, 2002 ESO Conference and Workshop Proceedings, Vol. 58, ISBN 3923524617, p. 65*

Dierickx, P., Brunetto, E. T., Comeron, F., Gilmozzi, R., Gonte, F. Y. J., Koch, F., Le Louarn, M., Monnet, G. J., Spyromilio, J., Surdej, I., Verinaud, C. and Yaitskova, N., 2004, in J. Oschmann (ed.), *Proc. SPIE vol.5489, Ground-based telescopes*, pp. 391–406

Doel, P., Kendrew, S., Brooks, D., Dorn, C., Yates, C., Dwan, R. M., Richardson, I. and Evans, G., 2004, in D. Bonnaccini Calia, B. Ellerbroek and R. Ragazzoni (eds.), *Proc. SPIE vol. 5490, Advancements in adaptive optics*

Ealey, M. A., Pohlhammer, C. F. and Wellman, J. A., 1996, in A. E. Hathaway (ed.), *Proc. SPIE vol. 2865, Actuator technology and applications*, pp. 42–45

Ealey, M. A. and Wellman, J., 1989, in *Precision engineering and optomechanics; Proceedings of the Meeting, San Diego, CA, Aug. 10, 11, 1989 (A91-20951 07-74). Bellingham, WA, Society of Photo-Optical Instrumentation Engineers, 1989, p. 66-84.*, pp. 66–84

Ellerbroek, B., Britton, M., Dekany, R., Gavel, D., Herriot, G., Macintosh, B. and Stoesz, J., 2005, in R. K. Tyson and M. Lloyd-Hart (eds.), *Proc. SPIE vol. 5903, Astronomical adaptive optics systems and applications II*, p. in press

Enard, D., Maréchal, A. and Espiard, J., 1996, *Rep. Prog. Phys.*, **59**, 601

Etrema Products Inc., 2002, *Actuator Line Specifications*, Technical report

European Southern Observatory, 1998, *The VLT Whitebook*, online, http://www.eso.org/outreach/ut1fl/whitebook/index.html

European Southern Observatory, 2006, *OWL Concept Design Report: Phase A design review*, online, http://www.eso.org/projects/owl/

Evans, C., Smartt, S., Lennon, D., Dufton, P., Hunter, I., Mokiem, R., De Koter, A. and Irwin, M., 2005, *The Messenger*, **122**, 36

Foy, R. and Labeyrie, A., 1985, *Astron. Astrophys.*, **152**, 129

Fried, D. L., 1965, *J. Opt. Soc. Am.*, **55**, 1427

Gallieni, D. and Biasi, R., Sep 2004, *VLT adaptive secondary study: IF's analysis and straw man design*, Presentation to the Opticon JRA1

Gilmozzi, R., Delabre, B., Dierickx, P., Hubin, N. N., Koch, F., Monnet, G., Quattri, M., Rigaut, F. J. and Wilson, R. N., 1998, in *Proc. SPIE Vol. 3352, p. 778-791, Advanced Technology Optical/IR Telescopes VI, Larry M. Stepp; Ed.*

Glaswerke, S., 2006, *Zerodur Glass Ceramic*, Technical report

Glaswerke, S., Oct 2004, *Report TIE33: Design strength of optical glass and ZERODUR*, Technical report

Goncharov, A., 2003, *Extremely Large Telescopes: Optical design and wavefront correction*, Ph.D. thesis, University of Lund

Goncharov, A., Owner-Petersen, M., Andersen, T., Beckers, J. and Devaney, N., 2002, in J. R. P. Angel and R. Gilmozzi (eds.), *Proc. SPIE vol. 4840, Future Giant Telescopes*, pp. 36–46

Greenwood, D. P., 1977, *J. Opt. Soc. Am.*, **67**, 174

Hardy, J., 1998, *Adaptive optics for astronomical telescopes* (Oxford University Press)

Hile, T., 2005, *in Guide to Composites*, online, www.netcomposites.com/education.asp

Hobbs, T. W., Edwards, M. J. and VanBrocklin, R. R., 2003, in W. A. Goodman (ed.), *Proc. SPIE vol. 5179, Optical materials and structures technologies*, pp. 1–11

Hook, I. and Gilmore, G. (eds.), 2005, *The science case for the European Extremely Large Telescope* (Holly Benson Communications)

Kendrew, S. and Doel, A. P., 2004, in D. Bonaccini Calia, B. Ellerbroek and R. Ragazzoni (eds.), *Proc. SPIE vol. 5490, Advancements in adaptive optics*, pp. 1591–1599

Kendrew, S., Doel, A. P., Brooks, D., Dorn, C., Yates, C., Dwan, R. M., Richardson, I. and Evans, G., 2006, *Optical Engineering*, **45**(3)

King, A. M., Feb 2006, *Description of MatLab for Wyko data analysis*, Private communication

Krödel, M., 2004, in E. Atad-Ettedgui and P. Dierickx (eds.), *Proc. SPIE vol. 5494, Optical fabrication, metrology and material advancements for telescopes*, pp. 297–310

Lardiere, O., Salinari, P., Jolissaint, L., Carbillet, M., Riccardi, A. and Esposito, S., 2004, in A. L. Ardeberg and T. Andersen (eds.), *Proc. SPIE vol. 5382, Second Backaskog Workshop on Extremely Large Telescopes*, pp. 550–559

Lee, J. H., 1999, *A deformable secondary demonstrator for adaptive optics*, Ph.D. thesis, University of London

Lee, J. H., Walker, D. D. and Doel, A. P., 1999*a*, *Optical Engineering*, **38**, 1456

Lee, J. H., Walker, D. D. and Doel, A. P., 2000, *Optical Engineering*, **39**, 1057

Lee, J. H., Yan, P., Walker, D. D. and Bingham, R. G., 1999*b*, in D. Bonaccini (ed.), *Proc. of the ESO/OSA topical meeting on astronomy with adaptive optics: present results and future programs*, pp. 235–240

Lilly, S., 2000, in E. P. Smith and K. S. Long (eds.), *NGST Science and Technology Exposition, ASP Conference Series*, volume 207, pp. 226–239

Lloyd-Hart, M., Brusa, G., Wildi, F. P., Miller, D. L., Fisher, D. L. and Riccardi, A., 2003, in *Astronomical Adaptive Optics Systems and Applications. Edited by Tyson, R. K.; Lloyd-Hart, M. Proc. SPIE, Vol. 5169, pp. 79-89*

Lorell, K. R., Aubrun, J., Clappier, R. R., Shelef, B. and Shelef, G., 2003, in J. R. P. Angel and R. Gilmozzi (eds.), *Proc. SPIE vol. 4840, Future Giant Telescopes*, pp. 471–485

Lukin, V., Goncharov, A., Owner-Petersen, M. and Andersen, T., 2003, in G. G. Matvienko and V. P. Lukin (eds.), *Proc. SPIE vol. 5026, Ninth Joint Symposium on Atmospheric and Ocean Optics/Atmospheric Physics: Part I*, pp. 120–126

MacLean, J. F., 2000, in H. Lewis (ed.), *Proc. SPIE vol. 4009, Advanced telescope and instrumentation control software*, pp. 276–287

MacNeal, B., 1993, in J. Brauer (ed.), *What every engineer should know about finite element analysis* (Marcel Dekker Inc), chapter 9, pp. 289–314

Madec, P. Y., 1999, in Roddier (1999), chapter 6, pp. 131–154

Martin, F., Conan, R., Tokovinin, A., Ziad, A., Trinquet, H., Borgnino, J., Agabi, A. and Sarazin, M., 2000, *Astron. Astrophys. Suppl. Ser.*, **144**, 39

Martin, H. M., Cuerden, B., Dettmann, L. R. and Hill, J. M., 2004, in J. M. Oschmann (ed.), *Proc. SPIE vol. 5489, Ground-based telescopes*, pp. 826–837

Matson, L. E. and Mollenhauer, D., 2003, *Proc. IEEE*, **4**, 1681

Matthews, F. L., Davies, G. A. O., Hitchings, D. and Soutis, C., 2003, *Finite element analysis of composite materials and structures* (CRC Press)

Max, C., 2003, *Concepts of wavefront error and wavefront budget*, Lecture notes, 2003

McCray, W., 2004, *Giant telescopes: astronomical ambition and the promise of technology* (Harvard University Press)

Mueller, R. W., Hoeness, H. W. and Marx, T. A., 1990, in L. D. Barr (ed.), *Proc. SPIE vol. 1236, Advanced technology optical telescopes IV*, pp. 723–734

Myers, R. M., Longmore, A. L., Benn, C. R., Buscher, D. F., Clark, P., Dipper, N. A., Doble, N., Doel, A. P., Dunlop, C. N., Gao, X., Gregory, T., Humphreys, R. A., Ives, D. J., Oestensen, R., Peacocke, P. T., Rutten, R. G., Tierney, C. J., Vick, A. J. A., Wells, M. R., Wilson, R. W., Worswick, S. P. and Zadrozny, A., 2003, in

P. L. Wizinowich and D. Bonaccini (eds.), *Proc. SPIE vol. 4839, Adaptive Optical System Technologies II*, pp. 647–658

Nakagawa, T. *et al.*, 2004, *Advances in Space Research*, **34**, 645

Nelson, J., 2003, in J. R. P. Angel and R. Gilmozzi (eds.), *Proc. SPIE vol. 4840, Future Giant Telescopes*, pp. 47–59

Noethe, L., 1991, *J. Mod. Optics*, **38**(6), 1043

Noethe, L., Franza, F., Giordano, P., Wilson, R. N., Citterio, O., Conti, G. and Mattiani, E., 1988, *J. Mod. Optics*, **35**(9), pp. 1427

Noll, R. J., 1976, *J. Opt. Soc. Am.*, **66**(3), 207

Northcott, M. J., 1999, in Roddier (1999), chapter 7, pp. 155–168

Ozaki, T. and Hahn, S., 2003, in A. Ardeberg and T. Andersen (eds.), *Proc. SPIE vol. 5382, Second Backaskog workshop on extremely large telescopes*, pp. 305–312

Parks, R. E., Wortley, R. W. and Cannon, J. E., 1990, in L. D. Barr (ed.), *Proc. SPIE vol. 1236, Advanced technology optical telescopes IV*, pp. 735–743

Parsonage, T., 2004, in E. Atad-Ettedgui and P. Dierickx (eds.), *Proc. SPIE vol. 5494, Optical fabrication, metrology and material advancements for telescopes*, pp. 39–48

Pauschinger, D., Egle, W. J., Glatzel, H., Salmen, H. and Becker, W., 1994, in R. B. Hoover (ed.), *Proc. SPIE vol. 2011, Multilayer and grazing incidence X-ray/EUV optics II*, pp. 138–148

Pearson, J. E. and Hansen, S., 1977, *J. Opt. Soc. Am.*, **67**(3), 325

Physik Instrumente, 1996-2006, *Fundamentals of piezoelectricity*, online, http://www.physikinstrumente.com/en/products/prdetail.php?sortnr=400600.00

Ragazzoni, R., Nov 2004, private communication

Rawal, S., 2001, *Journal of Materials*, **53**(4), 14

Riccardi, A., Brusa, G., Del Vecchio, C., Biasi, R., Andrighettoni, M., Gallieni, D., Zocchi, F., Lloyd-Hart, M., Martin, H. M. and Wildi, F., 2001, in E. Vernet, R. Ragazzoni, S. Esposito and N. Hubin (eds.), *ESO Workshop and Conference Proceedings, vol. 58, Beyond conventional adaptive optics*, pp. 55–64

Riewaldt, H., 2003, *M2 Study: thickness and actuator force (Euro50 technical note)*, Technical report, Lund Observatory

Riewaldt, H., Lastiwka, M., Quinlan, N., McNamara, K., Wang, X., Andersen, T. and Shearer, A., 2004, in J. Antebi and D. Lemke (eds.), *Proc. SPIE vol. 5495, Astronomical structures and mechanisms technology*, pp. 537–548

Roddier, F., 1981, *Progress in Optics*, **19**, 281

Roddier, F. (ed.), 1999, *Adaptive optics in astronomy* (Cambridge University Press)

Roddier, F., 1999, in Roddier (1999), chapter 2, pp. 9–22

Rozelot, J. P., 1995, in J. P. Rozelot and W. Livingston (eds.), *Proc. of the international workshop on mirror substrate alternatives* (OCA/CERGA), pp. 3–18

Salinari, P., Del Vecchio, C. and Biliotti, V., 1993, in F. Merkle (ed.), *Proc. ISO-16 Satellite Conference on Active and Adaptive Optics*, pp. 247–254

Schier, J. A., 2001, *Summary of the CELT mirror segment actuator survey*, Technical Report CELT report 15, The Pilot Group, La Crescenta, CA

Schneider, J., 2006, *The extrasolar planets encyclopedia*, online, http://vo.obspm.fr/exoplanetes/encyclo/

Schutz, J. B., 1998, *Cryogenics*, **38**, 3

Schwesinger, G., 1988, *J. Mod. Optics*, **35**(7), 1117

Séchaud, M., 1999, in F. Roddier (ed.), *Adaptive optics in astronomy* (Cambridge university press), chapter 4, pp. 57–90

Shih, R. H., 2000, *Introduction to finite element analysis using I-DEAS8* (SDC Publications, Kansas, USA)

Sims, G. and Bishop, G. e., 2001, *UK Polymer composites sector: Foresight study and competitive analysis*, Technical report, National Physical Laboratory and NetComposites for the UK Department of Trade and Industry (DTI)

Soutis, C., 2005, *Progress in Aerospace Sciences*, **41**, 143

Stahl, H. P., 2003, in H. P. Stahl (ed.), *Proc. SPIE vol. 5180, Optical manufacturing and testing V*, pp. 1–5

Stepp, L. and Strom, S. E., 2004, in A. L. Ardeberg and T. Andersen (eds.), *Proc. SPIE vol. 5382, Second Backaskog Workshop on Extremely Large Telescopes*, pp. 67–75

Streetman, S. and Kingsbury, L., 2003, in J. C. Mather (ed.), *Proc. SPIE vol. 4850, IR space telescopes and instruments*, pp. 274–285

Stute, T., Wulz, G. and Scheulen, D., 2003, in W. A. Goodman (ed.), *Proc. SPIE vol. 5179, Optical materials and structures technologies*, pp. 292–302

Takeya, H., Kume, M., Hahn, S., Ozaki, T., Kohara, N., Otsubo, M. and Tsuneta, S., 2004, in J. C. Mather (ed.), *Proc. SPIE vol. 5487, Optical, infrared and millimeter space telescopes*, pp. 1084–1091

Tyson, R. K., 1990, *Optical Engineering*, **29**(10), 1165

Tyson, R. K. and Frazier, B. W., 2004, *Field guide to adaptive optics* (SPIE Press)

UGSPLM, 2002, *I-DEAS Online help collection*, manual

Ulmer, M. P., Graham, M. E., Vaynman, S., Echt, J. I., Ehlert, S. R., Varlese, S. J. and Hermiller, J. M., 2005, in W. A. Goodman (ed.), *Proc. SPIE vol. 5868, Optical materials and structures technologies II (in press)*

Varlese, S. J., Ulmer, M. P., Hermiller, J., Young, K., Graham, M., Vaynman, S. and Snyder, B., 2005, in H. A. MacEwen (ed.), *Proc. SPIE vol. 5899, UV/Optical/IR space telescopes: Innovative technologies and concepts II (in press)*

Walker, D. D., Doel, A. P., Bingham, R. G., Brooks, D., King, A. M., Peggs, G., Hughes, B., Oldfield, S., Dorn, C., McAndrews, H., Dando, G. and Riley, D., 2002, *The primary and secondary mirrors for the proposed Euro50 telescope, A study commissioned by the Instituto de Astrofisica de Canarias on behalf of the Euro50 Project*, Technical report, University College London, Zeeko, NPL, QinetiQ

Walker, D. D., Lee, J. H., Bingham, R. G., Brooks, D., Dryburgh, M., Nixon, G., Jamshidi, H., Kim, S. W. and Bigelow, B., 1998, in D. Bonaccini and R. K. Tyson (eds.), *Proc. SPIE vol. 3353, Adaptive optical system technologies*, pp. 872–878

Wallace, B., Bradley, C. and Hampton, P., 2003, in J. D. Gonglewski and M. A. Vorontsov (eds.), *Proc. SPIE vol. 5162, Advanced wavefront control: Methods, devices and application*, pp. 70–78

Wildi, F. P., Brusa, G., Riccardi, A., Lloyd-Hart, M., Martin, H. M. and Close, L. M., 2003, in *Adaptive Optical System Technologies II. Edited by Wizinowich, P. L.; Bonaccini, D.. Proc. SPIE, Vol. 4839, pp. 155-163*

Wilson, R. N., 1999, *Reflecting telescope optics. Vol I: Basic design theory and its historical developement. Vol. II: Manufacture, testing, alignment, modern techniques* (Springer Verlag), W99

Wilson, R. N., Franza, F., Giordano, P., Noethe, L. and Tarenghi, M., 1989, *J. Mod. Optics*, **36**(11), 1415

Wilson, R. N., Franza, F. and Noethe, L., 1984, in *Proc. of the IAU Colloquium no. 79: Very large telescopes, their instrumentation and programs*, pp. 23–40

Wilson, R. N., Franza, F. and Noethe, L., 1987, *J. Mod. Optics*, **34**(4), 485

Wilson, R. N., Franza, F., Noethe, L. and Andreoni, G., 1991, *J. Mod. Optics*, **38**(2), 219

Winker, D. M., 1991, *J. Opt. Soc. Am.*, **8**(10), 1568

Yates, C., 2003, private communication

Yates, C., 2004, *Progress report: Summary of active mirror modelling (unpublished)*, Qinetiq

Zamkotsian, F., Dohlen, K. and Ferrari, M., 2000, in P. L. Wizinowich (ed.), *Proc. SPIE vol. 4007, Adaptive optical systems technology*, pp. 547–554

Zienkiewicz, O. C. and Taylor, R. L., 2000, *The Finite Element Method, Vol. 1 - The basics, Vol. 2 - Solid mechanics* (Elsevier), 5th edition